Universitat de Girona

BASIN-SCALE HYDRODYNAMICS IN A MEDITERRANEAN RESERVOIR. IMPLICATIONS FOR THE PHYTOPLANKTON DYNAMICS

Javier VIDAL HURTADO

ISBN: 978-84-690-7685-9
Dipòsit legal: GI-716-2007

Basin-Scale Hydrodynamics in a Mediterranean reservoir. Implications for the phytoplankton dynamics.

Javier Vidal Hurtado

Thesis work supervised by
Xavier Casamitjana Vila

Universitat de Girona
Nov 2006

El chiquillico será "més que mestre"
Fortunato Hurtado

INDEX

Acknowledgments

This work was supported by the Spanish government (MEC) through a FPI scholarship associated to the REN2001-2239 project.

Esta tesis ha sido posible gracias a una beca FPI (MEC) asociada al proyecto REN2001-2239.

First of all I would like to thank my director Xavier Casamitjana to provide me with this opportunity and his guidance in the way. Likewise, thanks to the environmental physics group, especially to Marianna Soler, Jordi Colomer and Teresa Serra for their help in the field experiments and a large etc... Gràcies a tots per acollir-me en el vostre grup i per tot el suport que m'heu donat. Arribats a aquest punt espero que sigui tant sols un Hasta luego.

I would like to thank to Jörg Imberger for hosting me in the CWR and provide me with the model CWR-ELCOM. A Sebastian Morillo y Andres Gomez-Giraldo por instruirme con el modelo y sus inestimables comentarios. Also the rest of the CWR members and visitors (Yanti, Ryan, Alessio, Sergio, Laura, Sam, Rocio, Trish, those nice Koalas, etc…) for making an unforgettable stay at Perth.

To Alfred Wüest for hosting me at the APEC-EAWAG, and the rest of the group and visitors I met there (Dan, Daniella, David, Andrea, Maria, Annika, Torsten, Jutta, Alexander, Sonya, and a large etc…). That was a really wonderful experience in a lovely place.

Al Servei Meteorològic de Catalunya, Aigües Ter-Llobregat y la Agencia Catalana del Agua por su colaboración.

Son muchos los que me han ayudado de una u otra forma durante el periodo de realización de esta Tesis, y espero que me perdonen si no les nombro aquí por motivos de tiempo (estoy deseando entregar esta tesis), espacio o meramente despiste… de todas formas gracias a todos.

A Francisco Rueda por cederme los datos de Beznar incluidos en esta tesis y darme la oportunidad de seguir el camino. Joan Armengol, Rafa Marcé y el grupo de ecología de la UB, por su ayuda (una pena no haber tenido una colaboración más fluida o un mejor entendimiento…). A Miguel Alvarez por mirarme las alguitas de Sau. Als meus companys: Imma, Jordi (Bad and Bon), Francesc, Alex, Nuri, Eduard (y su soporte técnico-informático), Lluis, Toni, etc...

Y por supuesto, los más importantes, a mis padres y familia por apoyarme en todo momento y a Bea por estar siempre ahí…

RESUMEN

Procesos hidrodinámicos determinan, en un alto grado, la respuesta ecológica de un embalse frente a agentes externos, tanto meteorológicos como la entrada de ríos o la extracción de agua desde la presa. Debido a esto, la limnología física se ha desarrollado considerablemente en los últimos años. Sin embargo, en embalses españoles, apenas se han llevado a cabo estudios enfocados en los procesos físicos. Ante esta perspectiva, en la presente tesis se ha indagado en los principales procesos que gobiernan la hidrodinámica en los embalses Mediterráneos; enfocando el estudio sobre el embalse de Sau, un embalse de tamaño medio localizado en Cataluña, al noreste de España, aunque resultados obtenidos sobre el embalse de Beznar son introducidos para su comparación. El embalse de Sau fue seleccionado principalmente por dos razones: primero, ser representativo de muchos embalses españoles, y segundo, por ser un embalse ampliamente estudiado desde que se lleno por primera vez en 1964.

Durante los últimos cuatro años (2002-2006) varias campañas experimentales se han llevado a cabo para determinar los principales procesos que afectan a la hidrodinámica de Sau. La presente tesis es fruto de los resultados obtenidos en dichas campañas, en combinación con la aplicación de técnicas numéricas (especialmente el modelo hidrodinámico CWR-ELCOM). Los resultados están expuestos en cinco capítulos, cada uno presentado en formato de articulo con sus propias secciones: introducción, material y métodos, resultados y discusión y/o conclusión. Este hecho hace que algunos conceptos se repitan, pero dotan a cada capítulo de independencia y un sentido global.

El embalse de Sau es un embalse bastante eutrófico, siendo, además, el primero de una cadena de tres embalses que suministran agua al área de Barcelona. Así pues, el estudio de los principales procesos físicos que afectan al embalse y su respuesta ecológica, está de sobra justificado, y puede ser una interesante herramienta de ayuda para su gestión. Sau es un embalse encañonado, que transcurre por el valle del río Ter. La morfología de Sau hace que el embalse esté dividido en dos zonas influenciadas por diferentes agentes externos. La primera zona más abierta, esta comprendida en la parte más ancha del embalse, cerca de la presa; esta parte del embalse se comporta como un lago, influenciada principalmente por el viento reinante. La segunda zona se trata de la zona estrecha con meandros que se extiende valle arriba a hasta la entrada del río Ter. Esta parte del embalse esta abrigada del viento y está dominada por la entrada del río.

Durante la primavera-verano el embalse se estratifica debido al calentamiento producido en las capas superiores, formándose un grueso metalimnion. El viento que actúa en la parte lacustre del embalse genera la aparición de ondas internas

estacionarias, también conocidas como secas internas (*seiches*). En Septiembre del 2003 dos cadenas de termistores a ambos lados de la parte lacustre fueron emplazadas junto con un correntímetro ADCP. Los resultados analizados demostraron la presencia y dominancia de una seca con tres nodos verticales (V3), formada por cuatro capas horizontales oscilando periódicamente. Dicho modo ha sido rara vez descrito en la literatura científica y es considerado como extraño; sin embargo, tras la aplicación de un modelo de dos dimensiones se demostró que la resonancia con el viento fue el desencadenante de que dicho modo dominara en el sistema.

El viento en Sau es bastante constante, y una brisa con periodicidades de 12 y 24 horas domina durante los meses veraniegos, cuando el embalse está estratificado. Durante los meses del verano del 2004, los termistores y correntímetro fueros de nuevo emplazados para estudiar la evolución de las ondas estacionarias sometidas a dicho régimen. De estos estudios se dedujo que el embalse se comporta como un oscilador periódicamente forzado. En Julio un modo vertical dos (V2) con un periodo de 12 horas dominaba en el embalse; y en Septiembre, al igual que durante el 2003, el modo V3 con un periodo de 24 horas dominaba, ambos pues con igual periodicidad que la del viento reinante. La aplicación de un modelo de tres dimensiones (CWR-ELCOM) demostró que los modos dominantes eran los modos naturales con periodo más cercano a los periodos del viento; así pues, dichos modos fueron seleccionados del espectro de modos naturales debido a la resonancia con el viento. Otros modos no resonantes, por el contrario, eran mucho menos importantes en el sistema; así pues, la periodicidad del viento juega un papel fundamental en la excitación de los modos dominantes en Sau. El modelo, también reveló el papel de la zona encañonada con meandros en las ondas internas. En esta zona, otro punto nodal horizontal fue encontrado, oscilando en fase con ambos extremos del embalse en fase; por tanto, en Septiembre, el modo dominante era el llamado V3H2, con tres nodos verticales y dos horizontales. Adicionalmente, el modelo mostró que en la parte central del embalse, donde su anchura es comparable a el radio de deformación de Rosby, el efecto de la rotación hacia girar la seca en el sentido contrario a las agujas del reloj, es decir, como una onda de Kelvin.

En el área Mediterránea hay muchos embalses de tamaño medio que presentan metalímnions anchos y están sometidos a vientos periódicos al igual que Sau. Esté es el caso de el embalse de Beznar, que fue elegido para comparar los resultados obtenidos en Sau. El estudio de la evolución estacional en el embalse de Beznar demostró que dicho embalse también responde a la periodicidad del viento. Así pues, modos V3H1, V4H1 y V5H1, según evolucionaba progresivamente la estratificación, con periodicidad de 24 horas y en resonancia con el viento, fueron dominantes durante el año 2005. Cuando la periodicidad del viento se rompía debido al paso de frentes, modos más sencillos (V1H1 y V2H1) se convertían en dominantes. Estos resultados junto con los obtenidos en Sau, demuestran que en embalses Mediterráneos la periodicidad del viento

juega un papel fundamental en la excitación y dominancia de los modos oscilatorios, y que modos altos complicados pueden ser excitados y comunes debido a la resonancia.

El efecto combinado de viento y ondas internas estacionarias, además de tener un papel importante en la mezcla vertical y en la resuspensión de sedimentos, pueden jugar un papel importante en la distribución del fitoplancton. Así pues, durante el año 2003, se realizaron dos estudios de 24 horas incluyendo medidas horarias con un fluorímetro, para determinar el efecto de las ondas internas en dicha distribución. Dichos experimentos revelaron que las distintas poblaciones de fitoplancton están afectadas por las oscilaciones verticales que producen las ondas internas, de manera que varían la profundidad a la que están situadas, y por tanto también la radiación solar que reciben influyendo así en su crecimiento. Además la advección producida por estas ondas arrastra a las poblaciones, generando heterogeneidades tanto espaciales como temporales en el embalse.

Finalmente la entrada del río en el embalse fue investigada. Estudios anteriores habían descrito la evolución estacional de dicha entrada; sin embargo, dichos estudios no habían tenido en cuenta la variación a pequeñas escalas temporales o a escala diaria. El estudio llevado a cabo durante los últimos días de Julio de 2005 reveló, que la interacción río embalse es muy dinámica, el río pasa rápidamente de insertarse en superficie (*overflow*) a insertarse a cierta profundidad (*interflow*). Dicha variación diaria es debida a la variación diaria en la temperatura del río como consecuencia del ciclo diario. Tener un sistema tan variable origina una gran mezcla vertical en la zona de intersección entre el río y el embalse, es decir, en los primeros kilómetros del embalse. Además, la ocurrencia de *overflows* inyecta agua rica en nutrientes procedente del río en la superficie del embalse, generando un *bloom* de Cianobacterias, bien localizado en la zona donde el agua del río se mezcla con el agua del embalse. Dicho *bloom* pone de manifiesto la importancia de procesos físicos en la respuesta ecológica del embalse. La aplicación de un modelo de calidad del agua acoplado a con el modelo hidrodinámico tridimensional (ELCOM-CAEDYM) revela que dichos eventos pueden ser simulados de forma bastante precisa; por lo que estos modelos pueden ser una herramienta interesante en la gestión de embalses.

SUMMARY

Physical processes determine, to a large degree, the ecological response of a reservoir to inflows, outflows and meteorological forcing. For this reason, physical limnology has developed significantly in recent years. However, not many physical studies have been carried out in Spanish reservoirs. This PhD thesis therefore aims to give an assessment of the main physical mechanisms governing Mediterranean reservoirs. We focus on the Sau reservoir, a medium-sized reservoir located in Catalonia, in the northeast of Spain, but some of the results obtained here can be extended to other medium-sized Mediterranean reservoirs. The Sau reservoir is a quite eutrophic in nature and is the first of three reservoirs that supply drinking water to the Barcelona area. Therefore, having a better understanding of the main physical processes and the ecological response of the reservoir to such processes may be of significant help in its management.

Sau is a canyon type reservoir, which can be divided into two morphological zones each influenced by different forcing agents. The first one, the wide, lacustrine, part of the reservoir is located near the dam. This zone is quite open and behaves as a lake, where the main forcing mechanism is the wind. The second zone (consisting of a riverine zone and a transition zone) is the meandering, narrow part of the reservoir which extends upstream up into just one inflow river, the river Ter. This part of the reservoir is sheltered from the wind and is dominated by the river inflow.

During the Spring-Summer season the reservoir stratifies and a thick metalimnion is formed. The wind forcing in the lacustrine zone generates basin-scale internal waves known as seiches. In September, 2003, two thermistor strings and an ADCP current meter were deployed at both sides of the lacustrine zone. The results analyzed showed that during this period, a vertical mode three seiche (V3), with four oscillating vertical layers, was dominant in the system. This mode has rarely been observed in natural systems but, by using a two dimensional model, it was shown that resonance with the wind was responsible for it being dominant.

The wind in the Sau reservoir is quite constant and a sea-breeze, with periodicities of 24 hours and 12 hours is dominant in the summer months, when the reservoir is stratified. During the summer months of 2004, thermistor strings were again deployed to study the evolution of the basin-scale internal waves under this wind forcing. These studies revealed that the reservoir behaves as a forced oscillator. In July a vertical mode two wave (V2) with a periodicity of 12h dominated the internal wave field but, by September, as in the year 2003, the V3 mode with a period of 24 h was

again dominating the system. The application of a three dimensional model (CWR-ELCOM) showed that the dominant modes were those modes with a natural period similar to the wind forcing period. Thus, these modes were selected out of the spectrum of natural modes in response to the wind resonance. That is to say, the V2 mode with a period close to 12h was excited due to the wind resonance in July and then, as the stratification of the reservoir evolved, the vertical mode V3 - whose natural period was close to the 24 h wind forcing period - was then excited. Other less important modes were found to a lesser extent. The model also revealed that the meandering part of the reservoir played a role in the basin-scale internal waves. In this zone, another horizontal nodal point was found. As a result, the vertical mode V3 associated with an horizontal mode 2 H2, forming the so-called V3H2 mode. In addition, the model also showed that in the central part of the reservoir, where the width is comparable with the internal Rossby radius of deformation, earth rotation made the internal wave rotate anti-clockwise, as in a Kelvin seiche.

In the Mediterranean area, there are a many medium-size reservoirs with a large metalimnion, subjected to periodic winds as in the Sau reservoir. This is the case of the Beznar reservoir, which was chosen for purposes of comparison with the Sau reservoir. The seasonal evolution of the basin-scale internal wave field in Beznar showed that this reservoir responded with dominant modes of 24 h periods, the same period as the wind forcing. As the stratification evolved, modes V3H1, V4H1 and V5H1 were excited and dominated the internal wave field during different periods; all these modes have periods close to 24h and are resonant with the wind. When the wind periodicity was disrupted by the passage of a front, other lower modes (V1H1 and V2H1) become dominant in the system. Those results, together with the results obtained in the Sau reservoir show that, in Mediterranean reservoirs, the wind periodicity plays a fundamental role in the excitation of basin-scale internal waves. Thus, the excitation and dominance of high vertical modes due to wind resonance may be a common feature in these reservoirs.

Internal waves, apart from having an important role in mixing and resuspension of particles, may play a role in the distribution of phytoplankton populations. Therefore, during the year 2003, a 24–hour field experiment in which fluorimeter measurements were taken every hour, was carried out to determine the influence of the internal waves on the different phytoplankton populations in the Sau reservoir. Data from thermistor strings and an ADCP was also available. This experiment revealed that the different populations were affected by the vertical oscillations produced by the internal waves, shifting their vertical position in the water column and therefore the amount of light available to them. Likewise, the induced horizontal advection generated temporal and spatial heterogeneities.

Finally, the river inflow was investigated. Previous studies had described the seasonal circulation of the River Ter into the reservoir; however these studies didn’t

show the short term variations of the inflow. Our study, carried out during the last days of July, 2005, revealed that the river inflow is a highly dynamic system, changing from overflow to interflow in response to the daily temperature variation. These dynamics resulted in the mixing of the inflow along the water column during the first few kilometres after the river entered the reservoir. Furthermore the overflow events injected rich nutrient water into the surface of the reservoir, generating a clearly located bloom of cyanobacteria. This bloom event evidences the biological response to a physical process. The application of a water quality model coupled with the three dimensional model (ELCOM-CAEDYM) reveals that such events can be accurately simulated, making the model an interesting tool for water management.

INTRODUCTION

STATE OF THE ART

GENERAL FRAME

A much greater understanding of the hydrodynamics in lakes and reservoirs has developed in the last few years. With the appearance of new, more sophisticated instruments, the power of observation has increased and the computational power of new processors allow us to run complex hydrodynamic models, giving us a deeper insight into the physics governing motion and mixing in aquatic systems. Hydrodynamics in aquatic systems is closely linked with the motion of stratified fluids influenced by external forcing; these systems stratify in response to the solar energy input at the water surface. In reservoirs and lakes, wind, river inflows and outflows all modify the stratification and are the main mechanisms energizing the water motion. The momentum input of these three sources leads to both currents and internal waves. Hydrodynamics, on a large or basin-scale down to small scale, turbulence and mixing, has been studied. In general a basin-scale motion, such as internal seiching, is gradually degenerated into smaller scale motions, becoming a mechanism of instability that produces internal mixing. It is estimated that up to 90% of the input energy is lost to dissipation.

Although it appears impossible to describe all the hydrodynamic processes going on in an aquatic system, some authors have reviewed the main mechanisms, from large scale (Mortimer 1974, Serruya et al. 1984, Csanady 1975, Hutter 1984, Imberger and Hamblin 1982) to small scale and mixing processes (Wüest, 2003, Fernando 1991) or both (Imberger 1994, Imberger 1990, Fischer et al. 1979). Having a better understanding of the hydrodynamics of a system is important because the mixing and transport processes occurring in a reservoir determines, to a large degree, the ecological response of the reservoir to meteorological forcing, inflows and outflows (Imberger 1998); however such process have rarely been taken into account in water management, especially in Spanish reservoirs. The aim of the present study is to contribute to a better understanding of the main physical processes affecting a Mediterranean medium-size reservoir, emphasizing the large scale hydrodynamics and the possible implications on the biological community.

STUDY SITE

The Sau reservoir was selected as the main study site and the focus of this PhD for two reasons; firstly, it is representative of many Spanish reservoirs and second, it has been widely studied since it was first filled in 1964. Though, I will also briefly discuss the Beznar reservoir in Chapter 3 in comparison with the Sau reservoir.

The Sau is a river valley reservoir which, at full capacity, is 18 km long, with a maximum width of 1.3 km close to the dam and a maximum depth of about 75m. It is located in Catalonia in the northeast of Spain being the first of three reservoirs that supply drinking water to the Barcelona region. The main tributary and main water source is the River Ter which begins in the Pyrenees, with a nivopluvial hydraulic regime, and a watershed of 1,523 km^2 (Sabater et al. 1995). Sau has a volume of 168 Hm^3, a surface area of 580 ha and an altitude of 426m above sea level.

Sau is an eutrophic reservoir with incoming nutrients from the polluted River Ter due to human activity in the watershed (Vidal and Om 1993, Armengol et al. 1994). The eutrophication process and evolution since it was first filled have been described by Vidal (1977).

River valley reservoirs, such as the Sau reservoir, are often large and narrow, receiving water from a single river inflow. These reservoirs have important longitudinal changes controlled by the river intrusions across them (Hejzlar & Straskraba, 1989). Thus we can describe these reservoirs as hybrid systems between rivers and lakes (Margalef, 1983), with a progressive transformation from a river to a lake system, not only in the environmental variables, but also in their morphology and hydrodynamic characteristics. In general, a reservoir can be divided along the longitudinal axis into three zones (Kimmel et al., 1990), the riverine zone, the transition zone and the lacustrine zone. The riverine zone is characterized by higher flow, short residence time, and high values of nutrients and suspended solids. The transition zone, where the river meets the reservoir, is characterized by high phytoplankton productivity, decreasing flow velocity, increased water residence and large sedimentation. Finally, the lacustrine zone consists of the area near the dam with longer residence time, lower available nutrients and lower suspended matter. The boundaries between the three zones are not well defined and can be highly dynamic, in response to inflow characteristics. The canyon-type morphology of the Sau reservoir (Figure 1) results in a marked longitudinal heterogeneity in the community populations (Armengol et al. 1999, Comerma 2003) and also affects the hydrodynamics. The main body of the reservoir, where the dam is located, roughly corresponds to the lacustrine zone; this zone behaves as a lake where the wind is the main forcing mechanism influencing the hydrodynamics. However the riverine and transition zones are narrow and meandering, sheltered from the wind forcing. Hydrodynamics in these zones are mainly affected by the river inflow. Of

course, no strict boundaries between the zones exist and the hydrodynamics generated in one zone can affect the rest of the reservoir. Nevertheless, separating the reservoir into these zones will be useful in studying the main processes taking place in each one.

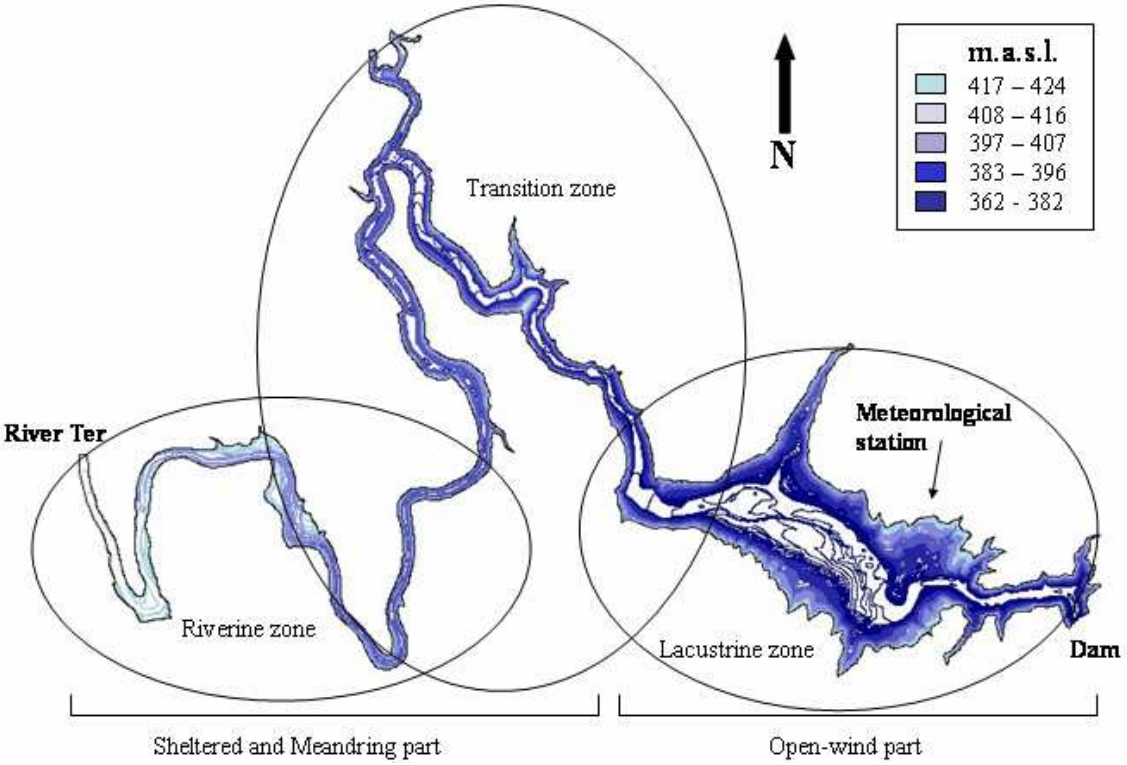

Figure 1. Bathymetric map of Sau Reservoir

SEASONAL THERMAL STRUCTURE

Mediterranean lakes and reservoirs develop thermal stratification with the system dividing into epilimnion, metalimnion and hypolimnion layers. The hydrodynamics are directly affected by this stratification, which tends to stabilize the system and therefore reduce the mixing process. The main process affecting the seasonal evolution of the thermal structure of a reservoir is heat transfer at the surface. Solar radiation and long wave radiation tend to heat the water, while evaporation, sensible heat transfer and radiation from the water surface mostly cool the water. The net balance of heat sources depends not only on the season, but also on the changing meteorological conditions so that the balance can change even from hour to hour. Other external forcing, such as wind, inflows and outflows, also affect the stratification. The wind, together with convection, is the main mechanism for mixing at the water surface, with the thickness of the epilimnion being a factor of such mechanisms (Imberger 1985, Imberger and Parker, 1985). The presence of river inflows and outflows is responsible for the main differences in the hydrodynamics and stratification of lakes compared to reservoirs, although some lakes are also influenced by inflows. The degree of the stratification can be affected by the inflow temperature (Straskraba 1993, Armengol et al. 1994).

The resultant stratification is the product of the surface heating/cooling and all the mixing process occurring in the reservoir/lake. The main mechanisms of mixing are due to the effect of internal waves, inflows, outflows, wind-momentum, shear, diffusion, etc (see Fischer et al. 1979, Imberger and Patterson 1990 or Wüest and Lorke, 2003). These processes are summarized in Figure 2.

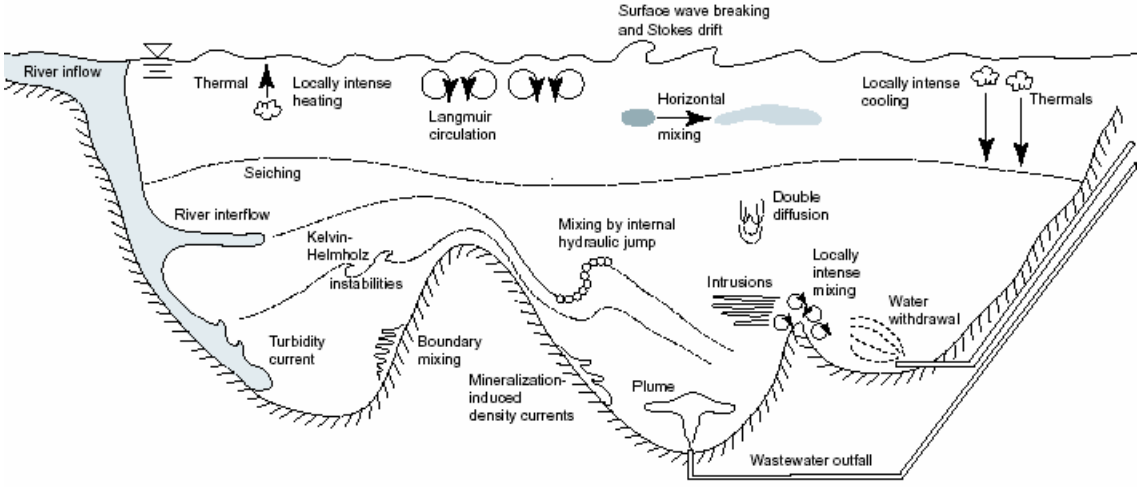

Figure 2 Schematic representation of mixing processes in a lake. Taken from Imboden and Wüest (1995).

Sau, like many other Spanish reservoirs, can be defined as a warm monomictic reservoir with a sharp metalimnion during the summer stratification (Armengol 1994). A description of the seasonal evolution of the thermal structure in Sau reservoir can be found in Han et al. (1999) where the thermal structure was also simulated by the one dimensional model, DYRESM.

ACTION OF THE WIND: BASIN-SCALE INTERNAL WAVES

The wind forcing at the surface, during the period of stratification, introduces both momentum and turbulent kinetic energy (TKE) into the water at the surface layer (Imberger 1985). The TKE causes the momentum to be distributed vertically downward, and generating movement in the water surface in the direction of the wind. The water movement displaces the metalimnion downward at the downwind end and causes upwelling at the upwind end of the reservoir. This continues until the baroclinic pressure gradient, associated with the tilted metalimnion, balances the introduced inertia. When the wind forcing stops, the baroclinic pressure gradient acts as a restoring force, inducing a long internal wave mostly of vertical mode one, but higher modes may also be induced. Basin-scale internal waves or internal seiches (in the absence of rotation) were first described by Mortimer (1952 & 1953) who explained the formation of internal seiches in a two-layered lake (epilimnion and hypolimnion) separated by a

thin metalimnion, as a response to a wind forcing event (Figure 3). Stevens and Lawrence (1997) estimated the thermocline deflection induced by wind-driven currents, at the setup of basin-scale internal waves. Once initialized, these waves propagate throughout the lake and may be damped due to (1) degeneration into non-linear waves (Horn et al. 2001, Boegman et al. 2005b), in which the lake sloping plays a role (Boegman et al. 2005a); (2) wave-wave interaction, (3) dissipation and shoaling (Michallet and Ivey 1999). Stevens et al. (1996) estimated that over 80% of the potential energy in the internal wave setup may be lost in just one internal wave period.

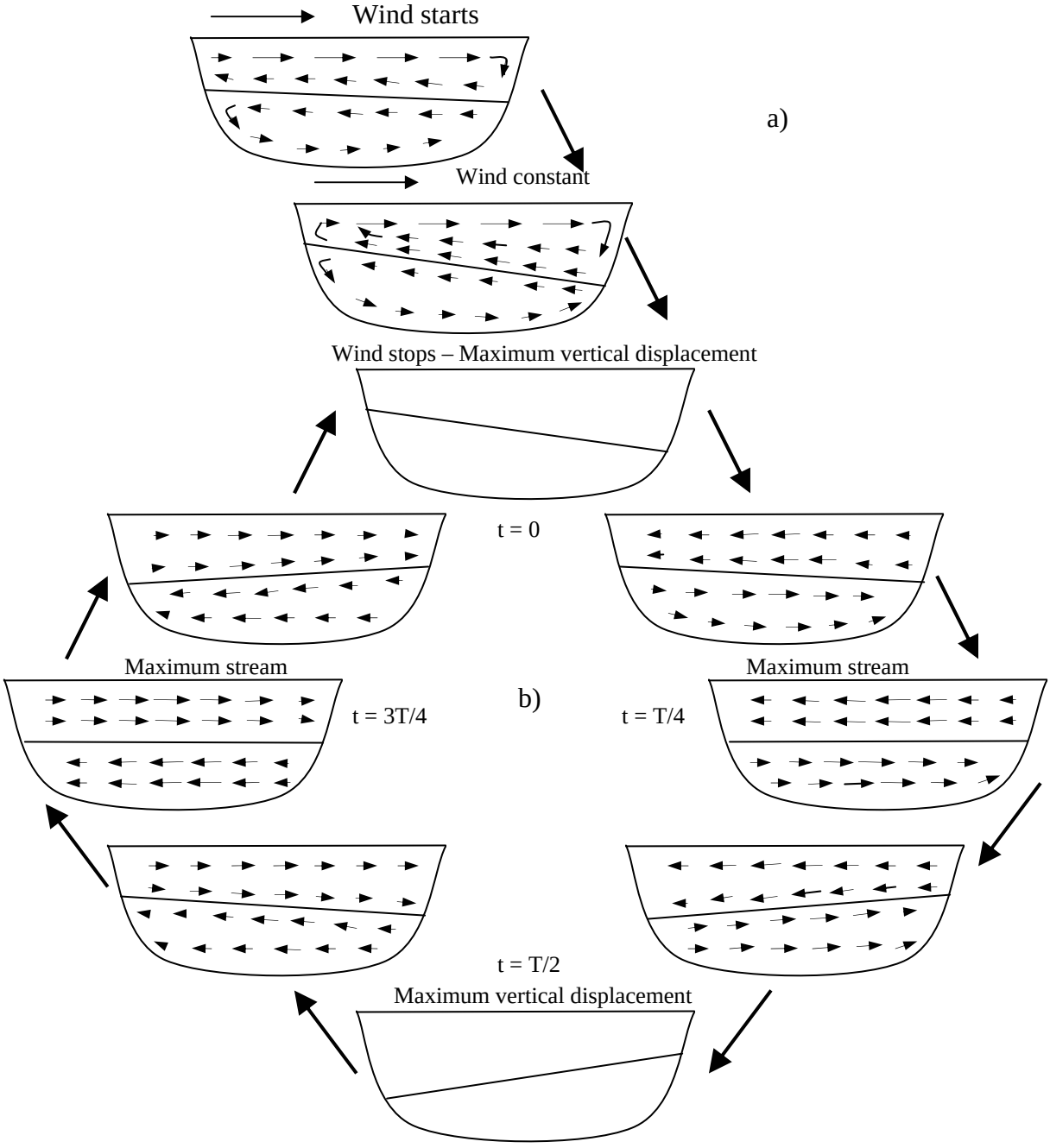

Figure 3. (a) Excitation and (b) Evolution of a seiche. Adapted from Mortimer (1952)

Horizontal internal waves, or seiches, in absence of rotation are usually classified using the nomenclature V*i*H*j*, where *i* =1,2,… are the number of vertical nodal points, and *j* = 1,2,… the number of horizontal nodal points. Figure 4 shows the main oscillatory modes, where the mode V1H1 is the most frequently excited mode corresponding to that described by Mortimer (see Figure 3). However, higher modes are also observed and their importance may depend on the stratification, morphology of the lake/reservoir and the strength, duration, distribution or even the periodicity of the wind field, as will be discussed throughout Chapters 1, 2 and 3.

Vertical modes two (V2) have been described by LaZerte (1980), Wiegan and Chamberlain (1987), Münnich et al. (1992) and Roget et al (1997) among others. Roget et al. (1997) showed the presence of a V2H2 mode in Lake Banyoles, where the bathymetry of the lake plays a fundamental role.

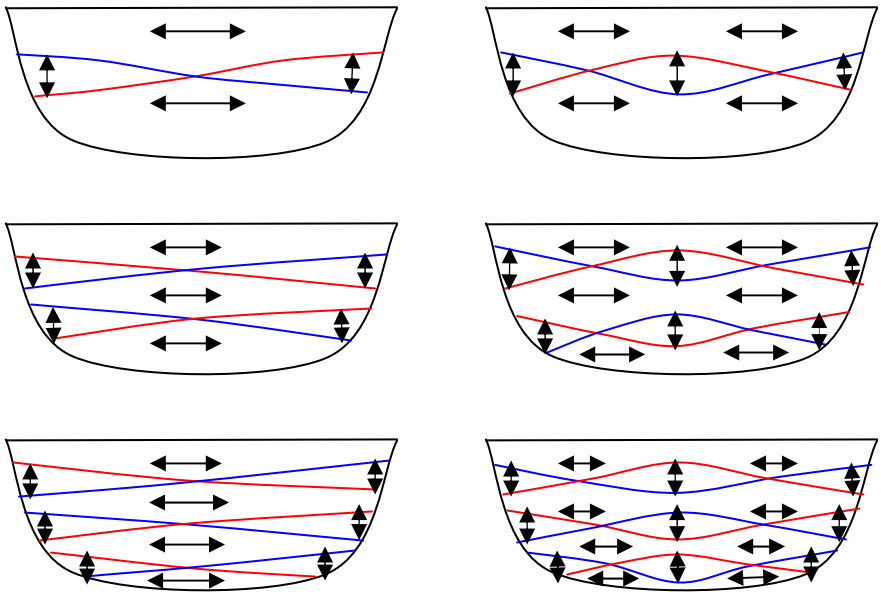

Figure 4. Main oscillatory modes of horizontal internal waves. Red and blue lines indicate the oscillation due to the internal wave in two opposite phases of maximum vertical displacement.

On time scales of the order of individual wind events, the response of the pycnocline (fundamentally formed by temperature differences → thermocline) to wind stress can be analyzed on the basis of the values of the Wedderburn *W* and Lake numbers L_N (Stevens and Imberger 1996). The Wedderburn number *W* can be defined as (Imberger and Patterson 1990):

$$W = \frac{1}{L}\frac{g'h^2}{u_*^2}, \qquad (1)$$

where g' is the reduced gravity (= $g\Delta\rho/\rho$) h is the thickness of the surface mixed-layer, L the basin length and u_*^2 is the water friction velocity due to wind stress. This number is dimensionless and represents the ratio of the baroclinic pressure force at the point of upwelling and the surface force imposed on the surface layer. The Lake number L_N is a dimensionless ratio of the buoyancy forces in the lake due to stratification to the external forces applied to the water column, such as wind, that act counter to the buoyancy forces. Describing this forces as moments around the centre of volume we can define the Lake number as:

$$L_N = \frac{M_{bc}}{M_w} = \frac{M_{bc}}{\tau A_s z_v}, \qquad (2)$$

where M_{bc} is the baroclinic moment about the center of the embayment volume; M_w is the wind moment applied by the wind blowing along the lake surface, τ is the surface shear stress, A_s is the surface area and z_v is the depth of the center of volume.

Low Lake numbers (L_N <1) are associated with vertical mode 1 tilting, whereas low Wedderburn numbers ($W \sim O(1)$ or $W < 1$) are associated with a higher vertical mode 2 response. Values of W and L_N >>1, and according to Stevens and Imberger's (1996) analysis of W and L_N , metalimnetic water was pushed upwind, where isotherms should have stretched. This way the Wedderburn and Lake number can be a useful tool to predict the tilt of the pycnocline (or excitation of the internal waves) and the modal response.

The earth's rotation may also affect internal waves when the relative importance of the Coriolis effect on buoyancy forces is significant, and the natural modes become Kelvin and Poincaré waves (Mortimer 1974). Kelvin wave solution is one in which the velocity perpendicular to the shore is considered to be zero. These waves propagate parallel to the boundary with the maximum amplitude at the shore, where the waves crests to the right (in the northern hemisphere) when looking along the direction of propagation. The amplitude of the wave decays offshore. In the lake interior we might expect plane progressive Poincare waves to be present; where the frequency approaches the inertial frequency, the current vectors rotate anti-cyclonically and the majority of energy is in the kinetic form (see, for example, Antenucci et al. 2000).

Basin-scale internal waves contain the largest part of the internal energy of a lake and play an important role in horizontal dispersion and, especially, in vertical mixing, which may help to incorporate rich hypolimnetic waters with the consequent increase in primary production (Ostrovsky 1996). Living organism distribution and abundance (Levy et al. 1991, Gaedke and Schimmele, 1991), and re-suspension of particles and nutrients (Gloor et al. 1994), may also be associated with internal waves,

playing an important role in the water quality of a lake. For this reason, internal waves have been widely studied (Hutter 1984, Saggio and Imberger 1998, Bäuerle 1998, among many others). Hutter (1984) published a review paper of basin-scale hydrodynamics, including internal waves.

The periodicity of the wind may play an important role in the basin-scale internal waves. Many reservoirs exhibit a periodic pattern in the wind forcing due to weather behaviour. In general, a 24-hour land-breeze periodicity is found, as in the case of Lake Kinneret (Neumann and Stanhill 1978). However, other different periodicities have also been reported; Lake Lugano has a period of 60-90h (Mysack et al. 1985), and Loch Ness has a period of ≈ 50h (Thorpe, 1974). These periodicities in the wind reveal a different scenario to that proposed by Mortimer (see figure 3), where the wind stops after a certain time. Modes with similar periods to that of the wind may be energized by resonance, which increases the energy of these modes (Antenucci and Imberger, 2003). All in all, most of the models designed to simulate internal seiches use only a two or three layer approximation and the literature on seiches in continuous, stratified lakes is rather sparse.

INFLOWS AND OUTFLOWS

Inflows

Inflows into reservoirs are of special interest since many of the incoming nutrients or contaminants come from the river inflows. River inflows coming into a lake, reservoir, or coastal region often have a different density than that of the receiving ambient water. The main differences in the density are due to temperature as well as the concentration of dissolved and suspended solids. When the inflowing water has a different density than the ambient water, the water flows into the receiving ambient water until a balance is reached between the momentum of the inflowing water and the baroclinic pressure that results from the density difference. When the inflowing water is less dense than the ambient water, it separates from the bottom up and goes over the surface of the ambient water, generating an overflow. In the case of inflows with a higher density than the ambient water, the inflow plunges under the surface to form a gravity-driven density current, along the bottom, downward up to the level of neutral buoyancy where it inserts (interflow) or to the bottom of the basin (underflow) (See Figure 5). The region previous to the overflow or underflow plunge is momentum-dominated while in the region after the plunge occurs, the density current becomes buoyancy-dominated. On the way towards the dam, mixing occurs and water of the ambient body entrains into the inflow, a process defined as entrainment; at the same time, water from the inflow entrains into the ambient water, a process defined as detrainment. The entrainment implies a flow of ambient water into the turbulent layer generated in the boundary of the inflow and the ambient layer, as in a free shear region.

Ellison and Turner (1959) suggested that the velocity of the inflow into the turbulent region must be proportional to the velocity of the layer, with the constant of proportionality being the so called entrainment constant *E*. For a 2D flow in a diverging channel with a sloping bottom, the entrainment is defined by the relation:

$$\frac{d(UA)}{dx} = EUb, \tag{3}$$

where *A* is the cross-section of the inflow, *U* the mean velocity of the layer and *b* the width of the channel that can be defined as $b(x)= b_0 + 2x \tan \delta$, for δ the diverging angle of the channel. Entrainment is governed by the bottom slope, the friction with the bottom (underflows) and the mixing in the free boundaries or shear regions. This mixing mechanism can be parameterized using the overall Richardson number defined as:

$$Ri = \frac{g'h}{U^2}\cos\alpha, \tag{4}$$

where $g' = g(\rho_a - \rho_0)/\rho_a$ is the buoyancy based on the excess in density of the inflow (ρ_0) over the ambient density (ρ_a), *g* is the acceleration of gravity, *h* is the depth of the inflow and α is the bottom slope of the thalweg.

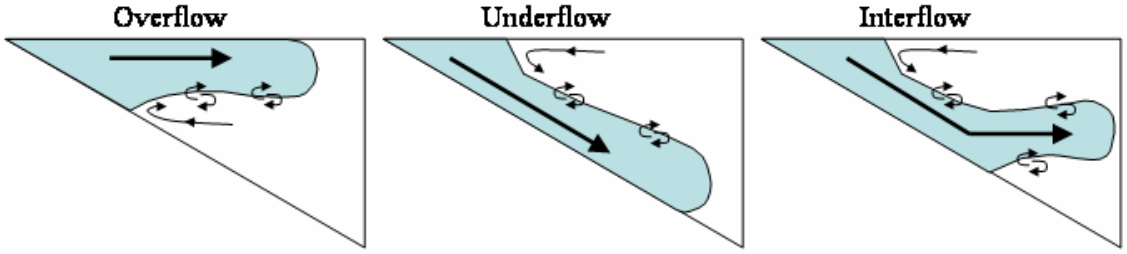

Figure 5. Inflow dynamics

In the following sections, we will explore in more detail the three different inflow dynamics, divided into overflows, underflows and interflows.

Overflows

Inflows that are less dense than the receiving water encounter the denser ambient water. The increasing buoyant forces offset the momentum force, forcing the inflow to overflow at the water surface. The inflow water then spreads over the water surface as a function of the inflow rates, density differences and basin confinement.

A description of an overflow event in an estuary, where the effect of the density differences and topography are described, can be found in Csanady (1982). Safaie

(1979) also investigated, in the laboratory, overflows in laterally unconfined receiving waters. He expressed the separation point as:

$$h_s=0.914\cdot h_0\cdot Fr^{1/2}, \quad (5)$$

where h_s is the depth at the separation point, h_0 the initial upstream inflow depth, and Fr is the inflow densimetric Froude number, defined as:

$$Fr=\frac{U_0}{\sqrt{g'\cdot h_0}}, \quad (6)$$

where U_0 is the inflow velocity. Observations found that no attachment to the bottom occurred for inflow densimetric Froude numbers ≤ 2.5, where the Froude number is based on the stream area (A_0) defined as:

$$Fr_\Delta=\frac{U_0}{\sqrt{g'\cdot\sqrt{A_0}}} \quad (7)$$

By using the assumption that Fr_Δ=2.5 at the separation point, Safaie also determined an equation for the dilution of the overflow as:

$$\Gamma=\frac{q}{q_0}=\left[1+\left\{\frac{Fr_\Delta^2-6.25}{5.22\cdot Fr\ -6.25}\right\}\left\{\frac{h^2}{h_0^2}-1\right\}\right]^{1/2}, \quad (8)$$

where q is the flow rate after the separation and q_0 just before the separation point. However, field prediction of the inflow mixing in the separation zone and the entrainment of the inwards overflow is still complicated. Several factors may affect the overflow, like meteorological forcing, including wind and heating and cooling, which makes it a difficult aspect to determine in natural waters.

Underflows

The underflow is generated when the denser water flows into the lighter ambient body of water (Akiyama and Stefan, 1984). The buoyancy force generated by pushing the lighter water back into the reservoir retards the momentum of the inflowing water. Eventually, the momentum of the inflowing water is reduced to such a point that its excess gravitational attraction becomes dominant and the denser water then plunges beneath the surface of the ambient water, subsequently flowing as a density current along the inclined bottom of the reservoir to the bottom.

Observations of laterally confined underflow events have been reported by Howard (1953), Wunderlich and Elder (1973), Hebbert et al. (1979) and Ford and Johnson (1981, 1983). Concerted efforts have been undertaken to determine the plunge location and entrainment coefficients for different basin geometries. Ellison and Turner (1959), in their studies found that the entrainment coefficient (*E*) was a decreasing function of the bulk Richardson number *Ri*, such that:

$$E = E(Ri^{-k}), \tag{9}$$

where *k* is a constant between 0 and 3/2, and *Ri* is defined as:

$$Ri = \frac{g'h}{U^2}\cos\alpha = \frac{1}{Fr_{\Delta}^2}, \tag{10}$$

here, *h* correspond to the depth of the underflow, and Fr_{Δ} is the densimetric Froude number defined above. The results of Ellison and Turner (1959) and Lofquist (1960) showed a consistent decrease in entrainment with increasing *Ri*. Hebbert et al. (1979) found - for a narrow, non-prismoidal, drowned river channel - a relationship as follows:

$$E = \frac{C_K C_D^{\frac{3}{2}} \frac{dp}{dx}}{\frac{dT}{dx}(Ri^* - Cs)}, \tag{11}$$

where *P* is the perimeter and *T* the top width of the inflow current for a distance *x*, C_D is the bottom drag coefficient for the inflowing water, C_K is a coefficient parameterizing the efficiency of the TKE introduced at the boundary and C_S is a coefficient measuring the efficiency of the local shear production; Sherman et al. (1978) suggested universal values for C_K = 2.2 and C_S = 0.2. Finally the generalized Richardson number is defined as:

$$Ri^* = \frac{g'\left(\frac{dA}{dh}\right)\left(\frac{dT}{dh}\right)^{-1}}{u^2}, \tag{12}$$

where *dA/dh* and *dT/dh* are the variations in the inflow area *A* and top width *T* with the inflow depth *h*. Dallimore et al. (2001) modified this parameterization for a more generally applicable entrainment law, for the whole range of Richardson numbers, which may be written for a generic section of the drowned river channel as:

$$E = \frac{C_X}{Ri^* \dfrac{dT}{dx} + 10C_X}, \tag{13}$$

in which $C_X = C_K C_D^{3/2} dP/dx + C_S dT/dx$.

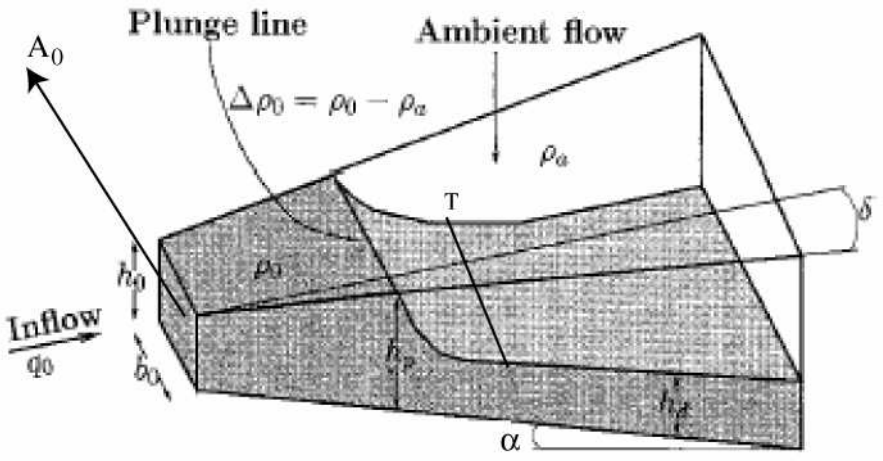

Figure 6. Definition sketch of relevant parameters for diverging channel with sloping bottom. Adapted from Bournet et al. 1999.

Likewise, the plunge point has been determined by many authors. The plunging depends on physical parameters as well as the geometrical characteristics of the reservoir. The plunge zone is controlled by the inflow per unit width upstream q_0, the ambient fluid density ρ_a, the inflow density ρ_0, the acceleration of gravity g, the inflow depth h_0, the bottom drag coefficient C_D, the bottom slope $S = tan\alpha$ and the initial mixing coefficient Γ (see Fig 6). Γ is defined as the amount in the inflow discharge due to the entrained ambient water at the plunge point. The normalized plunge depth h_p/h_0, where h_p is the depth of plunging, can be obtained as a function of the aforementioned parameters (Akiyama and Stefan 1984):

$$\frac{h_p}{h_0} = f\left[\left(\frac{q_0^2}{g' h_0^3}\right)^{1/3}, S, C_D, \Gamma\right], \tag{14}$$

Semi-empirical relations for the plunge point depth in different geometries have been obtained by different authors (Singh and Shah 1971, Hauenstein and Dracos (1984)). For a channel of constant width, the different semi-empirical relations can be expressed in the general form (Stefan et al. 1988):

$$h_p = \left(\frac{1}{Fr_p^2}\right)^{1/3} \left(\frac{q_0^2}{g'}\right)^{1/3}, \tag{15}$$

where Fr_p is the densimetric Froude number at the plunge point, often empirically obtained. For the case of a diverging channel with a sloping bottom, Johnson et al. (1987) found a relationship of:

$$\frac{h_{p1}}{h_{p2}} = \left(\frac{Fr_{p2}^2}{Fr_{p1}^2}\right)^{1/3} \left[\frac{b_0}{b_{p2}}\right]^{-2/3}, \tag{16}$$

where h_{p1} is the plunge point depth for a channel of constant width and h_{p2} for a diverging channel, while the geometrical properties of the diverging channel and a small inclination α are given by:

$$b_{p2} = b_0 + 2(h_{p2} - h_0)\frac{\tan\delta}{\sin\alpha}, \tag{17}$$

in which b_{p2} is the width of the diverging channel at the plunge depth h_{p2}.

Interflows

An interflow is generated when the inflowing water of an underflow event reaches the level of neutral buoyancy and then intrudes at this level. Fischer and Smith (1983) described an interflow event that could reach the surface, being responsible for nutrient input at the water surface. Other interflow events can be found in the papers of Chung and Gu (1998) and Gu and Chung (2003), where the fate of a contaminant interflow was described and also simulated by a two-dimensional model. Inflow intrusions were also analyzed by Imberger et al (1976), applying similar techniques to those used for withdrawal problems.

In many reservoirs, or at least in most Mediterranean reservoirs, the density of the inflow and ambient water is mainly dependent on the temperature. This results in seasonal behaviour in the inflow dynamics, since the reservoir and inflow heat up and cool down at different rates. The seasonal behaviour in the circulation of river inflows has been reported by Carmack et al. (1986), Pickrill and Irwin (1982) and Carmack et al. (1979). In the case of the Sau reservoir, the seasonal circulation was described by Armengol et al. (1999), however, the effect of short term and daily variations - which may, in fact, play an important role in the inflow dynamics, as shown by Pickrill and Irwin (1982) - were not taken into account in this report.

Outflows

Outflows constitute the main difference between a lake and a reservoir. Commonly, reservoirs are provided with outlets at different levels so that the reservoir can be used to control the temperature of the outflowing water and/or other water quality parameters. Such control allows the operators to select the type of water for specific necessities, for example, cold water for fish or warm water for irrigation.

The effect of selective withdrawal also directly affects the stratification by sharpening the thermocline where the outlet is located (Casamitjana et al. 2003, Martin and Arneson, 1978). When the fluid is stratified, the outflow is influenced by the buoyancy force. When the outlet structure is open, it generates a pressure that instantaneously sets up a radial flow pattern towards the outlet. However, such radial convergence near the sink quickly distorts the isopycnals. Buoyancy forces initiate a set of internal waves that propagate upstream (Kataoka et al. 2001) and adjust the isopycnals back to a horizontal neutral position and the initial radial flow collapses into a jet-like structure (Figure 7).

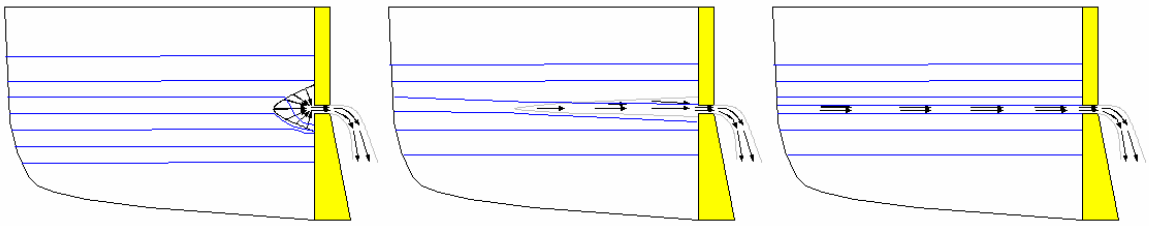

Figure 7. Evolution of the outflow from the opening of the outlet to the generation of the jet flow. Blue lines represents isopycnals

The effect of the selective withdrawal depends on the outlet characteristics and the stratification of the system, so that they are usually classified into two categories: the sink type (line or point sink) and stratification type (linear, two-layered, etc). A review of such processes can be found in Imberger and Paterson (1990). However, we will focus on the effect of the withdrawal on the stratification. The Sau reservoir usually presents a thick thermocline, so the outlet structure affects such stratification by sharpening the gradient at the level at which the outlet, is placed (Figure 8).

The shift in the stratification and the decrease in the water level produced by the withdrawal also directly affect the basin-scale internal waves by modifying their natural frequency of oscillation and structure, because the frequency of the internal waves is a function of the stratification.

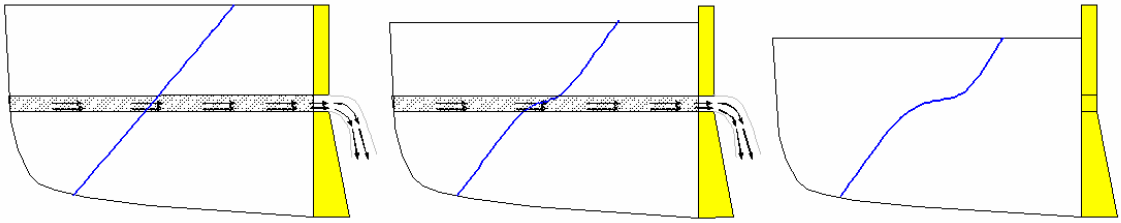

Figure 8. Stratification process due to the water withdrawal from a selective outlet. The blue line indicates the temperature profile evolution and the shadowed area indicates the sink line.

OBJECTIVES

Most of the biological and chemical processes occurring in a reservoir are linked to physical processes, and therefore the importance of such processes is obvious. The aim of this PhD thesis is to gain a better understanding of the main hydrodynamic processes - with special emphasis on the large scale hydrodynamics - occurring in a Mediterranean type reservoir, as is the case of the Sau reservoir. Some physical processes, such as the seasonal thermal structure, the river retention time, or the seasonal evolution of the river flow into the reservoir, have already been reported by other authors (Han et al. 1999, Rueda et al. 2006, Armengol et al. 1999). They are therefore not dealt with here and the reader is referred to the original papers. Essentially, this thesis focuses basically on the generation of basin-scale internal waves and the short term variations in the dynamics of the river inflow into the reservoir, including some aspects of the linking between such processes with the phytoplankton community.

During the last four years (2002-2006), various field experiments have been carried out to determine the large-scale hydrodynamics in the Sau reservoir and the results of these studies are presented in five chapters. Each chapter has been written as an independent paper with its own introduction, discussion and conclusion; some of them having already been published and others submitted or in process of being submitted. The fact that they are written as individual papers means that some of introductory concepts or references can be repetitive for the reader but, on the other hand, each chapter can be read independently. The chapters are arranged in a logical order, starting with observations of basin-scale internal waves in the Sau reservoir and continuing with more specific questions about the behaviour of such waves at seasonal scales and in comparison with another Mediterranean reservoir (Beznar) and ending with the behaviour of the river inflow and the consequences on the phytoplankton population. The main objectives of each chapter are summarized as follows:

- **Chapter 1** describes a basin-scale internal wave mode V3H1 in resonance with the wind forcing, considered rare in natural waters, found in the lacustrine part

of the reservoir in September 2003, and the modelling of this mode using a simple two-dimensional model. The objective of this section was to determine the presence of internal waves in the Sau reservoir.

- **Chapter 2** describes the evolution of the internal wave field during the summer stratification of 2004 - when high vertical modes where also found - and the modelling of this period using a more sophisticated three dimensional model. The main objective of this chapter was to obtain the evolution of the internal wave field. In addition, I try to solve the questions derived from the observations of the internal waves, such as the role of the variation in stratification and the effect of periodic winds on the internal waves, but also the effect of the rotation and the role that has the meandering and sheltered zone of the reservoir in the internal wave field. I also attempt to validate a three dimensional model for the solution of internal waves in the Sau resevoir.

- **Chapter 3** describes the seasonal evolution of the internal wave field in the Beznar reservoir, where high vertical modes (up to mode V5) in resonance with the wind and low vertical modes in the absence of resonance, were found. The objective of this section was to compare the results of another medium-size Mediterranean reservoir, the Beznar, with the results found in chapters 1 and 2 for the Sau reservoir, and consequently, to generalize the internal wave features of Mediterranean reservoirs characterized by thick metalimnions and periodic wind forcing.

- **Chapter 4** describes the effect of physical processes, focusing mainly on internal waves, in the phytoplankton population of the lacustrine zone of the reservoir. The objective of this chapter was to determine the effect of the advection and vertical displacements produced by the wind-driven currents and internal waves in the phytoplankton distribution.
  *Note that this chapter has been extracted from the paper by Serra et al. (*in press*) where a more detailed discussion about convective processes is carried out. However, in this chapter, the effect of internal waves is emphasised in order to give continuity to the line adopted in this thesis and the work made by the author.

- **Chapter 5** describes the river inflow into the reservoir and the consequences of the nutrient distribution along the reservoir on the phytoplankton population, with particular emphasis on a bloom event. The objective of this section is to study the short term and daily variations in the inflow dynamics, in addition to the seasonal evolution studied by Armengol et al. (1999), and the consequences of such dynamics on the nutrient distribution linked with the phytoplankton populations.

In all, this PhD thesis aims to provide the reader with a global vision of the main hydrodynamic processes governing the Sau reservoir and, by extension, the main processes that govern many of the Mediterranean reservoirs and, in addition, of some of the interlinking physical and biological processes.

MATERIAL AND METHODS

Various methodologies have been used in this study to attain the different objectives proposed in each chapter; this means that the deployment stations, measuring stations, instruments or numerical models were different in each case. Therefore, the methodology followed is introduced separately in each chapter. Nevertheless, here is a brief description of the main instruments and numerical models used in this study.

INSTRUMENTS

All the instruments used are well-known instruments in the field of Limnology and Oceanography and so, only a brief description is given. For further information, the reader is referred to the manufacturers.

Thermistors

Two different loggers were used during the studies.

- An Aanderaa Tr7 thermistor string, consisting of an electric cable with 11 temperature sensors with a precision of 0.05ºC and a resolution of 0.03ºC.
- An Aanderaa DL7 thermistor string with 5 temperature sensors)with a resolution of 0.045ºC and accuracy of 0.1 ºC) along with 5 conductivity sensors (with a resolution of 2.5 $\mu S/cm$ and accuracy of 20 $\mu S/cm$ of salinity). Both strings were connected to a data storing unit (DSU).

Current meters

- ADCP: An 600 kHz RDI Workhorse Sentinel ADCP was used for measuring current. The versatility of this instrument allows the user to deploy it and acquire the data in real time; it can also be either moored or moving when in use. Additional high resolution modes 5, 7 (shallow waters) and 12 were used. The ADCP signal processes data with very low noise. The 4-beams design improves data reliability by providing redundant data in the case of a blocked or damaged beam and by delivering an independent measurement of error velocity.

- Electromagnetic current meter: In addition to the ADCP, an electromagnetic current meter (ECM) was used. This is a versatile, single-point current meter, and it was used for autonomous deployments.

Fluorimeter

- Submersible Bbe FluoroProbe Moldaenke: This is a highly sensitive measuring instrument for chlorophyll analysis. The instrument has a resolution of 0.05 μg L^{-1} and a measuring range of 0-200 μg L^{-1}. This probe determines four different communities (green algae, diatoms, cyanophyceae and cryptophyceae) together with temperature, depth and transmission.

CTD

- The SBE 19*plus* SEACAT profiler is a self-powered CTD that measures conductivity, temperature and pressure up to 7000 meters (10,000 psia). It provides pump-controlled T-C ducted flow and records data (4 Hz) in FLASH RAM memory. The SEACAT profiler has real-time data capability, and *dual mode* programmability for profiling or moored time series recording. Additional turbidimeter and chlorophyll sensors were set in the CTD

Meteorological Station

The meteorological station (Campbell Scientific) belongs to the Catalonian Meteorological survey network (meteocat), and provides the following data:

- temperature and relative humidity (using a Vaisala HMP35AC instrument),
- atmospheric pressure (Vaisala PTB101B)
- far infrared radiation (Kipp & Zonen pyrgeometer CG 1, with a range of 5000 - 50000 nm),
- solar radiation (Kipp & Zonen CM3 pyranometer with a range of 300-3000nm),
- photosynthetic active radiation or PAR, (Skye Instruments Ltd. SKP215 quantum sensor, with a 400-700nm range),
- wind speeds (R.M. Young 05103 Anemometer) and
- rainfall (Munro R102 Rain gauge).

NUMERICAL MODELS

The increasing capability of new processors has led to the development of two dimensional models (see Munnich. 1996 and Fricker and Nepf. 2000) and quite sophisticated three dimensional models for lake and reservoir hydrodynamics (Casulli and Cheng (1992), Rueda et al. (2003), Hodges et al. 2000a, Schwab and Bedford, 1995). Here, the estuary and lake computer model (ELCOM) developed by the CWR-University of Western Australia will be used. This model has proved to be quite accurate in simulating the hydrodynamics of the aquatic systems. The ELCOM model has been used previously by Laval et al. (2003), Hodges et al. (2000), Appt et al. (2004), Laval et al. (2005), among others. The solution provided by the model, based on the TRIM model (Casulli and Cheng (1992)) is especially accurate in simulating the basin-scale internal waves, as shown in the papers of Hodges et al. (2000) and Gomez-Giraldo et al. (2006), both of which simulated basin-scale internal waves in Lake Kineret. But it is also a useful tool for river inflows, especially for underflows since the model is coupled with a two-dimensional model for underflows (Dallimore et al. 2003, Dallimore et al. 2004).

Furthermore, ELCOM can be coupled to the water quality model CAEDYM. The coupled model ELCOM-CAEDYM has proved to be an accurate model for simulating the biogeochemical paths in reservoirs (Romero et al. 2004, Romero and Imberger 2003) and algae bloom events (Robson and Hamilton, 2004), and can therefore be used as a management tool, or for predicting such events (Antenucci et al. 2003, Hipsey et al. 2004).

There follows a brief description of the two dimensional model used along this Thesis and a description of the ELCOM-CAEDYM models. For a further description, the reader is referred to the corresponding Science manuals (Hodges and Dallimore, 2006 and Hipsey et al. 2005) available at the CWR web page (www.cwr.uwa.edu.au/~ttfadmin/).

2D- Model (Münnich model)

Following Münnich (1993) here, we will start from the general equations of motion and applying the Boussinesq approximation, so that, the density is treat as constant except in the vertical momentum equation. We shall assume that the wave motion is inviscid. Neglecting also the non-linear terms and the effects of rotation we get:

$$\frac{\partial u}{\partial t} = -\frac{1}{\rho_0}\frac{\partial P}{\partial x} \qquad (18)$$

$$\frac{\partial v}{\partial t} = -\frac{1}{\rho_0}\frac{\partial P}{\partial y} \tag{19}$$

$$\frac{\partial w}{\partial t} = -\frac{1}{\rho_0}\frac{\partial P}{\partial z} - \frac{\rho g}{\rho_0} \tag{20}$$

$$\frac{D\rho}{Dt} = 0 \tag{21}$$

$$\frac{\partial u}{\partial x} + \frac{\partial v}{\partial y} + \frac{\partial w}{\partial z} = 0 \tag{22}$$

Where ρ_0 is a constant reference density; (18), (19) are the horizontal equations of movement and (20) the vertical equation of movement. Equation (22) is the continuity equation, and equation (21) is the frequently called "density equation". We can express such equations in terms of changes from a state of rest. This way, if we assume a background state in which the density $\overline{\rho}(z)$ and pressure $\overline{P}(z)$ are in hydrostatic balance:

$$0 = -\frac{1}{\rho_0}\frac{d\overline{P}}{dz} - \frac{\overline{\rho} g}{\rho_0} \tag{23}$$

When the motion develops, the pressure and density change to:

$$\begin{aligned} P &= \overline{P}(z) + P' \\ \rho &= \overline{\rho}(z) + \rho' \end{aligned} \tag{24}$$

The density equation becomes:

$$\frac{\partial}{\partial t}(\overline{\rho} + \rho') + u\frac{\partial}{\partial x}(\overline{\rho} + \rho') + v\frac{\partial}{\partial y}(\overline{\rho} + \rho') + w\frac{\partial}{\partial z}(\overline{\rho} + \rho') = 0\,, \tag{25}$$

where $\partial\overline{\rho}/\partial t = \partial\overline{\rho}/\partial x = \partial\overline{\rho}/\partial y = 0$. The non-linear terms $u\partial\rho'/\partial x$, $v\partial\rho'/\partial y$ and $w\partial\rho'/\partial z$ can be neglected, since we assume small amplitude motions; then equation (25) can be simplified to:

$$\frac{\partial \rho'}{\partial t} + w\frac{d\overline{\rho}}{dz} = 0 \tag{26}$$

This equation is the linearized form of equation (21).

Introducing now the *Brunt-Väisälä frequency N(z)* (buoyancy frequency) defined as:

$$N^2 = \frac{g}{\rho}\frac{d\rho}{dz}, \tag{27}$$

and after substituting equations (24) in the equations of movement (18)-(22), using the equation (23) and replacing the density equation (21) for its linearized form (26), the movement equations yields to:

$$\frac{\partial u}{\partial t} = -\frac{1}{\rho_0}\frac{\partial P'}{\partial x} \tag{28}$$

$$\frac{\partial v}{\partial t} = -\frac{1}{\rho_0}\frac{\partial P'}{\partial y} \tag{29}$$

$$\frac{\partial w}{\partial t} = -\frac{1}{\rho_0}\frac{\partial P'}{\partial z} - \frac{\rho' g}{\rho_0} \tag{30}$$

$$\frac{\partial \rho'}{\partial t} - \frac{N^2 \rho_0}{g} w = 0 \tag{31}$$

$$\frac{\partial u}{\partial x} + \frac{\partial v}{\partial y} + \frac{\partial w}{\partial z} = 0 \tag{32}$$

A useful equation for stratified flows is the one involving *w* only. The *u* and *v* can be eliminated by taking the time derivative of the continuity equation (32) and using the horizontal momentum equations (28) and (29). This gives:

$$\frac{1}{\rho_0}\nabla_H^2 P' = \frac{\partial^2 w}{\partial z \partial t}, \tag{33}$$

where $\nabla_H^2 \equiv \partial^2/\partial x^2 + \partial^2/\partial y^2$ is the *horizontal* Laplacian operator. Elimination of ρ' from (30) and (31) gives:

$$\frac{1}{\rho_0}\frac{\partial^2 P'}{\partial t \partial z} = -\frac{\partial^2 w}{\partial t^2} - N^2 w \tag{34}$$

Finally, we can eliminate *P'* by taking ∇^2_{H} of (34), and using (33). This gives:

$$\frac{\partial^2}{\partial t \partial z}\left(\frac{\partial^2 w}{\partial t \partial z}\right) = -\nabla_H^2\left(\frac{\partial^2 w}{\partial t^2} + N^2 w\right), \tag{35}$$

which can be written as:

$$\frac{\partial^2}{\partial t^2}\nabla^2 w + N^2 \nabla_H^2 w = 0\,, \tag{36}$$

where $\nabla^2 \equiv \partial^2/\partial x^2 + \partial^2/\partial y^2 + \partial^2/\partial z^2 = \nabla^2_H + \partial^2/\partial z^2$ is the three-dimensional Laplacian operator. This equation can be simplified by reducing it to two dimensions (eliminating the *y* component) taking into account the morphological characteristics of many lakes or reservoirs (i.e. elongated lakes); and applying the shallow-water approximation (*Münnich,* 1993). This way equation (36) can be reduced to:

$$\frac{\partial^4 w}{\partial^2 t \partial^2 z} + N^2 \frac{\partial^2 w}{\partial x^2} = 0 \tag{37}$$

For the boundary condition at the surface we use the rigid-lid condition $w(z = 0) = 0$. Internal waves (baroclinic) have very small surface elevations, so this is a good approximation to the true boundary condition. Furthermore, this condition filters the surface seiches (barotropic). At the other boundaries we can set no outflow, such that:

$$\boldsymbol{u} \cdot \boldsymbol{n_B} = 0, \tag{38}$$

where $\boldsymbol{u} = (u,w)^T$ represents the velocity components in the boundary and $\boldsymbol{n_B}$ is a vector is a vector normal to the boundary (i.e. bottom and surface). For a non-costant bottom this connects both u and w, so that it is not easy to incorporate in (37). Fortunately, in two dimensions we can introduce a stream function. Due to the incompressibility condition, we know that exists a stream function $\Psi = \Psi(x,z)$ such that:

$$\frac{\partial \psi}{\partial x} = w \quad , \quad \frac{\partial \psi}{\partial z} = -u \tag{39}$$

By substituting these expressions into the two-dimensional equations for internal waves yield:

$$-\frac{\partial^2 \psi}{\partial t \partial z} = -\frac{1}{\rho_0}\frac{\partial P'}{\partial x} \tag{40}$$

$$0 = -\frac{1}{\rho_0}\frac{\partial P'}{\partial z} - \frac{\rho' g}{\rho_0} \tag{41}$$

$$\frac{\partial \rho'}{\partial t} - \frac{N^2 \rho_0}{g}\frac{\partial \psi}{\partial x} = 0 \tag{42}$$

If we eliminate *ρ'* y *P'* from these equations we get a single equation in Ψ:

$$\frac{\partial^4 \psi}{\partial^2 t \partial^2 z} + N^2 \frac{\partial^2 \psi}{\partial x^2} = 0 \tag{43}$$

If *H(x)* is the depth of the thalweg, we have:

$$0 = \boldsymbol{u} \cdot \boldsymbol{n_B} = \begin{pmatrix} -\dfrac{\partial \psi}{\partial z} \\ \dfrac{\partial \psi}{\partial x} \end{pmatrix} \cdot \begin{pmatrix} -\dfrac{dH}{dx} \\ 1 \end{pmatrix} = \frac{\partial \psi}{\partial z}\frac{dH}{dx} + \frac{\partial \psi}{\partial x} \tag{44}$$

The right-hand side of this equation is simply the component of the gradient of Ψ along the thalweg. The boundary condition states that this gradient must vanish, and thus Ψ is a constant at the boundary. Also Ψ as a potential, is only determined up to a constant, so that the boundary condition can be put in the form:

$$\psi = 0 \qquad \text{at the boundary.} \tag{45}$$

For seiches modes, the time dependence must be sinusoidal, and then:

$$\psi = \phi(x, z)\sin(\omega t + \alpha), \tag{46}$$

where α is a constant and ω is the angular frequency of the seiche. Introducing (46) in (43) yields to the governing equation of internal waves:

$$\boxed{\frac{\partial^2 \phi}{\partial x^2} = \frac{\omega^2}{N^2}\frac{\partial^2 \phi}{\partial z^2}} \tag{47}$$

subject to the condition

$$\phi = 0 \qquad \text{at the boundary.} \tag{48}$$

Discretization of the governing equation.

We will solve the governing equation (47) numerically using finite difference approximations to the involved differentiations in a rectangular grid map. We can define the coordinates in the way:

$$x = i\Delta x \qquad (i = 1,2,\ldots), \tag{49}$$

$$z = j\Delta z \qquad (j = 1,2,\ldots), \tag{50}$$

where Δx y Δz are the distance between neighbours and indices i and j indicate the position in the grid (Fig 9).

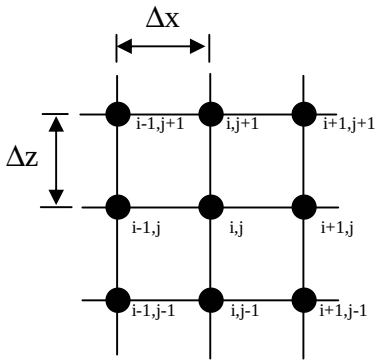

Figure 9. Rectangular grid map representation with points homogenously distributed.

This way we can represent the first derivative of the stream function ϕ in the point (i,j) by finite difference approximations in the way:

$$\left(\frac{\partial\phi}{\partial x}\right)_{i,j} \cong \frac{1}{\Delta x}\left(\phi_{i+\frac{1}{2},j} - \phi_{i-\frac{1}{2},j}\right) \tag{51}$$

$$\left(\frac{\partial\phi}{\partial z}\right)_{i,j} \cong \frac{1}{\Delta z}\left(\phi_{i,j+\frac{1}{2}} - \phi_{i,j-\frac{1}{2}}\right) \tag{52}$$

And solve the second derivative as:

$$\begin{aligned}\left(\frac{\partial^2\phi}{\partial x^2}\right)_{i,j} &\cong \frac{1}{\Delta x}\left[\left(\frac{\partial\phi}{\partial x}\right)_{i+\frac{1}{2},j} - \left(\frac{\partial\phi}{\partial x}\right)_{i-\frac{1}{2},j}\right] \\ &\cong \frac{1}{\Delta x}\left[\frac{1}{\Delta x}\left(\phi_{i+1,j} - \phi_{i,j}\right) - \frac{1}{\Delta x}\left(\phi_{i,j} - \phi_{i-1,j}\right)\right] \\ &\cong \frac{1}{\Delta x^2}\left[\phi_{i+1,j} - 2\phi_{i,j} + \phi_{i-1,j}\right]\end{aligned} \tag{53}$$

Likewise the second derivative:

$$\left(\frac{\partial^2\phi}{\partial z^2}\right)_{i,j} \cong \frac{1}{\Delta z^2}\left[\phi_{i,j+1} - 2\phi_{i,j} + \phi_{i,j-1}\right] \tag{54}$$

Substituting (53) and (54) in (47) we have:

$$\frac{1}{\Delta x^2}\left[-\phi_{i+1,j}+2\phi_{i,j}-\phi_{i-1,j}\right]=\frac{\omega^2}{N_j^{\,2}\Delta z^2}\left[-\phi_{i,j+1}+2\phi_{i,j}-\phi_{i,j-1}\right], \qquad (55)$$

where N_j is the N value at the depth of the $_j$ point; N is z dependent and horizontally homogeneous (non x dependent). For the neighbours point with the boundary we have to take into account the condition $\phi = 0$ at the boundary.

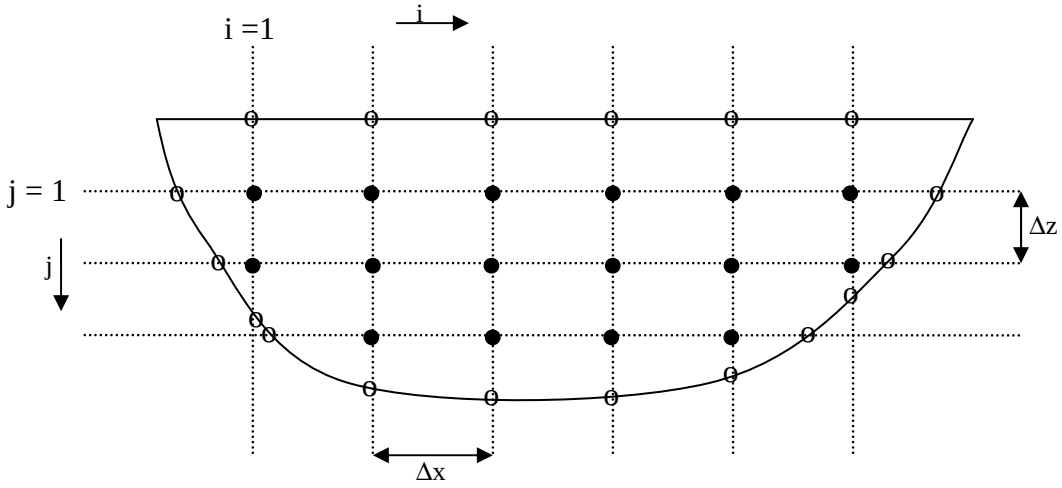

Figure 10. Grid used in the discretization. Filled and open circles are inner and boundary grid points, respectively (Adapted from Münnich, 1993).

If we renumber the grid points from top to bottom and left to right (see Fig 10) to yield a series of grid points with only one index, then for an inner point k we have:

$$\frac{1}{\Delta x^2}\left[-\phi_{k+n_i}+2\phi_k-\phi_{k-n_{i-1}}\right]=\frac{\omega^2}{N_j^{\,2}\Delta z^2}\left[-\phi_{k+1}+2\phi_k-\phi_{k-1}\right] \quad , \qquad (56)$$

where k = 1,…,M, being M the total number of inner points of the grid M=$\sum_{i=1}^{K} n_i$, where n_i is the number of points of the grid in the i column. If we set $\phi = \phi_1,\ldots, \phi_M$, we can write equation (56) in matrix notation:

$$\boldsymbol{A}\phi = \lambda \boldsymbol{B}\phi, \qquad (57)$$

where $\lambda = \omega^2$ and the matrix $\boldsymbol{A}$ and $\boldsymbol{B}$ have the entries (for l=1,…,M)):

$$A_{kl} = \begin{cases} -\dfrac{1}{\Delta x^2} & \text{If } l = k - n_{i-1}; \\ \dfrac{2}{\Delta x^2} & \text{If } l = k; \\ -\dfrac{1}{\Delta x^2} & \text{If } l = k + n_i; \\ 0 & \text{Each other} \end{cases} \tag{58}$$

$$B_{kl} = \begin{cases} -\dfrac{1}{N_j \Delta x^2} & \text{If } l = k - n_{i-1}; \\ \dfrac{2}{N_j \Delta x^2} & \text{If } l = k; \\ -\dfrac{1}{N_j \Delta x^2} & \text{If } l = k + n_i; \\ 0 & \text{Each other} \end{cases} \tag{59}$$

Matrices (58) and (59) are only valid for the inner points with no neighbours on the boundary. For a point with neighbour on the boundary of the lake we must distinguish between neighbours to its left, to its right, above it and below it:

$$\text{Left} \quad A_{kl} = \begin{cases} -\dfrac{2}{\Delta x(\Delta x + \sigma_k^x)} & \text{If } l = k - n_{i-1} \\ \dfrac{2}{\Delta x \sigma_k^x} & \text{If } l = k \\ 0 & \text{Each other} \end{cases} \tag{60}$$

$$\text{Right} \quad A_{kl} = \begin{cases} \dfrac{2}{\Delta x \sigma_k^x} & \text{If } l = k - n_{i-1} \\ -\dfrac{2}{\Delta x(\Delta x + \sigma_k^x)} & \text{If } l = k \\ 0 & \text{Each other} \end{cases} \tag{61}$$

$$\text{Up} \quad B_{kl} = \begin{cases} -\dfrac{1}{N_j^2 \Delta z^2} & \text{If } l = k + 1 \\ \dfrac{2}{N_j^2 \Delta z^2} & \text{If } l = k \\ 0 & \text{Each other} \end{cases} \tag{62}$$

$$\text{Down}\quad B_{kl} = \begin{cases} -\dfrac{2}{N_j^2 \Delta z(\Delta z + \sigma_k^z)} & \text{If } l = k-1 \\ \dfrac{2}{N_j^2 \Delta z \sigma_k^z} & \text{If } l = k \\ 0 & \text{Each other} \end{cases} \qquad (63)$$

Being σ_k^x y σ_k^z the horizontal and vertical distances respectively from the *k* point to the boundary. This way, the discretization yields to the generalized eigenvalue problem (57). The set of solutions for λ, being $\lambda = \omega^2$, and Φ are the eigenvalues and eigenvectors of our generalized eigenvalue problem can we solve using the Jacobi-Davidson Method together with the so called QZ algorithm (Bai et al 2000). The Jacobi-Davidson method was used in the model to make it suitable for all grid sizes and all general cases. The results are then sorted from lower to higher modes.

ELCOM Description

ELCOM (Estuary, Lake and Coastal Ocean Model) is a three-dimensional hydrodynamics model for estuaries, lakes and reservoirs, that solves the 3D, hydrostatic, Boussinesq, Reynolds-averaged Navier-Stokes equations and scalar transport equations of potential temperature, salinity and tracers in a Z-coordinate system. The model is used to predict the variation of water temperature and salinity in space and time; and likewise other scalars. The model can be run together with the CAEDYM water quality model, being the three-dimensional hydrodynamics driver of such model. Heat exchange through the water's surface is governed by standard bulk transfer models found in the literature (e.g., Amorocho and Devries (1980); Imberger and Patterson (1981); Jacquet (1983)). The energy transfer across the free surface is separated into non penetrative components of long-wave radiation, sensible heat transfer, and evaporative heat loss, complemented by penetrative shortwave radiation. Non-penetrative effects are introduced as sources of temperature in the surface-mixed layer, whereas penetrative effects are introduced as source terms in one or more grid layers on the basis of an exponential decay and an extinction coefficient (Beer's law). ELCOM computes a model time step in a staged approach consisting of:

1. Introduction of surface heating/ cooling in the surface layer
2. Mixing of scalar concentrations and momentum using a mixed-layer model
3. Introduction of wind energy as a momentum source in the wind-mixed layer
4. Solution of the free-surface evolution and velocity field
5. Horizontal diffusion of momentum
6. Advection of scalars, and
7. Horizontal diffusion of scalars

The fundamental numerical scheme is adapted from the TRIM approach of Casulli and Cheng (1992) with modifications for accuracy, scalar conservation, numerical diffusion, and implementation of a mixed-layer turbulence closure. The solution grid uses varying width orthogonal cells. The grid stencil is the Arakawa C-grid: Velocities are defined on cell faces with the free-surface height and scalar concentrations on cell centers. The free-surface height in each column of grid cells moves vertically through grid layers as required by the free-surface evolution equation. Replacement of the standard vertical turbulent diffusion equation with a mixed-layer model eliminates the tridiagonal matrix inversion for each horizontal velocity component and transported scalar required for ach grid water column in the original TRIM scheme. This provides computational efficiency and allows sharper gradients to be maintained with coarse grid resolution. Passive and active scalars (i.e. tracers, salinity and temperature) are advected using a conservative ULTIMATE QUICKEST discretization (Leonard 1991).

Governing Hydrodynamic equations

The transport equations are the unsteady Reynolds-averaged Navier-Stokes (RANS) and scalar transport equations using the Boussinesq approximation and neglecting the non-hydrostatic pressure terms. Table 1 shows a summary of the governing equations and fundamental models used for three-dimensional transport and surface thermodynamics in ELCOM. Here, the nomenclature used in the model will be used.

Transport of Momentum:	$\frac{\partial U_\alpha}{\partial t} + U_j \frac{\partial U_\alpha}{\partial x_j} = -g\left\{\frac{\partial \eta}{\partial x_\alpha} + \frac{1}{\rho_0}\frac{\partial}{\partial x_a}\int_z^\eta \rho' dz\right\} + \frac{\partial}{\partial x_1}\left\{\nu_1 \frac{\partial U_\alpha}{\partial x_1}\right\} + \frac{\partial}{\partial x_2}\left\{\nu_2 \frac{\partial U_\alpha}{\partial x_2}\right\} + \frac{\partial}{\partial x_3}\left\{\nu_3 \frac{\partial U_\alpha}{\partial x_3}\right\} - .pdfilon_{\alpha\beta} f U_\beta$
Continuity:	$\frac{\partial U_j}{\partial x_j} = 0$
Momentum Boundary Conditions - Free Surface:	$\frac{\partial U_\alpha}{\partial x_3} = 0$
Momentum Boundary Conditions - Bottom and Sides:	$U_i = 0$
transport of Scalars:	$\frac{\partial C}{\partial t} + \frac{\partial}{\partial x_j}(CU_j) = \frac{\partial}{\partial x_1}\left\{\kappa_1 \frac{\partial C}{\partial x_1}\right\} + \frac{\partial}{\partial x_2}\left\{\kappa_2 \frac{\partial C}{\partial x_2}\right\} + \frac{\partial}{\partial x_3}\left\{\kappa_3 \frac{\partial C}{\partial x_3}\right\} + S_c$
Scalar Boundary Conditions :	$\frac{\partial C_\alpha}{\partial x_j} = 0$
Free-Surface Evolution:	$\frac{\partial \eta}{\partial t} = -\frac{\partial}{\partial x_\alpha}\int_0^\eta u_\alpha dz$
Free-Surface wind shear:	$(u_*)_\alpha^2 = C_{10}\frac{\rho_{air}}{\rho_{water}}(W_\beta W_\beta)_{\frac{1}{2}} W_\alpha$
Momentum input by wind:	$\frac{\partial U_\alpha}{\partial t} = \frac{(U_*)_\alpha^2}{h}$

Table 1. Summary of the governing equations in ELCOM.

The unsteady RANS equations are developed by filtering the unsteady Navier-Stokes equations over a time period that is long relative to sub-grid scale processes, but small relative to the unsteady grid-scale processes that are of interest. In an unsteady RANS numerical method the time scale of the averaging is the time step used in advancement of the evolution equations. Thus, the maximum time step for a given grid resolution is fundamentally limited by the grid scale physics, regardless of the numerical method. For a stratified flow, the model uses explicit discretization of the baroclinic terms in the momentum equation, leading to a time step constrain based on the internal wave Courant-Friedrichs-Lewy condition (CFL) such that

$$(g'D)^{1/2}\frac{\Delta t}{\Delta x} < \sqrt{2}\,, \tag{64}$$

is required. The left-hand side is defined as the baroclinic CFL number, where *g'* is the reduced gravity due to stratification, the effective depth is *D*, $(g'D)^{1/2}$ is an approximation of the wave speed of an internal wave. This baroclinic stability is generally the most restrictive condition in a density-stratified flow. The omission of such condition derives in instabilities in the model. The governing equations are then discretized on a Cartesian solution grid (or cells) in a staggered formulation where velocity components are defined on each face and scalars are defined at the cell centers

Wind momentum.

The momentum input of the wind is typically modeled (e. g., Casulli and Cheng (1992)) using a stress boundary condition at the free surface:

$$\nu \left.\frac{\partial u}{\partial x}\right|_{z=\eta} = u_*^2\,, \tag{65}$$

where ν is an eddy viscosity and u_*^2 is the wind stress. This boundary condition requires solution of vertical viscosity/ diffusion terms of the form

$$\frac{\partial}{\partial x}\left\{\nu\frac{\partial U_\alpha}{\partial x_3}\right\}; \frac{\partial}{\partial x}\left\{k\frac{\partial C}{\partial x_3}\right\}, \tag{66}$$

in place of the Reynolds stress terms in the momentum and scalar transport equations, terms that are modeled in ELCOM using the 3D mixed-layer model. The purpose of the eddy-viscosity term is to model the introduction of momentum into the wind-mixed layer. The resulting prediction of mixed layer depth using a coarse vertical grid is usually unsatisfactory. Instead, it will be solved in two steeps; by a sub-model for predicting the wind-mixed layer depth and a sub-model for the distribution of

momentum over the depth. The wind-mixed layer is the mixed layer that includes the free surface, with depth (h) of the wind-mixed layer computed in a discrete form as:

$$h_{i,j} = \sum_{m=k_a(i,j,k_\eta)}^{k_b(i,j,k_\eta)} \Delta Z_{i,j,m} \,, \tag{67}$$

where k_a and k_b are the lower and upper grid cell indices of the discrete wind-mixed layer in the water column (i, j) that has free surface grid cell k_η . To first order, we can approximate the introduction of wind momentum as a uniform distribution over the mixed layer (Imberger and Patterson, 1990):

$$\left.\frac{dU}{dt}\right|_{i,j,k} = \frac{\left.u_*^2\right|_{i,j,k}}{\left.h\right|_{i,j}}; \eta - h < \sum_{m=1}^{k} \Delta z_m < \eta \,, \tag{68}$$

where η is the free surface height in water column (i, j). Equation (68) is applied separately in the x and y directions to provide a direct increase in the velocity field in the wind-mixed layer before solution of the Navier-Stokes equations.

Surface Thermodynamics and mass fluxes.

The surface exchanges include heating due to short wave radiation penetration into the lake and the fluxes at the surface due to evaporation, sensible heat (i.e. convection of heat from the water surface to the atmosphere) and long wave radiation. Short wave radiation (280nm to 2800nm) is usually measured directly. Long wave radiation (greater than 2800nm) emitted from clouds and atmospheric water vapour can be measured directly or calculated from cloud cover, air temperature and humidity.

Solar (short wave) radiation flux - The depth of penetration of short wave radiation depends on the net short radiation that penetrates the water surface and the extinction coefficient. The net solar radiation penetrating the water can be written as:

$$Q_{sw} = Q_{sw(total)}(1 - r_a^{(sw)}) \,, \tag{69}$$

where $Q_{sw(total)}$ is the short wave radiation that reaches the surface of the water on Q_{sw} is the net short wave radiation penetrating the water surface, and $r_a^{(sw)}$ is the shortwave albedo. Once the short wave has penetrate the water surface, the short wave penetrates in depth following the Beer-Lambert law, such that

$$Q(z) = Q_{sw} e^{-\eta_a z}, \tag{70}$$

where *z* is the depth below the water surface and η_a is the attenuation coefficient. Thus the shortwave energy per unit area entering layer k through its upper face is

$$\Delta Q_k = Q_k - Q_{k-1} \tag{71}$$

Long wave energy flux - The Longwave radiation is calculated by one of three methods, depending on the input data. Three input measures are allowed: (a) incident long wave radiation, (b) net long wave radiation, and (c) cloud cover. The net longwave radiation energy deposited into the surface layer for a period Δt is calculated as:

$$\text{(a) } Q_{lw} = (1 - r_a^{(lw)}) Q_{lw(incident)} - .pdfilon_w \sigma T_w^4, \tag{72}$$

by using incident long wave radiation; where $r_a^{(lw)}$ is the albedo for long wave radiation, which is taken as a constant = 0.03 (Henderson-Sellers, 1986), $.pdfilon_w$ is the emissivity of the water surface (=0.96), σ is the Stefan-Boltzmann constant (σ = 5.6697x10 - 8Wm^{-2}K^{-4}), and *Tw* is the absolute temperature of the water surface (i.e. the temperature of the surface layer).

$$\text{(b) } Q_{lw} = (1 - r_a^{(lw)}) Q_{lw(net)}, \tag{73}$$

by using net long wave radiation; and

$$\text{(c) } Q_{lw} = (1 - r_a^{(lw)})(1 + 0.17C^2).pdfilon_a(T_a)\sigma T_a^4 - .pdfilon_w \sigma T_w^4, \tag{74}$$

where *C* is the cloud cover fraction ($0 \le C \le 1$), *C.pdfilon* = 9.37x10-6K^{-2}; and $.pdfilon_a(T_a) = C.pdfilonT_a^2$

Sensible heat flux - The sensible heat loss from the surface of the lake for the period Δt may be written as (Fischer et al. (1979) eq 6.19)

$$Q_{sh} = C_s \rho_a C_P U_a (T_a - T_s) \Delta t, \tag{75}$$

where C_s is the sensible heat transfer coefficient for wind speed at 10 m reference height above the water surface (= 1.3x10^{-3}), ρ_a the density of air in kg m^{-3}, C_P the specific heat of air at constant pressure (= 1003 J kg^{-1} K^{-1}), U_a is the wind speed at the 'standard' reference height of 10 m in m s^{-1}, with temperatures either both in Celsius or both in Kelvin.

Latent heat flux - The evaporative heat flux is given by (Fischer et al. (1979) eq 6.20)

$$Q_{lh} = \min\left(0, \frac{0.622}{P} C_L \rho_a L_E U_a (e_a - e_s(T_s))\Delta t\right), \quad (76)$$

where P is the atmospheric pressure in pascals, C_L is the latent heat transfer coefficient (=1.3x10^{-3}) for wind speed at reference height of 10m, ρ_a the density of air in kg m^{-3}, L_E the latent heat of evaporation of water (= 2.453x106 J kg^{-1}), U_a is the wind speed in ms^{-1} at the reference height of 10m, e_a the vapour pressure of the air, and e_s the saturation vapour pressure at the water surface temperature T_S; both vapour pressures are measured in pascals.

Thus, the total non-penetrative energy density deposited in the surface layer during the period Δt is given by

$$Q_{non-pen} = Q_{lw} + Q_{sh} + Q_{lh} \quad (77)$$

Surface mass fluxes - The surface mass fluxes are based in a balance between evaporation and rainfall, changing the mass of the surface layer cells.

Mixing

The 3D mixed-layer approach for ELCOM model is based in the mixing energy budgets developed for 1D lake modelling (Imberger and Patterson (1981), Spigel et al. (1986), Imberger and Patterson (1990)). The model applies a separate 1D mixed-layer model to each water column to provide vertical turbulent transport, whereas 3D transport of turbulent kinetic energy (TKE) is used to provide the dynamic effect of 3D motions on the TKE available for vertical mixing. The resultant mixing is a balance between:

1. The TKE available for mixing, TKE_A
2. The TKE required for mixing, E_{req}
3. The TKE dissipated, $E._{pdfilon}$ and
4. The residual mixing energy, $E_{M.}$

Of these, only the last, which is effectively the sum of the others at the end of the mixing algorithm, is considered a transported variable. Second, it is useful to characterize two types of mixing events in a stratified fluid:

1. convective mixing of unstable density gradients that decreases the potential energy of the fluid and releases TKE
2. mixing of stable density gradients that dissipates TKE and increases potential energy.

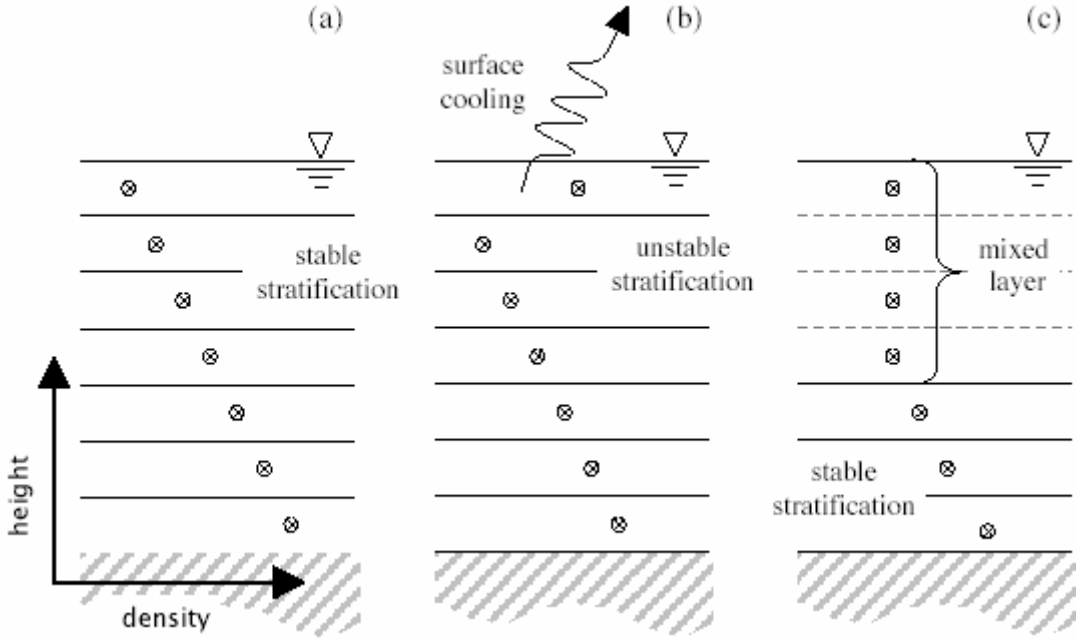

Figure 11 (extracted from Hodges et al. 2000). Development of a mixed layer due to surface cooling and unstable stratification. (a) Stable stratification at start of time step; (b) surface cooling creates unstable density profile; (c) unstable grid cells have been mixed.

The former is one of the TKE sources for mixing (TKE_A), whereas the latter is exactly the local energy required to mix (E_{req}). These two density gradient terms are computed from the vertical buoyancy scale. Finally, a definition for a 'mixed layer' is needed; this is taken to be a set of vertically contiguous grid cells that share the same density, scalar concentrations, and grid-scale velocity. According to this definition, the discrete version of a linear stratification with seven grid cells shown in Figure. 8a is a system with seven mixed layers, whereas the system in Figure. 8c has the same number of vertical grid cells but only four mixed layers.

The heat transfer changes the density stratification, either providing TKE_A (unstable density gradients produced by net cooling) or increasing *Ereq* (stable stratification produced by net warming). Once the new density field is calculated, the mixing process is modelled on a layer-by layer basis through each (i, j) water column by comparing the available mixing energy (TKE_A) from convective overturns, shear production, wind stirring, and TKE storage (E_M) to the potential energy increase (E_{req}) required to mix a grid cell up into the mixed layer above itself.

The mixing is calculated by the model following the next steps:

1. Calculate wind energy input, E_{wind}
2. If the boundary condition is being used in the model, calculate bottom energy input by drag. E_{drag}
3. For each column cycle from surface cell to bottom cell
4. Calculate generation of TKE by shear, E_{shear}
5. Calculate energy required for mixing, E_{req}
6. Calculate total energy available if two cells were totally mixed, TKE_{mixed}
7. Calculate time estimate for total mixing T_{TKE}
8. If unstable calculate time estimate based on convective overturn T_{conv}
9. Calculate mixing fraction η_f
10. If there is enough energy then mix cells
11. End of cycle from surface cell to bottom cell
12. Dissipate excess mixing energy

Equations

1. $E_{wind} = \frac{1}{2} C_n^3 dt u_*^3$

2. $E_{drag} = C_b \left(|u_{bot}| + |v_{bot}| \right)^{\frac{3}{2}} dt$

3. Mix surface layers till η_f <1

4. $E_{shear} = \frac{1}{2} C_s S^2 dz_l$

5. $E_{req} = -g' dz_l dz_{ml}$

6. $TKE_{mixed} = \begin{cases} TKE_{ml} + TKE_l + E_{shear} & if \quad E_{req} \geq 0 \\ TKE_{ml} + TKE_l + E_{shear} - C_c E_{req} & if \quad E_{req} < 0 \end{cases}$

7. $T_{TKE} = C_{TT} dz_l \sqrt{\frac{C_s dz_{ml} + dz_l}{2TKE_{mixed}}}$

8. $T_{conv} = C_{TC} dz_l \sqrt{\frac{dz_l}{g'}}$

9. $\eta_f = \min\left(\frac{\Delta t}{\min(T_{TKE}, T_{conv})}, 1.0 \right)$

10.

$If \quad TKE_{mixed} \geq \eta_f E_{req} \quad mixing$

$If \quad TKE_{mixed} < \eta_f E_{req} \; no\_mixing$

If η_f =1 all scalar and velocity within the mixed layer are equal (total mixing)

$$C'_{ml} = \frac{C_{ml} dz_{ml} + C_l dz_l}{dz_{ml} + dz_l} \quad U'_{ml} = \frac{\rho_{ml} U_{ml} dz_{ml} + \rho_l U_l dz_l}{dz_{ml} + dz_l}$$

For partial mixing

$$C_k = \begin{cases} C_{ml} & k = k_l + 2 : k_{ml-top} \\ (1-\eta_f) C_{ml} + \eta_f \frac{C_{ml} dz_k + C_l dz_l}{dz_k + dz_l} & k = k_l + 1 \\ (1-\eta_f) C_l + \eta_f \frac{C_{ml} dz_{k+1} + C_l dz_l}{dz_{k+1} + dz_l} & k = k_l \end{cases}$$

11. End of cycle once the bottom cell is reached

12. $TKE = TKE - \frac{1}{2} C._{pdfilon} \Delta t \left(\frac{TKE}{dz} \right)^{\frac{3}{2}}$

Parameters

u_* wind shear velocity

C_n mixing coefficient set to 1.33

C_b mixing coefficient set to 2.2

C_s mixing coefficient set to 0.15 ; S the shear;
l refers to the cell directly below the mixed layer
g' reduced gravity term
ml refers to values in the mixed layer

C_c mixing coefficient is set to 0.2

C_{TT} coefficient set to 50.0

C_{ml} is the scalar concentration of the mixed layer and C_l of the cell being mixed. The ‘ indicates value after mixing.

C_k is the concentration of layer k in the column,
k_l refers to the layer of the cell being mixed
$k_{ml\text{-}top}$ is the layer of the top of the mixed layer.

$C._{pdfilon}$ dissipation coefficient set to 1.15. Any TKE left after dissipation is transported before available for next step mixing

Table 2 summarized the equations used for such processes

CAEDYM description

CAEDYM is an aquatic ecological model designed to be readily linked to hydrodynamic models, which currently includes the 1D model DYRESM and the 3D model ELCOM. The coupling between CAEDYM and the hydrodynamic driver is dynamic; in particular, the thermal structure of the water body is dependent on the water quality concentrations by feeding back through water clarity.

The model includes comprehensive process representation of the C, N, P, Si and DO cycles, several size classes of inorganic suspended solids, and phytoplankton dynamics. Numerous optional biological and other state variables can also be configured. Hence, CAEDYM is more advanced than traditional N-P-Z models, as it is a general biogeochemical model that can resolve species- or group-specific ecological interactions. CAEDYM operates on any sub-daily time step to resolve algal processes (diurnal photosynthesis and nocturnal respiration), and is generally run at the same time interval as the hydrodynamic model. Algorithms for salinity dependence are included so that a diverse range of aquatic settings can be simulated. The user can prescribe whether the simulation is for freshwater, estuaries or coastal waters.

Figure 9 represents the major biogeochemical state variables in CAEDYM. The configuration file existing allows user to customize the model elements needed in any simulation. Parameters are introduced as an input file, so that, user doesn't need to modify the source; but inevitably, user may define variables not represented in CAEDYM, thus some modifications to the source may be needed.

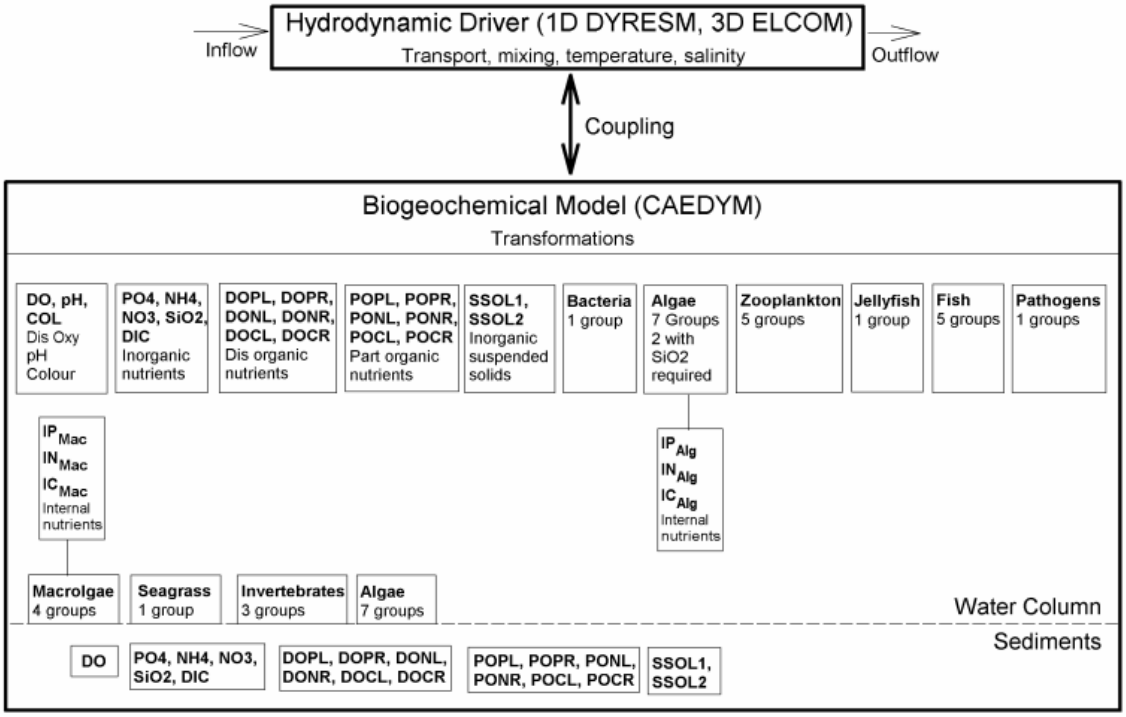

Figure 9. Summary of the biogeochemical paths simulated in CAEDYM.

CAEDYM simulates the *C,N, P, DO* and *Si* cycles with inorganic suspended solids, phytoplankton and optional biotic compartments such as zooplankton, fish, bacteria and others. The Model is divided in sub-routines or sections. Following we will see an overview of the main simulated variables.

Light

The shortwave incident radiation supplied by the hydrodynamic driver (ELCOM) is converted to the photosynthetically active component (*PAR*) based on the assumption that 45% of the incident spectrum lies between 400-700 nm (Jellison and Melack, 1993). *PAR* is assumed to penetrate into the water column according to the Beer-Lambert Law with the light extinction coefficient dynamically adjusted to account for variability in the concentrations of algal, inorganic and detrital particulates, and dissolved organic carbon levels. The ultra-violet compinent of the incident light can also be used for looking at pathogen inactivation and organic matter photolysis.

Inorganic Particles

Two inorganic particles groups (*SS*) can optionally be included within the simulation, with each group assigned a unique diameter and density, and modelled as a balance between resuspension and settling. Adsorption and desorption of aqueous-phase *FRP* and NH_4 onto inorganic particles (*PIP* and *PIN*) can also be configured. Particle settling is modelled on the basis of Stokes Law. *The inorganic particles is now being updated to six groups.

Sediments and Resuspension.

CAEDYM maintains mass balance of all simulate variables in both the water column and a single sediment layer; providing a complete description of the dominant pools and fluxes in the water column with only sufficient complexity of the sediments to maintain mass conservation. The sediment fluxes of dissolved inorganic and organic nutrients are based on empirical formulations that account for environmental sensitivities and require laboratory and field studies to establish parameter values.

Resuspension of inorganic (*SS*) and organic particles (*POM*) from the sediment-water interface require a number of parameters including the critical shear stress and the resuspension rate constant. The composition of the sediments is established in the CAEDYM initial conditions file.

Dissolved Oxygen

Dissolved Oxygen (*DO*) dynamics within CAEDYM include atmospheric exchange, the sediment oxygen demand (*SOD*), microbial use during organic matter mineralization and nitrification, photosynthetic oxygen production and respiratory oxygen consumption, and respiration by other optional biotic components. Microbial activity facilitates the breakdown of organic carbon (in particular, *DOC*) to CO_2, and a stoichiometrically equivalent amount of oxygen is removed. The process of nitrification also requires oxygen that is dependent on the stoichiometric factor for the ratio of oxygen to nitrogen ($Y_{O2:N}$) and the half-saturation constant for the effect of oxygen limitation (K_{NIT}). Photosynthetic oxygen production and respiratory oxygen consumption is summed over the number of simulated phytoplankton groups.

Carbon, Nitrogen, Phosphorus and Silica

The Cycles of nutrients simulated accounts for both inorganic and organic, and dissolved and particulate forms of *C, N* and *P*, along the degradation pathway of *POM* to *DOM* to dissolved inorganic matter (*DIM*). Nitrogen includes denitrification, nitrification and N_2 fixation. *Si* is included for the uptake of diatoms into the dissolved form. *C* cicle includes atmospheric fluxes of CO_2 based on the partial pressure of CO_2 differences (pCO_2).

Phytoplankton Dynamics

Up to seven phytoplankton groups can be simulated with CAEDYM. The algal biomass can be simulated either in *chla* ($\mu g\ chla\ L^{-1}$) or carbon (mg C L^{-1}). The growth rate is calculated based in the max growth rate for every specie multiplied by the temperature factor and minimum value of expressions for limitation by light or nutrients. Phytoplankton may be grazed by zoo, fish and clams. Light limitation on phytoplankton growth can be configured to be subject to photoinhibition or to be non-photoinhibited.

Nutrients dynamics within algae can be simulated by using a constant nutrient to *chla* ratio or by dynamic intracellular stores. The first is based in a simple Michaelis-Menten equation to model nutrient limitation with half-saturation constant for the effect of external nutrient concentrations. Metabolic loss of nutrients from mortality and excretion is proportional to a constant multiplied by the loss rate and the fraction of excretion and mortality that returns to detrital pool. The latter model uses dynamic intracellular stores that are able to regulate growth. This model allows for the phytoplankton to have variable internal nutrient concentrations with dynamic nutrient uptake bounded by minimum and maximum values. Nutrient losses are calculated from internal nutrient concentrations.

Loss terms for respiration, natural mortality and excretion are modelled with a single respiration rate coefficient. This loss rate is then divided into the pure respiratory fraction and losses due to mortality and excretion. The constant f_{DOM} is the fraction of mortality and excretion to the dissolved organic pool with the remainder into the particulate organic pool.

Bacteria

Bacterial biomass and organic matter mineralization may also be simulated. The bacteria are prescribed a fixed C:N:P ratio that is constant over the course of simulation. The incoming nutrients, primarily received from dissolved organic matter pool, are converted to CO_2, NH_4 and *FRP* and released back to the water column.

Zooplankton

CAEDYM assumes each zooplankton group has a fixed *C:N:P* ratio and depending on the *C:N:P* ratio of the various food sources, the groups balance their internal concentration by excretion of labile dissolved organic matter. The grazing preference of each group is user defined, and can be for any of the simulated algal, zooplankton, bacterial or detrital groups. Faecal pellets can also be specified as either hard, soft or in between, and lost to the sediment or returned to the detrital pool.

Higher biology

CAEDYM has the facility to model higher organisms such as fish, jellyfish, and bethic organisms including macroalgae, benthic macroinvertebrates and clams/mussels

Pathogens and Microbial Indicator Organisms

CAEDYM has an optional pathogen model for users interested in simulating microbial pollution in a lake, reservoir, estuary or coastal environment. The model was developed based on *Cryptosporidium* sp. dynamics, and also contains variations for simulating indicator organisms such as coliform bacteria.

Governing Equations

The main equations followed by CAEDYM of the biogeochemical paths are summarized in table 4. Likewise a list of symbols and variables used are summarized in Table 5.

Table 4.

Major equations used in CAEDYM

Rate of change of phytoplankton concentration (mg chl $a\,m^{-3}$ per day)	$\frac{\delta C_i}{\delta t} = (\mu_i - R_i)C_i + V_i + H_i$
Phytoplankton growth rate (per day)	$\mu_i = \mu_{\max i} f_i(T) f_i(S) \min\left[f_i(N), f_i(P), f_i(I), f_i(Si)\right]$
Phytoplankton respiration and mortality rate (per day)	$R_i = \frac{k_{Ri}\vartheta_i^{T-20}}{f_i(S)}$
Temperature limitation	$f_i(T) = \psi_i^{T-20} + \psi_i^{d_i(T-a_i)} + b_i$ (Griffin et al., 2001)
Light limitation	$f_i(I) = \begin{cases} (I/I_S)\exp(1 - I/I_S), & \text{photoinhibited(freshwaterdiatoms)} \\ 1 - \exp(-I/I_{ki}), & \text{non-photoinhibited(othergroups)} \end{cases}$
Nitrogen limitation	$f_i(N) = \frac{\mathrm{IN}_i}{\mathrm{IN}_{\max i} - \mathrm{IN}_{\min i}}\left(1 - \frac{\mathrm{IN}_{\min i}}{\mathrm{IN}_i}\right)$
Phosphorus limitation	$f_i(P) = \frac{\mathrm{IP}_i}{\mathrm{IP}_{\max i} - \mathrm{IP}_{\min i}}\left(1 - \frac{\mathrm{IP}_{\min i}}{\mathrm{IP}_i}\right)$
Silica limitation	$f_i(\mathrm{Si}) = \begin{cases} \frac{\mathrm{Si}}{\mathrm{Si} + K_{Si\,i}}, & \text{diatoms} \\ 1, & \text{other groups} \end{cases}$
Salinity limitation (freshwater species: *M. aerugtnosa*, chlorophytes and freshwater diatoms)	$f_i(S) = \begin{cases} 1, & S \le S_{\mathrm{opi}} \\ \frac{(S_{\max i} - S_{\mathrm{opi}})^2}{(S_{\max i} - S_{\mathrm{opi}})^2 - (\beta_i - 1)(2S_{\mathrm{opi}}S - S^2 - S_{\mathrm{opi}}^2)}, & S > S_{\mathrm{opi}} \end{cases}$
Salinity limitation (marine species: marine diatoms and dinoflagellates)	$f_i(S) = \begin{cases} 1, & S > S_{\mathrm{opi}} \\ \frac{S_{\mathrm{opi}}^2}{(S^2 - 2S_{\mathrm{opi}})(\beta_i - 1) + \beta_i S_{\mathrm{opi}}^2}, & S \le S_{\mathrm{opi}} \end{cases}$
Rate of change of nitrate concentration (mg N m^{-3} per day)	$\frac{\partial \mathrm{NO_3}}{\partial t} = -\sum((1 - P_{\mathrm{Ni}})U_{\mathrm{Ni}}) - D + \mathrm{Nit} + H_{\mathrm{NO_3}}$
Phytoplankton assimilation preference for NH_4 over NO_3	$P_{\mathrm{Ni}} = \left[\frac{\mathrm{NH_4} \cdot \mathrm{NO_3}}{(\mathrm{NH_4} + K_{\mathrm{Ni}})(\mathrm{NO_3} + K_{\mathrm{Ni}})}\right]\left[\frac{\mathrm{NH_4} \cdot K_{\mathrm{Ni}}}{(\mathrm{NH_4} + \mathrm{NO_3})(\mathrm{NO_3} + K_{\mathrm{Ni}})}\right]$
Rate of change of ammonium concentration (mg N m^{-3} per day)	$\frac{\delta \mathrm{NH_4}}{\delta t} = \sum(E_{\mathrm{Ni}} - P_{\mathrm{Ni}}U_{\mathrm{Ni}}) - \mathrm{Nit} + M_{\mathrm{N}} + X_{\mathrm{N}} + H_{\mathrm{NH_4}}$
Rate of change of organic nitrogen concentration (mg N m^{-3} per day)	$\frac{\delta \mathrm{ON}}{\delta t} = -M_{\mathrm{N}} + V_{\mathrm{ON}} + H_{\mathrm{ON}}$
Rate of change of internal (cellular) phosphorus concentration for phytoplankton group i (mg P (mg chl a)$^{-1}$ per day)	$\frac{\delta \mathrm{IP}_i}{\delta t} = \frac{U_{\mathrm{P}i} - E_{\mathrm{P}i}}{C_i} + V_i \mathrm{IP}_i + H_{\mathrm{IP}i}$
Rate of change of phosphate concentration (mg P m^{-3} per day)	$\frac{\delta \mathrm{PO_4}}{\delta t} = \sum(E_{\mathrm{P}i} - U_{\mathrm{P}i}) + M_{\mathrm{P}} + X_{\mathrm{P}} + H_{\mathrm{PO_4}}$
Rate of change of organic phosphorus concentration (mg P m^{-3} per day)	$\frac{\delta \mathrm{OP}}{\delta t} = -M_{\mathrm{P}} + V_{\mathrm{OP}} + H_{\mathrm{OP}}$
Rate of change of internal (cellular) nitrogen concentration for phytoplankton group i (μg N (mg chl a)$^{-1}$ per day)	$\frac{\delta \mathrm{IN}_i}{\delta t} = \frac{(U_{\mathrm{N}i} - E_{\mathrm{N}i})}{C_i} + V_i \mathrm{IN}_i + H_{\mathrm{IN}_i}$
Phytoplankton phosphorus uptake (mg P m^{-3} per day)	$U_{\mathrm{P}i} = \mathrm{UP}_{\max i} C_i \left[f_i(T)\left(\frac{\mathrm{IP}_{\max i} - \mathrm{IP}_i}{\mathrm{IP}_{\max i} - \mathrm{IP}_{\min i}}\right)\left(\frac{\mathrm{PO_4}}{K_{\mathrm{P}i} + \mathrm{PO_4}}\right)\right]$
Phytoplankton nitrogen uptake (mg N m^{-3} per day)	$U_{\mathrm{N}i} = \mathrm{UN}_{\max i} C_i \left[f_i(T)\left(\frac{\mathrm{IN}_{\max i} - \mathrm{IN}_i}{\mathrm{IN}_{\max i} - \mathrm{IN}_{\min i}}\right)\left(\frac{\mathrm{NO_3} + \mathrm{NH_4}}{K_{\mathrm{Ni}} + \mathrm{NO_3} + \mathrm{NH_4}}\right)\right]$
Release of phosphate through phytoplankton excretion (mg P m^{-3} per day)	$E_{\mathrm{P}i} = R_i f_i(S) \mathrm{IP}_i C_i$
Release of ammonia nitrogen through phytoplankton excretion (mg N m^{-3} per day)	$E_{\mathrm{N}i} = R_i f_i(S) \mathrm{IN}_i C_i$
Denitrification (mg N m^{-3} per day)	$D = k_{\mathrm{N_2}} \vartheta_{\mathrm{D}}^{T-20}\left(\frac{K_{\mathrm{DO}}}{K_{\mathrm{DO}} + \mathrm{DO}}\right)\mathrm{NO_3}$
Nitrification (mg N m^{-3} per day)	$\mathrm{Nit} = k_{\mathrm{NO}} \vartheta_{\mathrm{N}}^{T-20}\left(\frac{\mathrm{DO}}{K_{\mathrm{NIT}} + \mathrm{DO}}\right)\mathrm{NH_4}$

Table 4 (continued)

Mineralisation of organic phosphorus ($mg\,P\,m^{-3}$ per day)	$M_P = \left[k_{OAP}\upsilon^{T-20}\frac{K_{MIN}}{K_{MIN}+DO} + k_{OP}\upsilon^{T-20}\frac{DO}{K_{MIN}+DO}\right]OP$
Mineralisation of organic nitrogen ($mg\,N\,m^{-3}$ per day)	$M_N = \left[k_{OAN}\upsilon^{T-20}\frac{K_{MIN}}{K_{MIN}+DO} + k_{ON}\upsilon^{T-20}\frac{DO}{K_{MIN}+DO}\right]ON$
Release of phosphate from bottom sediments ($mg\,P\,m^{-3}$ per day)	$X_P = \begin{cases} \frac{S_P(K_{DOS}/(K_{DOS}+DO_b)+(\lvert pH_b-7\rvert)/(K_{pH}+\lvert pH_b-7\rvert))}{dz_b}, & \text{bottom layer} \\ 0, & \text{other layers} \end{cases}$
Release of ammonia nitrogen from bottom sediments ($mg\,N\,m^{-3}$ per day)	$X_N = \begin{cases} \frac{S_N(K_{DOS}/(K_{DOS}+DO_b)+(\lvert pH_b-7\rvert)/(K_{pH}+\lvert pH_b-7\rvert))}{dz_b}, & \text{bottom layer} \\ 0, & \text{other layers} \end{cases}$
Rate of change of dissolved oxygen ($g\,O_2\,m^{-3}$ per day)	$\frac{\delta DO}{\delta t} = F - U_b - U_{OC} - Y_{O:N}Nit + \sum P_i + H_{DO}$
Rate of change of dissolved oxygen due to exchange across the air–water interface ($g\,O_2\,m^{-3}$ per day)	$F = \begin{cases} \frac{wu^2(O_a-DO_s)}{dz_s\sqrt{Sc/660}}, & \text{surface layer} \\ 0, & \text{subsurface layer} \end{cases}$ (Wanninkhof, 1992)
Dissolved oxygen concentration in the air phase near the air–water interface, i.e., saturation concentration ($g\,O_2\,m^{-3}$)	$O_a = 1.42763\exp\left(-173.3292 + 249.6339\frac{100}{T} + 143.3483\log\left(\frac{T}{100}\right) - 21.8492\frac{T}{100} + S\left[-0.033096 + 0.014259\frac{T}{100} - 0.0017\left(\frac{T}{100}\right)^2\right]\right)$ (Riley and Skirrow, 1974)
Schmidt number (dimensionless)	$Sc = \left(0.9 + \frac{0.1S}{35}\right)[1953.4 - 128.0T + 3.9918T^2 - 0.050091T^3]$ (Wanninkhof, 1992)
Rate of change of dissolved oxygen concentration due to uptake by bottom sediments ($g\,O_2\,m^{-3}$ per day)	$U_b = \begin{cases} \left(\frac{K_F\upsilon^{T-20}}{dz_b}\right)\left(\frac{DO_b}{K_S+DO_b}\right), & \text{bottom layer} \\ 0, & \text{other layers} \end{cases}$
Net production of oxygen due to phytoplankton production and respiration ($g\,O_2\,m^{-3}$ per day)	$P_i = Y_{O:C}Y_{C:chla}C_i[\mu_i(1-k_p) - R_i]$
Utilisation of oxygen due to remineralisation of organic materials in the water column ($g\,O_2\,m^{-3}$ per day)	$U_{OC} = k_{OC}\vartheta_{OC}^{T-20}Y_{O:C}OC\left[\frac{DO}{K_{OC}+DO}\right]$
Rate of change of labile organic carbon concentration ($mg\,C\,m^{-3}$ per day)	$\frac{\partial OC}{\partial t} = \sum \chi_i - B_{OC} + H_{OC} + V_{OC}$
Breakdown of organic carbon in the water column ($mg\,C\,m^{-3}$ per day)	$B_{OC} = k_{OC}\vartheta_{OC}^{T-20}OC\left[\frac{DO}{K_{OC}+DO} + k_{an}\frac{K_{OC}}{K_{OC}+DO}\right]$
Contribution to labile organic carbon pool from phytoplankton mortality and excretion ($mg\,C\,m^{-3}$ per day)	$\chi_i = (1-j_i)R_iY_{C:chla}C_i$
Net change in concentration of substance Y due to settling and resuspension from bottom sediments ($mg\,m^{-3}$ per day) where $l-1$ is the layer above the current layer, l	$V_Y = \begin{cases} (\Re_Y - v_{YT(l)}Y_l)/dz_b + v_{YT(l-1)}Y_{l-1}/dz_{l-1}, & \text{bottom layer} \\ -v_{YT(l)}Y_l/dz_l + v_{YT(l-1)}Y_{l-1}/dz_{l-1}, & \text{bottom layers} \end{cases}$
Settling rate of substance Y at the current water temperature, T of layer l (m per day)	$v_{YT(l)} = v_{Y20}\left(\frac{\eta_{20}\rho_T}{\eta_T\rho_{20}}\right)$
Rate of change in concentration of substance Y due to resuspension ($mg\,m^{-3}$)	$\Re_Y = \begin{cases} \frac{\alpha_Y((\tau-\tau_c)/\tau_{ref})}{dz_b}, & \text{diatoms and organic C, N and P} \\ 0, & \text{other substances} \end{cases}$ (Winterwerp, 1998)
Shear stress ($N\,m^{-2}$)	$\tau = \tau_s + \tau_w$
Shear stress due to steady currents ($N\,m^{-2}$)	$\tau_S = C_D\overline{U}^2\rho_T$ (Engelund and Hansen, 1972)

Table 4 (continued)

Drag coefficient of the bed (dimensionless)	$C_D = \frac{0.03}{\log^2(12h/k_d)}$ (Engelund and Hansen, 1972)
Oscillatory shear stress due to waves ($N\,m^{-2}$)	$\tau_w = 0.25 f_w U_m^2 \rho_T$ (Coastal Engineering Research Center, 1975)
Maximum orbital velocity ($m\,s^{-1}$)	$U_m = \frac{\pi H}{T_w \sinh(2\pi dz_1/L)}$ (Coastal Engineering Research Center, 1975)
Wave friction factor (dimensionless)	$f_w = \exp\left\lfloor 5.213(k_d/a_w)^{0.194} - 5.977 \right\rfloor$ (Swart, 1974)
Maximum bottom amplitude of shallow-water waves (m)	$a_w = \frac{H}{2\sinh(2\pi h/L)}$ (Coastal Engineering Research Center, 1975)
Wavelength (m)	$L = \frac{2\pi h \left\lfloor \tanh(4\pi^2 h/gT_w^2) \right\rfloor}{4\pi^2 h/gT_w^2}$ (Coastal Engineering Research Center, 1975)
Wave period (s)	$T_w = 2.40\pi u \left\lfloor \frac{\tanh[0.833(gh/u^2)^{0.375}]}{g} \right\rfloor \tanh \left\lfloor \frac{0.077(gF/u^2)^{0.25}}{\tanh[0.833(gh/u^2)^{0.375}]} \right\rfloor$ (Coastal Engineering Research Center, 1975)
Wave height (m)	$H = 0.283u^2 \left\lfloor \frac{\tanh[0.530(gh/u^2)]}{g} \right\rfloor \tanh \left\lfloor \frac{0.0125(gF/u^2)^{0.42}}{\tanh[0.530(gh/u^2)^{0.75}]} \right\rfloor$ (Coastal Engineering Research Center, 1975)

Table 5

List of symbols and units for variables

C_i	Chlorophyll *a* concentration of phytoplankton group i ($mg\,chl\,a\,m^{-3}$)
DO	Dissolved oxygen concentration ($g\,m^{-3}$)
DO_b	Dissolved oxygen concentration in the bottom layer ($g\,m^{-3}$)
DO_s	Dissolved oxygen concentration near the water surface ($g\,m^{-3}$)
dz_b	Thickness of the bottom layer of the water column (m), from the hydrodynamic model
dz_i	Thickness of layer i (m), from the hydrodynamic model
dz_s	Thickness of the surface layer of the water column (m), from the hydrodynamic model
F	Fetch length over which wind blows (m), determined from model grid
h	Depth of water (m), from the hydrodynamic model
H_i	Net flux of phytoplankton group i into the grid-cell due to advection and mixing ($mg\,chl\,a\,m^{-3}$ per day)
H_{INi}	Net change in intracellular nitrogen for phytoplankton group i due to advection and mixing ($mg\,N\,(mg\,chl\,a)^{-1}$ per day)
H_{IPi}	Net change in intracellular phosphorus stores for phytoplankton group i due to advection and mixing ($mg\,P\,(mg\,chl\,a)^{-1}$ per day)
H_{NH_4}	Net flux of NH_4 into the grid-cell due to advection and mixing ($mg\,N\,m^{-3}$ per day)
H_{NO_3}	Net flux of NO_3 into the grid-cell due to advection and mixing ($mg\,N\,m^{-3}$ per day)
H_{OC}	Net flux of labile organic matter into the grid-cell due to advection and mixing ($mg\,m^{-3}$ per day), calculated in the hydrodynamic model
H_{ON}	Net flux of organic nitrogen into the grid-cell due to advection and mixing ($mg\,N\,m^{-3}$ per day), calculated in the hydrodynamic model
H_{OP}	Net flux of organic phosphorus into the grid-cell due to advection and mixing ($mg\,P\,m^{-3}$ per day), calculated in the hydrodynamic model
H_{PO_4}	Net flux of PO_4 into the grid-cell due to advection and mixing ($mg\,P\,m^{-3}$ per day), calculated in the hydrodynamic model
H_Y	Net flux of substance Y into the grid-cell due to advection and mixing ($g\,O_2\,m^{-3}$ per day)
I	Irradiance ($\mu E\,m^{-2}\,s^{-1}$)
i	Phytoplankton group index
IN_i	Internal (cellular) nitrogen concentration ($mg\,N\,(mg\,chl\,a)^{-1}$) in phytoplankton group i
IP_i	Internal (cellular) phosphorus concentration ($mg\,P\,(mg\,chl\,a)^{-1}$) in phytoplankton group i
NH_4	Ammonium concentration ($mg\,N\,m^{-3}$)
NO_3	Nitrate concentration ($mg\,N\,m^{-3}$)
OC	Labile organic carbon ($mg\,C\,m^{-3}$)
ON	Organic nitrogen concentration ($mg\,N\,m^{-3}$)
OP	Organic phosphorus concentration ($mg\,N\,m^{-3}$)
pH_b	pH in the bottom layer
PO_4	Phosphate concentration ($mg\,P\,m^{-3}$)
S	Salinity
Si	Silica concentration ($mg\,Si\,m^{-3}$)
T	Water temperature (°C)
u	Wind speed 10 m above the water surface ($m\,s^{-1}$)
$\overline{U}$	Mean bottom layer current velocity ($m\,s^{-1}$), from the hydrodynamic model
Y	Concentration of substance Y (units as given for each substance)
ς_T	Dynamic viscosity of water at temperature T
$\tilde{n}_T$	Density water at temperature T ($kg\,m^{-3}$)

Finally, parameters used by Robson and Hamilton (2004) is included in Table 6, as a configuration example.

Table 6

Parameter values used in CAEDYM

τ_c	0.001 diatoms 0.05 organic carbon, nitrogen and phosphorus	Critical shear stress for resuspension ($N\,m^{-2}$)
τ_{ref}	1.0	Reference shear stress ($N\,m^{-2}$)
α_f	0.02 diatoms 0.85 organic phosphorus 4.3 organic nitrogen	Resuspension rate constant ($mg\,m^{-2}$ per day)
a_i	Dinoflagellates: 32.0 *M. aeruginosa*: 30.095 Chlorophytes: 27.372 Marine diatoms: 29.559 Freshwater diatoms: 26.396	Coefficient for temperature limitation function for phytoplankton (dimensionless)
b_i	Dinoflagellates: 0.05 *M. aeruginosa*: 0.182 Chlorophytes: 0.126 Marine diatoms: 0.028 Freshwater diatoms: 0.049	Coefficient for temperature limitation function for phytoplankton (dimensionless)
ϑ_D	1.08	Temperature multiplier for denitrification (dimensionless)
d_i	Dinoflagellates: 1.01 *M. aeruginosa*: 2.19 Chlorophytes: 4.25 Marine diatoms: 4.99 Freshwater diatoms: 5.41	Coefficient for temperature limitation function for phytoplankton (dimensionless)
g	9.81	Acceleration due to gravity ($m^2\,s^{-2}$)
I_{ki}	Dinoflagellates: 180 *M. aeruginosa*: 500 Chlorophytes: 200 Marine diatoms: 380	Irradiance parameter for non-photoinhibited phytoplankton growth ($\mu E\,m^{-2}\,s^{-1}$)
$IN_{max\,i}$	Dinoflagellates: 9.3 *M. aeruginosa*: 5.0 Chlorophytes: 10.5 Marine diatoms: 12.0 Freshwater diatoms: 7.5	Maximum internal nitrogen concentration ($mg\,N\,(mg\,chl\,a)^{-1}$)
$IN_{min\,i}$	Dinoflagellates: 4.5 *M. aeruginosa*: 2.5 Chlorophytes: 4.0 Marine diatoms: 5.0 Freshwater diatoms: 5.6	Minimum internal nitrogen concentration ($mg\,N\,(mg\,chl\,a)^{-1}$)
$IP_{max\,i}$	Dinoflagellates: 0.60 *M. aeruginosa*: 0.80 Chlorophytes: 1.24 Marine diatoms: 0.60 Freshwater diatoms: 1.0	Maximum internal phosphorus concentration ($mg\,P\,(mg\,chl\,a)^{-1}$)
$IP_{min\,i}$	Dinoflagellates: 0.27 *M. aeruginosa*: 0.40 Chlorophytes: 0.20 Marine diatoms: 0.20 Freshwater diatoms: 0.25	Minimum internal phosphorus concentration ($mg\,P\,(mg\,chl\,a)^{-1}$)
I_S	Freshwater diatoms: 120	Photoinhibited saturation irradiance ($\mu E\,m^{-2}\,s^{-1}$)
f_i	Dinoflagellates: 0.7 *M. aerugtnosa*: 0.7 Chlorophytes: 0.78 Marine diatoms: 0.7 Freshwater diatoms: 0.7	Fraction of respiration and mortality not contributing to labile organic carbon pool for phytoplankton (dimensionless)
k_{an}	0.3	Decrease in anaerobic decomposition relative to aerobic decomposition (dimensionless)
k_d	1.0 diatoms 5×10^3 organic carbon 5×10^2 organic nitrogen 1×10^2 organic phosphorus	Coefficient controlling resuspension ($mg\,m^{-2}$)
K_{DO}	0.3	Oxygen half-saturation constant for denitrification ($g\,O_2\,m^{-3}$)
K_{DOS}	1.0	Oxygen half-saturation constant for release of ammonia nitrogen and phosphate from bottom sediments ($g\,O_2\,m^{-3}$)

Table 6 (continued)

K_F	6.0	Reference sediment oxygen uptake rate ($g O_2 m^{-2}$ per day)
K_{MIN}	1.5	Mineralisation half-saturation constant for oxygen ($g m^{-3}$)
k_{N2}	0.4	Denitrification rate coefficient (per day)
K_{Ni}	Dinoflagellates: 52 *M. aerugtnosa*: 30 Chlorophytes: 30 Marine diatoms: 15 Freshwater diatoms: 40	Half-saturation constant for nitrogen uptake ($mg m^{-3}$)
K_{NIT}	4.0	Nitrification half-saturation constant for oxygen ($g m^{-3}$)
k_{NO}	0.2	Nitrification rate coefficient (per day)
k_{OAN}	7.0×10^{-3}	Anaerobic organic nitrogen mineralisation rate coefficient (per day)
k_{OAP}	7.0×10^{-3}	Anaerobic organic phosphorus mineralisation rate coefficient (per day)
k_{OC}	0.07	Mineralisation rate coefficient for organic matter (per day)
K_{OC}	0.5	Half-saturation constant for remineralisation of organic matter ($g O_2 m^{-3}$)
k_{ON}	0.01	Aerobic organic nitrogen mineralisation rate coefficient (per day)
K_{OP}	0.05	Aerobic organic phosphorus mineralisation rate coefficient (per day)
k_p	0.14	Fraction of oxygen production lost through photosynthetic respiration (dimensionless)
K_{pH}	7	pH coefficient controlling release of nutrients from sediments
K_{Pi}	Dinoflagellates: 5 *M. aerugtnosa*: 6 Chlorophytes: 12 Marine diatoms: 3 Freshwater diatoms: 10	Half-saturation constant for phosphorus uptake ($mg m^{-3}$)
k_{Ri}	Dinoflagellates: 0.05 *M. aerugtnosa*: 0.08 Chlorophytes: 0.07 Marine diatoms: 0.15 Freshwater diatoms: 0.1	Respiration rate coefficient (per day)
K_S	2.0	Oxygen half-saturation coefficient for sediment oxygen uptake ($g O_2 m^{-3}$)
K_{Si}	Marine diatoms: 220 Freshwater diatoms: 440	Half-saturation constant for the effect of silica concentration on diatom growth ($mg Si m^{-3}$)
ϑ_N	1.08	Temperature multiplier for nitrification (dimensionless)
$S_{max\,i}$	Dinoflagellates: 29 *M. aerugtnosa*: 25 Chlorophytes: 12 Marine diatoms: 18 Freshwater diatoms: 18	Maximum salinity for salinity response function (practical salinity units)
S_N	20	Maximum potential sediment flux of nitrogen ($mg m^{-2}$ per day)
S_{opi}	Dinoflagellates: 25 *M. aerugtnosa*: 4 Chlorophytes: 9 Marine diatoms: 20 Freshwater diatoms: 3	Optimal salinity for salinity response function (practical salinity units)
S_P	4	Maximum potential sediment flux of phosphorus ($mg m^{-2}$ per day)
$UN_{max\,i}$	Dinoflagellates: 1.5 *M. aerugtnosa*: 1.5 Chlorophytes: 4.0 Marine diatoms: 12 Freshwater diatoms: 15	Maximum rate of nitrogen uptake ($mg N (mg chl\ a)^{-1}$ per day)
$UP_{max\,i}$	Dinoflagellates: 0.06 *M. aerugtnosa*: 0.2 Chlorophytes: 0.4 Marine diatoms: 0.3 Freshwater diatoms: 0.2	Maximum rate of phosphorus uptake ($mg P (mg chl\ a)^{-1}$ per day)
υ	1.08	Temperature multiplier for mineralisation and sediment oxygen demand (dimensionless)
$v_{Y\,20}$	0.35 diatoms 0.47 organic carbon 0.15 organic nitrogen 0.10 organic phosphorus	Settling rate of substance Y at 20 °C (m per day)
w	7.44×10^{-2}	Coefficient for Wanninkhof equation, including unit conversion ($s^2 m^{-1}$ per day)

Table 6 (continued)

$Y_{C:chla}$	Dinoflagellates: 52 *M. aerugtnosa*: 40 Chlorophytes: 50 Marine diatoms: 42 Freshwater diatoms: 40	Ratio of carbon to chlorophyll *a* (mg C (mg chl *a*)$^{-1}$)
$Y_{O:C}$	2.67×10^{-3}	Stoichiometric ratio of oxygen to carbon in photosynthesis (g O (mg C)$^{-1}$)
$Y_{O:N}$	3.43×10^{-3}	Ratio of oxygen to nitrogen during nitrification (g O (mg N)$^{-1}$)
β_i	Dinoflagellates: 3 *M. aerugtnosa*: 3.5 Chlorophytes: 8 Marine diatoms: 8 Freshwater diatoms: 8	Slope parameter for salinity response function (dimensionless)
η_{20}	1.4×10^{-3}	Dynamic viscosity of water at 20 °C (kg m^{-1} s^{-1})
$\mu_{max\,i}$	Dinoflagellates: 0.7 *M. Aeruginosa*: 1.2 Chlorophytes: 1.5 Marine diatoms: 1.6 Freshwater diatoms: 1.8	Maximum specific growth rate at 20 °C (per day)
ρ_{20}	998	Density of water at 20 °C (kg m^{-3})
Ψ_i	Dinoflagellates: 1.10 *M. aerugtnosa*: 1.08 Chlorophytes: 1.06 Marine diatoms: 1.07 Freshwater diatoms: 1.05	Temperature multiplier for temperature limitation of phytoplankton growth (dimensionless)
ϑ_i	Dinoflagellates: 1.06 *M. aeruginosa*: 1.08 Chlorophytes: 1.03 Marine diatoms: 1.07 Freshwater diatoms: 1.05	Temperature multiplier for respiration (dimensionless)
ϑ_{OC}	1.08	Temperature multiplier for mineralisation of organic matter (dimensionless)

CHAPTER 1

The internal wave field in Sau reservoir: Observation and modeling of a third vertical mode.

*** From:** Vidal, J., X. Casamitjana, J. Colomer, and T. Serra. 2005. The internal wave field in Sau reservoir: Observation and modeling of a third vertical mode. Limnol. Oceanogr. **50**(4): 1326–1333.

Abstract

Water withdrawal from Mediterranean reservoirs in summer is usually very high. Because of this, stratification is often continuous and far from the typical two layered structure, favoring the excitation of higher vertical modes. The analysis of wind, temperature and current data from Sau reservoir (Spain) shows that the third vertical mode of the internal seiche (baroclinic mode) dominated the internal wave field at the beginning of September 2003. We used a continuous stratification 2-D model to calculate the period and velocity distribution of the various modes of the internal seiche and calculated the period of the third vertical mode is ~24 h, which coincides with the period of the dominating winds. Due to the resonance between the third mode and the wind, the other oscillation modes were not excited during this period.

Introduction

Standing internal waves, or seiches, are a ubiquitous feature of lakes, existing mainly due to the wind force acting on a stratified water column. Internal seiches are important for many processes in lakes and reservoirs. Part of the kinetic energy introduced at the water surface by the wind is transferred to internal seiches and becomes available for mixing. Imberger (1998) and Wüest et al. (2000) showed that most of the momentum and energy that passes through the surface mixed layer and enters the interior is transferred to internal wave motions. This energy is typically about

10% of the total wind energy input into the lake (Wüest and Lorke 2003). The vertical excursions of fluid associated with the wave motions have been shown to affect the spatial distribution of different organisms (Levy et al. 1991). The bottom currents induced by internal seiches contribute to the mixing and resuspension of sediments in the benthic boundary layer (Gloor et al. 1994). MacManus and Duck (1988) showed that seiche induced resuspension was responsible for sediment scouring patterns observed along the sides of Loch Earn. Therefore, given that internal seiches play a significant role in a broad range of physical, chemical and biological processes, there is a lot of interest in their assessment and evaluation.

Although there are many possible mechanisms that induce seiches, like air pressure fluctuations, earthquakes, etc., it is mainly the lake's response to the wind forcing that causes the seiche excitation. The wind forcing in lakes is often periodic because of the periodicity in weather patterns. Wind applied to the surface can cause a surface setup of water at the downwind end. This pressure force is balanced by the metalimnion tilting in the opposite sense- that is downward at the downwind end (Spiegel and Imberger 1980). When the wind forcing relaxes the water surface oscillates, as does the metalimnion. The so called external seiche is the oscillation of the water surface (a barotropic mode) while the internal seiche (baroclinic mode) is the oscillation of the metalimnion. In large lakes the picture becomes more complicated because of the effects of the Earth's rotation (Antenucci and Imberger 2003).

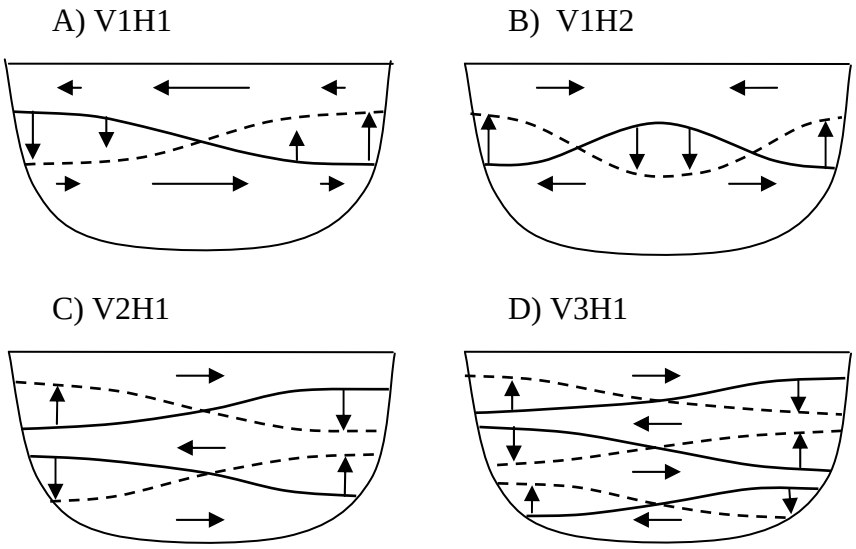

Figure 1. Schematic view of various seiche modes in a closed basin. The notation used to characterize the mode takes the form ViHj = ith vertical, jth horizontal mode. Vertical and horizontal vectors show the direction of flow between an initial state of maximum vertical displacement (continuous line) and one-half period later (dashed line).

Internal seiches can be divided into different categories, depending on the nodal points (ViHj) where i and j are the number of vertical and horizontal nodes (Fig. 1). The

most commonly observed, the V1H1, has one vertical and one horizontal nodal point. This kind of standing wave results when the metalimnion's thickness is small and the lake can be approximated by a two-layer body. Medium or large sized lakes often have a temperature profile that makes reasonable the two or three layer approximation. However, the temperature profile of many reservoirs is very far from the typical three-layer pattern (Casamitjana et al. 2003). This is mostly due to the high demand for water in summer, which contributes to the creation of an additional stratification where the outlet structures of the reservoir are located. Surface mixing phenomena together with water withdrawal and the development of internal seiches create a vertical thermal structure where temperature gradients of different intensities are found.

When the internal waves have periods of similar magnitude to the wind, the possibility of resonant forcing should be taken into account. In two or three layer structures the frequency spectrum is discrete, but in a continuous stratification structure the spectrum is dense and any forcing frequency can lead to resonance seiching (Münnich 1996). However, the resonant modes can have such a high order of structures that in practice they are never excited. This is because of the dampening produced by the large amount of shear existing in higher modes. Anntenucci et al. (2000) presented evidence of the resonant forcing of a Kelvin wave in Lake Kinneret, which, during the time that they were measured, had a period of ~24 hours coinciding with the wind forcing return period over the lake.

Although observations of higher horizontal modes along with the first vertical mode are not unusual in lakes (see for example Lemmin and Mortimer 1986), higher vertical modes are more rarely reported. Second vertical modes have been reported by LaZerte (1980), Wiegan and Chamberlain (1987), Münnich et al. (1992) and Roget et al. (1997). Münnich et al. (1992) showed that the second vertical mode V2H1 is dominant in the wave field of Alpnacher See, a side basin of Lake Lucerne, and that resonance with diurnal wind is responsible for the high amplitudes of the mode. Until now the only experimental evidence of a third vertical mode has been reported in Perez et al. (2003), where measurements carried out with a thermistor string show the existence of four layers oscillating with a 24 hours period; however in their paper it was not shown if the oscillating mode was an eigenvalue to the actual stratification.

In the present paper we present experimental evidence of a third vertical mode with a period of ~ 24 hours occurring in a Spanish reservoir. This mode was found to dominate the internal wave field during the first days of September 2003, when the stratification was fully developed. In addition, the modeling of the reservoir wave field shows us that the third mode is an eigenvalue, with the same period as the wind. Given that the natural and the forcing frequency coincide, we conclude that resonance between the wind and the third mode is responsible of the minor excitation of other modes like

the V1H1, which can be found in the wave field of the reservoir during other periods, for example at the end of July 2003.

Materials and Methods

Study site - Sau is a canyon shaped reservoir 18.225 km long situated in the central part of the river Ter, which is 200 km long, with its source in the Pyrenees in the NE of Spain (Fig. 2). However, the length of the lacustrine part of the reservoir is 3600 m and the maximum width is 1300 m (Armengol et al. 1999). The elongated geometry, along with the wind driven forces following the canyon, make us expect that the internal seiches follow the main axis of the reservoir. Here, we present the results of different surveys carried out in July 2003 and September 2003 during the stratification period of the reservoir. An electromagnetic current meter (ECM), an acoustic Doppler current meter (ADCP) and a thermistor string (TS1) where deployed at station-1, while another thermistor string (TS2) was deployed at station-2 (ADCP: from 21-24 Jul and 09-17 Sep; ECM: from 09-17 Sep; TS1 from 21 Jul-20 Aug and 09 Sep-02 Oct; TS2 from 09 Sep-02 Oct).

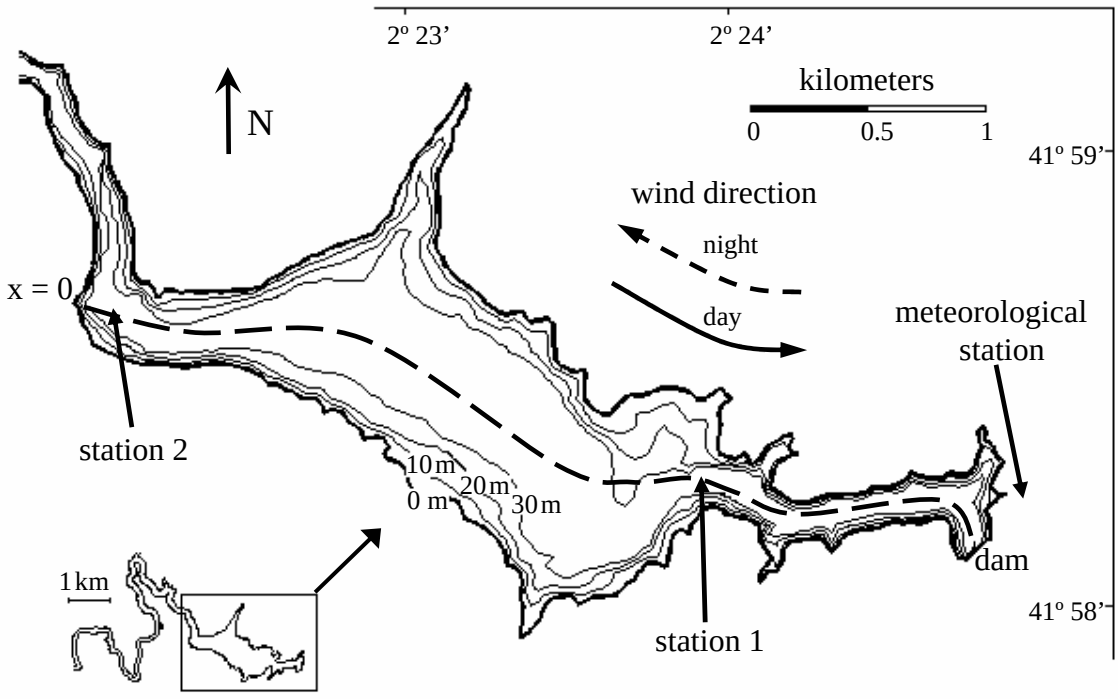

Figure 2- Bathymetric map of Sau reservoir showing the location of the measuring stations and the meteorological station. The dotted line represents the main axis of the reservoir (x) and the direction in which the wind velocity and the water currents are projected.

The ADCP (RDI 600 kHz Workhorse Sentinel) was deployed in the water surface with the beams facing downwards. In this way we were not able to get information about the water surface velocity and therefore we also used an ECM (ACM8M, Alec Electronics, Tokyo). Data from the ADCP was received from 20 depth

bins, each 2 m high. The sampling rate was set at 1 Hz with the raw data processed to obtain 7.5 min averaged data, with a standard deviation of 0.1 cm s^{-1}. In the processed data the bottom boundary layer was cut out because of the lack of confidence in the velocity, due to bottom vegetation. The first depth bin was set at 3 m, then, a range between 3 and 30 m was processed. The ECM sampled the two components of the horizontal velocity at 2 Hz and was deployed 1 m from the water surface. The thermistor chain TS1 was composed of 11 thermistors placed at the following depths: 3 m, 4 m, 5 m, 6 m, 7 m, 8 m, 9 m, 11 m, 15 m, 16 m, and 17 m, while TS2 was composed of 4 thermistors regularly spaced between 5 m and 15 m. The sampling period of both thermistor chains was 10 minutes.

Results

Experimental evidence of the third mode - In summer the habitual 24 hour pattern for the wind is the one corresponding to the first five days in Fig. 3A. During the day wind blows towards the dam (Fig. 2), i.e., a positive direction in Fig. 3A; during the night there is a slight breeze in the opposite direction. This happens with the prevalent summer antyciclonic conditions; however, from time to time the pattern is disrupted when storms come over. Wind and water velocities in Fig. 3 have been obtained by projecting their values in the x direction (Fig. 2). Experimental data shows that values perpendicular to the x direction are much less important. The wind velocity (Fig. 3A) has a strong correlation with the surface water velocity (Fig. 3B). Most of the time the wind blows towards the dam and the surface water moves in the same direction. After the wind stops there seems to be a residual water velocity towards the dam and, finally, the velocity remains close to zero. Because of this, the velocity of Fig. 3B reflects the existence of a wind-driven current. The velocity at 19 m (Fig. 3C) follows a similar pattern that the surface water velocity, although the surface layer velocity is nearly never negative. However water velocities at 11 m and 27 m were out of phase, indicating that a third mode may take place. This is also evident when looking at Fig. 4A. Here light and dark colours indicate currents in opposite directions (light: current towards the dam, dark: current from the dam). Water changes its direction between water layers 2-3-4, as a consequence of the third mode. Water direction in the first layer, which roughly corresponds to the surface mixed layer, can not be used in this line of argument because of the many physical processes occurring here, such as convection, wind stirring, etc., that can mask the third mode. In addition, in Fig. 4A it can be seen that there is a shifting in the velocity direction time series between the different layers. This shifting can be explained by the existing delay in the transmission of the moment from the wind between the layers. Fig. 4B shows the temperature profile measured on the 09 September near the middle of the reservoir, where the vertical displacements of the H1 modes is assumed to be small (Fig. 1). The stratification profile of Fig. 4B shows a four layer structure which corresponds approximately to the four layer structure of the velocity field (Fig. 4A) that could favour the development of the third vertical mode.

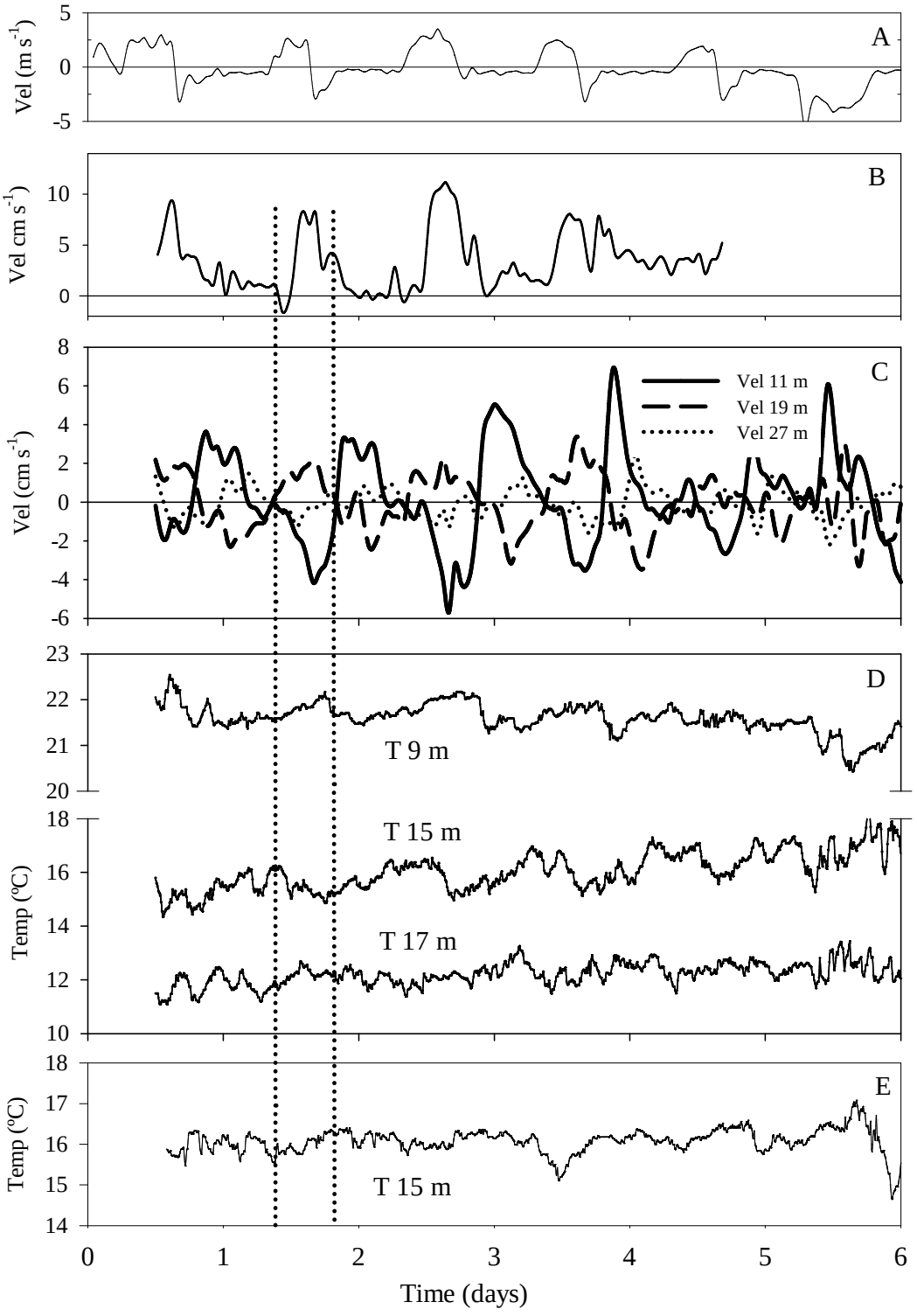

Figure 3. (A) Wind velocity, (B) surface water velocity, and (C) water velocity, projected following the main axis of the reservoir at station 1 (see Fig. 2). Values of water velocity have been averaged at 1 hour periods. (D) Water temperature measured by the thermistor string at station 1 and (E) at station 2. Day 0 corresponds to 09 September 2003. The dotted lines show the experimental evidence for mode V3H1.

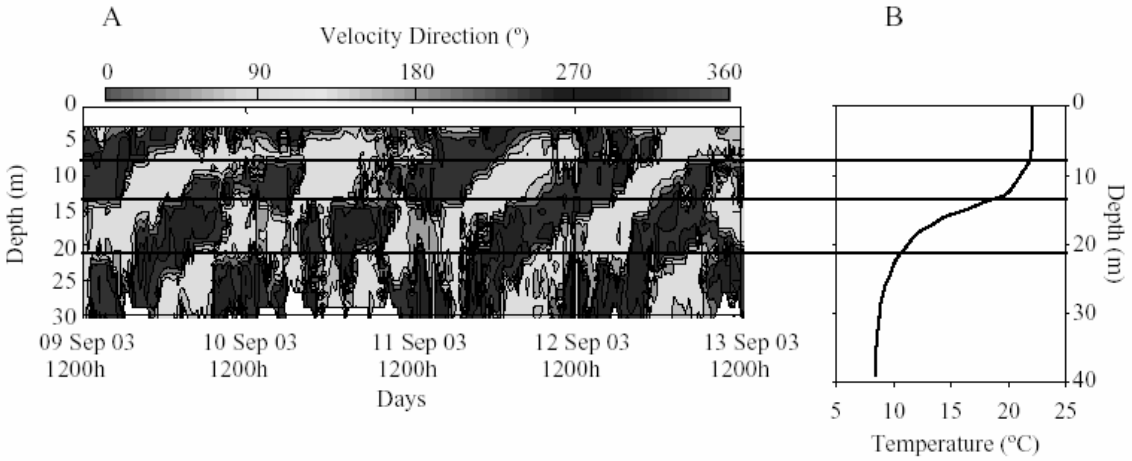

Figure 4. (A) Velocity direction from the ADCP between 09 and 13 September 2003, and (B) vertical temperature profile on the 09 September 2003. The lines show the 4 layers present in the dynamic behavior. Values of water velocity have been averaged at 1/2 hour periods.

The third mode can also be observed when looking at temperature measurements in Fig. 3D. Here the temperature at 15 m is in the opposite phase compared to the temperatures at 9 m and 17 m, indicating the vertical displacements of the three interface layers. Unfortunately we were not able to look at deeper depths due to the length of the thermistor string. The temperature at 15 m at station 2 is also in the opposite phase compared to the temperature at 15 m at station 1 (Fig. 3E), suggesting that a horizontal H1 mode may be excited (Fig. 1). To gain a better understanding of the temperature results, in Fig. 5A we represented the cross covariance functions of the time series of the temperature at 15 m depth at station 1 compared with the temperature at 9 m depth and 17 m depth at station 1, and also with the temperature at 15 m depth at station 2. Note that for t=0 the cross covariance is negative for all cases. Also note that, in spite of a certain delay, these time series with a 24 hour period oscillate in phase. Figure 5B shows the cross covariance of the time series of velocity in layers 2 and 3 compared with the temperature at 15 m depth at station 1. This depth roughly corresponds to the interface between layers 2 and 3. If the third mode oscillation occurs one would expect that the velocity is at its maximum or minimum when the vertical displacements are zero. This would mean that the cross-covariance should be close to 0 at t=0, ±12 h, ±24 h, etc. and maximum or minimum at t=±6 h, ±18 h, ±30 h, etc. which is approximately the pattern in Fig. 5B. All in all, these results suggest that a vertical V3H1 mode may have been occurring in Sau reservoir at the beginning of September 2003. To confirm this assessment we will use a numerical model to calculate the eigenmodes for the Sau reservoir.

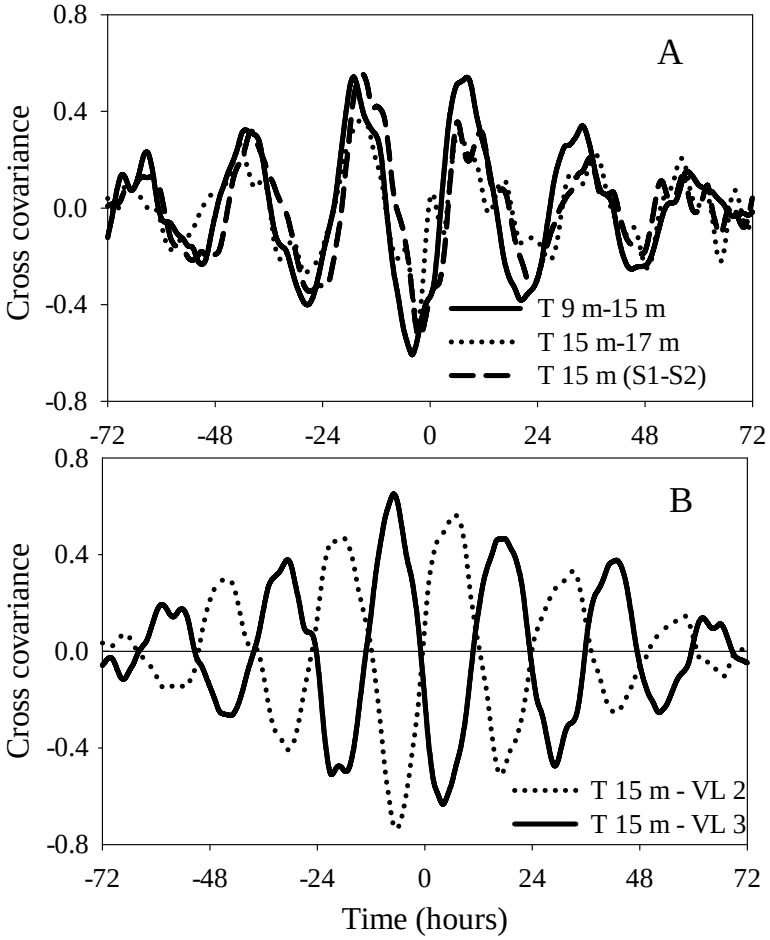

Figure 5. Cross covariances normalized to one, for different time series. (A) Temperature at 9 and 15 m depth at station 1 (T9 m-15 m), temperature at 15 m and 17 m depth at station 1 (T 15m-17 m) and temperature at 15 m depth at stations 1 and 2 (T15 m (S1-S2)). (B): Temperature at 15 m depth and velocity in the layer 2 (T 15m-VL2), and temperature at 15 m depth and velocity in layer 3 (T 15m-VL3).

Numerical model - Although the stratification is often continuous, until recent years, modeling seiches has been confined mostly to two or three layer models, accounting for the epilimnion, metalimnion and hypolimnion (Salvadé et al.1988). Although these models are able to describe different horizontal modes, they can only describe a maximum of two vertical modes. However, increased computing power has allowed the development of progressively more sophisticated internal seiche models that are able to resolve the internal standing waves produced by a continuous stratification profile and therefore they can account for higher vertical modes (Münnich 1996; Fricker and Nepf 2000; Antenucci and Imberger 2003).

The size of the Sau reservoir (Fig. 2), together with the fact that internal seiches are excited by the wind that blows through the canyon valley, made us think that the effects of the earth's rotation could be neglected. The internal Rossby radius of deformation $R_I = c/f$, where c is the phase speed of the internal wave and f the Coriolis

parameter, represents the length scale over which Coriolis forces balance the pressure gradient generated by a tilted interface. Following Patterson et al. (1984), the criterion for the absence of rotational effects is $R = R_I/B > 1$, where B is the maximum width of the reservoir. If the reservoir length is L=3842 m and the period of the internal seiche for the V3H1 mode is T=24 h, the phase speed can be estimated to be c=2L/T= 0.09 m s^{-1}. Therefore if f= 1.02 10^{-4} s^{-1} and B= 700 m, we obtain $R_I \sim 880$ m and R= 1.25. Although slightly higher, this value is close enough to 1 to make us think that rotational effects can not be discarded at the central part of the reservoir, where an internal Kelvin wave can be generated. However, due to the fact that the reservoir is elongated and only slightly narrower than R_I, the period of the Kelvin seiche should be almost identical to the seiche without rotation. At station 1, where the reservoir width is small, the effect of the Kelvin mode is very similar to the effect that would have been caused by a mode without rotation, and therefore we will not include rotational effects in the model.

The numerical model that we will use is similar to the one proposed by Münnich (1996). In two dimensions, the governing equation for a stream function Ψ of free, infinitesimal internal gravity waves in a hydrostatic Boussinesq fluid is

$$\frac{\partial^4 \psi}{\partial^2 t \partial^2 z} + N^2 \frac{\partial^2 \psi}{\partial x^2} = 0 \qquad (1.1)$$

where x and z are the horizontal and the vertical dimensions, t is time, $u = -\partial\psi/\partial z$ and $w = \partial\psi/\partial x$ are the horizontal and the vertical components of the velocity and N=N(z) denotes the Brunt-Väisälä frequency. Employing the rigid lid condition eliminates the surface waves. Then assuming that there is no outflow at the boundaries, we get the condition Ψ =0. For seiches the time dependence has the form, $\Psi=\Phi(x,z)e^{i(\omega t + \sigma)}$, where ω is the angular frequency of the seiche and σ is a constant, which yields to the so called generalized eigenvalue problem for the stream function Φ given by the equation

$$\frac{\partial^2 \Phi}{\partial x^2} = \frac{\omega^2}{N^2} \frac{\partial^2 \Phi}{\partial z^2} \qquad (1.2)$$

The domain was discretized, using centered finites differences, on a grid where x follows the main axis of the reservoir; that way, along with the boundary conditions, the matrix formulation of the problem has the generalized eigenvalue form,

$$A\Phi = \lambda B\Phi\,, \qquad (1.3)$$

where A is a matrix determined by the discretization on the x axis and B a matrix determined by the buoyancy frequency and the discretization on the z axis. x=0

has been chosen at the position indicated in Fig. 2. The direction of the main axis of the reservoir makes a nearly 90º turn at the boundary x=0. Visual observations of the wind and the surface waves show us that they drop to small values upstream of x=0. As far as the wind acts throughout that zone we should expect only one horizontal mode in the main body of the reservoir. Because of this, we believe that the boundary will reflect the internal waves generated in the whole basin, although the veracity of this still has to be confirmed by the model results. The set of solutions for λ, being $\lambda = \omega^2$, and Φ are the eigenvalues and eigenvectors of our generalized eigenvalue problem that we solve using the Jacobi-Davidson Method together with the so called QZ algorithm (Bai et al 2000). The Jacobi-Davidson method was used in the model to make it suitable for all grid sizes and all general cases. In the case of Sau, a 25 x 39 grid was used. As the maximum depth for the period of September 2003 was 39 meters, we needed to estimate the N^2 value for every meter depth.

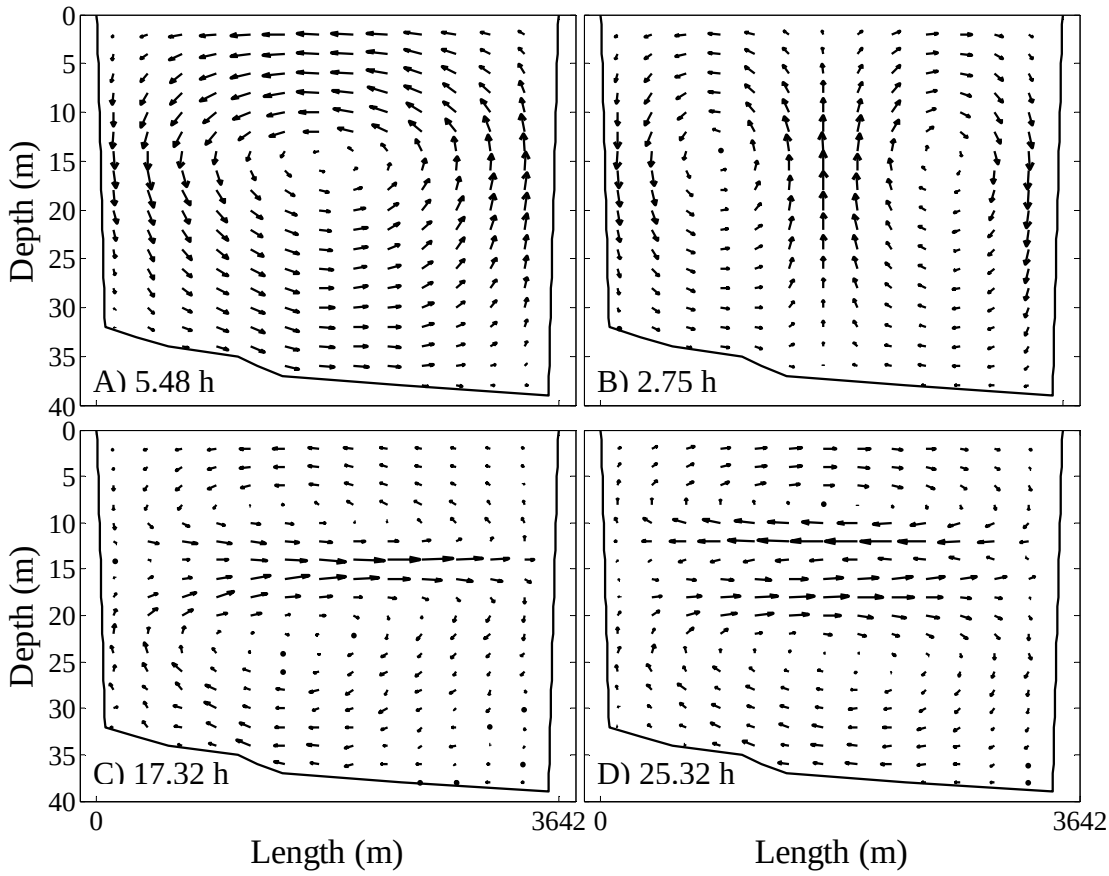

Figure 6- Velocity field predicted by the model corresponding to modes (A) V1H1, (B) V1H2, (C) V2H1, and (D) V3H1. The corresponding predicted periods are (A) 5.48 h, (B) 2.75 h , (C) 17.32 h, and (D) 25.32 h.

The eigenmodes obtained were sorted by the overall shear connected to the flow field. The corresponding eigenvalues lead to the characteristic periods for the different modes. After Φ is obtained, the velocity components, u and w follow easily. In Fig. 6, the velocity field, together with the period obtained for the lowest modes is represented.

Although the solution was computed in a 26 x 39 grid mesh, for the sake of clarity, in Fig. 6 we have only represented the values over a 13 x 19 grid mesh. The temperature profile used corresponds to the 09 of September 2003 (Fig. 4B). Given that the theoretical period obtained for the V3H1 mode is close to 24 h, we conclude that the observed oscillation corresponds to this mode.

To compare the model results to the thermistor chain observations, we have calculated the vertical fluid displacements from the model by using

$$\zeta = \int w dt = \frac{1}{i\omega}\frac{\partial \psi}{\partial x} = \frac{w}{i\omega} \tag{1.4}$$

As the used model is an eigenvalue model for the stream function, we are only interested in comparing the envelope of the seiche motion and not the absolute magnitude. Therefore the value $(i\omega)^{-1}$ will be ignored. To determine seiche amplitude from the thermistor data, we follow the method proposed by Fricker and Nepf (2000), where a mean temperature profile $\overline{T}(z)$ is first constructed by averaging the time series temperature profiles from the period 09 Sep – 13 Sep. A root mean square (RMS) temperature deviation ΔT_{RMS} is then computed for the predominant V3H1 mode in our system by using

$$\Delta T^{i}_{RMS} \equiv \sqrt{\frac{2}{N}\sum_{n=1}^{N}\left[T(z_i, t_n) - \overline{T}(z_i)\right]^2}, \tag{1.5}$$

where $\overline{T}(z_i) = \frac{1}{N}\sum_{n=1}^{N} T(z_i, t_n)$, N is the number of points in the thermistor data, and z_i is the depth of the thermistor i. Finally, RMS vertical displacements are determined as

$$\zeta^{i}_{RMS} = \frac{\Delta T^{i}_{RMS}}{\partial \overline{T}/\partial z}, \tag{1.6}$$

where the local gradient $\partial \overline{T}/\partial z$ is computed from the mean temperature profile $\overline{T}(z)$. Note that the ΔT_{RMS} values obtained represent the absolute value of the wave envelope and therefore a study of the phase of the different time series, as shown in Figure 5A, has been carried out in order to determine the sign of the vertical displacement.

Figure 7 compares the results of the maximum vertical displacements obtained from the model with the RMS vertical displacements from the thermistor chain at station 1. Unfortunately, 5 thermistors were deployed in the surface mixed layer and temperature gradients were too small to be used in (6); also another thermistor was not

operative during the measuring period and therefore we were only able to use records from 5 thermistors. Notice that the envelope of the seiche obtained from the model fits the experimental results quite well. The maximum vertical displacements obtained by the model (ζ) have arbitrary units as the resultant eigenvectors of the model are not real velocity field vectors; in that sense, a constant α,was used to fit experimental values to model results, so that $\zeta^* = \alpha\zeta$, where ζ^* values are represented in Figure 7.

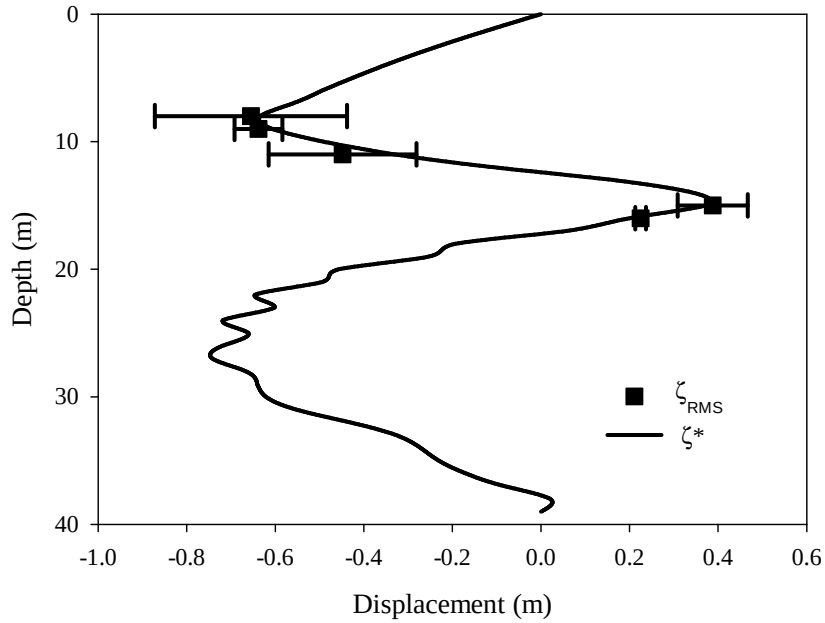

Figure 7- Line: Variation of ζ^* (vertical displacement, ζ obtained by the model multiplied by a constant α) with the depth at station 1. Squares: Variation of ζ_{RMS} (RMS vertical displacement deduced from thermistor chain data) according to depth at station 1. The bars indicate the estimated error, which comes mainly from the determination of $\partial\overline{T}/\partial z$.

Likewise, we can compare the maximum horizontal velocity field obtained from the model with the maximum experimental velocity field obtained with the ADCP (Fig. 8). Once again, the velocity field obtained from the model has arbitrary units and a constant β is used for comparison with the experimental data, where $u^*=\beta u$, and u is the horizontal velocity computed with the model. We have represented the maximum experimental velocities obtained on 10 and 11 Sep 2003. Note once again that the envelope of the seiche fits the experimental results quite well. It is important to point out the fact that the surface layer velocities are small compared to velocities in the second and third layers. Because of that, and the existence of the surface wind-driven current detected in Fig. 3B, the V3H1 mode is not clearly appreciated in the surface layer.

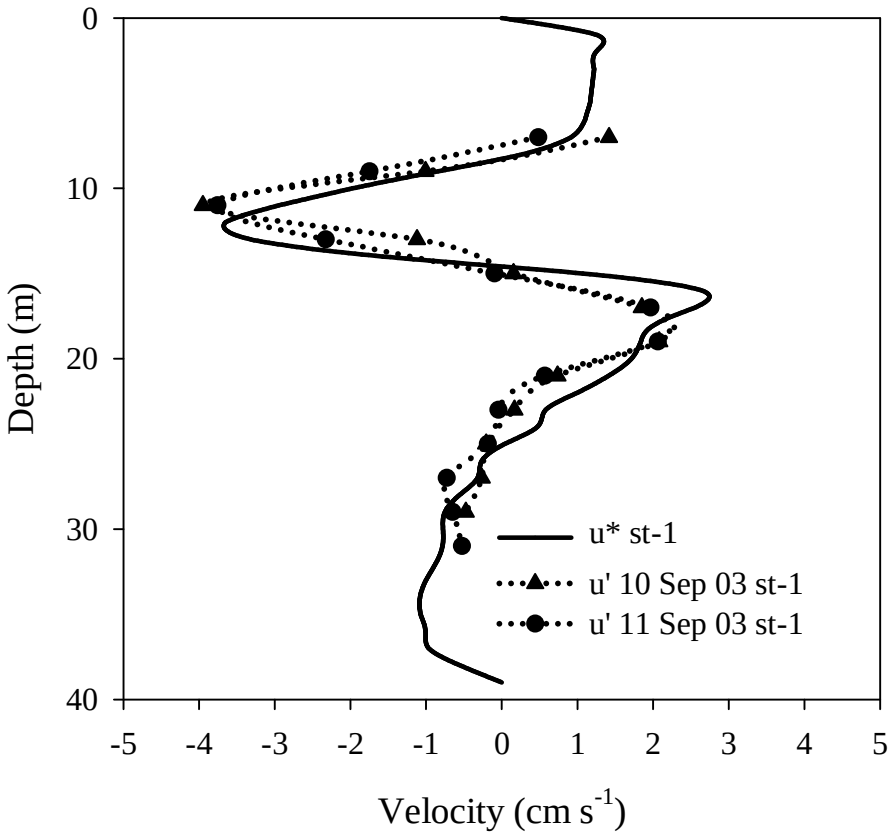

Figure 8- Comparison between u (horizontal velocity obtained by the model multiplied by a constant β) and the maximum horizontal velocity obtained with the ADCP, u', for the dates: 10 September 2003 and 11 September 2003 at different depths in station 1.*

It is interesting to compare the spectral analysis for the period 09-15 September 2003 with the period 21-30 July 2003. In September 2003 (Fig. 9) the peak around 24 hours appears in the time series for wind, velocity and temperature. We attribute this peak to mode V3H1. However the peak around 12 hours that also appears in the time series does not correspond with the predicted modes (Fig.6); this peak is probably the reservoir's response to a sub-daily wind pattern. The 5 hour peak in the velocity and temperature series does not have a corresponding peak in the time wind series. As the mode V1H1 has a period of ~5 hours (Fig. 6), we attribute the peak to this mode. In normal conditions we would expect higher energy in mode V1H1, but the fact that mode V3H1 is resonant with the wind is probably causing the dampening of this mode. This can be corroborated by looking at the time series in Jul 2003 (Fig. 10). The temperature series show two peaks around 12 h and 7 h. The model calculations give periods of 6.2 h (V1H1), 11.7 h (V2H1), and 18.3 h (V3H1). Therefore we attribute these peaks to modes V2H2 and V1H1.

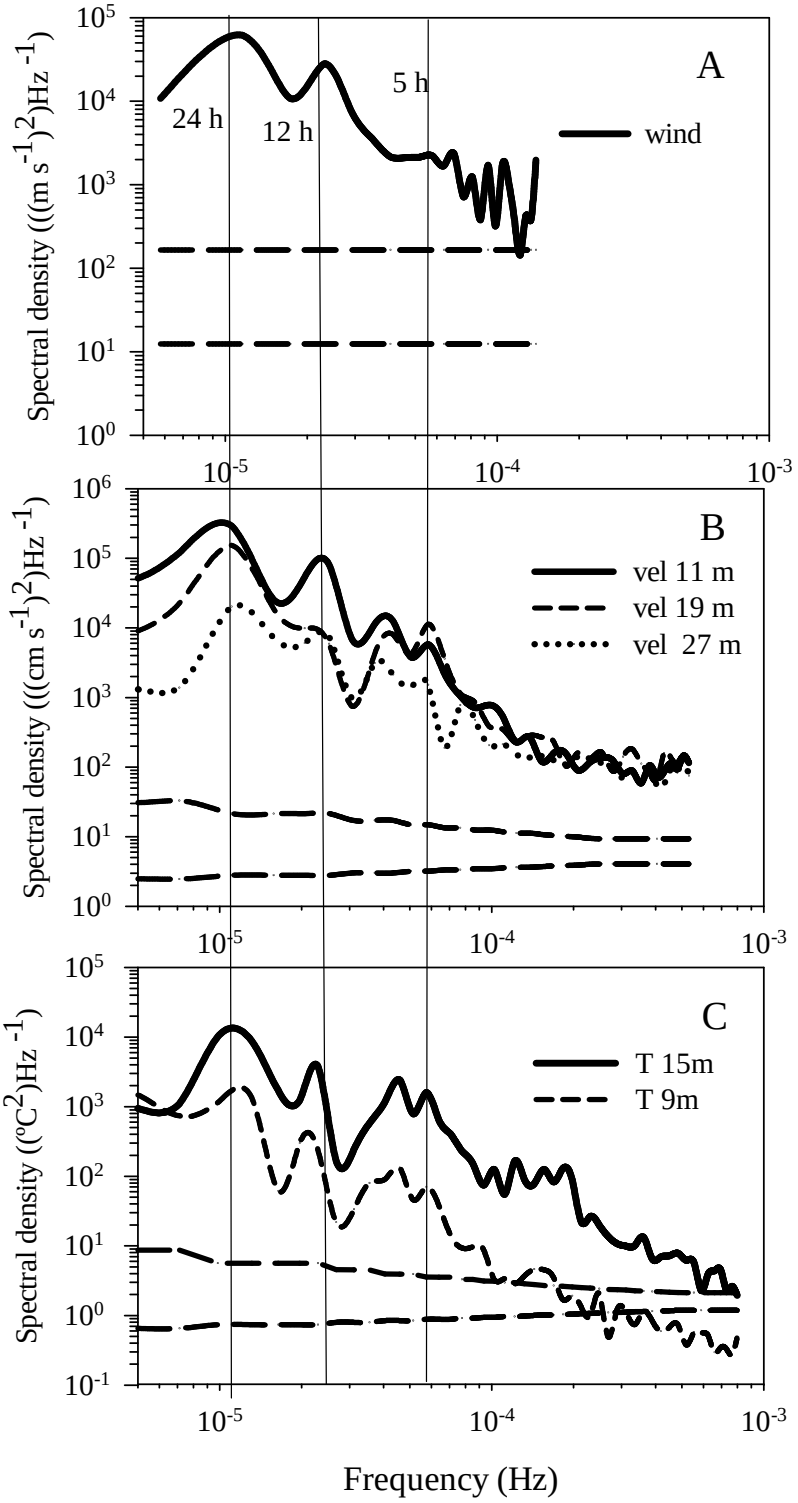

Figure 9- (A) Power spectra density for the wind velocity, (B) velocity current and (C) temperature series from 09-15 September 2003. Spectra in (B) and (C) have been smoothed in the frequency domain to improve confidence; dashed line shows confidence at the 95% level. Wind and velocity are projected following the mean axis of the reservoir. Continuous lines show the periods corresponding to the maximum peaks.

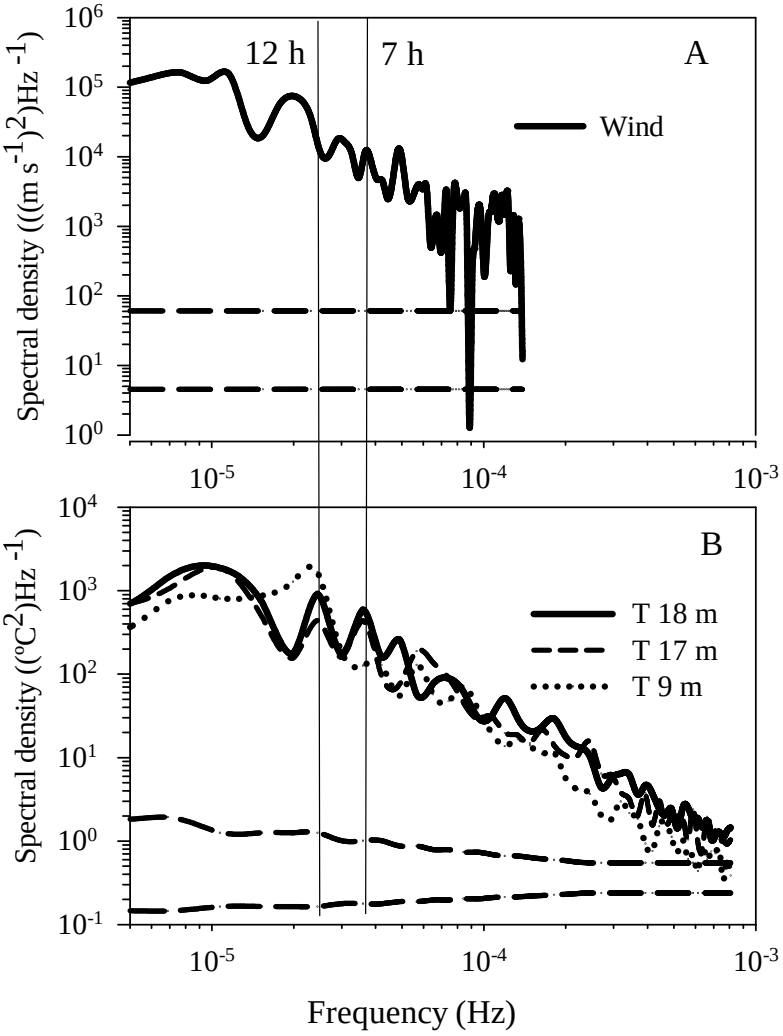

Figure 10. (A) Power spectra density for the wind velocity and (B) temperature series from 21- 31 July 2003. Spectra for the velocity has been smoothed in the frequency domain to improve confidence; dashed line shows confidence at the 95% level. Wind is projected following the mean axis of the reservoir. Continuous lines show the periods corresponding to the maximum peaks.

Conclusions

All in all, when the metalimnion occupies a sufficiently large proportion of the water column, higher vertical modes may become excited by periodic winds. Such conditions are quite common in Mediterranean reservoirs at the end of the summer, when the mixed layer phenomena combined with the water being withdrawn create continuous stratification profiles. Given that continuous stratification profiles have a dense eigenfrequency spectrum, reservoirs can oscillate at many frequencies. Limitations on the oscillation modes will be imposed by the structure of the oscillation cells: a higher number of cells, a greater attenuation of the mode. In Sau reservoir the presence of the V3H1 mode is obvious, especially from the current measurements. Resonance with the wind is a definitive contribution to the excitation of the V3H1 mode

and in general to the higher modes. Typically the wind pattern has a period of ~ 24 h and therefore higher modes are excited when they have this periodicity.

CHAPTER 2

Forced resonant oscillations as a response to periodic winds in Sau reservoir.

*** From:** Vidal, J. and X. Casamitjana. Forced resonant oscillations as a response to periodic winds in Sau reservoir. Journal of Hydraulic Engineering. *Submitted*.

Abstract

The response of Sau reservoir to a wind field characterized by having marked periodicities of 12 h and 24 h has been studied. Measurements of temperature, with a thermistor string, and currents, with an ADCP, show that the reservoir also responds with the same water periodicities. During certain times of the stratified period some of the natural oscillation modes of the reservoir are close to these forcing wind periods. In particular, in mid July the vertical mode V2 is close to 12 h and in mid-end of September the vertical mode V3 is close to 24 h. In these situations, these modes are selected out of the spectrum of possible internal waves and the reservoir behaves as a forced oscillator in resonance with the wind. The structure and the period of these vertical modes have been elucidated by using the 3- D model ELCOM. Both modes are affected by the earth's rotation at the widest part of the reservoir.

Introduction

Basin-scale, wind-induced motions depend on interactions of spatially and temporally varying wind forcing with bathymetry, density distribution, and the earth's rotation (Laval et al., 2003). These motions include wind-driven currents and basin-scale internal waves. Basin internal waves are commonly excited in the following way: wind stress forces the surface water toward the downwind end of the lake, thus giving rise to a horizontal pressure gradient, which, in turn, accelerates the deeper water toward the upwind end. After the wind forcing relaxes the metalimnion oscillates, generating a standing internal wave, or seiche. The amplitudes and the periods of these oscillations have been described in numerous studies (see for example: Spigel and Imberger, 1980; Stevens et al., 1996 and Lemmin et al., 2005). Currents and vertical displacements have been showed to affect the spatial distribution of different organisms (Levy et al. 1991; McManus et al. 2005). The bottom currents induced by internal waves also contributes

to the mixing and resuspension of sediments in the benthic boundary layer (Gloor et al. 1994). Therefore, internal waves play an important role to take into account in the water management.

Internal seiches can be divided into different categories, depending on the nodal lines. In a two-dimensional system it is usual to represent the modes as: ViHj where i and j are the number of vertical and horizontal nodes (Münnich et al. 1992). Furthermore, horizontal modes can be longitudinal or transversal, depending on the position of the horizontal node line (Lemmin et al., 2005). As many lakes can be approximated by a two-layer body (epilimnion and hypolimnion), separated by a narrow interface (metalimnion), the V1 is the most commonly excited mode. However, the presence of a thick metalimnion combined with the resonance between the wind and higher modes can lead to the excitation of these modes. Second vertical modes have been reported by LaZerte (1980), Wiegand and Chamberlain (1987), Münnich et al. (1992) and Roget et al. (1997). Wiegand and Chamberlain (1987) observed that for the case of Wood Lake (British Columbia), with a thick metalimnion, after a wind event, initial excitation of the V1 mode was typically followed by excitation and dominance of the V2 mode. Münnich et al. (1992) showed that the second vertical mode is dominant in the wave field of Alpnacher See, a side basin of Lake Lucerne, and that resonance with diurnal wind is responsible for the high amplitudes of the mode. In Lake Kinneret, the largest internal wave energy response occurred when the natural internal wave frequency was similar to the forcing frequency of the wind. This was shown to occur at two different periodicities: 24 h and 50 h (Antenucci and Imberger, 2003).

In Chapter 1 experimental evidence of a third vertical mode (V3), with a period of ~ 24 hours, occurring in Sau reservoir has been presented. This mode was found to dominate the internal wave field during the first days of September 2003, when the stratification was fully developed. In addition, a two-dimensional eigenvalue model for the stream function (Münnich 1996, Fricker and Nepf 2000) was applied in the lacustrine zone, under the assumption that only one horizontal mode will be generated in such zone, where the wind acts. Under such assumption the model showed that the V3H1 mode (only taking into account the lacustrine zone) was an eigenvalue, with the same period as the wind. Therefore resonance between the wind and the third mode was responsible for the excitation of this mode. Although internal Rossby radius estimations showed that rotational effects could be important, they were not taken into account in the two-dimensional model. The elongated shape of the reservoir led to the assumption that the effect of the Kelvin mode is very similar to the effect that would have been caused by a mode without rotation and that the period of the Kelvin seiche should be almost identical to the seiche without rotation.

In this paper we will demonstrate that, in continuous stratified reservoirs, stratification together with the wind resonance are the key factors in the selection of the

predominant modes of oscillation of the reservoir. In concrete, in Sau reservoir, the vertical modes V2 and V3 have been selected as the oscillation modes in response to the wind patterns of 12-h and 24-h periodicity. Model calculations will show us that these periods are the corresponding natural periods of these modes. Therefore, the analogy between the reservoir and a forced damped oscillator is straightforward. In comparison with modes V2 and V3 the excitation of mode V1 is much less important. In addition, the rotational effects in the central part of the reservoir are shown, and the role of the meandering zone of the reservoir in the horizontal structure of the internal waves is establish.

Materials and Methods

Sau is a canyon shaped reservoir 18.225 km long situated in the central part of the river Ter, which is 200 km long, with its source in the Pyrenees in the NE of Spain (Armengol et al. 1999). The length of the widest part of the reservoir, called from now on, the "lacustrine zone", is 3600 m and the maximum width is 1300 m; the narrowest part of the reservoir will be called "the meandring zone" (Fig. 1), that contains the riverine and transition zones (see INTRODUCTION of this PhD Thesis). Here, we present the results of different surveys carried out in the period July 2004-October 2004, during the stratification period of the reservoir.

An acoustic doppler current meter (ADCP) and a thermistor string (TS) were deployed at station 1 (Fig. 1). The ADCP was active from 20 July 2004 - 4 August 2004 and from 7- 9 September, and the TS from 8 July - 5 September and from 9 September - 9 October. Wind data was obtained from a meteorological station placed nearby the lake (Fig. 1). The ADCP (RDI 600 kHz Workhorse Sentinel) was deployed in the water surface with the beams facing downwards. Data from the ADCP was received from 55 depth bins, each 1 m high, with the first bin at 2m. The sampling rate was set at 1 Hz with the raw data processed to obtain 7.5 min averaged data, with a standard deviation of 0.1 cm s^{-1}. Between 8 July - 5 September, the available temperature records obtained with the TS were those of the following depths: 3 m, 4 m, 5 m, 6 m, 7 m, 8 m, 9 m, 11 m, 15 m, 16 m, and 17 m. Between 9 September and 9 October the depths of the sensors were changed to better fit the new stratification. At that time, the available temperature records were obtained at 8 m, 10 m, 11 m, 12 m, 13 m, 14 m, 16 m, 20 m, 21 m, 22 m, 27.5 m, 30 m, 32.5 m and 37.5 m. depth.

In addition to the experimental results, numerical simulations were carried out with the Estuary and Lake Computer Model (ELCOM). This model solves the 3D hydrostatic, Boussinesq, Reynolds-averaged Navier Stokes and scalar transport equations, separating mixing of scalars and momentum from advection. Simulated processes include baroclinic and barotropic responses, rotational effects, wind stresses, surface thermal forcing, inflows and outflows. For a model description the reader is

referred to Hodges, 2000 and Hodges et al (2000), or Introduction of this PhD. Previous applications (Hodges et al. 2000; Laval et al. 2003; Gomez-Giraldo et al 2006) show that the model reproduces the internal wave field well in lakes, and therefore it will be used to support our interpretation of the results.

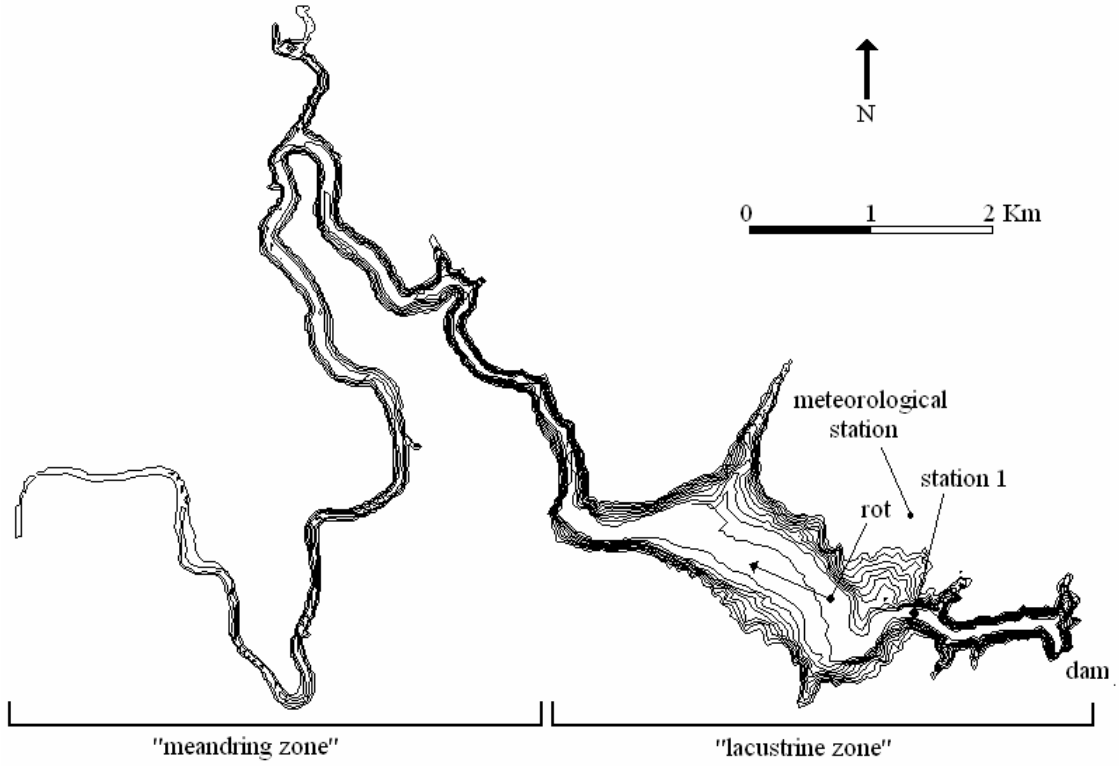

Figure 1- Bathymetric map of Sau Reservoir showing the location of the measuring station, the meteorological station and the point selected for the rotational analysis (rot). The arrow represents the direction in which the wind velocity and the water currents are projected. The reservoir has been divided into two sections: "river part" and "lake part".

For the application of ELCOM model, the "meandring zone" of Sau reservoir (Fig. 1) was straightened following Hodges (2001), in order to decrease the numerical diffusion in that zone; the bathymetry was then discretized using a 35x35x1 m grid and time steps of 45 s. To run the model we used hourly mean meteorological data from the meteorological station indicated in Fig.1. Wind was set to zero in the "meandring zone " of the reservoir (Fig. 1), because here the reservoir is sheltered from the wind.

Results

In normal anticyclonic conditions, which are prevalent during summer, the daily wind pattern of Sau reservoir is quite regular. During most of the day hours, the wind blows toward the dam, its direction being ~ 250º (Fig.2A). In the afternoon, wind changes direction to ~ 70º and blows upstream of the reservoir. Figure 2B shows the projected wind velocity over the main axis of the reservoir. The highest values of the

wind velocity are recorded during the changing interval. The wind drops in the evening, but a slight breeze remains during the night. Figure 2B gives an average pattern for the wind conditions in the summer period. It has to be noted, however, that this pattern is disrupted when a front passes, although this is not very usual in summer time.

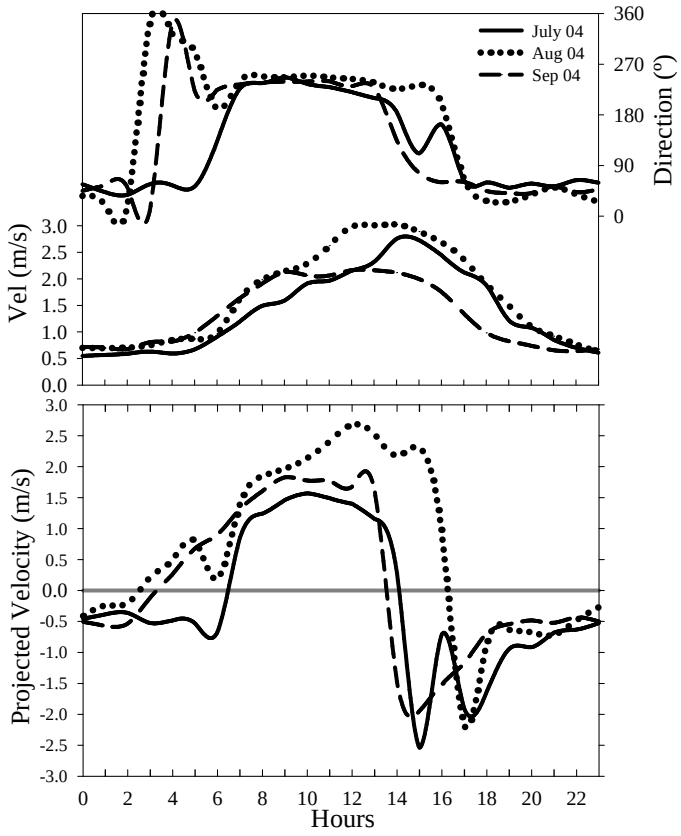

Figure 2- (A) Summer 2004 averaged hourly values for the wind velocity and the wind direction. (B) Summer 2004 averaged hourly values for the wind velocity projected following the direction indicated in Fig.1.

Figure 3A shows the evolution of the wind spectral density, for the stratified period of 2004. The spectral analysis was carried out every two days over a period of ten days. As in Fig. 2B, the wind velocity has been projected following the main axis of the reservoir (Fig. 1). A dominant period of 24 hours can be clearly seen, and a secondary sub-daily mode of 12 h. While the 24-h periodicity could be anticipated given the daily wind pattern represented in Fig. 2, the 12-h periodicity is not so obvious, although changes in the wind direction are probably at the origin of this sub-daily wind pattern. In a similar way, Fig. 3B shows the spectral density evolution of the potential energy per unit of volume calculated as: $EP(t) = \frac{1}{2} N^2(t) \rho_0(t) \xi^2(t)$, where $N^2 = -\frac{g}{\rho_0}\frac{d\rho}{dz}$ is the buoyancy frequency, g is the gravity acceleration, ρ is the

water density and ξ is the displacement of a selected isotherm. Values of N^2 and ρ_0 have been obtained from averaged values over the period in which the spectrum has been carried out. The selected isotherm has to be representative of the wave field of the system and has been chosen as the temperature at the depth where the vertical displacements are higher. As its value changes with time, we have changed the isotherm approximately every 4 days, beginning with 19 ºC on 15 July, increasing up to 22.5º C on 31 August and decreasing to 21ºC on 4 October. For both modes, the maximum vertical displacements occur at a depth of around 10m, deepening slightly at the end of the summer. This depth roughly corresponds to the first layer's interface for both modes. In Fig. 3B it can also be seen that the 12-h and 24-h periods dominate the internal wave field; it will be seen later that these periods roughly correspond to forced V2 and V3 modes respectively.

Figure 3A shows the evolution of the wind spectral density, for the stratified period of 2004. The spectral analysis was carried out every two days over a period of ten days. As in Fig. 2B, the wind velocity has been projected following the main axis of the reservoir (Fig. 1). A dominant period of 24 hours can be clearly seen, and a secondary sub-daily mode of 12 h. While the 24-h periodicity could be anticipated given the daily wind pattern represented in Fig. 2, the 12-h periodicity is not so obvious, although changes in the wind direction are probably at the origin of this sub-daily wind pattern. In a similar way, Fig. 3B shows the spectral density evolution of the potential energy per unit of volume calculated as: $EP(t) = \frac{1}{2} N^2(t) \rho_0(t) \xi^2(t)$, where $N^2 = -\frac{g}{\rho_0}\frac{d\rho}{dz}$ is the buoyancy frequency, g is the gravity acceleration, ρ is the water density and ξ is the displacement of a selected isotherm. Values of N^2 and ρ_0 have been obtained from averaged values over the period in which the spectrum has been carried out. The selected isotherm has to be representative of the wave field of the system and has been chosen as the temperature at the depth where the vertical displacements are higher. As its value changes with time, we have changed the isotherm approximately every 4 days, beginning with 19 ºC on 15 July, increasing up to 22.5º C on 31 August and decreasing to 21ºC on 4 October. For both modes, the maximum vertical displacements occur at a depth of around 10m, deepening slightly at the end of the summer. This depth roughly corresponds to the first layer's interface for both modes. In Fig. 3B it can also be seen that the 12-h and 24-h periods dominate the internal wave field; it will be seen later that these periods roughly correspond to forced V2 and V3 modes respectively. Here it could have been interested to use wavelet analysis instead of spectral analysis, however the fact that we have changed the selected isotherm every 4 days produce discontinuities in the signal so that it can't be studied as a continuous signal.

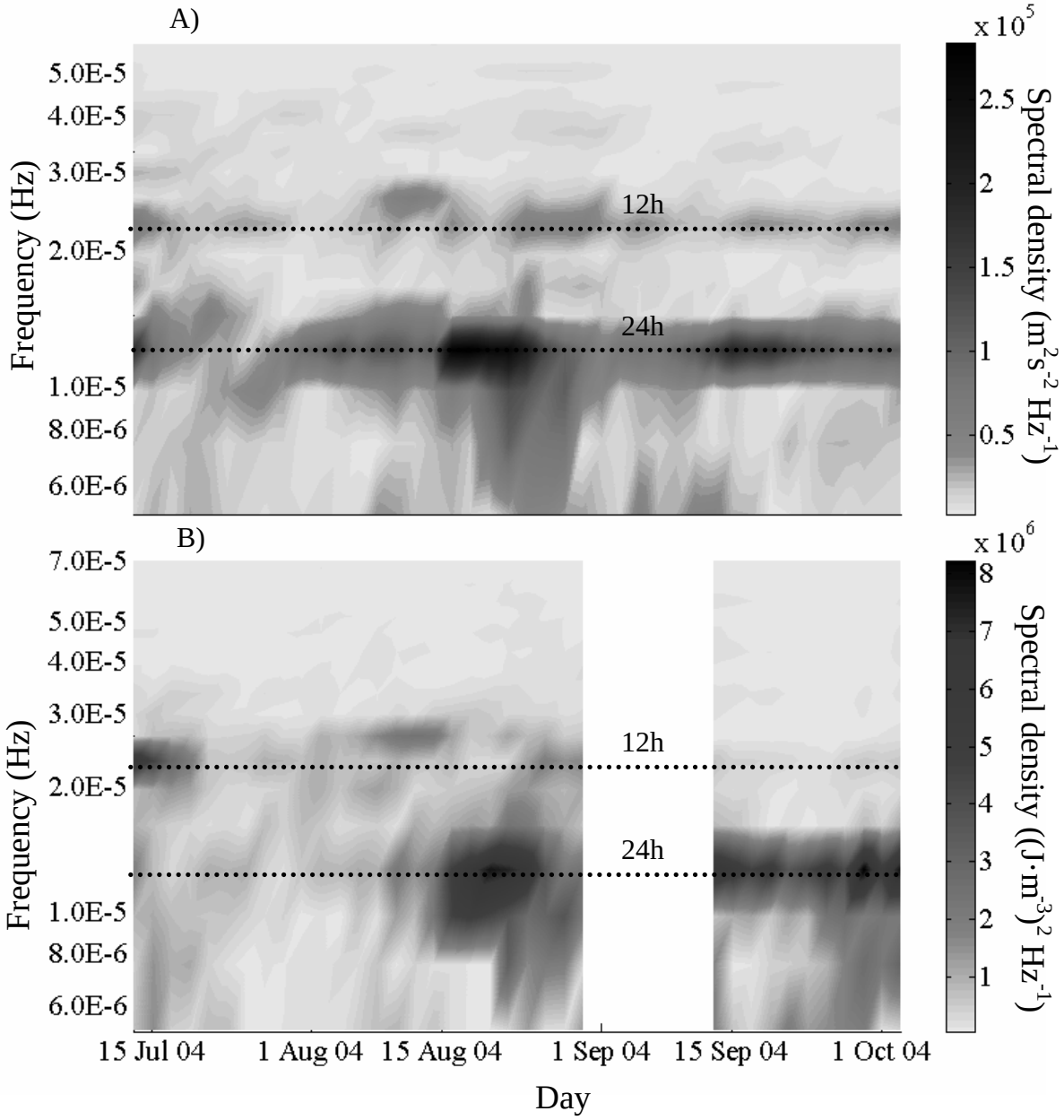

Figure 3- (A) Evolution of the power spectra density for the projected wind velocity and (B) for the potential energy per unit of volume (see the text).

In Fig. 3B it can be seen that the modes of 12 h and 24 h dominate the wave field in the second half of July and at the end of September respectively, coinciding with high spectral wind densities for the same modes. However, during the first 2 weeks of August, where the spectral density of the wind at 24h is similar to that found in September, the 24h mode for the wave field is quite low. Furthermore, in the last days of August, high spectral density is found over 24h; in a period where the wind spectral density was the higher of the survey. All in all, it seems quite clear that the reservoir responds to the wind forcing by trying to adjust its frequency to that of the wind. However the extent of the response will depend on the reservoir stratification. In the

following sections we will show that resonance between the wind and the internal modes of the reservoir will enhance this response.

Evidences of a V3 mode

The vertical displacement of three selected isotherms (22, 13.5, 8.5 ºC), shows that there is a predominant oscillation of 24 hours, coinciding with the wind period (Fig. 4A). This is especially clear from 19 September 2004 (day 9 in Figure 4A) onwards. Furthermore, the 22 ºC isotherm oscillation is in the opposite phase with the 13.5 ºC isotherm and in phase with the 8.5ºC isotherm (see dotted lines in Fig. 4A), indicating the presence of three vertical displacements and therefore a V3 mode. Note that in Fig. 4A, the vertical displacement scale for the different isotherms is not the same.

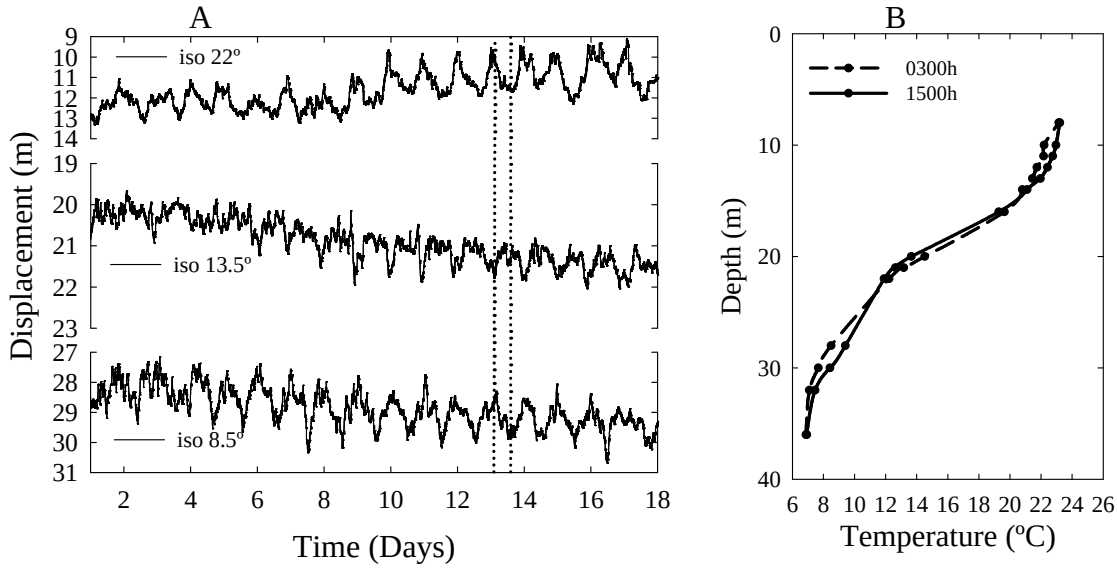

Figure 4- (A) Isotherm vertical displacements at station 1. Day 0 corresponds to 10 September 2004. Dotted lines show the experimental evidence for the mode V3. (B) Temperature profiles at two different hours measured with the thermistor string at station 1 on 22 September.

Figure 4B shows two temperature profiles measured within 12h difference, that is, half of the oscillation period, approximately when the maximum displacements are found (see dotted lines in figure 4B) on 22 September. The three vertical displacements, together with the layer structure of the V3 mode, are appreciated in Fig.4B. Note that the minimum vertical displacements correspond to the intermediate layer (13.5 ºC isotherm) where the temperature gradient is maximum and the stability higher. The presence of the V3 mode can be corroborated by making the spectral analysis of the isotherm time series for the three selected isotherms, where the 24-h peak is clearly enhanced (Fig. 5A). Also, in the 24-h peak, the 22 ºC and 13.5 ºC isotherms are coherent, but oscillate in the opposite phase (Figure 5B). Furthermore, the 13.5 ºC isotherm oscillate in opposite phase with the 8.5 ºC isotherm (Figure 5C), indicating

that each one of the three vertical oscillations are in opposite phase with the next. As the coherent oscillation that can be appreciated in the 12-h peak, for the 22 ºC, 13.5ºC and 8.5 ºC isotherms (see Fig 5B and 5C), corresponds to a very low spectral density

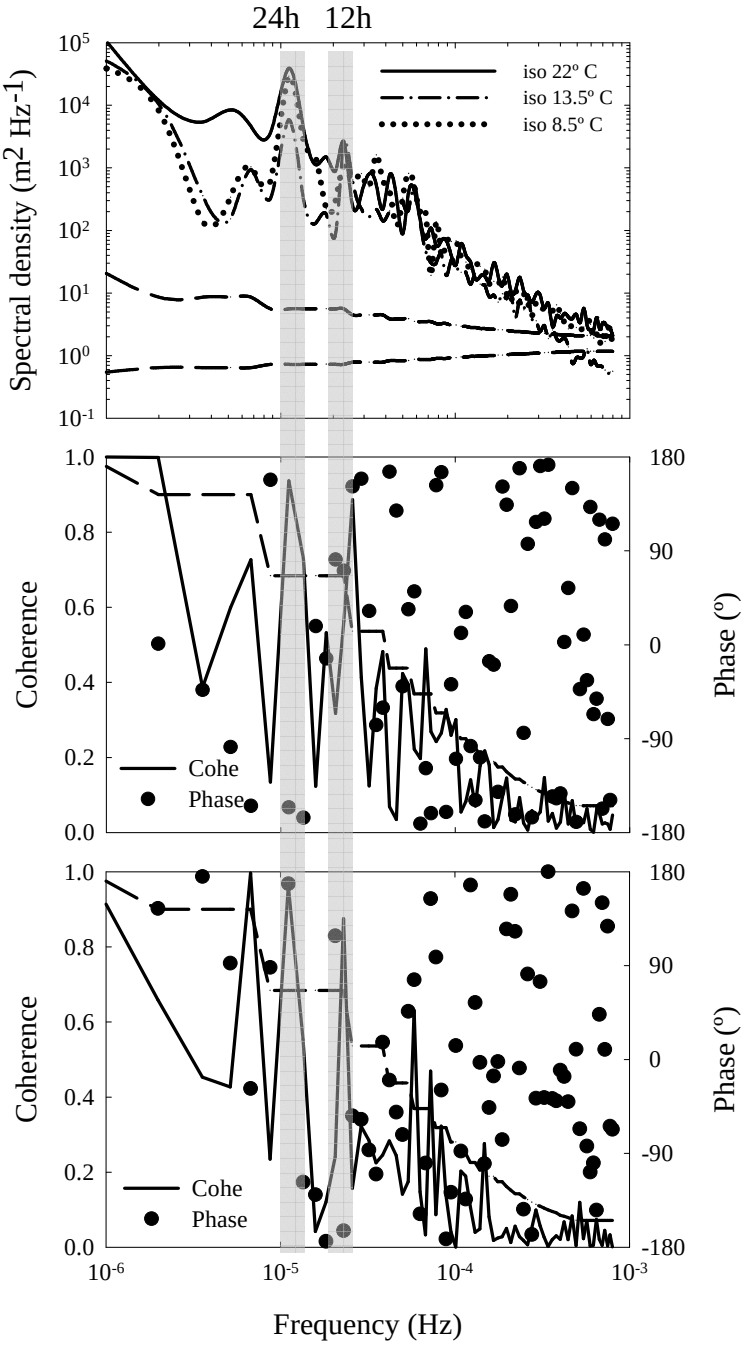

Figure 5- (A) Power spectra density for three selected isotherms for the period 18-28 September 2004. Spectra has been smoothed in the frequency domain to improve confidence; dashed line shows confidence at the 95% level. (B) Coherence and phase spectra for 22º C and 13.5ºC isotherms (C) Coherence and phase spectra of isotherms 13.5º and 8.5ºC. Dashed line shows confidence at 95% confidence. Shading lines show the periods corresponding to the maximum peaks.

Evidences of the V2 mode

As has been shown in Fig. 3B, at the end of July 2004, the 12-hour period dominated the frequency spectrum for the temperature. This also can be seen by looking at the power spectra density (PSD) for the 19ºC isotherm (Fig. 6A). As here the ADCP was measuring we will use velocity data to demonstrate the existence of a V2 oscillating mode. The spectral analysis for the velocity at different selected depths (5m 21 m and 40 m) show a dominant mode around 12-h, despite the existence of the 24-h oscillation as a consequence of the main wind periodicity (Fig. 6B). Furthermore, the velocity at 5 m depth and the velocity at 21 m depth oscillate in opposite phase (Fig. 6C), and the velocity at 21 m and velocity at 40 m also oscillate in opposite phase (Fig. 6D). This indicates the existence of three layers oscillating each one in opposite phase, as is characteristic of the V2 mode.

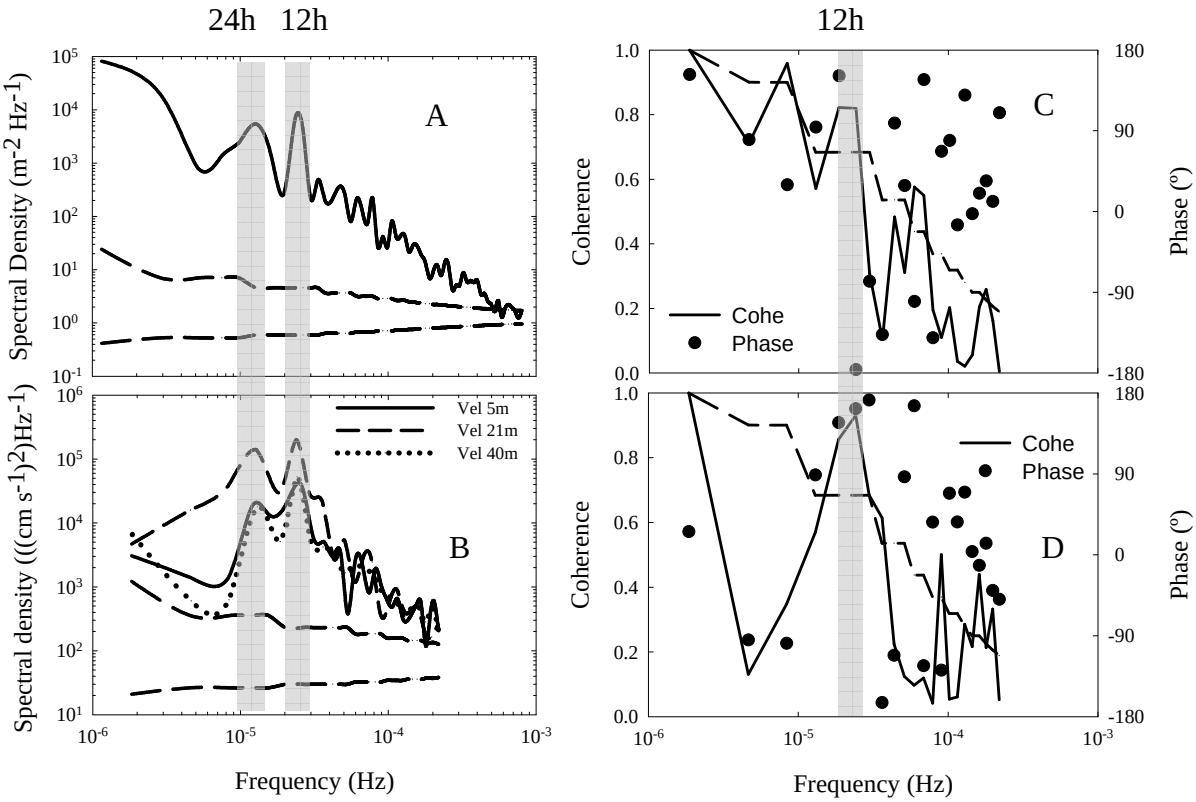

Figure 6- (A) Power spectra density for the 19ºC isotherm and (B) for the projected velocity at different depths, for the period 20 July - 30 July 2004. (C) Coherence and phase spectra for the projected velocities (following the direction indicated in fig 1) at 5 m and 21m and (D) for the projected velocities at 21 m and 40m depth. Spectra in (A) and (B) has been smoothed in the frequency domain to improve confidence. Dashed line shows confidence at 95% confidence. Shaded lines show the periods corresponding to the maximum peaks.

Additional proof of the presence of the V2 mode comes from the observation of the velocity field obtained with the ADCP (Fig. 7A), after passing a bandpass filtered

velocity over a period of 12 hours (Fig. 7B); the threelayered structure is clearly appreciated corresponding to the V2 mode. Note that the maximum and minimum vertical displacements of the isotherms (solid lines) take place when water velocity reverses its direction, as expected from the standing internal wave behaviour for the mode V2. Figure 7C shows the averaged vertical temperature profile at station 1 on 20 July 2004.

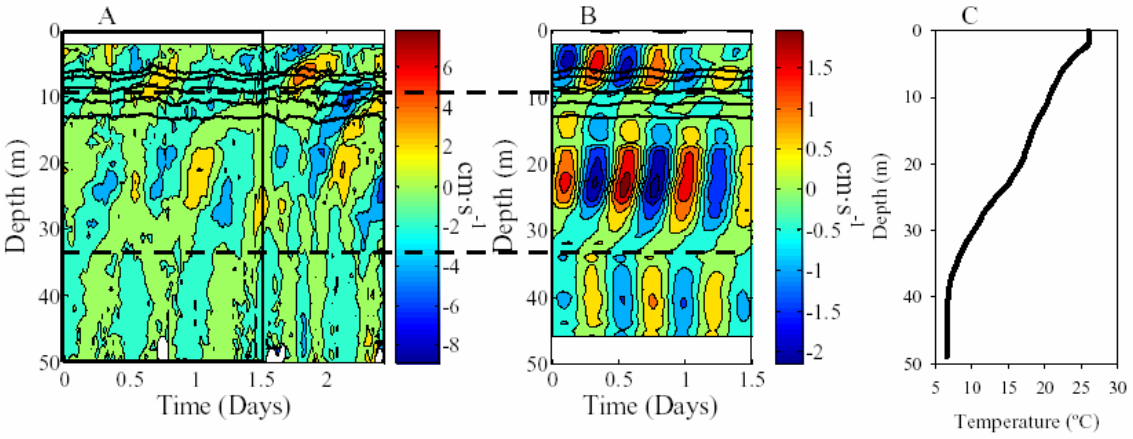

Figure 7- (A) Projected velocity, following the direction indicated in fig 1, obtained with the ADCP at station 1 and (B) after passing a band-pass filtered over a 12-h period. Day 0 corresponds to 27 July 2004; dashed lines show the three layers structure. (C) Averaged temperature profile at station 1 on 20 July.

Model results

Comparison of the model results with experimental data for September, in station 1 (Fig. 1) reveals quite good accuracy. In Fig. 8A the vertical displacements of three selected isotherms (22 ºC, 16 ºC and 8.5ºC) are compared with those obtained with ELCOM, during a 7-day period. It can be seen that the experimental and the modelled results for the 22ºC isotherm begin to diverge after the 4 day. As this isotherm is situated at the bottom of the surface mixing layer (Fig. 4B) and mixing in this zone is very active, we expect that here, the model diverges sooner that in the other zones. In fact, small differences in the turbulent kinetic energy budget could cause the displacement of the isotherm, rather than the internal wave dynamics. The fact that ELCOM underestimates the vertical displacements can be attributed to the artificial dissipation introduced by the non-normal flow boundary condition applied on the lake bottom discretization. This underestimation is even clearer for the case of Lake Kinneret (Gomez-Giraldo et al. 2006). The predicted and simulated spectral densities for the 16 ºC and 8.5ºC isotherms at station 1 (Fig. 8B and 8C) shows also the dominance of the 24-h period. The smallest scales are not obviously well resolved by the model and because of this, real and simulated values diverge at scales less than ~10^{-4} Hz.

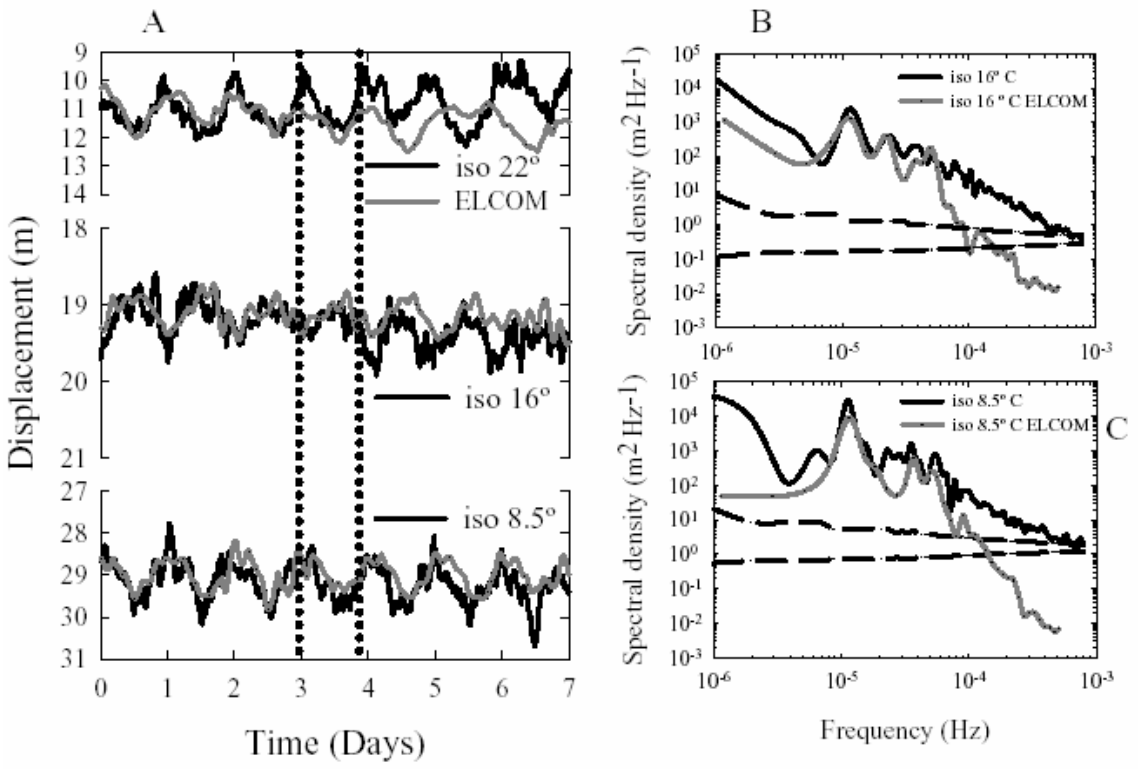

Figure 8- (A) Vertical displacement for three selected isotherms obtained with the thermistor string (black line) and ELCOM model (grey line) at station 1. Day 0 corresponds to 20 September 2004. (B) Power spectral density comparison between measured and predicted temperatures for the period 20-28 September for the 16ºC isotherm and (C) for the 8.5ºC isotherm.

Figure 9 shows the horizontal structure of the V3 mode predicted by ELCOM during a 24-h cycle at intervals of 6 hours (that is, at ¼ of the period) for the three selected isotherms (22 ºC, 16 ºC and 8.5ºC). Figure 9A corresponds to 20 September at 15:00 h. The model was initialized 4 days before and the used wind field was the real wind field measured at the meteorological station (Fig. 1). Unfortunately, we have no field data from stations other than station 1 to compare with the model results. However, the good agreement obtained at this station makes us think that the model can be useful to simulate the horizontal structure of Sau reservoir. Also, in a previous survey (Vidal et al., 2005), it was shown that the shallower layers in a station placed at the interface between the "lake part" and the "river part" (Fig. 1), oscillated in the opposite phase to the shallower layers at station 1, in agreement with model results predicted in Fig. 9.

In Fig 9A and 9C the vertical displacements are maximum and opposite each other. Figure 9E schematizes Fig. 9C.in order to appreciate the nodal lines. As there are two sets of three nodal lines the oscillation mode would be a V3H2 instead of a V3H1 as was predicted in Vidal et al.(2005) where only the "lake part" was considered. It has to be noted, however, that the ViHj classification for the modes applies to a rectangular

basin and loses meaning when the shape is different from that. Also, in Fig. 9, it can be seen as the nodal lines are displaced towards the dam in the deepest isotherms. Also in the river part of the reservoir the vertical displacements are smaller. This is to be expected, because internal waves originate from the wind field in the "lake part" of the reservoir. When they travel to the "river part", where the wind velocity was set to zero, dissipation increases. This penetration in the sloping "river part", can cause wave breaking and shear-induced convective mixing (Boegman et al. 2005a; Lorke et al. 2005), also increasing the mixing in the river inflow.

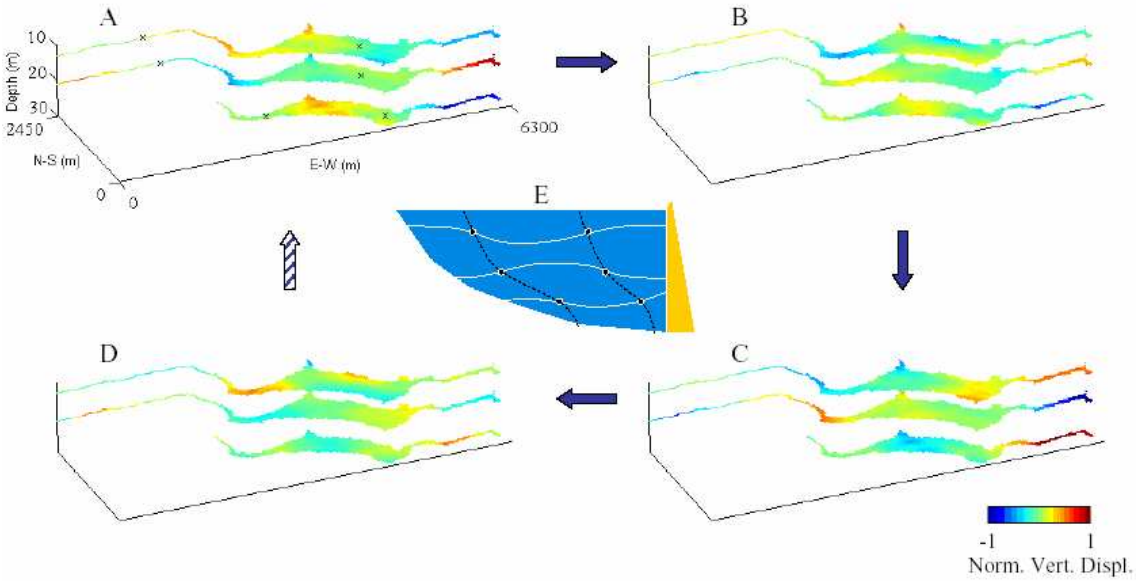

Figure 9- (A-D) Evolution of the ELCOM predicted vertical displacement of the 22º, 16º and 8.5ºC isotherms at intervals of 6h, normalized [-1 1] and band-pass filtered over a 24-h period corresponding to 20 September 04. (E) Sketch of the vertical structure corresponding to figure (C), showing the nodal points. Crosses in figure (A) shows the approximate position of the nodal points in the horizontal structure.

Rotational effects can be not negligible in the main body of Sau reservoir. By looking at Fig. 9, an anti-clockwise rotation in the upper layer (isotherm 22ºC) can be observed; however, in the deeper layer (isotherm 8.5ºC) the rotation is negligible. This fact is better clarified by looking at the rotational spectrum (Gonella, 1972) of both layers, carried out using model data from the point marked as "rot" in Fig. 1, where rotational effects could be expected (Fig. 10). A 24-h anticlockwise oscillation for the isotherm 22ºC is observed (Fig. 10A), although some clockwise components of the spectra indicate the elliptical shape of the rotation. For the isotherm 8.5ºC (Fig. 10B), both components (clockwise and anticlockwise) are almost identical, indicating a linear oscillation. These results are in accordance with the Rossby number. In fact, in the upper layer the Rossby radius Ro=c/f, where c is the phase speed of the internal wave and f the Coriolis parameter, can be estimated as follows. The phase speed will be λ/T, where T is 24 hours and λ is the length wave in the 22ºC isotherm following the

thalweg, which is $\lambda \approx$ 8000 m (see Fig. 9) and f is 1.02 $\cdot 10^{-4}$; therefore, Ro$\approx$ 900m, similar to the width of the reservoir, which is also around 900 m for that isotherm.

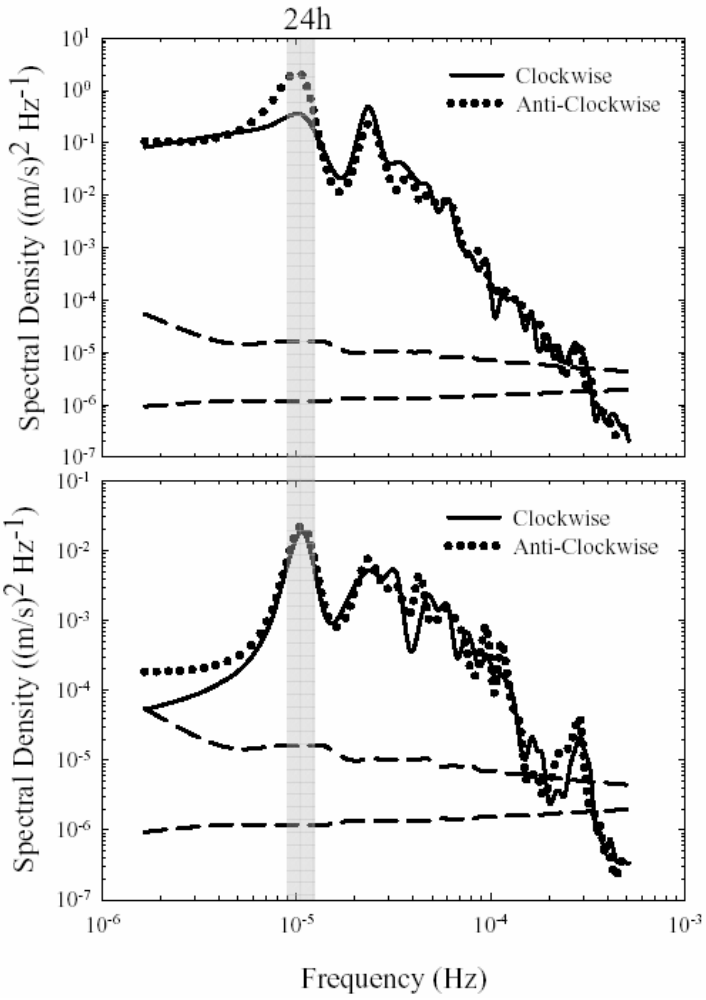

Fig 10- (A) Rotary power spectra, decomposed into clockwise and anticlockwise rotating components, for the horizontal speed of the depth corresponding for the 22ºC isotherm and (B) for the 8.5ºC isotherm. Both obtained with ELCOM model in the point "rot" (Fig. 1). Dashed lines show confidence limits at the 95% level with spectra smoothed in the frequency domain to improve confidence. The peak frequency corresponding to period of 24 h is shown.

Model results also reproduce the modal envelope quite well and the predicted periods for the oscillation of the V2 mode occurring in July 2004. Figure 11 shows the good agreement between the modelled and the measured velocity field at station 1 for the last days of July. Notice that the shifting in the velocity direction in time and in depth are almost identical in the model and in the measured ADCP velocities. Figure 12 shows the horizontal structure of the V2 mode predicted by ELCOM for the July survey for the three selected isotherms; 21.5 ºC, 20 ºC and 10ºC. The results in Fig. 12 correspond to 20 July. The model was initialized 4 days before and the used wind field was the real wind field measured. Note that the isotherms 21.5ºC and 20ºC (layers

located at approximately 8m and 12m respectively) oscillate in opposite phase with the isotherm of 10ºC (layer located at 30m), corresponding with the V2 mode. Due to the cut-off of the current in the deepest layer the structure of this mode is not simple. While the typical structure of a V2 mode can be appreciated in the main body of the reservoir, in the river part the layers oscillate in phase.

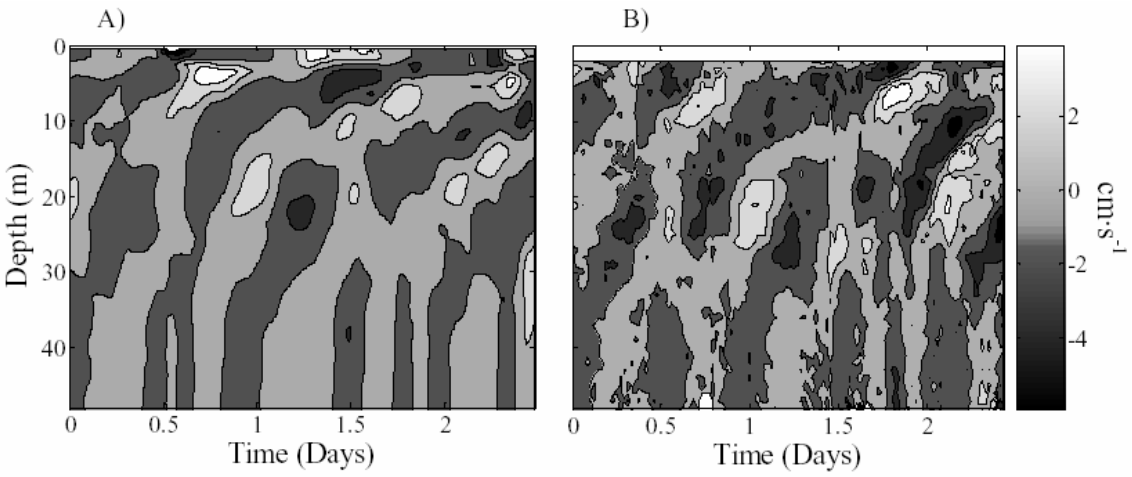

Figure 11- (A) Projected velocity comparison between ELCOM and (B) measured ADCP data at station 1. Day 0 corresponds to 27 July 2005.

Given the good description obtained with ELCOM for the Sau reservoir, the next step is the use of the model to calculate the period of the natural modes of oscillation. To undertake this task we will evaluate the oscillation response of the reservoir in the absence of wind with ELCOM, starting from an initial condition with tilted isotherms. We will use temperature data from 20 September (see Fig 9A) to calculate the natural period of the mode V3 and data from 20 Jul (see Fig. 12) to calculate the natural period of mode V2. In both cases the initial slope was chosen by taking data from the maximum vertical displacements, being previously band-pass filtered over 24h, for the V3 mode, and 12h for the V2 mode, in order to eliminate fluctuations. The resulting isotherm oscillation will be fitted to a damping sinusoidal function $X_i = A \cdot e^{-\alpha t} \cdot \sin(\omega t)$, where X_i are the vertical isotherm displacements from the equilibrium position, A is the initial amplitude and the parameter α is the inverse of the e-folding time. ω and ω_0 are the damped and the undamped natural frequencies, being related by the equation: $\omega^2 = \omega_0^2 - \alpha^2$. The natural damped periods of oscillation obtained are 25.5 h for the V3 mode and 12.3 h for the V2 mode, being close to 24 h and 12 h and because of this resonance may occur.

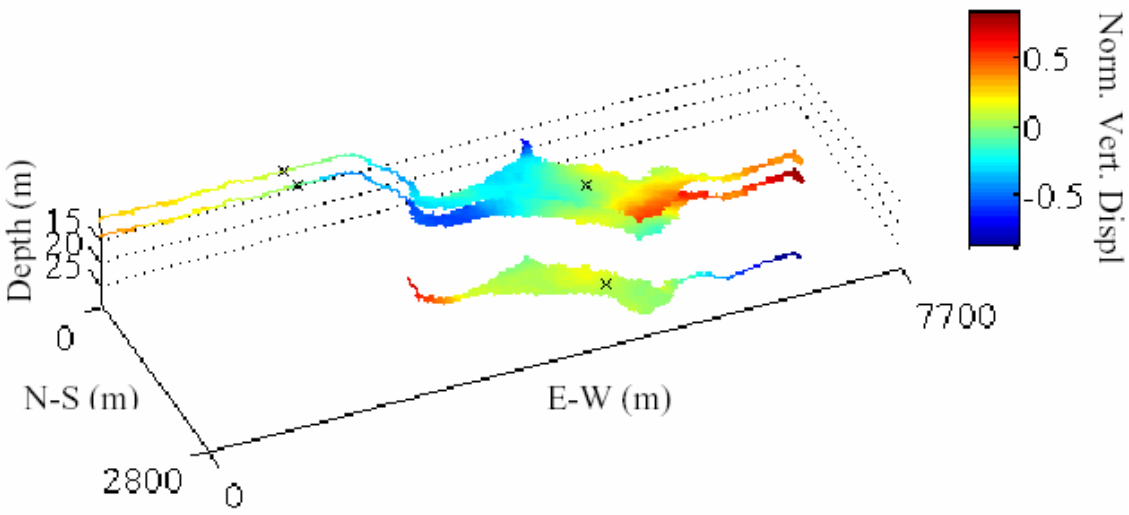

Figure 12- Evolution of the ELCOM predicted vertical displacement for the 21.5º, 20º and 10ºC isotherms; normalized [-1 1] and band-pass filtered over a 24-h period, corresponding to 20 July 2004. Crosses show the approximate position of the nodal points in the horizontal structure.

Discussion

While there are periods where the existence of the vertical modes V3 and V2 is clearly seen (Fig. 4 and Fig. 7), there are others, for example in early August (see Fig. 3), where vertical displacements are smaller and the spectral peaks are not so pronounced. Nevertheless, the response of the reservoir to wind forcing also shows predominant frequencies of 24 h and 12h (Fig 3), although now the reservoir response is probably due to the direct effect of the wind, rather than to internal waves. We hypothesize that in this case the stratification does not allow a mode with a similar period as the wind forcing and, therefore, the energy transfer to internal waves is much smaller. Estimations made with ELCOM corroborate that the period of oscillation for the modes V2 and V3 is in this case different from 12 h and 24 h.

Now we will demonstrate how Sau reservoir behaves as a forced oscillator. Forced oscillation theory shows that, after a certain period of time where transient effects can occur, the resultant frequency is the one of the forcing agent. When damping is small, if the forcing frequency is close to one of the natural frequencies of the oscillator, resonance takes place and the amplitudes are higher. We will use the model ELCOM to simulate the reservoir response to an idealized forcing wind characterized by a velocity $v_{wind} = v_o \cos \omega t$, where v_o is set up to $3 m \cdot s^{-1}$. The angular frequency will be varied from corresponding periods of 5 h to 24 h at 1h interval. The selected initial stratification will correspond to the temperature profile taken on 20 July (Fig. 7C). In this case the stratification was almost constant along the column, guaranteeing that all

the modes can be equally excited. The model was run for a 10-day period and the results were analyzed using spectral analysis.

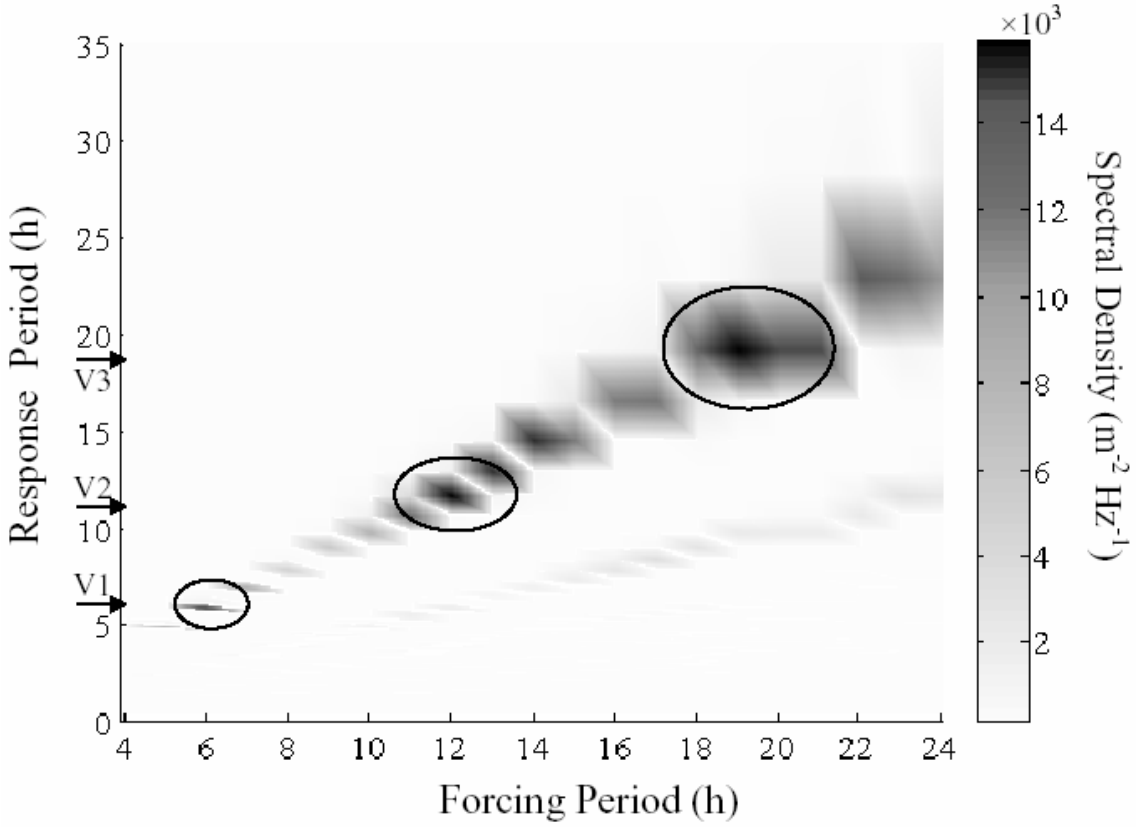

Figure 13- Contours of the power spectral density (PSD_M) integrated for the whole water column at station 1 as obtained with ELCOM for the different wind forcing periods. Circles and arrows in the y axis indicate when a forcing period coincides with the natural oscillation modes V1, V2 and V3 calculated with ELCOM.

Figure 13 shows the power spectral density (PSD_M) integrated for the whole water column at station 1 as obtained by ELCOM for the different wind forcing periods. (For the sake of clarity we use forcing periods instead of forcing frequencies). That is:

$$PSD_M = \frac{1}{H}\int_0^H PSD_{isotherm}(z)dz \quad , \qquad (2.1)$$

where H is the total depth, $PSD_{isotherm}(z)$ is the power spectral density of the isotherm at the depth z and dz was discretized to 1 m increments. Figure 13 shows that for each forcing period, the PSD_M is maximum coinciding with the period of the forcing wind. Furthermore, maximum values of PSD_M are found in 6 h, 12-13 h and 19-20 h (marked with circles in the figure). We should expect that these maximum values correspond to resonant periods where vertical displacements are amplified. Visual inspection of the oscillation dynamics for each period shows that the maximums roughly correspond to

the modes V1, V2 and V3. The displacement of the isotherms shows the existence of one vertical displacement, as expected for the mode V1, with a forcing period of 6 h (Fig. 14A); two vertical displacements for the mode V2, with a forcing period of 12 h (Fig. 14C) or three vertical displacements for the mode V3, with a forcing period of 19 h (Fig. 14D). Furthermore, for an intermediate period between two maximums as 8h (Fig. 14B), the response of the reservoir is not an organized motion, with smaller displacements, as expected in non-resonant periods.

The periods of the natural modes V1,V2 and V3 can also be obtained by rerunning ELCOM without the wind forcing. In this case the initial tilting of the isotherms has been deduced from the temperature profiles obtained in the previous runs of the model, where the position of the layers can be inferred. The corresponding natural periods are 5.8 h, for V1, 12.3 h for V2 and 19.7 h for V3, very similar to the periods where maximum values of PSD_M are obtained.

Therefore, given the initial stratification corresponding to 20 July 2004, if the reservoir is forced by winds of periods 6 h, ~ 12 h or ~ 19 h, maximum values of PSD_M are obtained indicating the existence of resonance between the wind and the internal wave field. Given that the wind field at mid July shows two forcing frequencies, corresponding to periods of 12 h and 24 h (Fig. 3A), and that the natural frequency of the mode V2 is close to 12 h, it can be expected that this would be the chosen oscillation mode, as in fact occurs, as shown previously.

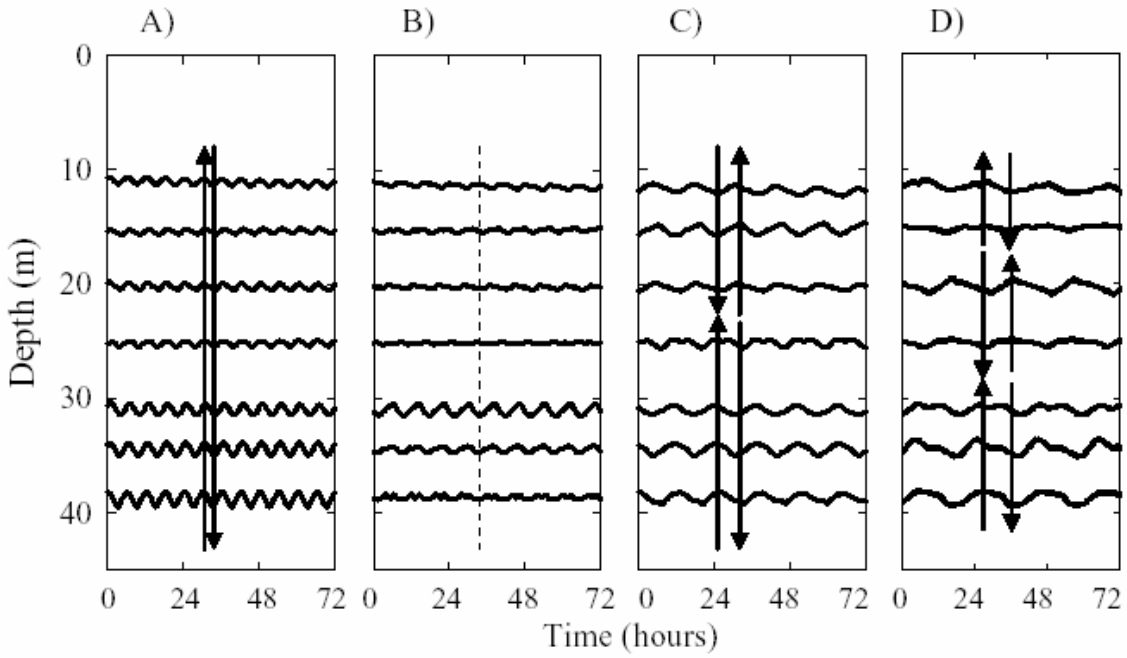

Figure 14- (A) Isotherm evolution obtained with ELCOM for a wind forcing period of 6h, (B) 8h, (C) 12h and (D) 19h. Arrows indicate the vertical displacement for two opposite states corresponding to modes V1 in (A), V2 in (C) V2 and V3 in (D).

Conclusions

We can conclude by remarking that, at higher scales, Sau reservoir behaves as a forced oscillator. It responds to the periodic winds of 12 h and 24 h with water movements of the same period. However, when stratification allows that one of the natural periods of the reservoir is close to the forcing periods, the energy transfer from the wind is higher because of the resonance. This happens at mid July, for the mode V2, resonant at 12 h, and at the end of August for the mode V3, resonant at 24 h. The model ELCOM shows that the structure of the mode V3 presents two horizontal nodal lines. The mode V2, instead, has two horizontal lines in the surface but one at the bottom. Both modes are affected by the earth's rotation in the widest part of the reservoir.

CHAPTER 3

The seasonal evolution of high-vertical mode internal waves in a deep reservoir. The case of Beznar

*** From:** Vidal, J., F.J. Rueda and X. Casamitjana. The seasonal evolution of high-vertical mode internal waves in a deep reservoir. The case of Beznar. Limnol. Oceanogr. *Submitted*.

Abstract

The casual mechanism and seasonal evolution of the internal wave field of a deep warm-monomictic reservoir are described in this work through the analysis of field observations and numerical techniques. The analysis period extends from the onset of thermal stratification in the spring until mid-summer. During this period, a shallow surface layer, overlying a thick metalimnion, characterizes the thermal stratification. This broad stratified region supports high vertical mode basin-scale seiches, and as the stratification evolves throughout the observation period, vertical modes whose periods are close to the 24-hour return period of the local wind field are preferentially excited. This way high vertical modes (from V3 to V5) were excited and dominant in Beznar reservoir during the year 2005.

Introduction

Basin-scale internal waves, commonly excited by the wind forcing acting directly on the surface of lakes and reservoirs, provide the main driving force for vertical and horizontal transport in stratified systems under the wind mixed layer (e.g. MacIntyre 1998). They constitute one of the key features in the physical environment of lakes and reservoirs having being related to the biogeochemical behaviour of these water systems. Their occurrence, for example, has been related to the generation of bottom boundary layers (Pierson and Weyhenmeyher 1994), the distribution of living organisms (Serra et al. 2006) or to the re-suspension of particles and nutrients (Gloor et al. 1994). In consequence, in the last few years the study and description of these waves

in stratified lakes has drawn a considerable amount of attention in the scientific literature (e.g. Hodges et al, 2000; Rueda et al 2005; Antenucci and Imberger, 2003 just to mention a few).

Internal waves at the basin scale have spatial characteristics and oscillation periods which, in small to medium size lakes, are controlled by the density stratification and the geometric properties of the enclosing basin. Internal wave motions can be classified according to the number of nodal points (ViHj), where i and j are the number of vertical and horizontal nodes. The most commonly observed mode, the V1H1, has one vertical and one horizontal nodal points and it is characterized by a unique recirculation cell in the containing basin. Observations of mode two and above internal waves are seldom reported, as these modes have been traditionally deemed as rare in nature (e.g. Stevens and Lawrence 1997). Second vertical modes, for example, have been reported by LaZerte (1980), Wiegan and Chamberlain (1987), Münnich et al. (1992) and Roget et al (1997) among others. Münnich et al (1992) showed that the second vertical mode V2H1 is dominant in the wave field of Alpnacher See, a side-basin of Lake Lucerna. Also recently, Vidal et al (2005) and Pérez-Losada et al (2003) have presented experimental evidence of third vertical modes oscillations occurring in reservoirs forced by diurnal winds. Here, it will be demonstrated, by means of a case example, that internal waves of high vertical modes (larger than three) can exist and even dominate the internal wave field in deep-warm monomictic reservoirs near the coast in Mediterranean regions at the time of maximum stratification. The arguments presented here together with previously published work, suggest that high vertical mode internal waves should, in theory, be a common feature in deep warm-monomictic reservoirs near coastal Mediterranean regions. Our work will examine the causal mechanisms that explain the occurrence of high vertical modes of motion in these water bodies. Furthermore, it examines the seasonal evolution of the internal wave field in the reservoir. This is in contrast with previously published work, in which the internal wave field in analyzed during limited periods of time in which the background stratification is presumed constant. Our study is based on the analysis of time series of water temperature collected at different depths during periods of up to several months in a deep reservoir in Spain, together with the results of simplified models applied to those water bodies.

Reservoirs near coastal regions in the Mediterranean, in general, are characterized by thick metalimnetic layers (e.g. Casatmitjana et al. 2003) with large temperature gradients. Simple scaling arguments support our working hypothesis, that waves of high vertical modes may become dominant features of the internal wave field in these reservoirs. Koseff and Street (1985) pointed out that the number of recirculation cells in a linearly stratified lid-driven cavity flow was related to the bulk Richardson number

$$Ri = g \frac{\Delta\rho}{\rho} \frac{D}{U_b^2} \tag{3.1}$$

Here g is the acceleration of gravity, $\Delta\rho$ is the density difference between the top and the bottom of the cavity, ρ is a reference density, D is the depth of the cavity and U_b is the speed of the lid or the speed of water parcels at the surface. For $Ri_b >> 1$, at least two secondary circulation cells are present in addition to the primary cell. For $Ri_b \sim 1$ Koseff and Street (1985) show that a primary circulation cell dominates the flow. For values of $Ri_b << 1$, the mixed layer penetrates to the lower boundary of the cavity and the circulation is similar to isothermal flow. Surface and bottom temperatures in deep (h_{max} > 30 m) reservoirs around the Mediterranean region of Spain, during summer are typically 24 ^{o}C and 10 ^{o}C respectively (Armengol 1994) and the corresponding value of $\Delta\rho/\rho$ is c.a. 2.4x10^{-3}. For values of U_b of O (10^{-1}) ms^{-1}, typically observed in lake surfaces (e.g. Rueda et al. 2005), Ri_b is of O (10^{2}), which suggests that indeed, we should expect flow structures of high vertical modes in deep reservoirs forced by wind.

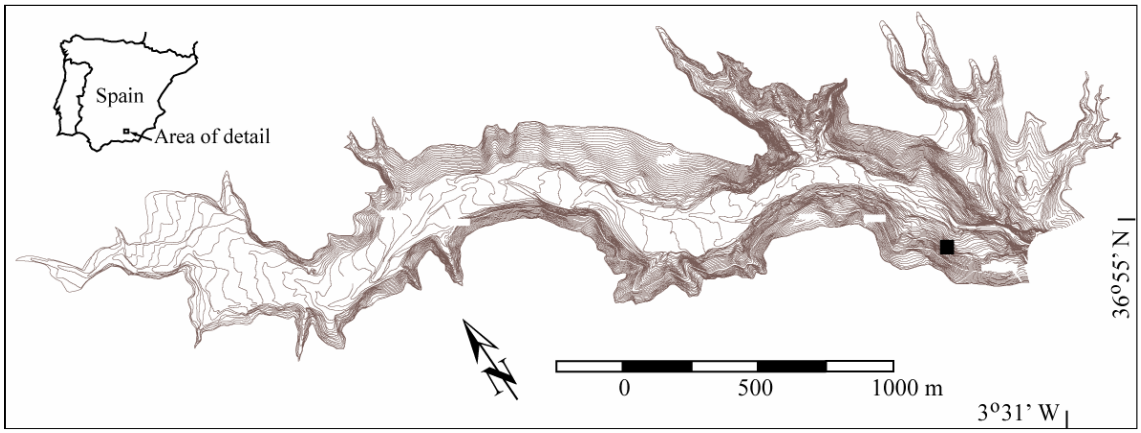

Figure 1. Lake Beznar bathymetry. The solid square near the dam (on the right) indicates the location of the thermistor chain. Izbor River enters the reservoir through the left.

Materials and methods

Lake Beznar - Lake Beznar is a mesotrophic reservoir located in Southern Spain (Fig. 1), draining a watershed that occupies the southwestern portion of Sierra Nevada. The watershed has a surface area of approximately 352 km^2 and changes in elevation of ca. 2500 m. The average inflow Q that enters the reservoir from its contributing watershed is 1.79 m^{3}s^{-1} (56.5 hm^3 annual volume) with large oscillations on seasonal scales. Maximum inflow rates occur during winter and spring, coinciding with rain or snowmelt events. Minimum flow rates occur during late summer and early fall. The maximum volume of water held in the reservoir V is 54.60 hm^3, hence, the nominal residence time of Lake Beznar, estimated as V/Q is aproximately one year. When full, the surface area of the reservoir is ca. 170.26 ha, the elevation of the free surface is 485 m.a.s.l. and its maximum depth 102.96 m at the dam. There exist two outlets located at 410 and 450 m.a.s.l. The bathymetry of the reservoir is shown in Fig. 2 with isobaths

every 2 m. The reservoir has an elongated shape oriented along the NW-SE direction. The largest inflows occur at the NW end through Izbor river. The river reach inundated by the reservoir is approximately 4400 m long and rather steep (the average slope is ca. 0.02). The valley is wide open in the tail of the reservoir, but with lateral slopes of up to 50% in the dam area.

Experimental data set - In 2005, and in order to characterize the evolution of the internal wave field on seasonal time scales, a thermistor chain was deployed near the dam (Fig 1) and left for 122 days, from day 95 to 217 (study period), during late spring and summer. Thermistors were deployed at the surface, and at 2, 4, 6, 10, 15, 20, 25, 30, 50 and 80 m depth, and they were programmed to record temperature at 30-min intervals. The shallow temperature sensors (< 30 m depth) were HOBO H20-001, and the remaining were Stowaway^{TM} Tibdit^{TM} thermistors. Hourly meteorological and daily hydrologic records were provided by the regional government of Andalucía. From day 155, a second meteorological station was deployed on the lake shore and collected air temperature, relative humidity, solar radiation, wind speed and wind direction on 5-min intervals.

Natural internal wave modes - The frequency and the spatial structure of the natural modes of the internal oscillations in Lake Beznar were analyzed with a model, which was initially proposed by Münnich (1996) and applied in Chapter 1 to Sau reservoir. It is based on the numerical solution of the generalized eigenvalue problem for the stream function ϕ in a vertical plane given by

$$\frac{\partial^2 \varphi}{\partial x^2} = \frac{\omega^2}{N^2}\frac{\partial^2 \varphi}{\partial z^2} \tag{3.2}$$

Here x, z are the along-the-thalweg and vertical coordinates, ω is the oscillation frequency of the internal wave and N^2 the Brunt-Väisälä or buoyancy frequency (= -g/ρ dρ/dz, with ρ being the density of water and g the acceleration of gravity), which, in general, is a function of z. Lateral variations in this model are ignored. This simplifying 2D assumption is deemed reasonable given the narrow and elongated shape of Lake Beznar (see Fig. 2). Although, variations in the width of the reservoir or the sinuosity of the river valley will determined the detailed characteristics of the internal wave field, it is presumed that the overall characteristics as the mode structure and periodicity can be well represented by a two-dimensional wedge. Furthermore, the internal Rossby radius of deformation Ro for Lake Beznar's latitude and the stratification existing during the study period is about 900 m, larger than the maximum width of the lake (400 m). This fact suggests that the Earth rotation will not affect the internal motions (e.g Patterson et al, 1984). The validity of the 2D assumption was

further supported by the simulations conducted with three-dimensional models (see below).

Given the large spacing exiting among some of the thermistors, and in order to provide the 2D model an accurate description of the thermal structure of the water column in Lake Beznar, the data was interpolated to 2 meters using an approach which blended observational and modeling data. Linear interpolation was used above 30m, while from 30 m to the bottom the interpolation was exponential. This approach was chosen after inspection of simulations of the seasonal evolution of the thermal-structure of Lake Beznar (Rigosi 2006), conducted with a one-dimensional model (DYRESM, Imberger and Patterson, 1981). The model DYRESM is a process-based transport model which includes descriptions of mixing and transport processes associated with river inflow, natural or man-made outflows, diffusion in the hypolimnion and mixed-layer dynamics. It requires no hydrodynamic calibration, which implies that the level of process description, including temporal and spatial scales in the model, is fundamentally correct (Hamilton and Schladow, 1997). It has been used extensively in the existing peer-reviewed literature to predict the vertical distribution of temperature, salinity and water quality parameters in a wide range of applications for small to medium-size reservoirs (e.g. Heald et al., 2005; Gal et al., 2003; Antenucci et al., 2003; Campos et al., 2001; and McCord and Schladow, 1988). The DYRESM simulations of Rigosi (2006) suggested that water temperature below 30 m (where the withdrawal structures are located) undergoes small (<1oC) variations during the 3-month period in 2005 when the data was collected.

Internal waves and wind forcing - The relationship between the internal wave oscillations and the wind forcing was analyzed using a three-dimensional 3D hydrodynamic model, which accounts for complex geometries, time variations (periodicity) of the wind acting on the free surface and the possible influence of the Earth rotations. The model used in this work is the Estuarine and Lake Computational Model (ELCOM), initially proposed by Hodges et al (2000) and applied to the description of the internal waves by Laval et al. (2003) and Gomez-Giraldo et al (2006), among others. ELCOM solves the 3D hydrostatic, Boussinesq, Reynolds-averaged Navier Stokes and scalar transport equations (see Introduction of this PhD dissertation). The model was initialized and forced using the experimental data collected in 2005.

Results

Meteorological records - The hourly time series of local atmospheric variables recorded at the nearby meteorological station are shown in Fig. 2. Temperature records exhibit change both at diurnal and synoptic time scales. In general, temperature shows a warming tendency during the survey up to day 200. Wind exhibited a remarkable diurnal periodicity during the period of study, with maximum values during the

afternoon (from 1500 h to 1800 h), mostly from the southeast, and minimum values during night time and early morning. This wind regime persists during long periods of time and is only interrupted by the passage of fronts when winds, with average hourly speeds of up to 10 ms^{-1} and predominantly from the northwest, blow over the lake.

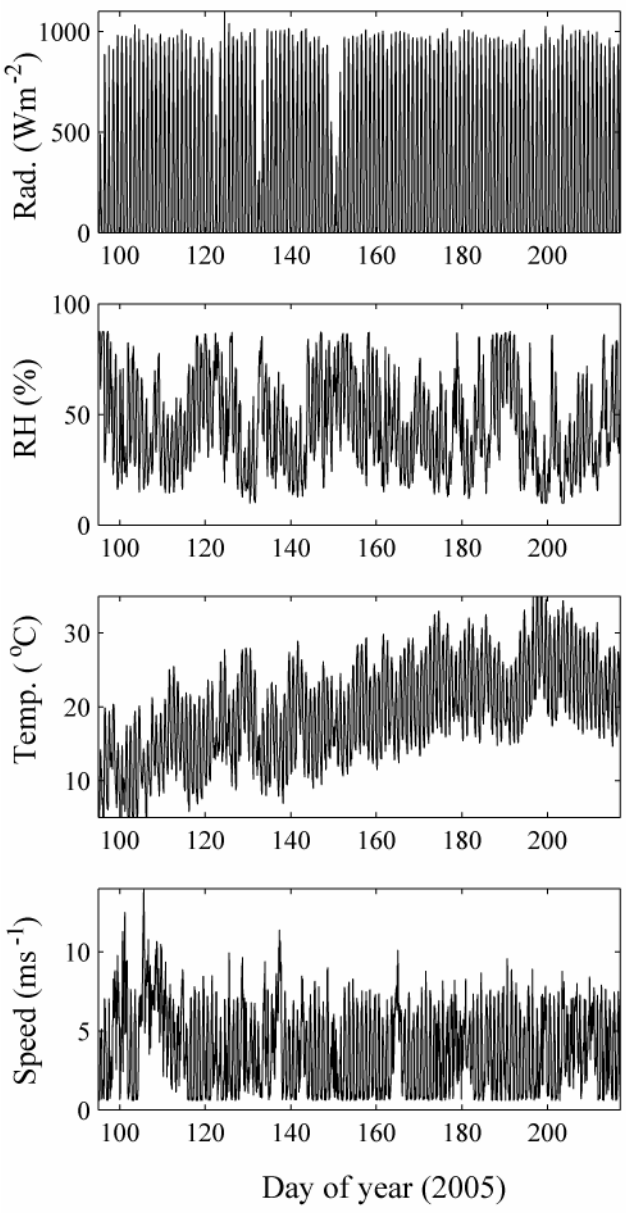

Figure 2. Meteorological records for Lake Beznar in 2005.

Hydrological records - Inflows and outflows control the long-term and seasonal evolution of the water level and the thermal structure in reservoirs, and therefore, although indirectly, they should be considered as factors explaining internal oscillations. However, inflows and, specially, outflows can be considered as forcing mechanisms exciting internal waves. As shown by Imberger (1980) the onset of flow through selective withdrawal structures (or, in general, any sudden change in the withdrawal

rate) could generate shear and internal waves of a wide range of modes. If the frequency at which withdrawal rates are changed coincide with the frequency of any natural mode of oscillation in the reservoir, resonance can occur. The inflows and outflow rates during the period of study is shown in Fig. 3. Withdrawal rates do not change on diurnal basis, hence, at least, at the daily time scales, inflows and outflow forcing does not resonate with the internal waves of diurnal periodicity. The water level during the study period varied from 478 m.a.s.l. to 471 m.a.s.l., corresponding with maximum depths of 96 m and 89 m respectively.

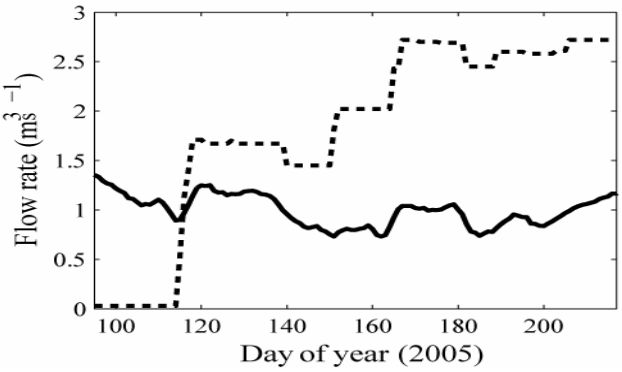

Figure 3. Inflow (continuous line) and outflow (dash line) rates.

Lake thermal structure - The evolution of the thermal structure in 2005 is shown in Fig. 4. During the beginning of the study period the reservoir is almost homogeneous, with top-bottom temperature differences of up to 4ºC, and a thermocline at 10 m of depth. The reservoir stratifies thereafter and by the end of the study period the metalimnion is almost 30 m thick with a temperature gradient of c.a. 0.5 ºC m^{-1}. While in the hypolimnion (below 30 m) the water temperature remains uniform and almost steady throughout the study period, in the metalimnion it undergoes oscillations at a range of scales, from those typical of wind events to daily periods. On time scales of the order of individual wind events, the response of the water column to wind stress can be analyzed on the basis of the values of the Wedderburn W and Lake numbers L_N (Stevens and Imberger 1996). The Wedderburn number W was calculated as (Imberger and Patterson 1990)

$$W = \frac{1}{L}\frac{g'h^2}{u_*^2}, \tag{3.3}$$

where g' is the reduced gravity (= $g\Delta\rho/\rho$) h is the thickness of the surface mixed-layer, and L the basin length, here assumed to be c.a. 4400 m. The base of the surface layer was estimated as the depth where the temperature is 0.2^{o}C lower than at the surface (MacIntyre 2002). The Lake number is estimated as

$$L_N = \frac{M_{bc}}{\tau A_s z_v}, \tag{3.4}$$

where M_{bc} is the baroclinic moment about the center of the embayment volume, τ is the surface shear stress, A_s is the surface area and z_v is the depth of the center of volume. In the calculation of L_N it was assumed that the metalimnion extended from 1.5 to 25.7 m of depth. The surface shear stress was calculated from the wind speed, using a simple bulk parameterization (Fischer et al 1979, Eq. 6.17) with a drag coefficient C_D = 1.5 x10^{-3}. For the calculation of M_{bc}, the location of the center of the metalimnion was estimated as follows. First the N^2 profile was estimated from interpolated daily average temperature information. Linear interpolation and smoothing was used to get profiles every 0.25 m. The metalimnion was defined as that part of the water column where $N^2 > 10^{-4}s^{-2}$. While this limit is arbitrary, in principle, the top of the metalimnion agreed well with the depth of the mixing layer estimated as in MacIntyre (2002). The depth equidistant from the top and the bottom of the metalimnion was chosen as the center of the metalimnion. Low Lake numbers (L_N <1) are associated with vertical mode 1 tilting of the temperature field, whereas low Wedderburn numbers ($W \sim O(1)$ or $W < 1$) are associated with a higher vertical mode 2 response.

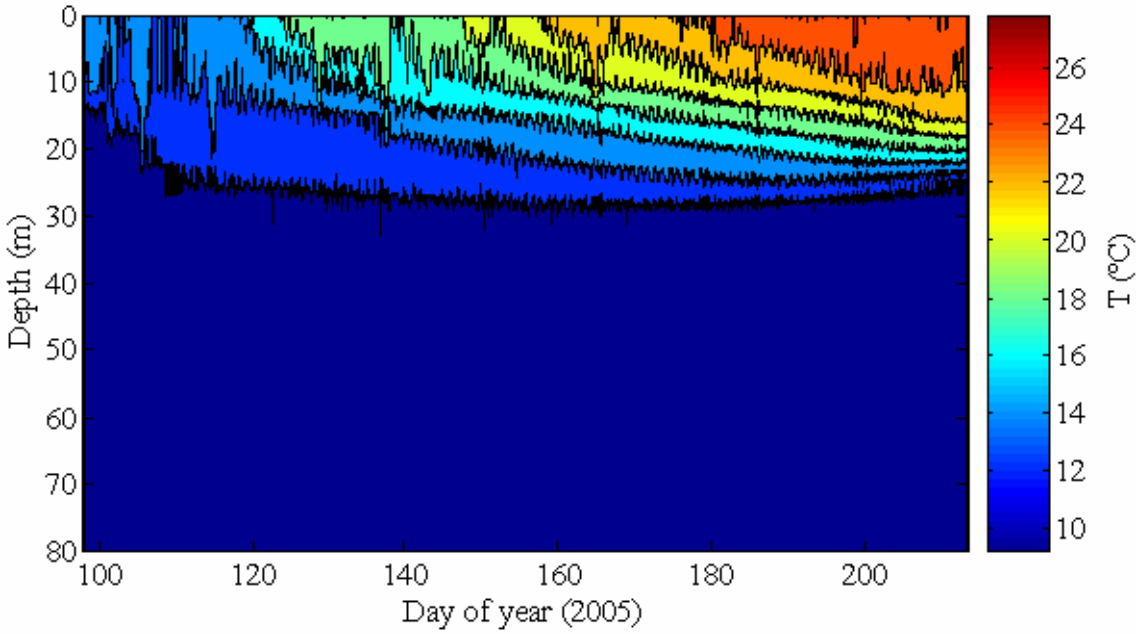

Figure 4. Thermal evolution in Beznar Reservoir

Values of W and L_N are shown in Fig. 5. High vertical modes (at least 2) are expected as response to wind events as predicted by O(1) values of W and L_N >>1. During those events, and according to Stevens and Imberger's (1996) analysis of W and L_N , metalimnetic water was pushed upwind, towards the inflow region, where isotherms should have stretched. Warm water was forced by the wind to accumulate in

the dam region, deepening the surface layer up to 10 m below the free surface and causing the isotherms to compress (see Fig. 4).

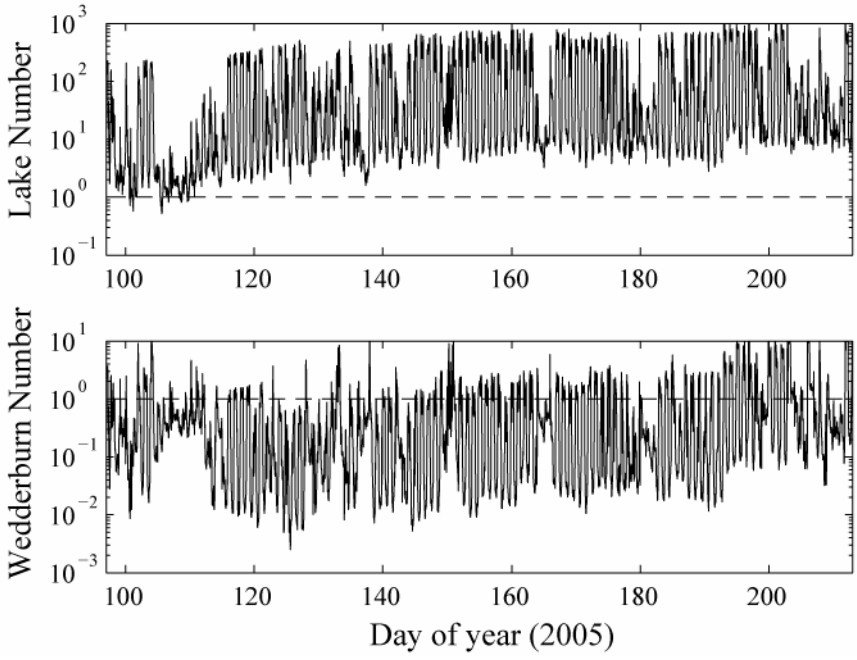

Figure 5. Lake and Wedderburn numbers for Lake Beznar during 2005. The temperature structure in the reservoir varies only from day to day in the estimation of Ln and W. Wind stress is calculated from unfiltered hourly wind speed records. $T_1/4$ values are c.a. 1.5 h, hence hourly values are deemed appropriate to evaluate the mode response of the lake.

High vertical modes under periodic conditions - The diurnal periodicity exhibited by the isotherm displacements in the upper 30 m of the water column (Fig. 4) persists throughout the study period. The internal wave field and its evolution was analyzed using continuous wavelet transform applied to time series of potential energy (PE) derived from temperature observations. Morlet wavelet transform was used since it allows the visualisation of the time evolution of the frequency and intensity of the different oscillatory modes (see Antenucci and Imberger 2003, Naithani et al. 2003). To estimate the PE, for every time step *t* a vertical temperature profile with 1m resolution was obtained by linearly interpolating the observations in the field. The potential energy (PE) was then estimated for each 1-m bin, located at *z* meters above the bottom and at any given time *t* as follows,

$$PE(z,t) = \rho(z,t)gz \tag{3.5}$$

Here, the density ρ was derived from temperature following Chen and Millero (1977). Continuous wavelet transforms were applied to the PE time series at each individual bins, and the absolute values of the continuous wavelets signal were then integrated. The real part of the wavelet coefficients gives an insight into the energy density and the phase at a certain depth (Naithani et al. 2003); then, integrating the

absolute value of the coefficients along the water column we can obtain an insight of the time evolution of the energy and phase of the different modes presents in the system. Given that the density variations below 30 m are small, only the density variations in the upper 30 m of the water column were used. Figure 6B shows the integrated signal of the continuous wavelet transform of the PE in the water column.

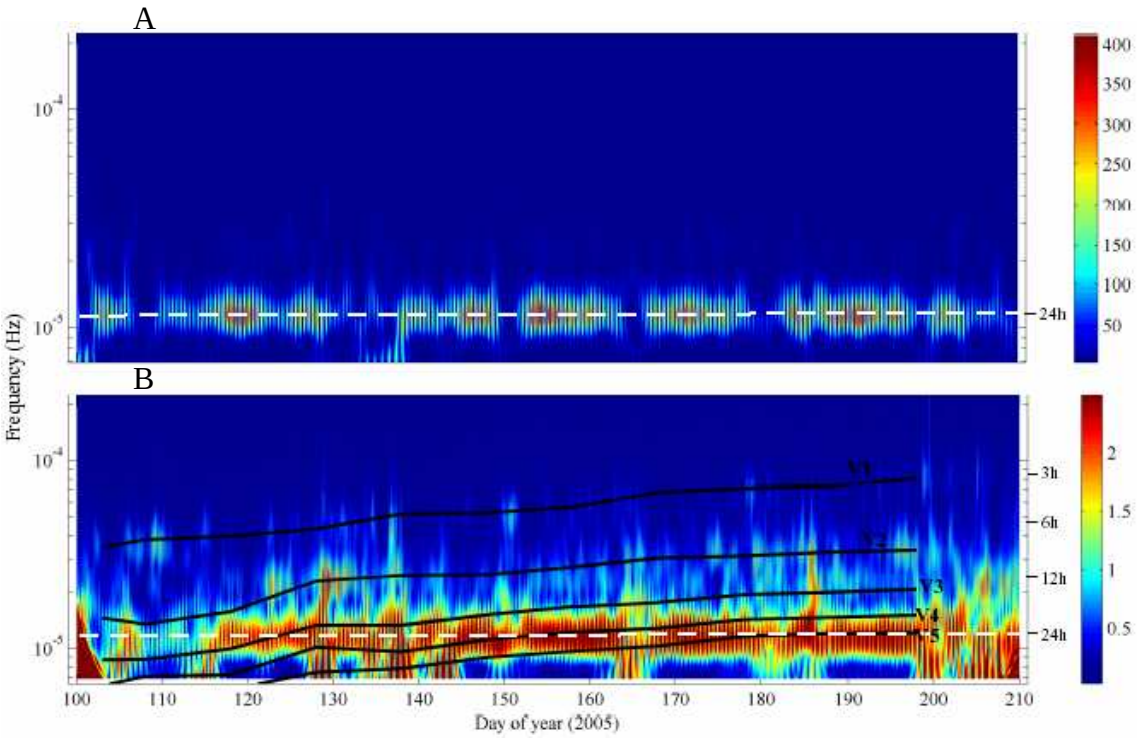

Figure 6. (A) Non-dimensional parameter of continuous wavelet transform in absolute values of square of the wind speed and (B) integrated signal of the continuous wavelet transform of discretized PE along the water column (see text).

The 24h periodicity in the internal wave field appears to be correlated with the strong diurnal periodicity that characterizes the wind regime. Figure 6A shows the evolution of the continuous wavelet transform of the square of the wind speed. The diurnal periodicity in the wind forcing (marked as a white dashed line) persists during most part of the study period, and is only disrupted by the passage of episodic fronts (see, for example, on day 106). Peaks of 24h in the continuous wavelet transform of the PE signal (Fig 6B) correspond to the peaks in the continuous wavelet transform for the wind, with a small lag; which suggests a close link and a causal relationship between the 24h internal waves and the wind forcing characterized by its diurnal periodicity (Fig. 6). The vertical structure of the internal waves with 24h period can be derived by comparing the temperature records from individual thermistors. A positive vertical displacement of the isotherms will result in decreasing temperature records at a fixed depth (water from lower layers reaching the thermistor) and viceversa. For example, between the days 119 to 123 the internal wave had a V3H1 mode, as evidence by the vertical displacements shown in Fig. 7. The modal structure of the internal wave, though, changes along the season, and the mode V4H1 becomes the dominant mode

around day 160, and even a mode V5H1 appears around day 190. These modes correspond with the natural modes of oscillation of the stratified basin, with periods that are near 24 hours. To show this extent, we will show that the frequency and spatial structure of the natural modes of internal oscillations and determined by the 2D eigenmodel, described in the *Materials and Methods* section, agree with those derived from observations.

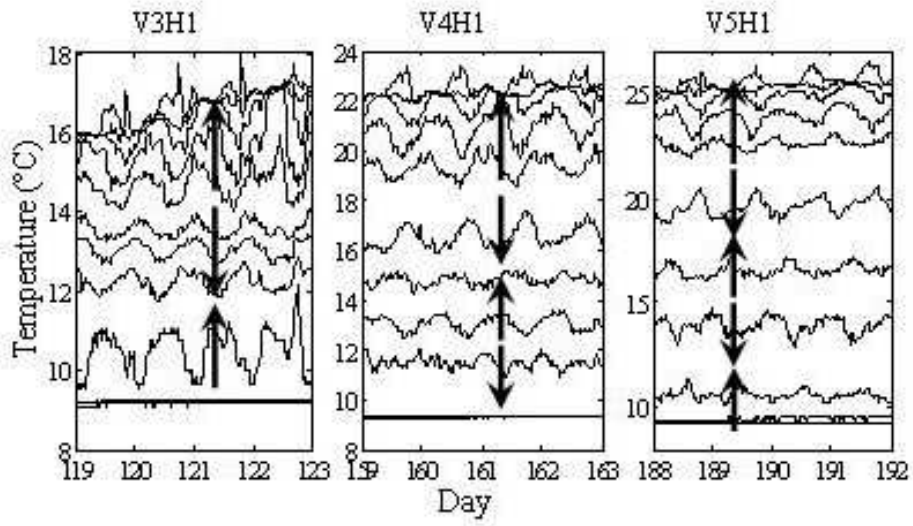

Figure 7. Temperature evolution for different periods when modes V3H1, V4H1 and V5H1 where dominant as shows the arrows.

Predictions of the eigenmodel were obtained every 10 days during the study period. The vertical temperature profiles used in Eq. 1 were obtained by (1) averaging in time the thermistor records corresponding to periods of five days and (2) interpolating the time averaged records in space, as described in the *Materials and Methods* section. The estimated frequency for the natural V1H1, V2H1, V3H1, V4H1, V5H1 and V6H1 modes of oscillations are shown in Table 1. Given that Lake Beznar is relatively short (4 km) and occupies the bottom of a deep V-shape valley with a unique branch, the wind acts near-uniformly along the lake's thalweg and horizontal modes larger than H1 should not be expected. Hence these modes were not considered in the analysis. This assumption was later deemed as valid, when inspecting the results of the 3D model (see *Wind forcing and internal wave field* section). As Table 1 shows, the periods of these natural modes tend to decrease as stratification evolves on seasonal time scales from early spring to late summer when top-bottom temperature differences reach their maximum. As the period of any given vertical mode gets close to 24h, the wind forcing appears to energize it, becoming the dominant mode of oscillation over others of less spatial complexity (lower vertical mode).

	103	**108**	**118**	**128**	**138**	**148**	**158**	**168**	**178**	**188**	**198**
V1H1	8	7.3	7	6.4	5.3	5.3	4.6	4.1	3.9	3.8	3.4
V2H1	19	20.5	17.6	12.1	11.3	11.2	10.2	9.1	8.9	8.5	8.3
V3H1	31.7	31.6	27.7	20.8	20.8	18.3	16.6	15.7	14.3	13.9	13.4
V4H1	43.7	39	38.2	27.2	28.7	24.8	22.6	21.6	19.4	18.9	18.4
V5H1	>>24	>>24	46	37	35.3	30.8	28.6	26.8	23.8	23	22.9
V6H1	>>24	>>24	>>24	43.6	41.5	38.7	35	31.4	29.8	28.3	27.4

Table 1. Periods in hours of the main modes estimated with the 2D-Model along the survey; from day 103 to day 198.

Figure 8D shows the comparison of predicted isotherm displacement amplitudes for the mode V5H1 against the observed displacements directly derived from the observations. Here, we have followed the methodology proposed by Fricker and Nepf (2000) and apply it to the temperature records collected from day 195 to day 199, when the V5H1 mode was the dominant mode of oscillation. A mean temperature profile was first obtained by time averaging temperature records at different depths, as

$$\overline{T}(z_i) = \frac{1}{M}\sum_{n=1}^{M} T(z_i, t_n), \tag{3.6}$$

here, M is the number of records in the time series at any given depth, and z_i denotes the depth of thermistor i. The root mean square (RMS) temperature deviation was then calculated as

$$\Delta T^{i}_{RMS} \equiv \sqrt{\frac{2}{M}\sum_{n=1}^{M}\left[T(z_i, t_n) - \overline{T}(z_i)\right]^2}, \tag{3.7}$$

the values of ΔT_{RMS} obtained represent the absolute values of the wave envelope. The RMS vertical displacements are determined from ΔT_{RMS} as

$$\zeta^{i}_{RMS} = \frac{\Delta T^{i}_{RMS}}{\partial T_{av}/\partial z}, \tag{3.8}$$

where the local gradient $\partial T_{av}/\partial z$ is, in turn, estimated from the smooth temperature profile obtained by time and spatial interpolation, as indicated above (see Chapter 1 for further details in the estimation procedures). The phase of the vertical displacements was estimated by analyzing, one by one, the cross-spectra calculated from the temperature recorded at 30 m (taken as reference) and the temperature recorded at other depths. For short periods of time when changes in stratification are not significant, cross-spectrum is an effective method to determine the vertical structure of the different

modes. The cross-spectra were estimated using records from days 195 to 205, a period of time which is longer than that used in estimating the RMS vertical displacements (from day 195 to 199). Using a longer period to estimate the cross-spectra was justified in that (1) we increase the confidence of the statistical estimates and (2) the vertical structure undergoes negligible changes during the 10 day period after day 195.

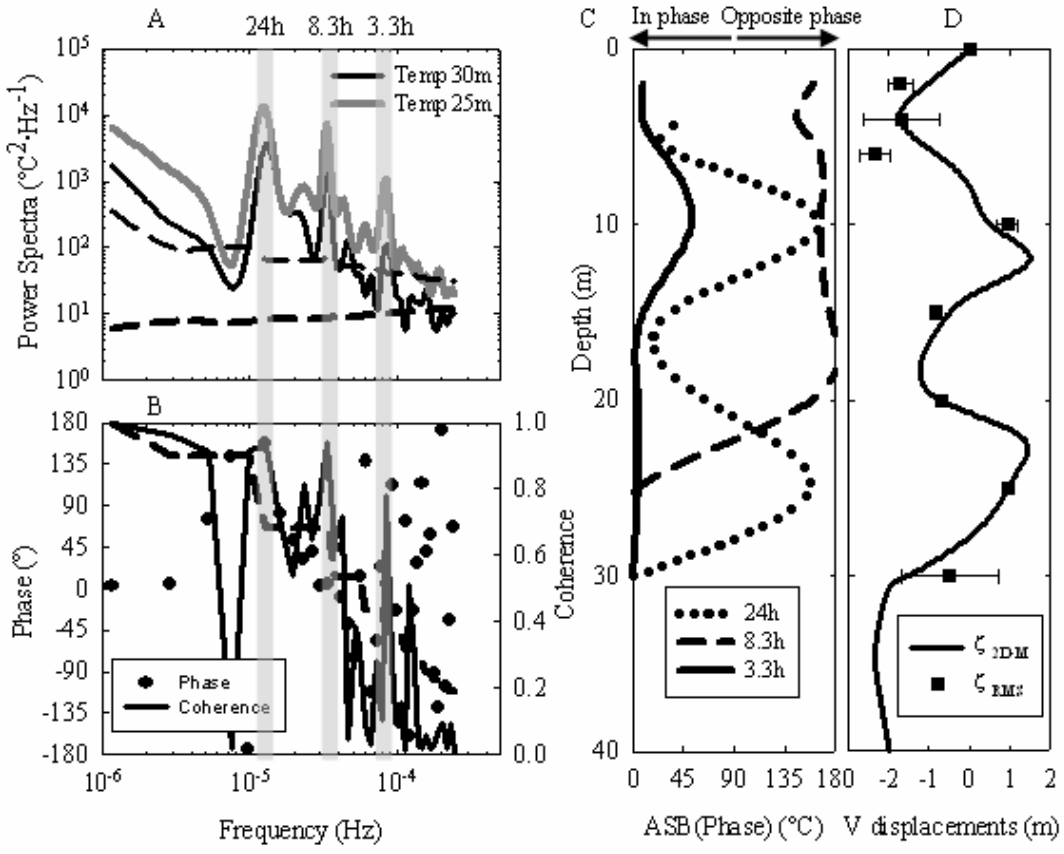

Figure 8. (A) Power spectra density for the temperature series from 195 to 205 (2005). (B) Coherence and phase spectra of Temperature at 25m Vs Temperature at 30m. Spectra have been smoothed in the frequency domain to improve confidence; dashed line shows confidence at the 95% level. (C) Phase in the water column of the main periods. (D) Vertical displacements computed with the 2D-Model ($\xi_{2D\text{-}M}$) Vs. Vertical displacements computed with the T-Chain (ξ_{RMS}).

The cross-spectrum of the temperature signals at 30 and 25 m are shown, as an example, in Fig. 8B. It shows that the signals at these two depths, for the 24h peak (Fig. 8A-B), are coherent (value close to one) exhibiting phases which are 180 degrees apart. Observed ξ_{RMS} values in Fig.8D with negative sign indicate displacements which are in phase with thermistor at 30 m and with positive sign displacements in opposite phase, based on the different phases found in the water column for the 24h period oscillation (Fig. 8C, dotted line). Figure 8D shows the comparison of the ξ_{RMS} versus the vertical envelope of the mode V5H1 computed with the 2D-model. The figure only shows the upper 40 m of the water column, for clarity in the presentation. Below 40m, no other vertical displacements were found. The vertical structure obtained with the model

agrees well with the vertical structure derived from the thermistors, especially in the shift of the vertical displacements. The largest differences between predictions and observations (in the magnitude) occur mainly in the surface, which might be the result of the direct influence of the wind forcing applied to the surface layers.

Non-diurnal oscillations - Apart from diurnal oscillations, wind events can also excite oscillatory motions at other frequencies. Peaks in the wavelet transforms, different to the 24h peaks, of the PE (Fig. 6B), are mainly in frequencies, which the eigenmodel (black lines) indicates corresponding to modes V1H1 and V2H1. The same cross-spectral analysis conducted from day 195 to 205 (see above) shows the presence of two additional peaks to the 24h one, at 8.3h and 3.3h in the thermistors at 30m and 25m (Figure 8A), with high coherence between them (Figure 8B). These peaks are also observables in the wavelets signals of the PE (Fig. 6B) in the same period of time. The study of the phases in the water column (Figure 8C) shows that the 3.3h oscillation correspond to a vertical mode 1, with the whole water column oscillating in phase, as showed by values close to 0º. Likewise, oscillation of 8.3h corresponds to the mode V2, with the first vertical displacement in the shallower layers up to 20m, oscillating in opposite phase with the deeper layers. These conclusions are further substantiated on the analysis done with the 2D-eigenmodel. The periods computed with the eigenmodel for the different modes and for the stratification existing in the lake on day 198 were: V1H1=3.4h, V2H1=8.3h, V3H1=13.4, V4H1=18.4, V5H1=22.9h and V6H1=27.4h.

Modes V2H1 and V1H1 appear throughout the study period. While mode V1H1 is more energetic than mode V2H1 in late spring, when stratification develops, mode V2H1 becomes more energetic than mode V1H1 later in the season. This is in agreement with the Wedderburn *W* and Lake number L_N calculations (see *Lake thermal structure* section), which suggests that mode V2H1 is probably excited by individual events. This is the case, even under periodic forcing; however, modes V2H1 and V1H1 are most energetic when the diurnal wind regime is disrupted by episodic events, when large northwesterly winds act on the lake surface (see Figs. 3 and 6). During those periods (see, for example days 108, 123, 129, 151, 187 or 198 in Fig. 6) modes of low vertical number (V1H1 and V2H1) are excited, and given their lower damping, in comparison with the higher vertical modes, they may become dominant in the system. Nevertheless the energy contend by such modes is much lower than the 24h oscillations under periodic wind forcing, commented in the previous section.

Wind forcing and internal wave field – The analysis shown in the previous sections suggest that (1) the reservoir exhibits a thick metalimnetic layer with temperature gradients of up to 0.5 ºC m-1; (2) internal waves are evidenced by the 30-min temperature records; (3) the vertical structure of the oscillations (vertical mode) changes as the stratification changes on seasonal time scales; the data reveal internal waves of up to mode V5; (4) the dominant mode of oscillation has in all cases the same

periodicity as the wind, i.e. 24h. This picture suggests that the reservoir behaves as a forced oscillator. A well known result in classical mechanics is that the amplitudes of the motions described by a forced harmonic oscillator depend on the energy of the forcing mechanism, the frequency of the forcing compared with the natural frequency of the oscillator, and their relative phase (see for example Wilson 1972). Those concepts are applicable to basin-scale internal waves as shown by Antenucci et al. (2000), given that isopycnal oscillations are forced by the wind. When the forcing frequency coincides with that of a given natural mode of oscillation of the system, resonance occurs and that mode becomes the dominant mode of oscillation. In Lake Beznar, the dominant mode of oscillation is selected from the spectrum of possible modes by the wind forcing, which during most of the time has a strong diurnal periodicity and predominantly from the east. Our observations agree with those of Munnich (1996) and Vidal et al. (2005), where a V2H1 and V3H1 modes become dominant modes due to resonance with diurnal wind regimes. Other examples of resonant internal wave modes are given, for example by Antenucci et al (2000) and Hodges et al (2000) in Lake Kinneret, where a V1H1 Kelvin mode (affected by the Earth's rotation) with the same 24h period as the wind forcing, becomes the dominant feature in the wave field; the seasonal evolution of the wind/internal wave field of the dominant modes was also described by Antenucci and Imberger (2003). Antenucci et al. (2000) presented, as well, an analytical model of the response of a two-layer rectangular basin undergoing internal oscillations, with the wind forcing applied impulsively. In that model, the wind amplifies the signal when a zero relative phase exists. At zero phase, the impulsive force is applied as the wave passes through zero from trough to crest and the wind energizes the internal wave. A relative phase of half the period of the internal wave, though, results in cancellation of the internal wave energy. Accordingly, we hypothesize that the strong and episodic northwesterly winds, acting out of phase with the dominant 24h oscillations (driven by diurnal easterly sea breezes), drains energy from them and energize V1 and V2 modes, instead.

Here, the role played by the wind field, in exciting and weaking the different modes of oscillation in the Lake Beznar, is examined by the means of numerical experiments in which the water motions are simulated with a three-dimensional model. In these simulations it is presumed that inflows and outflows are negligible and do not have any effect on either stratification or the internal wave field. This assumption is deemed appropriate given the short length of the simulations conducted and the fact that outflows did not undergo changes during the period of simulations. The ELCOM model, constructed with a grid with 40 x 40 x 1 m uniform cells, was first validated, by comparing the temperature predictions against the observations collected in the lake during a period of 10 days starting on day 188, 2005. For the validation exercise the model was initialized using horizontal isotherms and zero velocities, and forced using observed meteorological variables. The initial temperature profile was constructed from temperature records collected on the first day of the validation period; this profile is the

same as provided to the eigenmodel, whose results are shown in Fig. 8D. Figure 9A compares temperature observations and simulations at different depths for the validation run. The *L1* and *L2* norms calculated from observed and simulated temperatures, from 5 days of simulation after 2 days of warm up, and using the thermistors deployed at 4, 6, 10, 15, 20, 25 and 30 m, are 0.0152 and 0.0139. Such value is almost one order lower than the values reported by Hodges et al. (2000) for the simulations of internal waves in Lake Kineret.

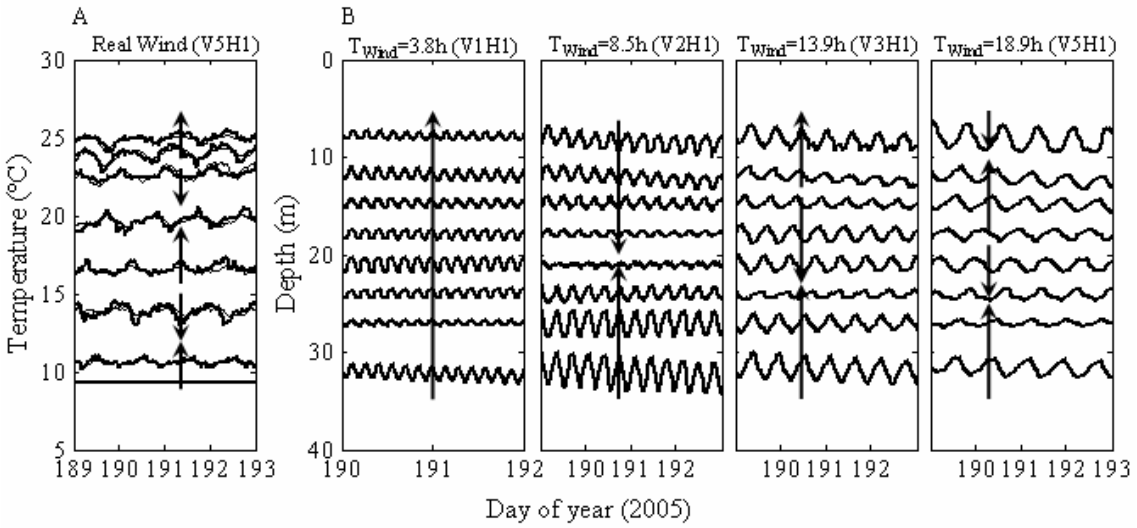

Figure 9. (A) Temperature evolution comparison of Thermistors (thick line) Vs ELCOM (thin line) at 4, 6, 10, 15, 20, 25, 30 and 50m depth. (B) Evolution of vertical displacement of selected isotherms as response to periodic winds of 3.8h, 8.5h, 13.9h and 18.9h, as computed with ELCOM. Arrows in (A) and (B) shows the number of vertical displacements.

The results of these experiments also showed that the assumptions made throughout this manuscript (i.e. unimportance of rotational effects and/or the nature of the oscillations in the horizontal which are presumed to be of mode 1) are correct. Figure 10A shows, for example, the structure of the velocity field along the thalweg, which agrees with the structure of a V5H1 internal wave. These same results are obtained by setting the Coriolis parameter to zero, supporting our neglecting rotational effects. Additionally, figure 10B shows the longitudinal structure of the mode V5H1 obtained with the 2D-model.

Once validated, the model was used to conduct experiments in which the lake is forced by synthetic wind time series of sinusoidal form. The heat fluxes are neglected in this series of simulations. The amplitude of the wind forcing was set to $6 m \cdot s^{-1}$, the average maximum speed observed in the reservoir. Its frequency ω was varied and selected from the range of frequencies predicted by the eigenmodel for the natural modes of oscillation on day 188 (see Table 1). The forcing periods tested are 3.8, 8.5, 13.9 and 18.9 h, corresponding to modes V1H1, V2H1, V3H1 and V4H1, respectively. The estimated period of the V5H1 mode is 23h, and this mode was selected as the

dominant mode of oscillation with winds of diurnal periodicity (Fig. 9A). The vertical response of the reservoir to the different forcing periods is shown in Fig. 9B. The dominant oscillation mode is V1H1 when forced using a wind period of 3.8h, V2H1 when forced at 8.5h, V3H1 in response to 13.9h forcing and, finally, and V4H1 in response to the 18.9h forcing. This series of experiments suggest that the dominance of higher vertical modes (up to mode V5) in the internal wave field in Beznar is the result of resonance.

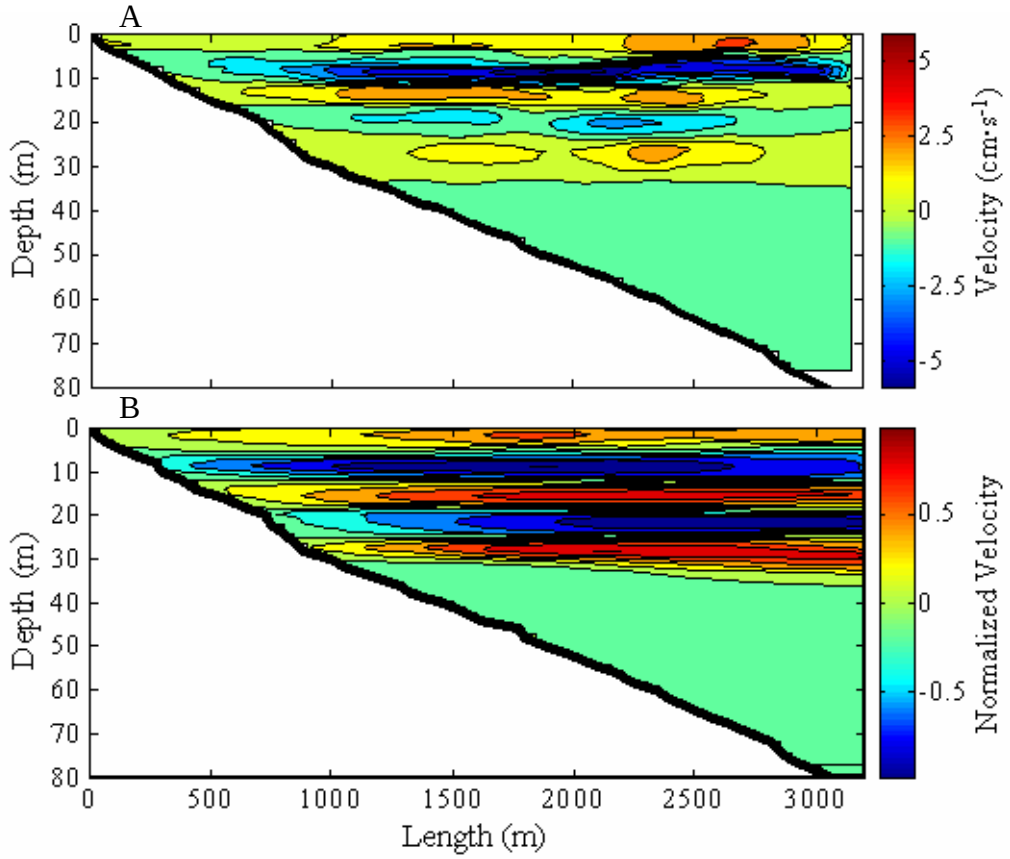

Figure 10. (A) Velocity longitudinal structure obtained with ELCOM on day 190.3, with positive values towards the dam. (B) Velocity longitudinal structure of the V5H1 mode obtained with the 2d-model.

Conclusions

There are several factors controlling the internal wave field in an aquatic system like stratification, morphology, forcing agent, etc.; that, in general, favor the presence of lower modes versus high vertical modes, with higher damping. In Lake Beznar and, in general, in deep Mediterranean reservoirs with large heat fluxes and deep submerged withdrawal structures draining large volumes of water (see Casamitjana et al. 2003), the thermal structure is characterized by deep metalimnetic layers, where stratification is nearly continuous (linear). In these types of systems (continuously stratified), the spectrum of internal oscillations is dense (Munnich 1996) and, a priori, any forcing frequency can lead to resonance in the seiching phenomena. That was the case of Lake

Beznar where the resonance with the strong daily periodicity lead to high vertical modes, from V3H1 to V5H1 as the stratification developed, to become dominants in the system. The presence of high vertical modes have been seldom described in the literature and have been consider rare in natural systems due to its high levels of damping. However the present study, together with the results obtained in Chapters 1 and 2 for Sau reservoir and the results of Pérez-Losada et al (2003) for Boadella reservoir, shows that the presence of high vertical modes is not such a rare feature in medium size Mediterranean reservoirs with thick metalimnions, where the wind periodicity plays a fundamental role in the excitation of the dominant modes. Beznar reservoir becomes then as a multimodal forced oscillator, where modes close to the forcing frequency are amplified and set to the forcing frequency. At the same time, lower modes in their natural frequency, like V1H1 and V2H1, can be excited by wind events, being especially important when the periodicity of the wind disrupts, due to its lower levels of damping and to be easily excited respect higher modes in absence of resonance. Nevertheless, such modes are much less energetic than resonant ones. All together, makes the internal wave field in Beznar (and in general, in Mediterranean reservoirs) quite complex, where different modes are excited as the stratification develops and as a function of the wind; that was the case of the year 2005 where up to five different vertical modes were described along the stratifying season.

CHAPTER 4

The role of basin-scale internal waves in phytoplankton distribution in Sau Reservoir

*** Extracted from**: Serra, T., Vidal, J., Casamitjana, X., Soler, M. and J. Colomer. The role of surface vertical mixing in phytoplankton distribution in a stratified reservoir. Limnol. Oceanogr. *In press.*

Abstract

We investigated the effect of basin-scale internal waves for the transport of phytoplankton cells in the water column by carrying out two daily surveys during the stratified period of the Sau reservoir. Green algae, diatoms, and cryptophyceae were the dominant phytoplankton communities during the surveys carried out in the middle (July) and end (September) of the stratified period. We show that a system with a linear stratification and which is subject to weak surface forcing, allows the formation of thin phytoplankton layers. Such layers are influenced by the pass of basin-scale internal waves, that, together with the wind-driven currents, produce vertical migrations and horizontal transport of the phytoplankton cells. At the same time, during the night such layers mix due to the cooling convection, while during the day the populations concentrate at certain depths following their requirements of light and nutrients and buoyancy.

Introduction

Many of the biological processes are closely linked with external physical forcing such as wind stress, cooling and heating rates or seiching. Transport processes like advection and vertical convective mixing determine the paths of suspended particles in aquatic ecosystems such as lakes, reservoirs, coastal areas and oceans (MacIntyre et al., 2002; Serra et al., 2003). Convection together with shear stress play a fundamental role in the vertical mixing in the water column and in the formation of the

diurnal mixing layer (Imberger, 1985). The wind-driven currents, on the other hand, play an important role in the advection and horizontal transport of particles. Internal waves or seiching may play a role in both vertical mixing -especially in the degeneration of internal waves (Boegman et al. 2005a, Boegman et al. 2005b)- and in the advection; besides, the vertical excursions of the suspended particles or phytoplankton produced by the pass of a basin-scale internal wave may change the light irradiance over them, affecting directly in their growth. Gaedke and Schimmele (1991) described the influence of internal seiches in the phytoplankton abundance at a fixed station.

Hedger et al. (2004) describe the effect of advection on the spatial distribution of two phytoplankton populations, one of dinoflagellates (*Ceratium hirundinella*) and another of cyanobacteria (*Microcystis spp.*). They find differences between the two populations which also depend on their light irradiance requirements. Experimental work was done with the aim of determining the effects of external forcing events on phytoplankton diversity (Rojo and Alvarez-Cobelas, 2001). Other studies have revealed the importance of the forcing time-scales in phytoplankton dynamics (Cloern, 1991). Simulation work with a phytoplankton model, PROTECH (phytoplankton responses to environmental change), showed that the frequency and intensity of the forcing events are the main factors affecting the diversity in the phytoplankton community of an environmental system (Elliot et al., 2001).

The time resolution used during the study has important implications on the observed dynamics. Despite the limited time resolution of most phytoplankton studies (Harris and Trimbee, 1986; Reynolds, 1990), it must be taken into account that many processes occur over periods shorter than one week. A decade of observations in the South San Francisco Bay demonstrated that phytoplankton biomass fluctuates in a timescale of days to weeks (Cloern, 1991). Recently, high-frequency sampling of surface picoplankton (with diameters below 3 μm) displayed 24-h periodicity in many biological variables (Jacquet et al., 1998). Spatial measurements are also crucial in order to understand the dynamics of thin phytoplankton layers, which are comprised of a large variety of organisms such as phytoplankton, zooplankton and marine snow, as well as marine viruses and bacteria. McManus et al. (2005) demonstrate the effect of both currents and internal waves on the thin zooplankton layers in a coastal system. Dekshenieks et al. (2001) evaluated the behaviour and occurrence of these layers depending on physical forces.

New submersible fluorimeters have been developed and tested (Beutler et al., 2002; Gregor and Marsalek, 2004) for estimating the total phytoplankton biomass by taking measurements of chlorophyll. These instruments have been found to be valuable for continuous sampling of phytoplankton species located in very thin layers. Leboulanger et al. (2002) used a submersible fluorometer for rapid monitoring of

freshwater cyanobacteria (*Planktothrix rubescens*) blooms. They found good agreement between the results from the fluoroprobe and the spectrofluorometric results obtained from measurements of samples harvested from the water column. Only some deviations were found in the surface layer (~ 5 m depth) where quenching of fluorescence due to high irradiance decreased the fluorescence yield.

In this study, the role of internal waves together with the vertical mixing processes and their role in the transport of phytoplankton is investigated during two different stratified periods. The suspended particles under study are the algae communities thriving in the epilimnetic layer of the water column. We pay special attention to whether the different algae communities show different behaviours or respond equally under the same physical forcing acting on the system.

Materials and Methods

In this study, carried out in Sau reservoir, the stations considered were S1, S2 and S3 (see Fig. 1). Fluorescence profiles of different phytoplankton communities were carried out using an in situ submersible five-channel fluorimeter (bbe Moldaenke) with a resolution of 0.05 μg L^{-1} and a measuring range of 0-200 μg L^{-1}. This probe determines four different communities (green algae, diatoms, cyanophyceae and cryptophyceae), which have been previously calibrated by the manufacturer by considering particular algae populations corresponding to each algae group. In addition, the depth was measured using a pressure sensor integrated into the probe and the temperature was measured with a sensor next to the transmission window (with a resolution of 0.01ºC and 5% accuracy). For a more detailed description of the fluoroprobe, see Beutler et al. (2002) and Gregor et al. (2005). Measurements of current velocity profiles were carried out with an acoustic Doppler profiler (RDI 600 kHz, Workhorse Sentinel). The ADCP was deployed on the water surface with the beams facing downwards. The ADCP was mounted on a swimming platform that was tied to the fixed buoy located in S2. As a result, we were not able to get information about the water surface velocity (i.e. from 0 to 3 m deep). Data from the ADCP were distributed in bins separated by 2 m. The sampling rate was set at 1 Hz with the raw data processed to obtain 7.5-min averaged data, with a standard deviation of 0.1 cm s^{-1}. All data was processed directly by the manufacturer software with bottom tracking to remove the ship's velocity from the measured velocity. The first depth bin was set at 3 m, and then data from a range of between 3 m and the bottom were processed. Continuous data from a moored thermistor string (Aanderaa Instruments) were also available. Temperature values had a range resolution of 0.03ºC and an accuracy of ±0.05 ºC. The thermistor string was deployed at station S2 (see Fig. 1) and composed of 11 thermistors placed at the following depths: 3, 4, 5, 6, 7, 8, 9, 11, 15, 16, and 17 m. The sampling period of the thermistor string was 10 minutes. From the meteorological station located near the dam of the reservoir the air temperature (T_a in ºC, with a resolution of 0.1ºC and an accuracy

of ±0.3ºC), the relative humidity (RH in %, with a resolution of 1% and an accuracy of ±3%), the short wave radiation (q in Wm^{-2}, with a resolution of 1 Wm^{-2} and an accuracy of ±5 Wm^{-2}) and the wind velocity (U in m s^{-1}, with a resolution of 0.1 m s^{-1} and an accuracy of ±0.3 m s^{-1}) were obtained with 1 minute frequency. Measurements of fluorescence were taken hourly during a 24-hour cycle at a fixed station (S2, Fig. 1) in the Sau reservoir. This study was carried out during two different stratified conditions of the water column. The first survey was in July 2003 and the second survey was in September of the same year. In July, the field campaign began at 16:00 h on the 23Jul and continued until 15:00 h on the 24Jul. In September, the field campaign went from 12:00 h on the 24Sept to 12:00 h on the 25Sept. For the survey carried out in September, measurements of fluorescence at larger time intervals (~ 4 hours) and at other stations (S1 and S3, see Fig. 1) were also taken. The ADCP measured velocity profiles at station S2 during the whole period in both surveys. In the September survey another ADCP with the same technical characteristics was available and was deployed at station S3 using the same procedure that was used at S2.

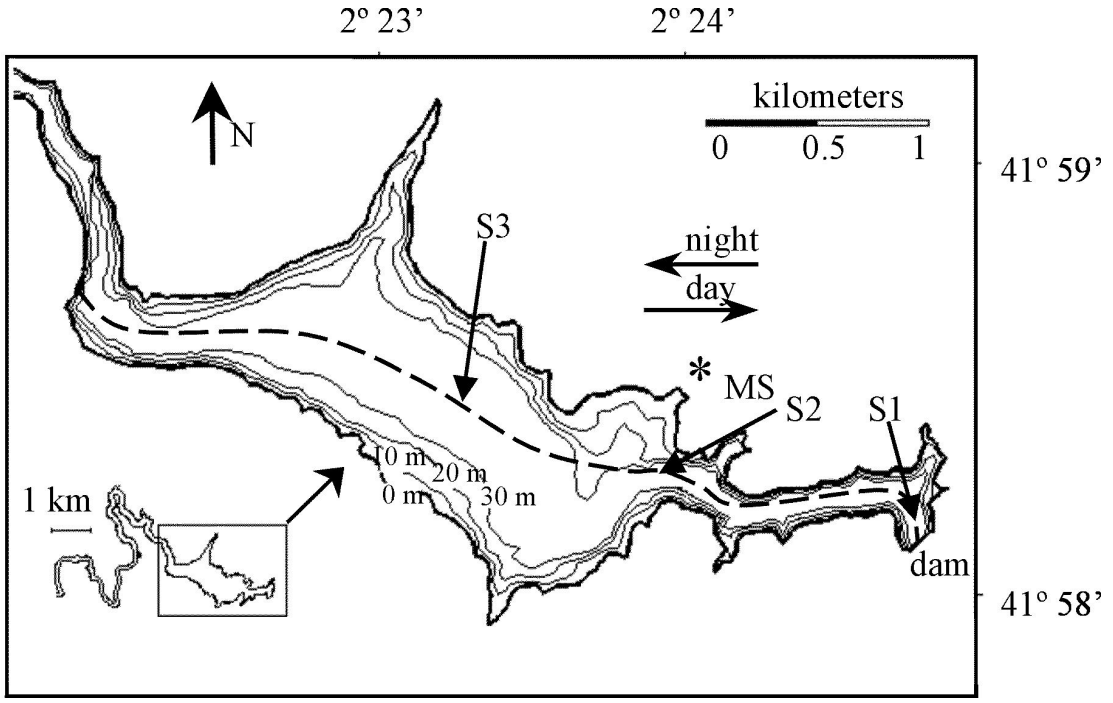

Figure 1. Bathymetric map of the Sau reservoir with the measured stations indicated as S1, S2, and S3. The dashed line represents the main axis of the reservoir and the direction in which the wind velocity and the water currents are projected. The meteorological station (MS) was located on shore.

Results

Meteorological data show differences between the July and September surveys. The air temperature and short wave radiation were higher in July than in September (Fig 2a and 2c Vs 2b and 2d). In July the reservoir was warming and stratifying and in September the reservoir was cooling with the epilimniun depth increasing. In both

periods the water surface was cooling during the night. Relative humidity shows a similar pattern in both surveys (Figures 2e and 2f): it was lowest during the morning and afternoon and reached a maximum of 100 % at night. The wind shows the usual 24h periodicity, with the wind blowing towards the dam in the morning, reversing in the evening, blowing towards the river, and remaining finally a weak breeze during the night (Figure 2g and 2h).

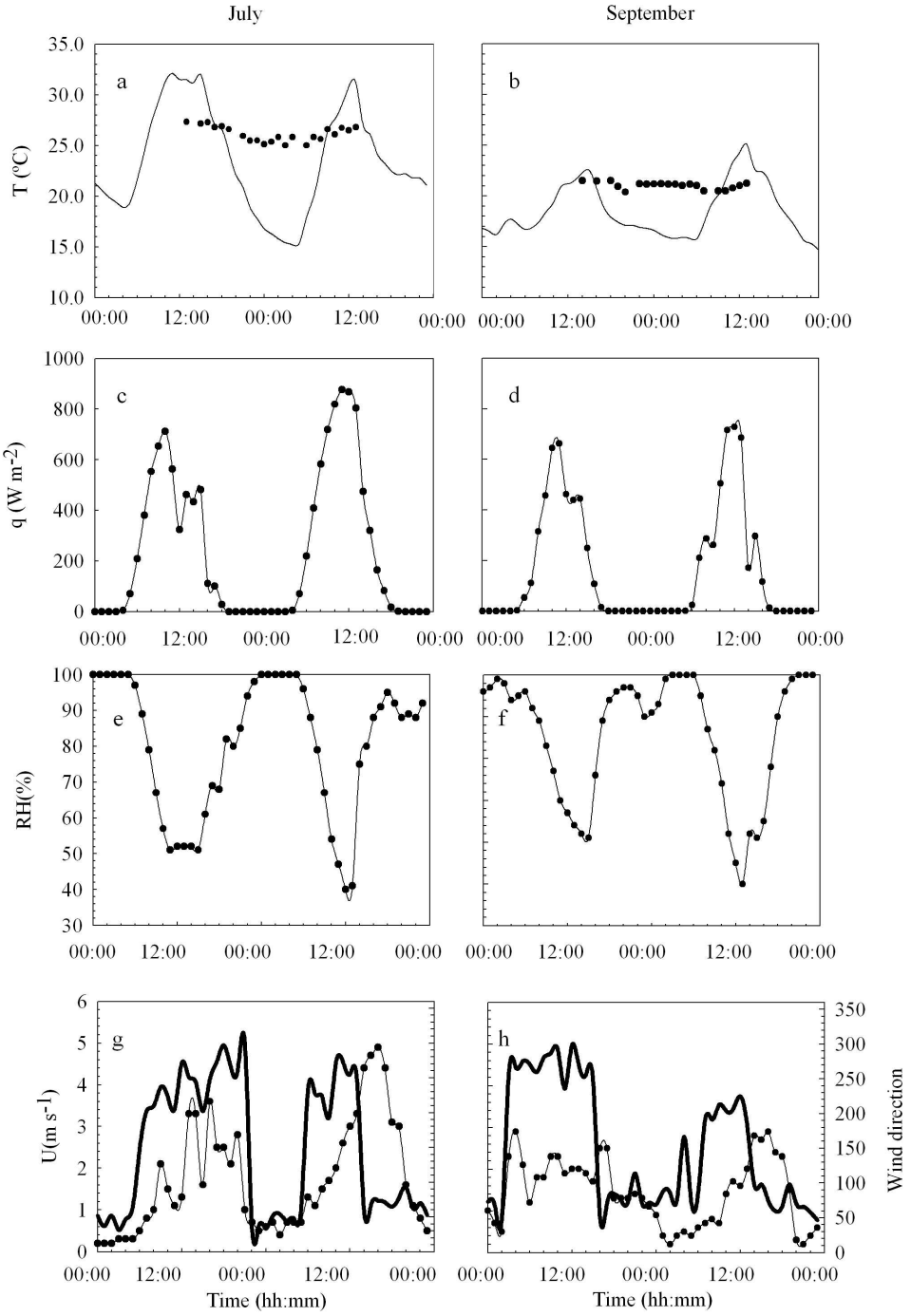

Figure 2. For the July and September surveys, (a, b) surface water temperature (circles) and air temperature (line), (c, d) short wave radiation, (e, f) relative humidity and (g, h) wind velocity (thin line) and wind direction (thick line).

System description

In July, the water column was stratified from the top of the water column downwards (Fig. 3a), which illustrates a shallow surface mixing layer at the top of the water column. The surface mixing layer increased from 1 m depth in the late afternoon to 4 m depth at night and early morning. During the day, a mixing layer 2 m deep was re-established again (see the profile taken at 11:00 h in Fig. 3a). Three different phytoplankton communities were found in the water column during both surveys (July and September): green algae, diatoms and cryptophyceae. In the July survey just a few exemplars of blue green algae were found, always in low concentrations (with values below 3 mg m^{-2}), integrated over the entire water column. Green algae were the most abundant and were found from the surface of the water column down to 10 m deep (Fig. 3b). Vertical profiles of green algae show a surface layer with a constant value of chlorophyll ranging from 6 to 12 μg L^{-1}. The depth of this layer changes with time attaining the deepest value (~ 4 m) at night (see 04:00 h profile, Fig. 3b). At sunrise, the layer shallows and reaches the shallowest depth at noon. Below this layer, the green algae population has a peak of maximum concentration located at a depth that varies with time. This maximum is ~5 m deep at 19:00 h after which it deepens to ~6 m and remains at this depth until the morning hours when the population forms a subsurface peak of 16 μg L^{-1} at a depth of ~2 m (see the profile taken at 11:00 h in Fig. 3b). Diatoms are distributed from the surface to a depth of 5 m (Fig. 3c). During the day diatoms form a subsurface peak at around 2 m deep while at night they are homogeneously distributed in a 4 m thick surface layer. Cryptophyceae show a pattern similar to diatoms (Figure 3d). During the day they form a subsurface peak of 4-6 μg L^{-1}, which is located at a depth of around 2 m (see the profile taken at 14:00 h in Fig. 3d). This pattern changes at night when vertical profiles of fluorescence show a constant value of 2 μg L^{-1} in a layer 4 m thick located at the surface of the water column.

In September, the temperature gradient is not as continuous as it is in July, and the temperature profile is close to a three-layer pattern: epilimnion, metalimnion and hypolimnion (Fig. 4a). It has to be pointed out that the hypolimnion is still slightly stratified, although it is not shown in Fig. 4a. The epilimnion, which extends from the surface to ~15 m depth, as in July, illustrated surface warming and nocturnal cooling with the most pronounced effects in the upper 5 m (Fig. 4a). In the September survey, green algae show similar behaviour to that found in July. At the surface of the water column there is a deep layer with a constant chlorophyll value from the beginning of the survey until sunset on the second day. This layer has a thickness of 3 m which increases to 5 m for night profiles (Fig. 4b). However, on the second day of the September survey, green algae form a subsurface peak at a shallow depth of 2 m (see the profile carried out at 12:00 h, Fig. 4b). Below this layer green algae form a second layer with approximately constant chlorophyll values. The bottom of this layer extends down to 12 m deep on the first day (see the 13:15 h profile, Fig. 4b) and shallows to 9 m depth on

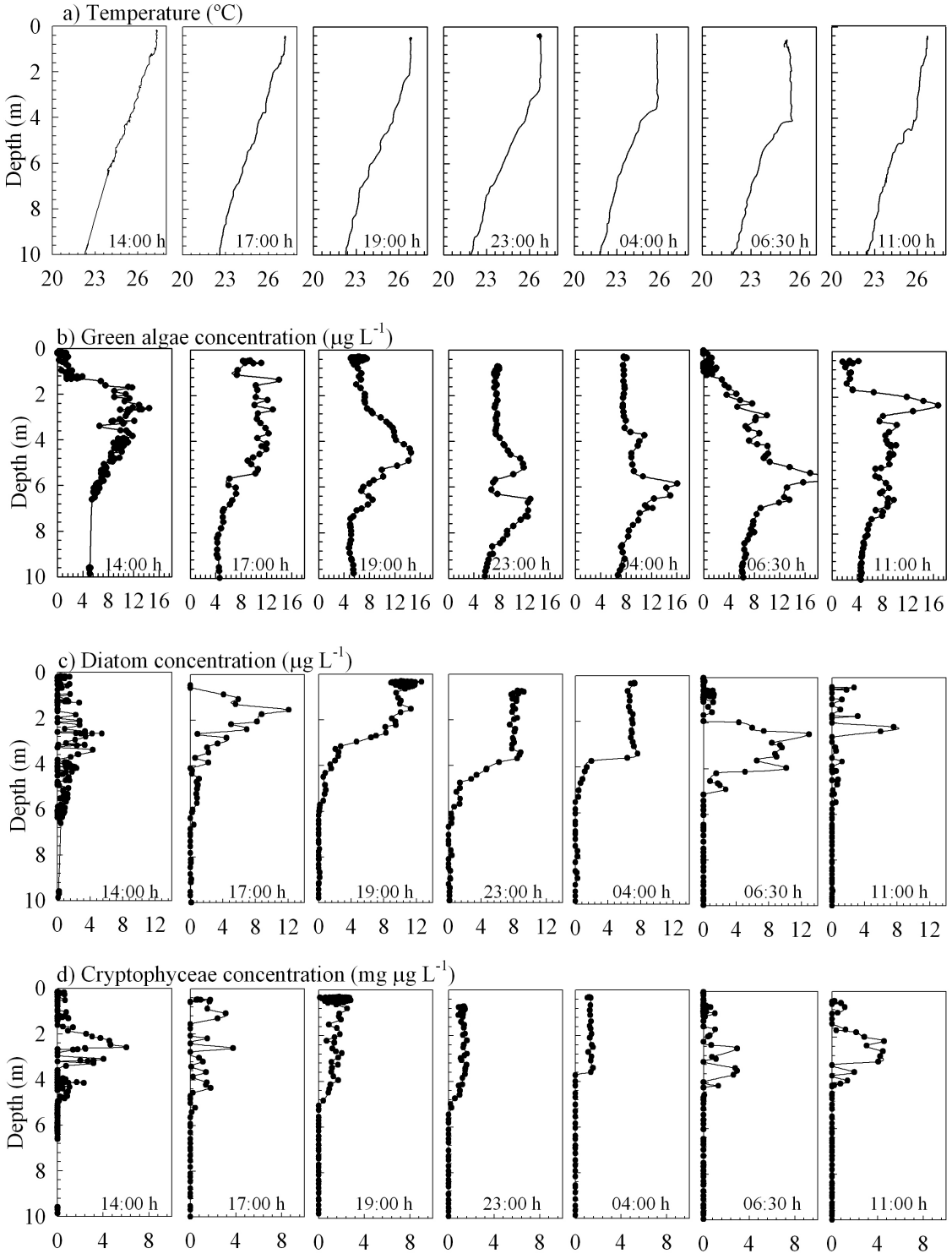

Figure 3. Selected profiles of (a) temperature, (b) green algae concentration, (c) diatom concentration and (d) cryptophyceae from the day-night survey carried out in July 2003.

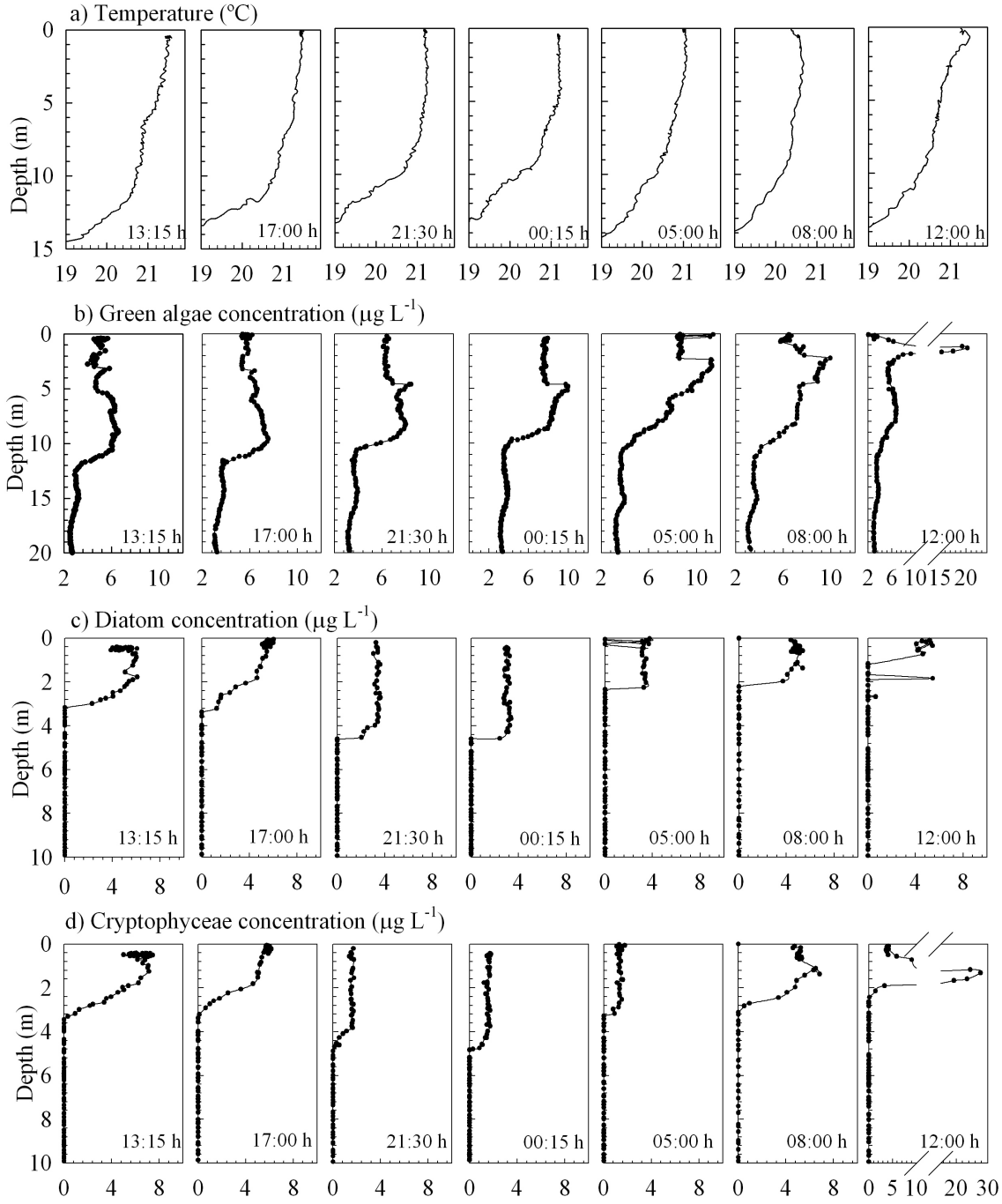

Figure 4. Selected profiles of (a) temperature, (b) green algae concentration, (c) diatom concentration, and (d) cryptophyceae from the day-night survey carried out in September 2003.

the second day (see the 12:00 h profile in Fig. 4b). In September, diatoms show a surface maximum decreasing slightly to 3 m depth for the daytime vertical profiles (Fig. 4c). For night profiles this pattern breaks down and diatoms distribute homogeneously throughout a surface layer that attains its deepest value at 4 m (see the profile carried out at 00:15 h in Fig. 4c). At sunrise this layer becomes shallower, reaching a thickness

of 2 m (see the profile carried out at 12:00 h in Fig. 4c). Cryptophyceae show similar behaviour to diatoms. During the daytime hours on the first day, they are at a maximum at the surface and decrease with depth down to 4 m (Fig. 4d). At night this pattern breaks down and they are homogeneously distributed (see the profile carried out at 00:15 h in Fig. 4d). On the second day, cryptophyceae move to a shallower depth and form a subsurface peak located at ~1 m depth (see the profile carried out at 12:00 h in Fig. 4d).

From the vertical profiles shown in Fig. 3 and 4 we can deduce that, in general, the phytoplankton populations are contained in thin layers. During the day the populations have the tendency to accumulate at a certain depths following their requirements (light mainly), coinciding with the formation of the diurnal mixed layer. Bormans et al. (1999) claim that changes in algal buoyancy appear to be mainly light dependent and not nutrient dependent. Meanwhile, during the night, the convective mixing due to cooling tend to mix vertically the community in the layer; showing, a homogeneous vertical distribution. Changes in size and in depth of the thin layers containing each phytoplankton community (green algae, diatoms and cryptophyceae) are influenced by the formation of the diurnal mixed layer, the daily night cooling and the pass of basin-scale internal waves. For the first two mechanisms the reader is referenced to the original paper of Serra et al. (*In Press*). Here we will focus in the effect of the internal waves together with the wind-driven currents.

The role of basin-scale internal waves

The internal wave field during the July survey had no dominant modes. A forced, 24-hour oscillation, especially in the first few meters, coexisted with a 12h oscillation. In September, however, a 24h oscillation was dominant; such oscillation corresponds to the V3 mode described in Chapter 1 which was for a period only two weeks before the present survey.

The oscillation in the flow velocity and the formation of layers due to the passage of internal waves is clearly shown in Figure 5, with positive values towards the dam. In particular, we focus on the shallower layers containing the phytoplankton populations (right-hand panels in Figs. 5a and 5b). In July, during the day, there is a layer at a depth of between 4 and 9 m which has negative velocity values in the range of -2 to -8 cm s^{-1}; this indicates that water flows from the dam to the main body of the reservoir, in the opposite direction of the wind. Unfortunately, the ADCP is not able to measure in the uppermost layer, but we can expect that the flow will follow the wind direction (Figure 5a). At night, this layer flows in the reverse direction, from the main body of the reservoir to the dam, also in the opposite direction of the wind, and has values of between 2 and 6 cm s^{-1} (Fig. 5a). In September, the depth of the maximum flow velocity became shallower, from 12 m deep at 20:00 h to 6 m at 07:00 h, and

remained at this depth flowing towards the dam until the end of the study period (Fig. 5b).

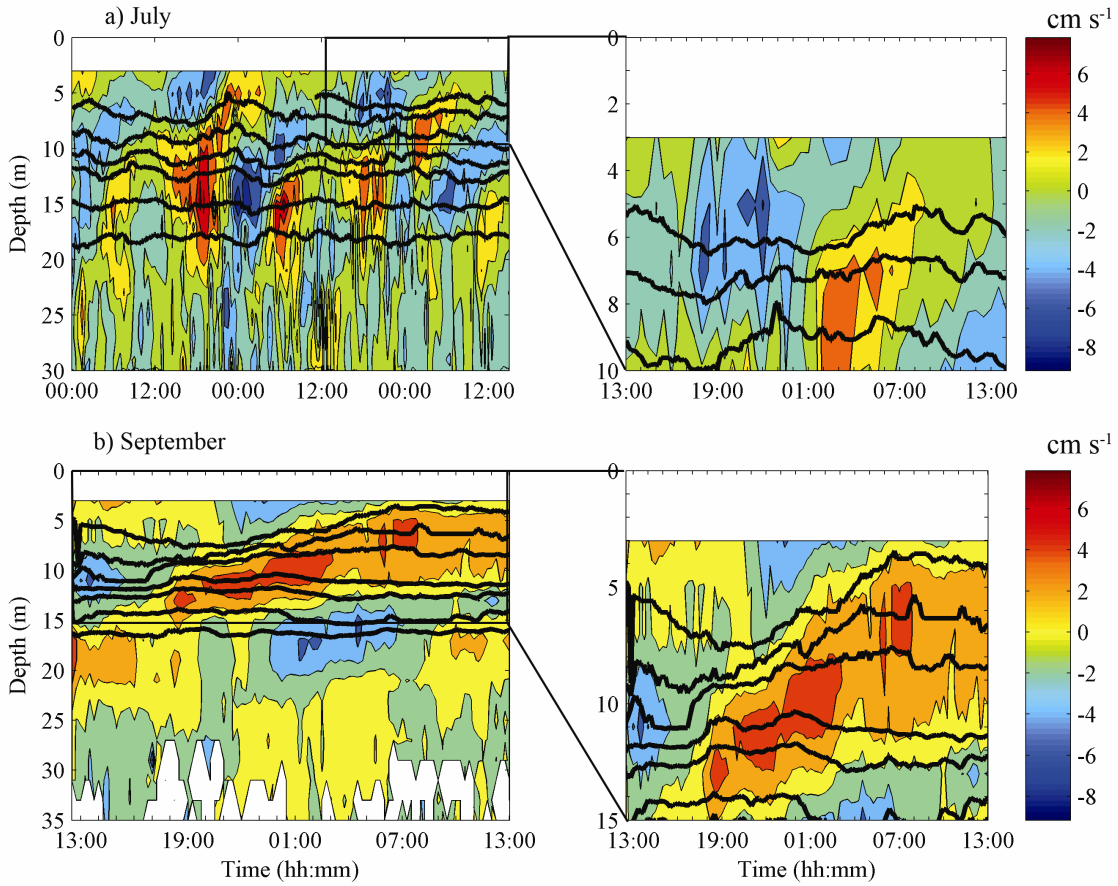

Figure 5. Velocity contours measured with the ADCP at S2 (see Fig. 1) for the (a) July and (b) September field surveys. Wind and velocity were projected following the main axis of the reservoir. The black lines represent the time evolution of some selected isotherms, from top to bottom, July: 25, 24, 23, 22, 21, 19, and 17°C; September: 21.4, 21.2, 21, 20, 19, 17, and 14°C.

Vertical displacements due to basin-scale internal waves (or seiches) are also clearly shown by the isotherms. Isotherms of 25, 24, 23, 22, 21, 19, and 17 ºC for the July survey and isotherms of 21.4, 21.2, 21, 20, 19, 17, and 14 ºC for the September survey show such oscillations (Figs. 5a and 5b respectively). Note that, especially in September at station (S2) in the east side of the reservoir, there are positive velocity values (toward the dam) in the upper layer and negative velocity values in the lower layer, which produced a deepening in the isotherms and vice versa, following the behaviour of the internal seiche. Figure 6, shows a sketch summarizing this behaviour.

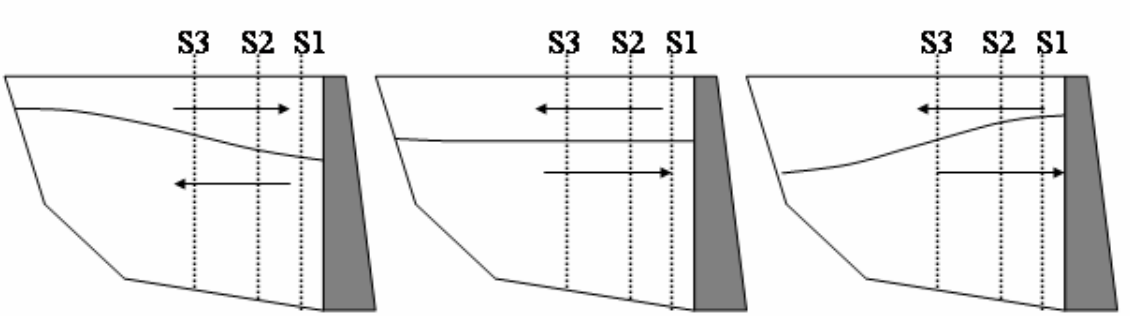

Figure 6. Sketch of the velocity field and vertical oscillation of isotherm evolution described in Fig. 5b for shallower layers, due to seiching.

It is evident that suspended matter, including phytoplankton will be affected by the vertical oscillations produced by the internal waves. This is especially evident during the September survey, when the mode V3, of 24h, was resonant with the wind forcing. Figure 7 shows the vertical evolution of the different populations (Fig 7b, 7c and 7d) in comparison with the velocity field and isotherms displacements (Fig 7a). Here it is clear that the bottom limit of the thin phytoplankton layers follow the isotherms displacements. The bottom limit of the layer containing diatoms (Fig. 7c) and cryptophyceae (Fig 7d) oscillate from 3m during the day (13:00h) to 5m at night (01:00h) and back to 3m the next day, following a similar pattern of behaviour to the 21.4 ºC isotherm (the uppermost isotherm), which is slightly deeper. This oscillation means that the shallow layer, containing these two populations, contracts and dilates with the passage of the seiches, modifying also the depth at which algae cells are located.

Green algae, (Fig. 7b), is also affected by seiches; however, the bottom limit of the green algae layer is deeper than the diatoms and cryptophyceae layer, or, in other words, the green algae layer is of a greater size. If we look at the layer containing the green algae, we see that the bottom limit follows the 21ºC isotherm (third isotherm from top). This bottom limit of the layer differs from the bottom limit of the diatoms and cryptophyceae shown above, and exhibits a different evolution. Here the bottom limit rises from 15:00h until 07:00h the following day and then decreases slightly until the end of the survey. The first interface of the V3 mode roughly corresponds to the 21.4ºC isotherm (uppermost isotherm), marked with velocities in one direction above it and velocities in the opposite direction below it. This means that green algae above the 21.4ºC isotherm will be transported to one side of the reservoir while the green algae below it will be transported to the opposite side.

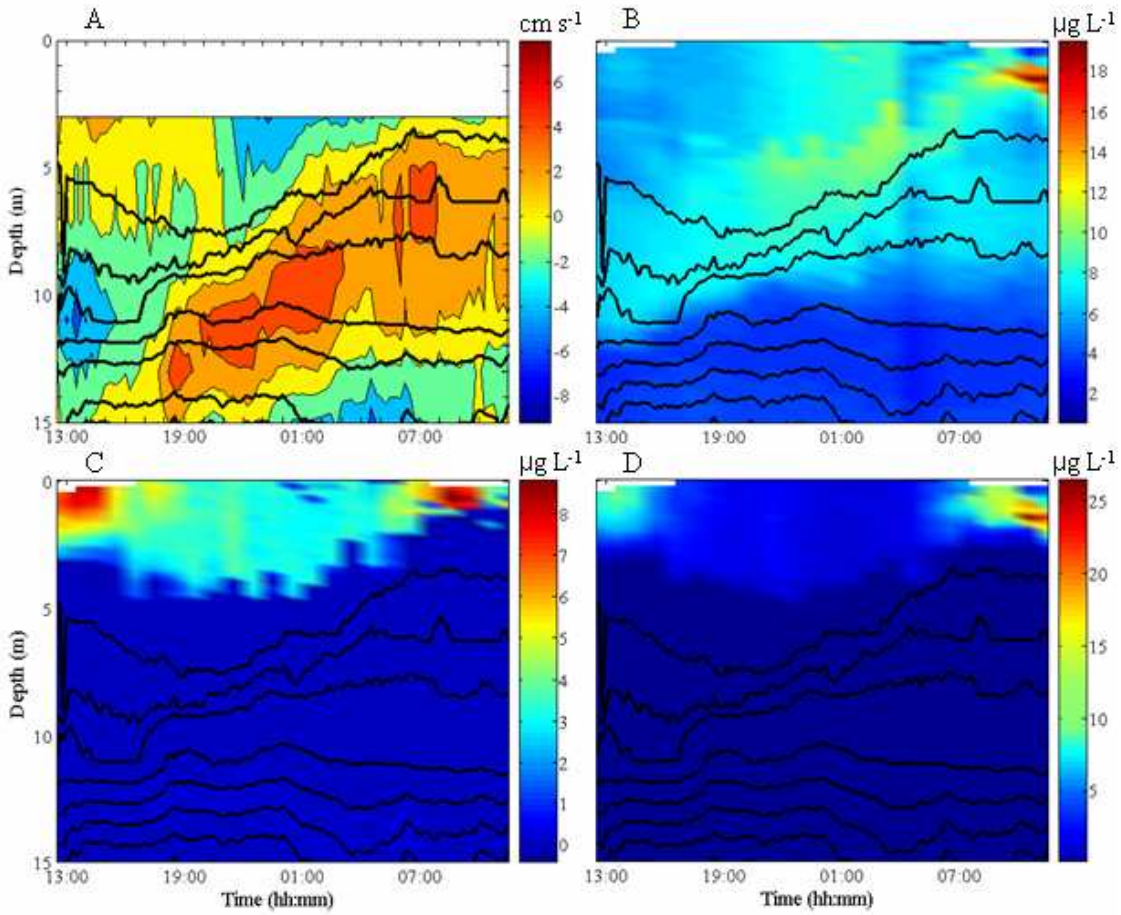

Figure 7. (a) Velocity contours measured with the ADCP at S2 (see Fig. 1) for the September field survey. Velocity was projected following the main axis of the reservoir. (b), (c) and (d) show the contours of the green algae, diatoms and cryptophyceae concentrations, respectively. Black lines represent the time evolution of some selected isotherms, from top to bottom, 21.4, 21.2, 21, 20, 19, 17, and 14°C.

In Figure 7 (as in Fig. 4) it is also clear that, during the day, the phytoplankton populations have a tendency to concentrate at certain depths, inside the thin layers, producing peaks of chlorophyll. This coincides with the formation of a weak stratification in the shallow layer, originated by the daily solar heating, so that algae can "keep" their position at certain depths. During the night, however, the layers are completely mixed due to convection and the vertical distribution of the populations is homogeneous.

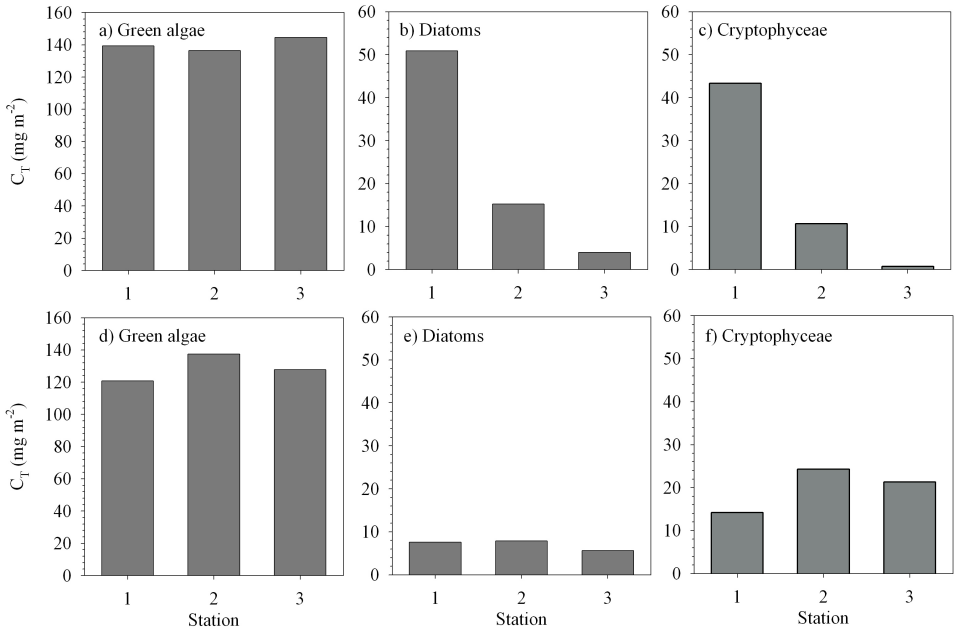

Figure 8. Total concentration of (a) green algae, (b) diatoms and (c) cryptophyceae at different measured stations on 24 September at 18:25 h, and total concentration of (d) green algae, (e) diatoms and (f) cryptophyceae at different measured stations on 25 September at 11:30.

The advection generated by the basin-scale internal waves, together with the wind driven currents, also plays an important role in the phytoplankton distribution. Integrated depth measurements of phytoplankton at the three stations in the reservoir (S1, S2 and S3, see Fig. 1) show differences in the horizontal distribution of each phytoplankton community (Fig. 8). These results may be due to the fact that there are sites along the reservoir with different phytoplankton growth rates due to different habitat conditions. It must be pointed out that this patchiness might be maintained by the spatial variability of heating during the day as well as by possible differences in the nutrient load at different stations of the reservoir. Also, the effect of the vertical transport produced by the internal waves on the variation in light intensity at which the populations are subjected may play an important role. Four more measurements carried out at these stations at different times showed similar results to the ones presented in Fig. 8. While green algae seem to have a nearly homogeneous distribution (Fig. 8a), horizontal heterogeneities are mainly observed for diatoms (Fig. 8b) and cryptophyceae (Fig. 8c). Spatial heterogeneities have been found previously by other authors such as Dickman et al. (1993), who reported spatial heterogeneities or patchiness of phytoplankton in a lake in northern Iceland; Einarsson et al. (2004), who reported spatial heterogeneities in the phytoplankton distribution in Lake Myvatn, and Cloern (1991), who reported horizontal heterogeneities in the South San Francisco Bay.

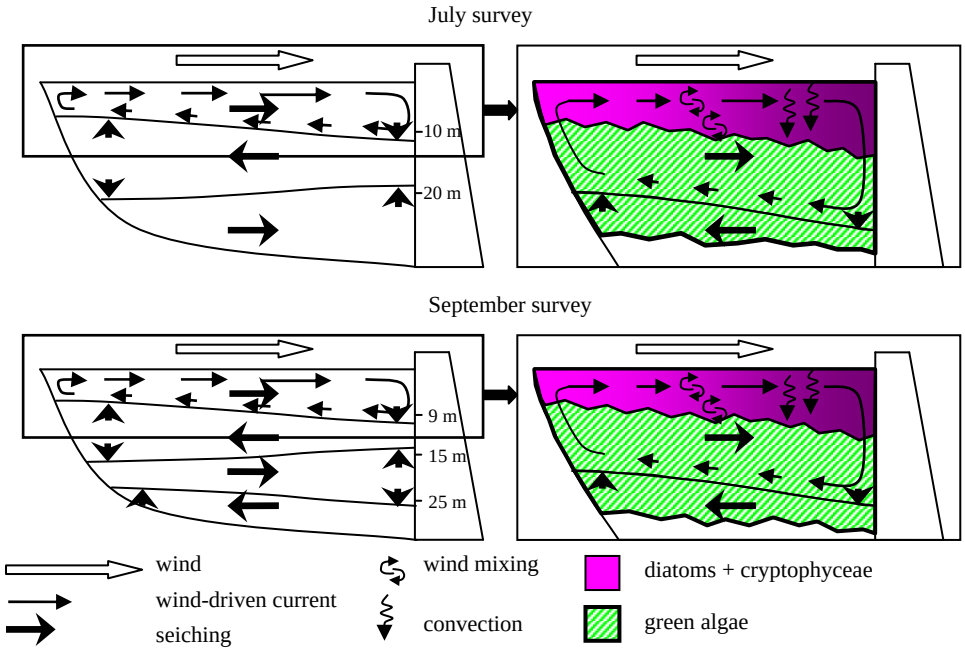

Figure 9. Schematic diagram of the seiching, the wind-driven current, the mixing due to wind and the surface cooling for both (a) July and (b) September surveys. The extension of green algae, diatoms and cryptophyceae is also indicated in the enlarged diagrams located in the right-hand panels of each figure.

In the Sau reservoir, however, one of the main reasons for the differences in algae distribution can be explained as follows: assuming that the surface layer (above the 21.4ºC isotherm) flows in the same direction as the wind then, during the day, the wind-driven current will transport the phytoplankton cells located within this layer downwind, i.e. towards the dam. This means that diatoms and cryptophyceae would accumulate at S1, which might account for the large concentrations of these populations found at station S1 compared to the concentrations found at S2 and S3 in the late afternoon (at 18:25 h, Figs. 8b and 8c). When the wind velocity is low and its direction reverses, the diatoms and cryptophyceae populations will be redistributed again, attaining similar concentration values at the different stations, as can be observed from the total concentration measured in the morning (11:30h, see Figs. 8e and 8f). In contrast, the integrated concentrations of green algae are quite constant through stations and time (Figs. 8a and 8d). Two reasons account for this pattern: first of all, green algae are homogeneously distributed in the reservoir; but secondly, green algae are distributed among the first two layers of the mode V3 (see Fig.9). This means that when the wind blows towards the dam, the green algae near the surface tend to accumulate near the dam, but the green algae under this layer will move in the opposite direction, i.e., towards the main body, contributing to a homogenization of the populations throughout the reservoir. Diatoms and cryptophyceae however, are only found in the first layer of the mode V3 (see Fig. 9), and are not affected by the reverse current moving towards the main body of the reservoir.

Conclusions

We can conclude by saying that, together with wind-induced turbulence, solar heating and night convection, the wind-driven currents and basin-scale internal waves will determine phytoplankton distribution in the water column in the reservoir from the surface down to deeper layers. It has been shown how the vertical oscillations produced by the internal waves produce a vertical oscillation of the populations, shifting their vertical position in the water column and therefore their exposure to the amount of available light. Also, the horizontal currents produced by the combined effect of wind-driven currents and internal waves transport the main kinds phytoplankton cells (green algae, diatoms, cryptophyceae) in different ways, producing the observed spatial and temporal heterogeneity and patchiness.

With this work, we also demonstrate the importance of considering both temporal and spatial measurements in order to describe the phytoplankton dynamics completely. Water management is usually based on a single monthly measurement at a fixed station. However, the heterogeneities observed here need to be taken into account.

CHAPTER 5

Dynamics of a river inflow into a reservoir. Consequences for the phytoplankton population.

Abstract

The dynamics of a river inflow into the Sau reservoir were investigated. During the final days of July, 2005, the daily variation of the river temperature caused the daily response to inflow change from overflow to interflow resulting in a highly dynamic system where mixing increased. Furthermore, during the overflow events, nutrients from the river were introduced into the surface of the reservoir and a bloom of cyanobacteria was clearly located in the mixing zone of these overflow events within the quiescent body of the reservoir. In this way, coupling between the physical and biological processes was seen to be enhanced. This event was also simulated using the ELCOM-CAEDYM model.

Introduction

River valley reservoirs, such as the Sau reservoir (Fig. 1), are often large and narrow, receiving water from a single river inflow. These reservoirs have important longitudinal changes controlled by the river intrusions across them (Hejzlar & Straskraba, 1989). Thus we can define reservoirs as hybrid systems between rivers and lakes (Margalef, 1983), with a progressive transformation from a river to a lake system, not only in the environmental variables but also in their morphology and hydrodynamics characteristics. In general, a reservoir can be divided along the longitudinal axis into three zones (Kimmel et al., 1990): the riverine zone, the transition zone and the lacustrine zone. The riverine zone is characterized by higher flow, short residence time, and high values of nutrients and suspended solids. The transition zone where the river meets the reservoir is characterized by high phytoplankton productivity, decreasing flow velocity, increased water residence and large sedimentation. Finally, the lacustrine zone consists of the area near the dam with longer residence time, lower available nutrients and lower suspended matter. The boundaries between the three zones are not well defined and can be highly variable, in response to inflow characteristics.

Sau is a canyon-shaped reservoir, 18.5 km long and up to 80m deep, situated in the central segment of the River Ter, which is 200 km long, and has its source in the Pyrenees, in the northeast of Spain. Because of its morphology, it can be divided into three hydrodynamic zones (Fig. 1). The hydrodynamics of the lacustrine zone are mainly dominated by the wind, which generates wind driven currents and internal waves (see Chapters 1 and 2). The riverine and transition zones, however, are narrow, meandering zones, sheltered from the wind; here, the hydrodynamic is mainly dominated by the river inflow.

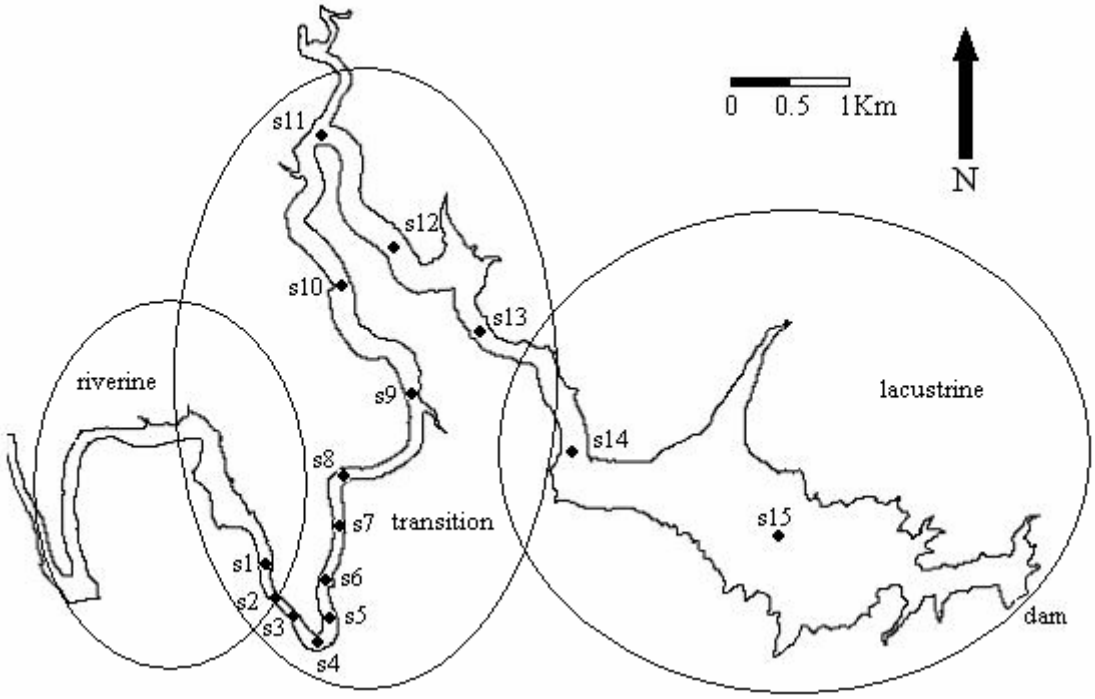

Figure 1- Situation of the measuring stations along the Sau Reservoir. The reservoir has been divided into riverine, transition and lacustrine zones.

The interaction of river inflows in aquatic systems is based on the density difference between the inflow and the main water body, which generates overflows, interflows or underflows. The interaction between the river and the aquatic system is important in determining the fate not only of nutrients or sediments, but also that of possible contaminants (Chung and Gu, 1998; Gu and Chung, 2003). Single water events have been widely studied and overflows (Csanady, 1984) interflows (Fischer, 1983) and underflows (Hebbert et al. 1979) have been described; likewise, entrainment and turbulence of such systems has also been determined (Dallimore et al. 2001, Baines 2001, Alavian (1986), among many others).

However, these events are not constant over time and inflow dynamics can change. Carmack et al. (1986) described the mechanisms influencing in the river inflow circulation and water mass distribution on both synoptic and seasonal scales. Seasonal

circulation of inflows in aquatic systems has also been reported by Carmack et al. (1979) and Pickrill and Irwin (1982); the latter also described variations in the inflow dynamics on short time scales together with the seasonal variations.

Armengol et al. (1999) studied the long term longitudinal processes associated with the river circulation in the Sau reservoir. In winter, the inflow temperature is lower than that of the reservoir resulting in an underflow. This deep flow continues until February, when the river temperature rises faster than the surface water of the reservoir, resulting in an overflow. From February to April-May, the surface flow corresponds to the start of the spring phytoplankton bloom due to the introduction of nutrients into the photic zone. The transition between spring and summer is characterized by an interflow that sinks progressively until mid November when it reaches the bottom as an underflow.

We will show in this paper that the hydrodynamics of the river inflow in the Sau reservoir is not only affected by seasonal variations, but also by synoptic variations. The quick response of the river temperature to daily and short term variations (days to weeks) make the river-reservoir interaction a highly dynamic system. Likewise, the fate and transport of the river-born incoming nutrients, and therefore the phytoplankton evolution, will depend on the inflow dynamics. During the survey period, algae blooms in zones with high nutrient concentration were found and these were related to the hydrodynamics of the river inflow. Therefore, our understanding of the coupling between the inflow physics and the biological processes was clearly enhanced.

Material and Methods

The survey was carried out between the 26th July to the 3rd August, 2005 (207-215 Julian day); during this period CTD profiles were taken from station s1 to s15 (see Figure 1) on days 207, 209, 210, 212 and 213. Also, on day 212, ADCP transects at stations s1 to s9, in a direction perpendicular to the river direction, were carried out (three at each station). A thermistor string and an ADCP were also deployed at station s6 during the survey. The thermistor string was composed of ten thermistors taking measurements every half meter between 0.5 m and 5 m, with a sampling interval of 2 minutes. The ADCP was deployed in the water surface with the beams facing downward with an interval rate of 10 min and a cell size of 20 cm. To obtain our data, we used a Seabird 19 plus CTD, coupled with a turbidimeter and a fluorimeter; a 600 kHz, RDI sentinel ADCP (set to high resolution mode 5 during the survey) and an AANDERAA Tr7 thermistor string. Finally water samples at stations s1 and s9 were taken during day 209 and chlorophyll and nutrients were measured in the laboratory using standard procedures. Meteorological data was supplied both from a nearby automatic meteorological station in the river Ter and from the station placed in the lacustrine part of the reservoir (Fig. 1). Finally, temperature, conductivity and nutrients

in the river were obtained from an automatic station located approximately 5 km upriver.

To compare field data with model simulations, the water quality model CAEDYM coupled with the 3D model ELCOM was used (see the introduction to this thesis for a detailed description of these models).

Results

The inflow dynamics is governed by the density difference between the river and the reservoir, while temperature is usually the main factor controlling density. The river temperature is highly dependent on the air temperature, quickly responding to short term variations in the latter (Fig. 2A). During the survey, the river inflow was around 2 to 3 m^3 s^{-1} (Fig. 2B) and the outflow, which was intermittent, was normally higher than the inflow so the water level was decreasing throughout the survey. The conductivity of the river (Fig. 2C), despite of showing pronounced peaks at different times during the survey, was always higher that the ambient reservoir conductivity, and then, it can be used as a tracer of the inflow. Phosphorous, is usually the limiting factor of the algal growth in Sau (Armengol et al. 1999) and is showed in figure 2D.

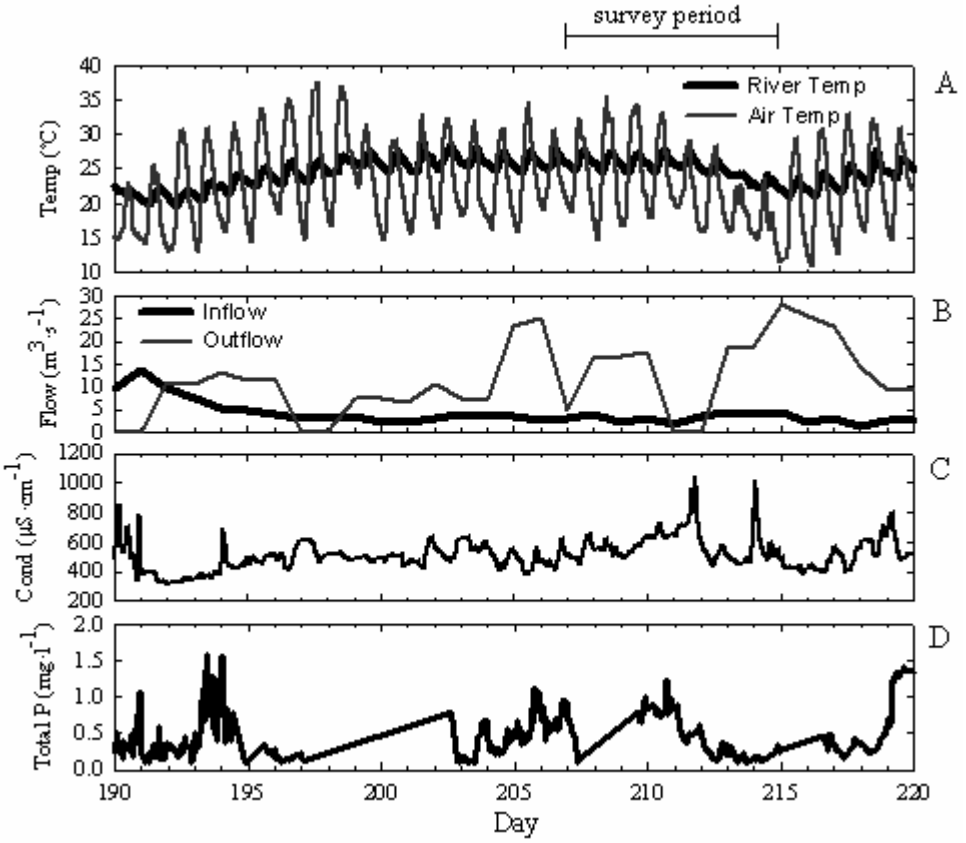

Figure 2- Evolution of (A) river temperature and air temperature from Julian day 190 (2005) till 220 (2005). (B): inflow and outflow. (C); river conductivity and (D): concentration of total phosphorus in the river.

Description of Dynamics

The last days of July 2005 were quite warm days, as can be seen in Fig 2A. The dynamics of the river inflow into the reservoir, were mainly influenced by the temperature variation, and therefore recording the influence of the meteorological variations on the inflow dynamics was straightforward. Fig. 2A shows that the response time of the river temperature to changes in air temperature is very short and occurs at different time scales, from daily to longer periods. Also, as the response of the river temperature is faster than the ambient reservoir water, the river insertion into the reservoir alternated between overflow and interflow. As the day went on, the river became warmer, eventually reaching temperatures similar to those of the surface water of the reservoir, thus generating an overflow in the afternoon and early in the night. However, during the night, the river became colder than the water surface and eventually, late in the night and morning an underflow intruding at a depth of between 6 and 7 metres occurred.

During the survey, the intersection of the river with the reservoir, where the plunge point occurred, was located between stations s2 and s3 (Fig. 1). The dynamics of the inflow can be observed by looking at the data from the ADCP and the temperature string, deployed at station s6 (Fig. 3). Figure 3A shows the velocity profiles during Julian days 208 - 210, where positive values indicate that the river flowed towards the dam. Here it is clear how the inflow changes from an underflow to an overflow with positive velocity values as the inflow moves from the bottom to the surface. Black lines in Figures 3A and 3B show the central position of the inflow, as estimated from the ADCP measurements. During the underflow episodes, cold dense water from the river goes into the warmer water of the reservoir; and during the overflow episodes, warm water from the river displaces the surface water of the reservoir, as shown in Figure 3B. In both processes, an upstream current is generated and water from the reservoir is entrained in the inflow, especially at the plunge point where the mixing is greater. That is, during the overflow events, cold water from lower layers travelled upstream (negative values in Fig. 3a) and during the underflow events, water from the surface of the reservoir travelled upstream. At station s6, the water column stratified during overflow and underflow events and the stratification decreases during the transition of such events (Fig. 3b). In Figures 3D to 3F, a schematic representation of these events is presented. Note that the time delay between an overflow (Fig. 3D) and an underflow (Fig. 3E) is 12h, and that the underflow became an interflow when it separated from the bottom. Finally, Figure 3F shows the transition between overflow and underflow.

The CTD measurements, together with the ADCP measurements carried out during the morning of 31 Jul 05 (Julian day 212) when an interflow situation occurred, are presented in Fig. 4 Unfortunately, we do not have measurements in the afternoons and nights, when overflows occurred and therefore no further comparison can be made.

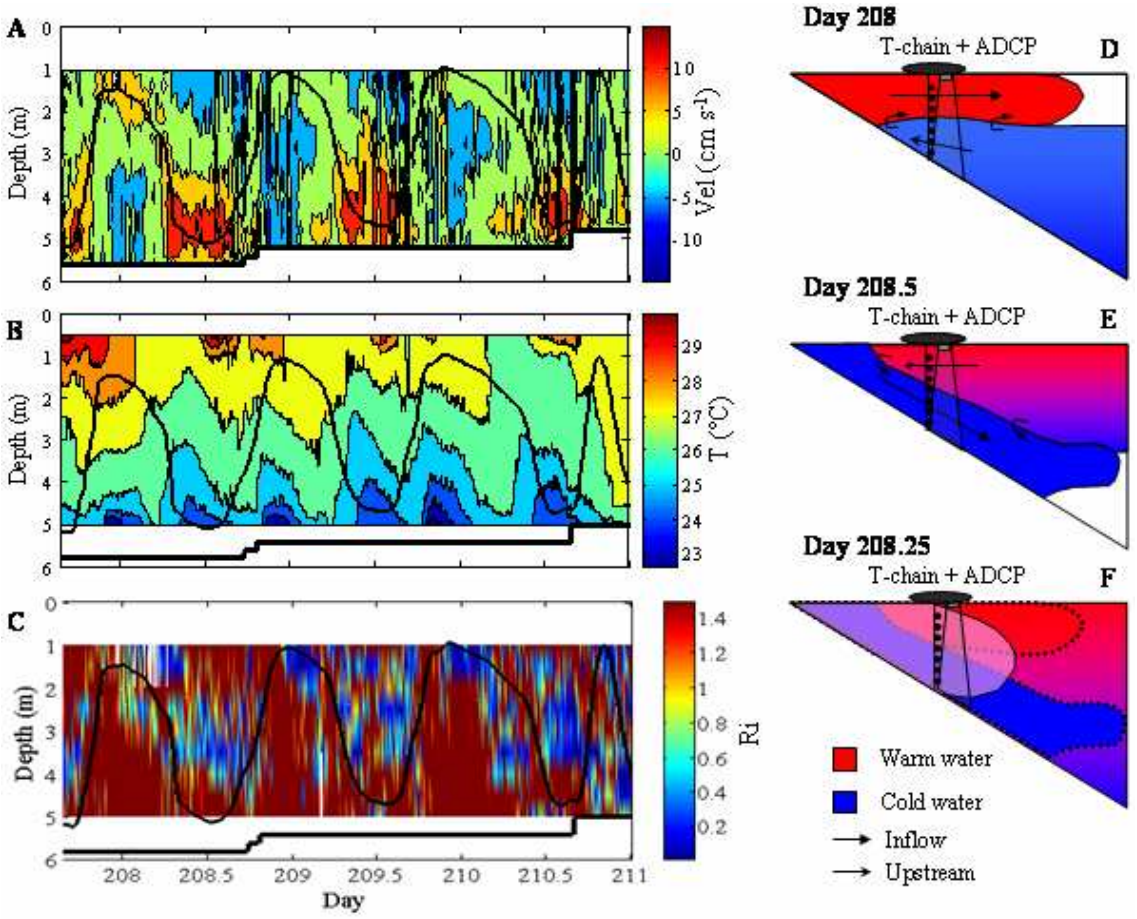

Figure 3-(A) Evolution of the temperature column at stations s6. (B) Evolution of the velocity in the water column at station 6. (C) Evolution of the gradient Richardson number at station 6. Black line indicates approximately the central position of the inflow. (D), (E) and (F) represent the overflow, interflow and transition events occurring at day 209, 209.5 and 209.25 respectively.

Based on the velocity profiles, represented by the arrows in Figure 4, the inflow evolution can be represented (see the green contours in the figure). When the interflow occurred, the temperature of the river was lower than the ambient surface temperature and the inflow plunged at about 1000m from station s1 (Fig. 4A). Then, the inflow behaved as an underflow until at aprox. 6m depth and 3000 m length, it reached the insertion point. High values of turbidity (Fig 4B), are associated with resuspension due to the presence of the underflow; however, after insertion, sedimentation took place and turbidity decreases. Inflow conductivity (Fig 4C), despite being quite variable, is higher than the conductivity of the reservoir water and can therefore be used as a natural tracer High conductivity values in the bottom can be attributed to the inflow, however, the high conductivity values occurring at the surface in layers up to ≈ 3000m long, surely correspond to past overflow events that have been injecting inflowing water into the surface. The Chlorophyll-a values (Fig. 4D) are characterized by two main peaks. The first one is clearly located in the plunge zone where the river converges with the ambient water and the accumulation of matter from the ambient water, including

phytoplankton, is expected. Part of this Chlorophyll entrains into the inflow and is dragged to the bottom, as can be seen in Fig. 4D. The second, higher peak, with values of more than 100 mg/m3, is located at around 3000-3500m distance coinciding with the head of the overflow events. This peak will be explained in detail in the *biological consequences* section (below).

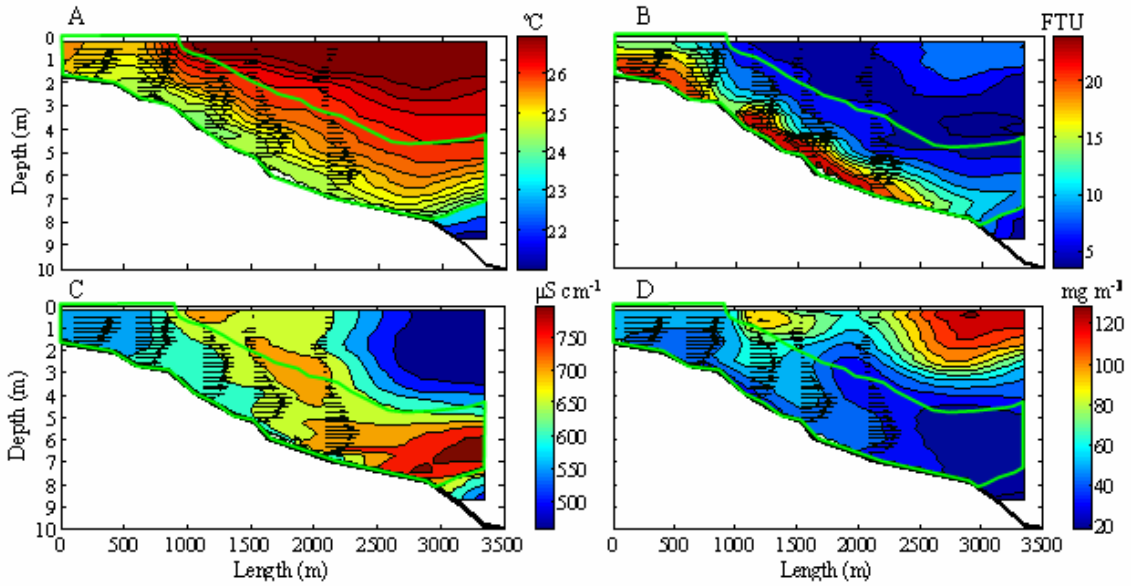

Figure 4. Longitudinal contours following the thalweg during day 212 of (A) Temperature, (B) Turbidity, (C) Conductivity and (D) Chlorophyll. Black arrows show velocity profiles while green contour shows the estimated interflow position.

Interaction between the river and the internal waves

As the internal waves described in Chapter 2 are excited by the wind in the lacustrine zone and penetrate the meandering and sheltered zone, a possible relationship between the seiching and inflow phenomena can be speculated. The cold water, (below 23ºC) reaching the bottom thermistors at s6 (Fig.3B), during the overflow events, seems most probably to originate from the internal waves, because the overflow-induced upstream current (Fig. 3D) could not account for the entrainment of such a cold water in the deepest layers.

In the lacustrine area, internal waves are produced by the daily wind forcing (see Chapter 2), but in the riverine and transition zones, which are sheltered from the wind, the inflow itself can also generate an internal wave following the mechanism explained in Fig. 5. In the morning, the momentum of the incoming underflow pushes down the ambient water generating a tilting in the ambient water isopycnals (Fig. 5A). When the underflow begins to change to an overflow, buoyancy forces will tend to restore the tilted isotherm to the horizontal position (Fig. 5B); moreover, inertial forces can make the tilting go further, producing the situation shown in Fig. 5C. This process can

promote a 24h period internal wave, that can be coupled with the 24h internal wave generated in the lacustrine area. This is also outlined in Fig. 5.

As explained in Chapter 2, during the morning, in the lacustrine area, the wind blows towards the dam while riverine and transition zones are sheltered. This generates the tilting of the isotherms in the lacustrine zone and also in the sheltered zone (Fig 5A). Note that, ahead the insertion, the tilting of these isotherms produced by the two mechanisms mentioned above, can be appreciated in Fig 4A. In the afternoon, the direction of the wind changes, inducing an H2 basin-scale internal wave because the wave has two horizontal nodes. Although the main agent in the generation of the internal wave is the wind, more research would be necessary to examine the contribution of the inflow to the wave.

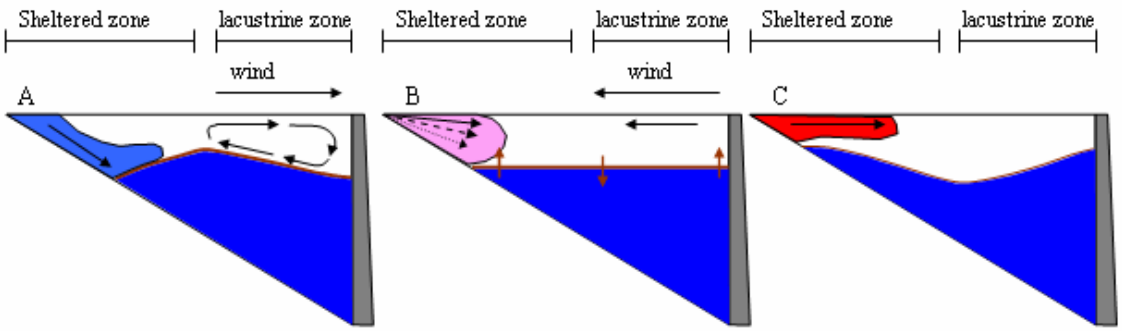

Figure 5. Schematic representation of the internal wave produced during the (A) morning, (B) afternoon and (C) night. Black arrows shows water and air movement, while brown arrows shows seiching movement.

Up to now, we have seen that, during the last days of July, the inflow dynamics were highly variable. Now, we will look at the physical and biological consequences of this variability.

Physical consequences

Having a better understanding of how the inflow mixes with and merges into the reservoir is crucial in understanding how nutrients or any possible contaminants will be distributed or diluted throughout the reservoir. In recent years, a great deal of effort has gone into determining the inflow entrainment coefficients (Dallimore 2001, Hebbert et al. 1979, Ellison & Turner 1959, Atkinson 1988). In the case of the Sau reservoir, however, the highly variable inflow, with the daily variation from overflow to interflow, makes it quite difficult to determine such coefficients. One way to estimate the entrainment coefficients is to measure the dilution of natural tracers, such as conductivity. In our case, this is quite difficult because mixing will depend not only on the difference between the inflow and the ambient quiescent water, but also on the difference between the inflow and the water from the preceding inflow event. For

example, the entrained water during an underflow event comes also from the preceding overflow event and therefore the tracer concentration is directly affected by the previous inflows. Nevertheless, using the data collected during our survey, we can get some idea of what is going on during the mixing process.

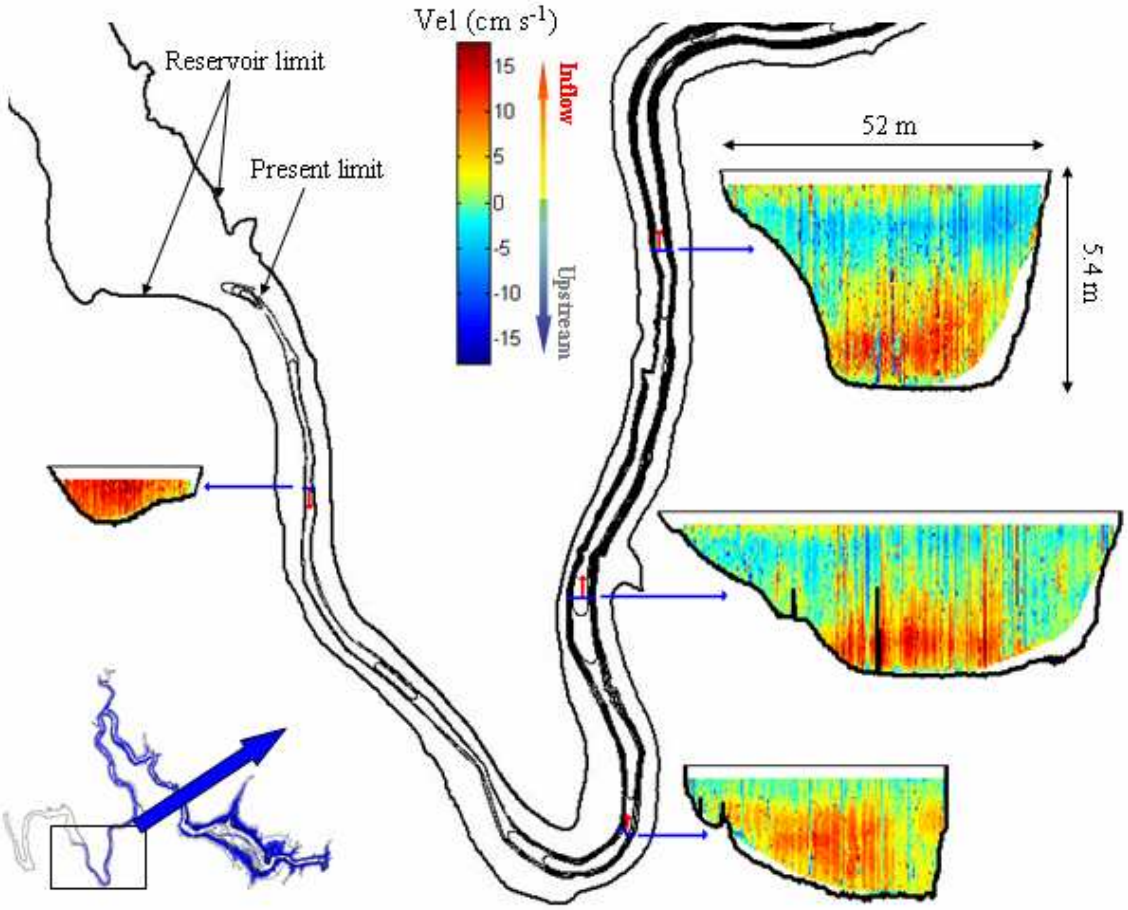

Figure 6. ADCP transects carried out during day 212.

Figure 6 shows some of the ADCP velocity transects carried out in August, 2005 (Julian day 212), during an interflow situation. The positive velocity values correspond to the inflow while the negative values correspond to the upstream current that is generated. The total flow rate, Q, can be calculated by using:

$$Q = \iint_S U ds \equiv \sum_{i=1}^{N} U_i (\Delta x \Delta y)_i \ , \qquad (5.1)$$

where the cross sectional area S have been discretized with the cells $(\Delta x \Delta y)_i$ obtained in the ADCP measurements, U_i is the velocity measured in the cell *i*, and *N* is the total number of cells.

As ADCP is not able to measure water velocity near the surface and close to the bottom, so some assumptions have to be made.

The missing ADCP data were extrapolated after fitting a curve to the original data. Two examples of such a fitting, corresponding to stations s1 (before the plunge point) and s5 (after the plunge point) are shown in Figure 7. Notice that after the plunge point, the velocity in the surface layer is negative due to the upstream current generated. A flow average over the total 9 transects gives a value of 3.26 ± 0.4 m^3/s.

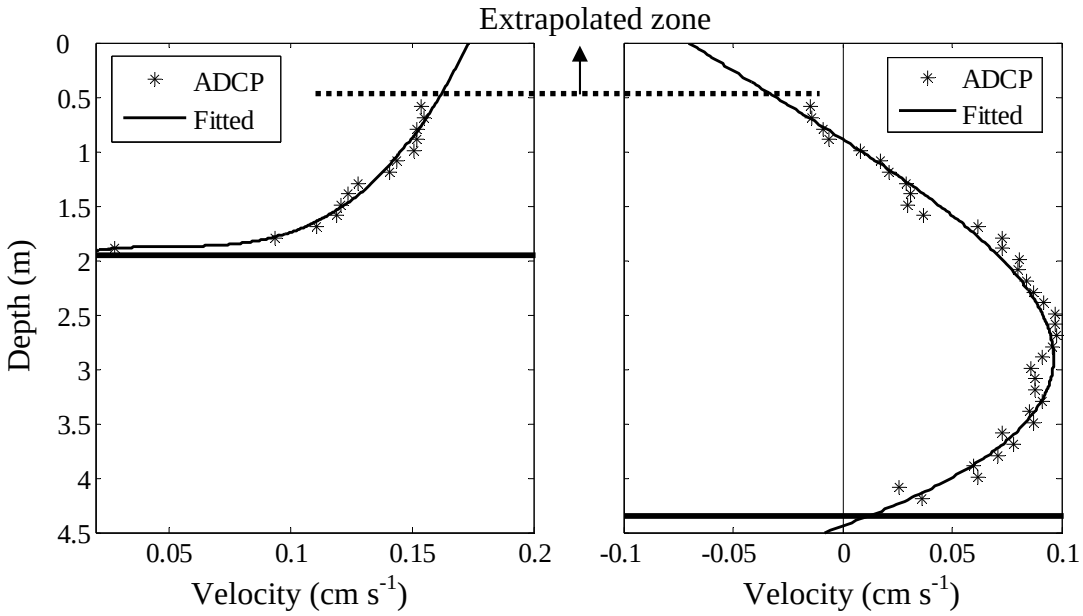

Figure 7. Curve fittings and extrapolated values used to fill the ADCP data gaps in the flow rate calculations.

ADCP transects can be used to estimate the dilution of the river as it merges into the reservoir. It is of interest to estimate the dilution coefficient of the river at the plunge point, because of the high degree of mixing that takes place there. If *Qo* and *Qd* are the inflows before and after the plunge point respectively, the dilution coefficient will be: $\Gamma = Qd/Qo$. The flow rate *Qo* is obtained from the average of the 3 transects carried out at station s1, just before the plunge point. Likewise, *Qd* is obtained in the same way but at station s4. To calculate the inflow rate, only positive values of the velocity should be taken into account; negative values would correspond to the upstream current in *Qd* and should therefore be disregarded. The dilution coefficient obtained was $\Gamma \approx Qd/Qo \approx 4.11 / 3.26 \approx 1.26$. For flow regimes attached to both walls, Johnson et al. (1989) found $\Gamma < 1.3$, i.e. dilutions of less than 30%. Elder and Wunderlich (1973) reported values of 1.02 to 1.04 for the Chilhowee Reservoir and 1.3 to 1.46 for the Norris reservoir. Initial mixing values of 1.04 to 1.28 were given by Ford and Johnson (1983) in the DeGray Lake in Arkansas. Nevertheless, as the dynamics of the river in the Sau reservoir change very quickly, so will the dilution coefficient and therefore the value Γ=1.26 will change as the interflow changes to overflow.

After the plunge point, both the dilution coefficient Γ and the entrainment coefficient (E) (defined as $E = \frac{w_e}{U}$ where w_e is the entrainment velocity, and U is the mean underflow velocity) are difficult to measure because of the large errors resulting from using the data of the ADCP in comparison with entrainment values. Ellison and Turner (1959) found that the underflow entrainment coefficient was a decreasing function of the bulk Richardson number *Ri*;

$$E = \frac{w_e}{U} = E(Ri^{-k}), \tag{5.2}$$

where k is a constant between 0 and 3/2, and Ri is defined as:

$$Ri = \frac{g'h}{U^2}\cos\alpha, \tag{5.3}$$

where $g' = g(\rho_a - \rho)/\rho_a$ is the buoyancy based on the excess in density of the current over the ambient density ρ_a, g is the acceleration of gravity, h is the depth of the inflow and α is the bottom slope.

In the case of Sau, as the river is highly dynamic, switching from overflow to interflow. it is also interesting to estimate how mixing changes in the water column. For this reason, instead of the bulk Ri number, it is better to use the gradient Richardson defined as:

$$Ri(z) \equiv \frac{N^2(z)}{(dU/dz)^2}, \tag{5.4}$$

where $N^2 = (gd\rho)/(\bar{\rho}\, dz)$ is the buoyancy frequency. The gradient Richardson number is essentially a ratio between the potential energy that mixing must overcome and the kinetic energy available in the shear flow. The critical Richardson number, below which mixing takes place is Ri_c, ~ 0.25, although values between 0.2 and 1 have been reported; large values indicates stability.

Figure 3C shows a profile of the gradient Richardson number obtained at station s6 from the ADCP and thermistor string data. In underflow situations, low Richardson numbers occurred at the interface of the underflow with the upstream current (ambient water). The interface was located at depths of around 3 - 4m. Here, the shear is high and therefore mixing was enhanced. Likewise, during the overflows, low Richardson numbers are found at depths of around 1 - 2m, at the interface of the overflow with the upstream current.

In the transition between overflows and underflows, low Richardson numbers were displaced vertically through the water column, at the same time that stratification weakened, decreasing the buoyancy (Fig. 3C). Such a mixing activity, involving the whole water column, contrasts with the most commonly described continuous underflow or overflow events where the mixing activity is less pronounced (Dallimore, 2001). In our case, in the first few kilometres of the reservoir, from station s1 to station s8-s9, the inflow water is distributed in the whole water column; this is apparent from the high values of conductivity in Fig. 8A. Also, another effect of such a dynamic system is the increase in the travel time of the inflowing water to the dam, i.e., the retention time of the river water in the reservoir.

The retention time of a river in a reservoir is usually calculated as the quotient between the reservoir volume and the inflow rate. However, Rueda et al. (2006) improved the way of calculating the retention time in the Sau reservoir by using the 1-D numerical model DYRESM (Imberger and Patterson, 1981) which takes into account, on a daily time scale, the insertion level of the river in the reservoir. However, we have seen that the insertion of the river changes on a shorter time scale and the mixing associated with the inflow oscillations of the river from underflow to overflow will increase the retention time of the river further than that predicted by the 1Dmodel.

Biological consequences

From a water quality point of view, it is important to know how the river nutrients will be distributed along the reservoir and the effect of such nutrients over the phytoplankton populations. Armengol et al. (1999) and Comerma (2003) described the longitudinal differences in the nutrient distribution in the reservoir. As the input of nutrients from the River Ter is high, it is important to know how they will be distributed throughout the reservoir, in order to be able to predict the phytoplankton evolution. The oscillating dynamics of the inflow mean that new nutrients are injected everyday into the reservoir surface. When the injected water, rich in nutrients but poor in phytoplankton, encounters the eutrophic quiescent reservoir water, conditions for phytoplankton growth are excellent. As conductivity can be used as a tracer of the river water, we can measure it, as it follows the thalweg, in order to explain the progression or evolution of the river and the head of the injected overflows (Fig. 8A). A bloom of phytoplankton located around station s9 (4 km) at the head of the injected overflowing water can be appreciated in Fig. 8B. Concentrations of dissolved phosphorus (0.172 mg/L) and nitrogen (3.1 mg/L) measured on day 209 at station s9 (see methods) were high enough to allow the formation of the algal bloom.

Water samples showed that the bloom found at station s9 was dominated by cyanobacteria (especially *Woronichia naegeliana* and *Aphanizomenon issatschenko* in minor concentration). Insignificant concentrations of other species (*Anabaena*

spiroides, dinoflagellates: *Peridiniopsis elpatiewskyi*, *Peridinium umbonatum*, *Gymnodinium sp.*; cryptophytas: *Cryptomonas marssonii*; chlorophytas: *Cosmarium reniforme*, *Pediastrum simplex*, *Phacotus lenticularis*, *Scenedesmus acutus*, *Scenedesmus ecornis*, *Scenedesmus spicatus*) were also found. Although the cyanobacteria *Aphanizomenon issatschenkoi* is able to fix atmospheric nitrogen, the inflow concentration of this dissolved nutrient was already high enough for the algal growth.

Phytoplankton concentrations in the river are much smaller than in the reservoir and no dominant population was found. River water samples showed diatoms (*Cyclotella meneghiniana*, *Nitzschia acicularis*, *Stephanodiscus hantzschii)*, some benthonic diatoms dragged up from the bottom (*Ceratoneis arcus*, *Cocconeis placentula*, etc.) and minor concentrations of chlorophytas *Coelastrum astroideum*, *Chlamydomonas sp.*, *Dictyosphaerium pulchellum*, *Pediastrum boryanum*, *Scenedesmus acuminatus*, *Scenedesmus spinosus*).

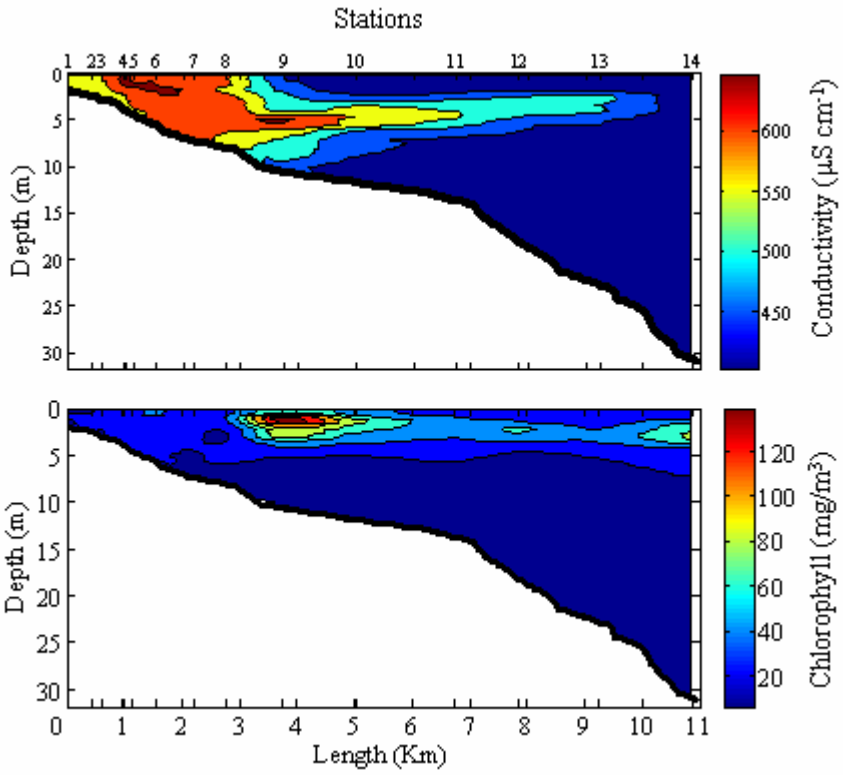

Figure 8- Longitudinal contour of (A) conductivity and (B) Chlorophyll following the thalweg during day 209.

The hydrodynamic variability associated with biomass fluctuation found in the Sau reservoir can be compared with tide-generated blooms found in some estuaries. Cloern (1991) demonstrated that phytoplankton biomass may fluctuate on a daily to weekly time scale and that much of this variability is associated with tides. He suggested that the daily variations in the rate of vertical mixing by tidal stirring might

control phytoplankton bloom dynamics in some estuaries. This behaviour is similar to what we found in the Sau reservoir where the forcing agent is the variation in temperature which induces the variability of the river inflow.

The concentration of the bloom changed during the survey and peaked on day 209 (Fig. 8B). From this day on, it started to decrease, probably as a result of the shadow effect produced by such high concentrations. During the first days of the survey, the location of the bloom was nearly constant, but on day 212, it started to move towards the plunge point, following the upstream current. This can be explained by the decrease in river temperature that took place from day 212 onwards (Fig 2A). At that time, the overflow events also decreased and the interflow events were dominant. The upstream current generated by the interflows displaced the bloom slowly towards the plunge point;

Furthermore, a smaller chlorophyll peak was found around station s14 (Fig. 8b), where the sheltered and the lacustrine zones meet (Fig. 5A). Two hypothesis can be proposed to explain the availability of nutrients required for this peak to be produced: As the interflow travelled through the reservoir, it was getting lighter due to the warmer water entraining into the inflow, so that the interflow slowly rose, as can be observed in Fig 8A, and nutrients were available for these populations in the euphotic zone (a similar behaviour was described by Fischer et al. (1983) where nutrients from an interflow reached the water surface). A second hypothesis for the nutrient availability is the upwelling produced by wind-driven currents on that zone (see Fig. 5A). More research is needed to explain the contribution of these two proposed mechanisms to this chlorophyll peak.

Numerical Modelling

Algae blooms, especially cyanobacteria, may be toxic and can generate certain diseases (Codd et al. 1999). For example, in the nearby Boadella reservoir, a cyanobacteria bloom caused a social alarm in 1993 (Baserba, 1993). Therefore, understanding the location and the conditions in which these blooms are generated may be valuable from an ecological and human health point of view. Here we will try to simulate the bloom event occurring in the last days of July 2005 by using a numerical model CAEDYM coupled with the Hydrodynamic model ELCOM (ELCOM-CAEDYM). Other authors have successfully simulated phytoplankton evolution using this model (Romero et al. 2004, Chan et al., 2003). Robson and Hamilton (2004) also simulated a bloom event of cyanobacteria (*Microcistys aeruginosa*) occurring in the Swan river estuary (Western Australia). Morillo et al. (*Accepted*) believe that the ELCOM model is a valuable tool for applying different strategies aimed at modifying the transport timescales and dilution capacity of a lake. Likewise, Hipsey et al. (2004)

defined the ELCOM-CAEDYM model as a new tool for risk management in the occurrence of bloom events of the toxic *Cryptosporidium* algae.

CAEDYM is an ecological model which simulates up to five phytoplankton groups, together with nitrogen, phosphorus and oxygen dynamics and transport. In our case, however, only one group was simulated since the bloom was completely dominated by cyanobacteria. The model can also simulate macrophytes, zooplankton, fish and benthic invertebrates. However, such populations were disregarded since they most probably do not have much relevance in the observed bloom. The main equations used in CAEDYM with relevance to the cyanobacteria population are shown in Table 1.

Rate of change of phytoplankton concentration (mg chl *a* m^{-3} per day):

$$\frac{\partial A_i}{\partial t} = \left\{ \underbrace{\mu_i}_{growth} - \underbrace{k_{ri} f(T)}_{respiration} + \underbrace{\frac{v_i}{\Delta z}}_{settling} \right\} A_i + resuspension$$

Phytoplankton growth rate (per day):

$$\mu_i = f_i(T)\mu_{\max i} \min[f(I), f(N), f(P)]$$

Temperature limitation:

$$f_i(T) = \theta^{T-20} + \theta^{k(T-a)} + b$$

Phosphorus limitation:

$$f(P) = \frac{FRP}{FRP + K_{pi}}$$

Nitrogen limitation:

$$f(N) = \frac{NH_4^+ + NO_3^-}{NH_4^+ + NO_3^- + K_{Ni}}$$

Light limitation:

$$f(I) = 1 - \exp\left(-\frac{I}{I_k}\right)$$

Temperature factor:

$$f(T) = \theta^{T-20}$$

A_i	Phytoplankton Concentration
I	Irradiance
NH_4^+	Ammonium
NO_3^-	Nitrate
FRP	Filterable reactive phosphorus

Table 1. Main equations used in CAEDYM

The main parameters used in the model are summarized in Table 2. It is difficult to simulate the observed values of the chlorophyll bloom exactly because of the uncertainty about which parameters to use for the different species and because the initial condition of nutrients is unknown. Therefore, instead of trying to reproduce the

bloom exactly, our goal will be to gain insight into the cyanobacteria response to a highly dynamic system, such as the one found in the Sau reservoir. Also, we will evaluate the ecological response of the model to the inflow dynamics, especially for predicting bloom events, which is always important for water management. The parameters used in CAEDYM were those used by Robson and Hamilton (2004) for the cyanobacteria *Microcistys aeruginosa,* which has been previously reported in Sau reservoir (Armengol et al. 1999), and a cyanobacteria similar to *Woronichia naegeliana*. For further description of the biochemical assumptions applied the reader is referred to the papers of Robson and Hamilton (2004) or Romero et al. (2004).

The hydrodynamic model ELCOM was run using a uniform horizontal 20 x 20m grid, with a previously straightened bathymetry (Hodges and Imberger, 2001). Different cell sizes were used in the vertical plane with high resolution (0.25m cells) in the first few meters and increasingly lower resolution (up to 1m cells) in the deeper layers. The simulation began by assuming an homogeneous longitudinal reservoir state and using the main vertical values of temperature and chlorophyll obtained during the survey at stations s10-s15 on day 202. Initial nutrients in the reservoir were set to mean values obtained in July at the reservoir during the years 1995-1997 (Armengol et al.1999). The input data included daily inflow and outflow rates, hourly nutrients, temperature and conductivity from the automatic station in the River Ter and hourly meteorological data from the reservoir's meteorological station (see methods)..

Parameter	Value	Description
K_{ri}	0.08	Respiration rate coefficient (per day)
v_i	-0.01	Algal settling velocities (m per day)
μ_i	1.2	Maximum specific growth rate at 20 ºC (per day)
θ	1.08	Temperature multiplier for temperature limitation of phytoplankton growth
k	2.19	Coefficient for temperature limitation function for phytoplankton (dimensionless)
a	30.095	Coefficient for temperature limitation function for phytoplankton (dimensionless)
b	0.182	Coefficient for temperature limitation function for phytoplankton (dimensionless)
K_{pi}	6	Half-saturation constant for phosphorus uptake (mg m^{-3})
K_{ni}	30	Half-saturation constant for nitrogen uptake (mg m^{-3})
Iki	500	Irradiance parameter for non-photoinhibited phytoplankton growth (μEm^{-2} s^{-1})

Table 2. Main parameters used in CAEDYM

Simulations started on day 202.5. Figure 9 shows a five-day evolution of total phosphorus, the usual limiting nutrient, and chlorophyll. It can be seen how the model is

able to reproduce the overflow and interflow fluctuation and how inflowing water, rich in phosphorous, is injected at the surface and at the insertion depth.

On day 203.5 (Fig 9A) the head of the surface overflow and the head of the interflow (at a depth of approximately 4m) are clearly seen. As the inflow evolves, from day 202.5 to day 207.5) the overflow head had travelled a distance of about 4 km and seemed to stop at that position, while the interflow head slowly advanced towards the dam (Fig 9A). Also, a cyanobacteria bloom is generated where the head of the overflow is located, (Fig. 9b). It is important to point out that the bloom was formed where the water from the river (rich in nutrients and poor in cyanobacteria) encountered the water from the reservoir (poor in nutrients but rich in cyanobacteria). Therefore, the model is able to predict the bloom observed in the field survey (compare Fig. 8 with Fig. 9).

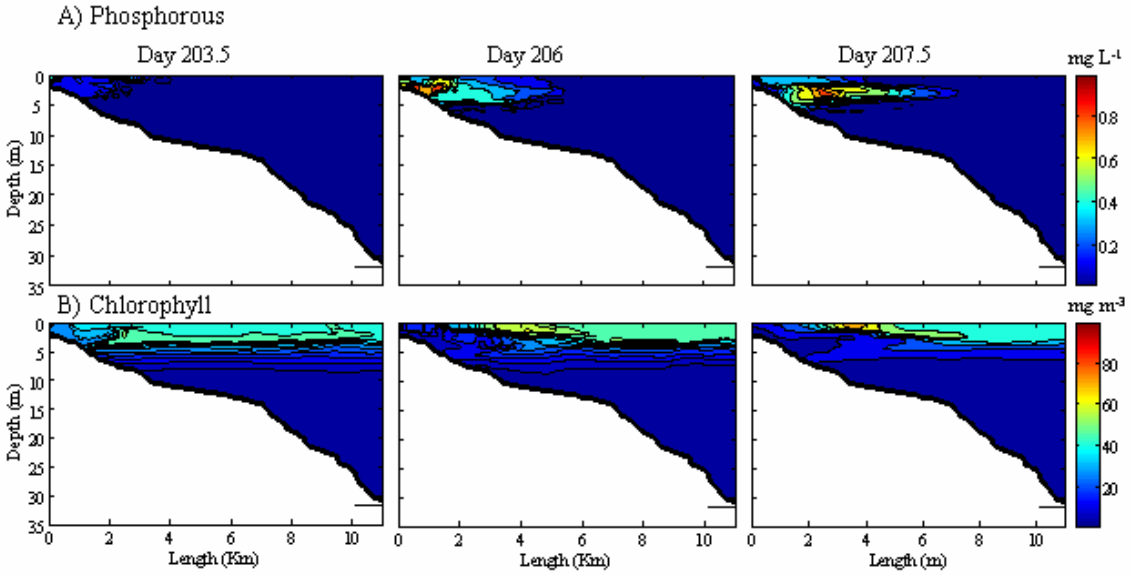

Figure 9. Evolution of Phosphorous Vs Chlorophyll obtained with ELCOM-CAEDYM, starting from homogeneous conditions at day 202.5.

The model has shown itself to be able not only to solve the changing hydrodynamics of the inflow, but also the phytoplankton response of the reservoir. We can therefore say that the ELCOM-CAEDYM model can be a useful tool for predicting bloom events, as well as intrusion of possible contaminants. Furthermore, the model can also provide us with information about the retention time of the river in the reservoir or about the inflowing water distribution throughout the reservoir.

Conclusions

River inflow temperature is directly affected by short term variations in the weather conditions and by the daily warming-cooling cycle. Such variations cause the river density to fluctuate, generating a highly dynamic system. During the last, warm,

days of July in the year 2005, the daily fluctuation made the inflow switch between overflow and interflow. This fluctuation increased the vertical mixing in the water column in the interaction zone between the river and the reservoir. The fate of the incoming nutrients from the river depends on the inflow dynamics, and during the last days of July, these dynamics were responsible for a bloom event at the head of the overflow events where the nutrient rich water from the river mixed with the eutrophic ambient water of the reservoir. With this study, we have also demonstrated that the inflow dynamics can be highly variable, with fluctuations on short time scales. Also, the inflow dynamics appear to be a determining factor in the phytoplankton response in the reservoir. Likewise, bloom episodes can be associated to specific inflow events. Using numerical models, such as ELCOM-CAEDYM, these events can be simulated or predicted.

GENERAL CONCLUSIONS

By means of field experiments and the application of numerical models, the hydrodynamic response of the Sau Reservoir to external forcing has been determined. The two main forcing mechanisms are wind forcing and river inflow. In general, reservoirs have an open zone close to the dam and a narrow and meandering zone upriver. In the open zone, the reservoir is mainly affected by wind forcing, while in the meandering zone, sheltered from the wind, the main forcing mechanism is river inflow. Both mechanisms are also subject to different interactions between them. The wind forcing generates basin-scale internal waves while the river inflow generates density-driven currents. These are some of the specific conclusions:

- In the Sau Reservoir, and generally in Mediterranean reservoirs, with large heat fluxes and deep submerged withdrawal structures draining large volumes of water, the thermal structure is characterized by deep metalimnetic layers, and the stratification is nearly continuous (linear). Under such conditions, almost every vertical mode of basin-scale internal waves, including high vertical modes, can be excited by wind events.

- The 24-hour sea breeze and the associated 12-hour sub-period, so common in Mediterranean reservoirs, may generate resonance in natural basin modes that have similar natural periods. The wind periodicities play an important role in determining the dominant modes since modes with similar wind periods are amplified.

- The natural period of the modes tends to decrease as summer stratification develops and buoyancy increases. That means that higher vertical modes may be excited by resonance from a fixed wind with a 24-hour period as stratification evolves; in this way, higher vertical modes may be found at the end of the summer season when stratification is completely developed. That is the case of the Sau and Beznar reservoirs where, as the summer advances, higher vertical modes are excited (V2 to V3 in Sau, and V3 to V5 in Beznar).

- Non-resonant modes, especially low modes, may also be excited; however, they contain much less energy than resonant modes.

- Vertical oscillations and horizontal advection produced by the wind-driven currents and basin-scale internal waves determine, to a large degree, the phytoplankton distribution, and may generate heterogeneities.

- The river responds faster to meteorological variability than the reservoir does; this makes the river inflow a highly dynamic system with the insertion changing at a daily timescale. The stirring induced by the inflow variability increases the mixing between the river and the reservoir. When the inflow enters as an overflow, nutrients are injected into the euphotic zone and phytoplankton blooms are generated.

- Three-dimensional hydrodynamic models coupled with ecological models can reproduce such events and are therefore interesting tools in water management.

REFERENCES

Akiyama, J., and H.G. Stefan 1984. Plunging Flow into a Reservoir: Theory. ASCE Journal of Hydraulic Engineering. **110**(4): 484-499.

Alavian, V. 1986. Behaviour of density currents on an incline. J. Hydr. Eng. **112**(1): 27-42.

Amorocho, J. & Devries, J.J. 1980. A new evaluation of the wind stress coefficient over water surfaces. J. Geophys. Res. **85**: 433–442.

Antenucci, J.P., J. Imberger and A. Saggio. 2000. Seasonal evolution of the basin scale internal wave field in a large stratified lake. Limnol. Oceanogr. **45**(7): 1621-1638.

Antenucci, J.P. and J. Imberger. 2003. The seasonal evolution of wind/internal wave resonance in Lake Kinneret. Limnol. Oceanogr. **48**(5): 2055-2061.

Antenucci J.P., R. Alexander, J.R. Romero, and J. Imberger. 2003. Management strategies for a eutrophic water supply reservoir - San Roque, Argentina. Water Science and Technology. **47**(7-8): 149-155.

Appt, J., J. Imberger and H. Kobus. 2004. Basin-scale motion in stratified Upper Lake Constance. Limnol. Oceanogr. **49**(4): 919-933.

Armengol, J., J. Toja, J., and Vidal, A. 1994. Seasonal rhythm and secular changes in Spanish reservoirs. *In* "Limnology Now: A Paradigm of Planetary Problems." (R. Margalef, ed.), pp. 237-253. Elsevier Science.

Armengol, J., J.C. Garcia, M. Comerma, M. Romero, J. Dolz, M. Roura, B.-H. Han, A. Vidal, and K. Simek. 1999. Longitudinal Processes in Canyon Type Reservoir: The Case of Sau (N.E. Spain), p. 313-345. *In* J.G. Tundisi and M. Straskraba [eds.], Theoretical Reservoir Ecology and its Applications. Backhuys Publishers.

Atkinson, J. 1988. Interfacial mixing in stratified flows. J. Hydr. Res. **26**(1): 27-31.
Bai, Z., J. Demmel, J. Dongarra, A. Ruhe, and H. van der Vorst. 2000. Templates for the Solution of Algebraic Eigenvalue Problems: A Practical Guide. SIAM.

Baines, P. G. 2001 Mixing in flows down gentle slopes into stratified environments. J. Fluid Mech. **443**: 237-270.

Baserba, C. 1999. Cicle annual de l'estat tròfic de l'embassament de Boadella (Febrer 1993 – Gener 1994). Minor Thesis. UdG. 82pp.

Baüerle, E. 1998. Excitation on internal seiches by periodic forcing. *In* J. Imberger [ed.], Physical processes in lakes and oceans. Coastal and Estuarine Studies. V. 54. AGU. pp. 167–178.

Beutler, M., K.H.Wiltshire, B. Meyer, C. Moldaenke, C. Lüring, M. Meyerhöfer, U.-P Hansen, and H. Dan. 2002. A fluorometric method for the differentiation of algal populations in vivo and in situ. Photosynthesis Research. **72** (1): 39-53.

Boegman, L., G.N. Ivey, and J. Imberger. 2005a. The degeneration of internal waves in lakes with sloping topography. Limnol. Oceanogr., **50**: 1620-1637.

Boegman, L., G.N. Ivey, and J.Imberger. 2005b. The energetics of large-scale internal wave degeneration in lakes. J. Fluid. Mech., **531**: 159-180.

Bormans, M., B.S. Sherman, and I.T. Webster. 1999. Is buoyancy regulation in cyanobacteria and adaptation to exploit separation on light and nutrients?. Marine Freshwater Research. **50** (8): 897-906.

Bournet, P.E., D. Dartus, B. Tassin, and B. Vincon-Leite. Numerical investigation of plunging density current. Journal of Hydraulic Engineering. **125**(6):584-594.

Campos, H., D.P. Hamilton, L. Villalobos, J. Imberger, and A. Javam. A modelling assessment of potential for eutrophication of Lake Riñihue, Chile. Archiv fur Hydrobiologie. **151**(1): 101-125.

Carmack, E. C. 1979. Combined influence of inflow on lake temperatures on spring circulation in a riverine lake. J. Phys. Oceanogr. **9**: 422-434.

Carmack, E.C., R.C. Wiegand, R.J. Daley, C.B.J. Gray, S. Jasper and C.H. Pharo. 1986. Mechanisms influencing the circulation and distribution of water mass in a medium residence-time lake. Limnol. Oceanogr. **31**(2): 249-265.

Casamitjana, X., T. Serra, C. Baserba and J. Pérez . 2003. Effects of the water withdrawal in the stratification patterns of a reservoir. Hydrobiologia, **504**: 21-28.

Casulli, V. and R.T.Cheng. 1992. Semi-implicit finite difference methods for three-dimensional shallow water flow. Int. J. Numer. Methods Fluids. **15**: 629–648.

Chan, T.U., D.P. Hamilton and B.J. Robson. 2003. Modelling phytoplankton succession and biomass in a seasonal West Australian estuary. Verh. Int. Verein. Limnol. 28.

Chen, C.T., and F.J. Millero. 1977. The use and misuse of pure water PVT properties for lake waters. Nature. **266**: 707-708.

Chung, S. and R. Gu. 1988. Two-dimensional Simulations of Contaminant Currents in a Stratified Reservoir. Journal of Hydr. Engineering, American Society of Civil Engineers, **124**: 704-711.

Cloern, J.E. 1991. Tidal stirring and phytoplankton bloom dynamics in an estuary. Journal of Marine Research. **49** (1): 203-221.

Coastal Engineering Research Center. 1975. Shore Protection Manual, vol. 1. U.S. Army Corps of Engineers, Washington D.C., 496 pp.

Codd, G.A., S.G. Bell, K. Kaya, C.J. Ward, K.A. Beattie and J.S. Metcalf. 1999. Cyanobacterial toxins, exposure routes and human health. Eur. J. Phycol. **34**: 405–415.

Comerma, M. 2003. Heterotrophic microbial processes in the Sau reservoir. PhD thesis. University of Barcelona. 192pp.

Csanady, G.T. 1975. Large-scale motion in the great lakes. J. Geophys. Res. **72**: 4151-62.

Csanady, G.T. 1984. Circulation Induced by River Inflow in Well Mixed Water over a Sloping Shelf. Journal of Physical Oceanography. **14**(11): 1703-1711.

Dallimore, C., J. Imberger and T. Ishikawa. 2001. Entrainment and turbulence in a saline underflow in Lake Ogawara. J. Hydr. Eng. **127**(11): 937-948.

Dallimore, C.J., B.R. Hodges and J. Imberger. 2003. Coupling an underflow model to a three-dimensional hydrodynamic model. Journal of Hydraulic Engineering. **129**(10): 748-757.

Dallimore, C.J., J. Imberger and B.R. Hodges. 2004. Modeling a plunging underflow. Journal of Hydraulic Engineering. **130**(11): 1068-1076.

Dekshenieks, M.M., P.L. Donaghay, J.M., Sullivan, J.E.B. Rines, T.R. Osborn, and M.S. Twardowski, 2001. Temporal and spatial occurrence of thin phytoplankton layers in relation to physical processes. Marine Ecology Progress Series. **223**: 61-71.

Dickman, M., K. Stewart, and M. ServantVildary. 1993. Spatial heterogeneity of summer phytoplankton and water chemistry in a large volcanic spring-fed lake in northern Iceland. Arctic Alpine Research. **25** (3): 228-239.

Einarsson, Á., G. Stefánsdóttir, H. Jóhannesson, J.S. Ólafsson, G.M. Gíslason, I. Wakana, G. Gudbergsson, and A. Gardarsson. 2004. The ecology of Lake Myvatn and the River Laxá: Variation in space and time. Aquatic Ecology. **38** (2): 317-348.

Elder, R.A. and W.O. Wunderlich. 1972. Inflow Density Currents in TVA Reservoirs. ASCE Proceedings, International Symposium of Stratified Flow, Novosibirsk, published in 1973, pp. 221-236.

Elliott, J.A., A.E. Irish, and C.S Reynolds. 2001. The effects of vertical mixing on a phytoplankton community: a modeling approach to the intermediate disturbance hypothesis. Freshwater Biology. **46** (10): 1291-1297.

Ellison, T.H. and J.S. Turner. 1959. Turbulent entrainment in stratified flows. J. Fluid Mech. **6**(3): 423-448.

Engelund, F.A. and E. Hansen. 1972. A Mongraph on Sediment Transport. Copenhagen, Teknisk Vorlag.

Fernando, H. J. S. 1991. Turbulent mixing in stratified fluids. Ann. Rev. Fluid Mech. **23**: 455-494.

Fischer, H.B., E.J. List, R.C.Y. Koh, J. Imberger, and N.H. Brooks. 1979. Mixing in inland and coastal waters. Academic Press, New York, 483 pp.

Fischer H.B. and R.D. Smith. 1983. Observations of transports to surface waters from a plunging inflow to Lake Mead. Limnol. Oceanogr. **28**: 258-272.

Ford, D.E., and M.C. Johnson 1981. Field Observations of Density Currents in Impoundments. ASCE Proceedings, Symposium on Surface Water Impoundments, Minneapolis, MN., pp. 1239-1248.

Ford, D.E., and M.C. Johnson 1983. An Assessment of Reservoir Density Currents and Inflow Processes. Environmental Lab, Waterways Experiment Station Technical report E-83-7, pp. 1-84.

Fricker, P.D. and H.M. Nepf. 2000. Bathymetry, stratification, and internal seiche structure. J. Geophys. Res. **105**: 14,237-14,251.

Gal, G., J. Imberger, T. Zohary, J.P. Antenucci, A. Anis, and T. Rosenberg. 2003. Simulating the thermal dynamics of Lake Kinneret. Ecological Modelling. **162**(1-2): 69-86.

Gaedke, U., and M. Schimmele. 1991. Internal seiches in Lake Constance: Influence on plankton abundance at a fixed sampling site. J. Plankton Res. **13**: 743-754.

Gloor, M., A. Wüest, and M. Munnich. 1994. Benthic boundary mixing and resuspension induced by internal seiches. Hydrobiologia. **284**: 59-68.

Gómez-Giraldo, A., J. Imberger, and J.P. Antenucci. 2006. Spatial structure of the dominant basin-scale internal waves in Lake Kinneret. Limnol. Oceanogr. **51**: 229–246.

Gonella, J. 1972. A rotary-component method for analyzing meteorological and oceanographic vector time series. Deep-Sea Res. **19**: 833-846.

Gregor, J. and B. Marsalek. 2004. Freshwater phytoplankton quantification by chlorophyll □: a comparative study of in vitro, in vivo and in situ methods. Water Research. **38** (3): 517-522.

Gregor, J., R. Geris, B. Marsalek, J. Hetesa, and P. Marvan. 2005. In situ quantification of phytoplankton in reservoirs using a submersible spectrofluorometer. Hydrobiologia. **548**: 141-151.

Griffin, S.L., M. Herzfeld and D.P. Hamilton. 2001. Modelling the impact of zooplankton grazing on phytoplankton biomass during a dinoflagellate bloom in the Swan River Estuary, Western Australia. Ecol. Eng. **16**: 373–394.

Gu, R. and S. Chung. 2003. A Two-Dimensional Model for Simulating the Transport and Fate of Toxic Chemicals in a Stratified Reservoir. Journal of Environmental Quality. **32**: 620-632.

Hamilton, D. P. and S.G. Schladow. 1997. Prediction of water quality in lakes and reservoirs: Part I: Model description. Ecological Modelling. **96**: 91-110.

Han, B, J. Armengol, J.C. García, M. Comerma, M. Roura, J. Dolz and M. Straskraba. 2000. The thermal structure of Sau Reservoir (NE: Spain): a simulation approach. Ecological Modelling. **125**: 109-122.

Harris, G.P. and A.M. Trimbee. 1986 Phytoplankton population dynamics of a small reservoir: physical biological coupling and the time scales of community change. Journal of Plankton Research. **8** (6): 1011-1025.

Hauenstein, W. and TH. Dracos. 1984. Investigation of Plunging Density Currents Generated by Inflows in Lakes. Journal of Hydraulic Research. **22**(3): 157-179.

Hebbert, B., J. Imberger, I. Loh and J. Patterson. 1979. Collie river underflow into the Wellington reservoir. Journal of the Hydraulics Division ASCE. **105**: 533-545.

Heald, P.C., S.G. Schladow, B.C. Allen, and J.E. Reuter. 2005. VOC loading from marine engines to a multiple-use lake. Lake and Reservoir Management. **21**(1): 30-48.

Hedger, R.D., N.R.B. Olsen, D.G. George, T.J. Malthus, and P.M. Atkinson. 2004. Modelling spatial distributions of *Ceratium hirundinella* and *Microcystis spp.* in a small productive British lake. Hydrobiologia. **528**: 217-227.

Hejzlar, J. and M. Straskraba. 1989. On the horizontal distribution of limnological variables in Rimov and other stratified Czechoslovack reservoirs. Arch. Hydrobiol. Beih. Ergebn. Limnol., **33**:41-55.

Henderson-Sellers. B. 1966. Calculating the surface energy balance for lake and reservoir modelling: a review. Reviews of Geophysics **24**(3): 625–649.

Hipsey, M. R., J.P. Antenucci, J.D. Brookes, M.D. Burch, R.H. Regel and L. Linden. 2004. A three dimensional model of Cryptosporidium dynamics in lakes and reservoirs: a new tool for risk management. Intl. J. River Basin Management. **2**(3): 1-17.

Hipsey, M.R., J. R. Romero, J.P. Antenucci and D. Hamilton. 2005. Computational Aquatic Ecosystem Dynamics Model: CAEDYM v2. Science Manual. Centre for Water Research. University of Western Australia.

Hodges, B. R. 2000. Numerical techniques in CWR-ELCOM. Technical report, Centre for Water Research, University of Western Australia, Nedlands, Western Australia, 6907. Reference WP 1422-BH.

Hodges, B.R., J. Imberger, A. Saggio, and K.B. Winters. 2000. Modeling basin-scale internal waves in a stratified lake. Limnol. Oceanogr. **45**(7): 1603-1620.

Hodges, B. R. and J. Imberger. 2001. Simple curvilinear method for numerical methods of open channels. ASCE Journal of Hydraulic Engineering, **127(11)**: 949-958.

Hodges, B.R. and C. Dallimore. 2006. Estuary, Lake and Coastal Ocean Model: ELCOM v2.2 Science Manual. Centre for Water Research. University of Western Australia.

Horn, D. A., J. Imberger and G.N. Ivey. 2001. The degeneration of large-scale interfacial gravity waves in lakes. J. Fluid Mech. **434**: 181–207.

Howard, C.S. 1953. Desnity Currents in Lake Mead. ASCE Proceedings, Minnesota International Hydraulics Convention, Minneapolis, MN., pp. 355-368.

Hutter, K. 1984. Hydrodynamics of lakes. Springer-Verlag, New York.

Imberger, J., R. Thompson and C. Fandry. 1976. Selective withdrawal from a finite rectangular tank. Journal of Fluid Mechanics. **78**(3): 489-512.

Imberger, 1980. Selective withdrawal: a review. Invited paper presented at the Second International Symposium on Stratified Flows. Trodheim, Norway, June 1980.

Imberger, J., and J. C. Patterson. 1981. A dynamic reservoir simulation model—DYRESM: 5. *In* Fischer, H.B. (ed.), Transport Models for Inland and Coastal Waters. Academic Press, New York, pp. 310–367.

Imberger, J. and P.F. Hamblin. 1982. Dynamics of lakes, Reservoirs and cooling ponds. Annu. Rev. Fluid Mech. **14**: 153-87.

Imberger J. 1985. The diurnal mixed layer. Limnology and Oceanography. **30**(4): 737-770.

Imberger, J. and G. Parker. 1985. Mixed layer dynamics in a lake exposed to a spatially variable wind field. Limnol. Oceanogr. **30**(3): 473-488.

Imberger, J., and J.C. Patterson. 1990. Physical Limnology. In: Advances in Applied Mechanics, T. Wu (ed). Academic Press, Boston. **27**: 303-475.

Imberger, J. 1994. Transport processes in lakes: A review. In Limnology Now, ed. R Margalef, pp. 99-193. Amsterdam: Elsevier.

Imberger, J. 1998. Flux path in a stratified lake: a review, p. 1-18. *In* Jorg Imberger [ed.], Physical Processes in Lakes and Oceans. Coastal and Estuarine Studies, Am. Geophys. Union.

Imboden, D. M. and A. Wüest. 1995. Mixing Mechanisms in Lakes, *In* A. Lerman, D. Imboden and J. Gat. Physics and Chemistry Lakes. Springer, New York. p 83-138.

Jacquet, J. 1983. Simulation of the thermal regime of rivers. Mathematical modeling of water quality: Streams, lakes and reservoirs. *In* G.T. Orlob (ed.). Wiley-Interscience.

Jacquet, S., J.F. Lennon, D. Marie, and D. Vaulot, 1998. Picoplankton population dynamics in coastal waters of the northwestern Mediterranean Sea. Limnology and Oceanography. **43** (8): 1916-1931.

Jellison, R. and J.M. Melack. 1993. Meromixis and vertical diffusivities in hypersaline Mono Lake, California. Limnol. Oceanogr. **38**: 1008-1019.

Johnson, T., G. Farrell, C. Ellis and H. Stefan. 1987. Negative buoyant flow in divergin channel. I: Flow regimes. J. Hydr. Engrg. ASCE. **115**: 437-456.

Johnson, T.R., C.R. Ellis and H.G. Stefan. 1989. Negatively Buoyant Flows in a Diverging Channel. Part IV: Entrainment and Dilution. Journal of Hydraulic Engineering. **115**(4): 437-456.

Kataoka, T., M. Tsutahara and S. Mizutani. 2001. Selective withdrawal through a line sink of non-rotating and rotating stratified fluid in a reservoir of finite depth. Eur. J. Mech. B – Fluids. **20**:167-186.

Kimmel, B. L., O.T. Lind, and L.J. Paulson. 1990. Reservoir Primary Production. pp. 133-193. In K. W. Thornton, B.L. Kimmel and F. E. Payne (eds.), Reservoir limnology. Ecological perspectives, John Wiley & Sons, Inc., NY.

Koseff, J.R., and R.L. Street. 1985. Circulation Structure in a Stratified Lid-Driven Cavity Flow. Jour. Hydr. Div. ASCE. **111**(2): 334-354

Laval, B., J. Imberger, B. Hodges, and R. Stoker. 2003. Modeling circulation in lakes: Spatial and temporal variations. Limnol. Oceanogr. **48**(3)**:** 983–994.

Laval, B.E., J. Imberger and A.N. Findikakis. 2005. Dynamics of a large tropical lake: Lake Maracaibo. Aquatic Sciences. **67**: 337-349.

LaZerte, B.D. 1980. The dominating higher order vertical modes of the internal seiche in a small lake. Limnol. Oceanogr. **25**(5): 846-854.

Leboulanger, C., U. Dorigo, S. Jacquet, B. Le Berre, G. Paolini, and J.-F. Humbert. 2002. Application of a submersible spectrofluorometer for rapid monitoring of freshwater cyanobacterial blooms : a case study. Aquatic Microbial Ecology. **30** (1): 83-89.

Lemmin, U. and C. H. Mortimer. 1986. Tests of an extension to internal seiches of Defant's procedure for determination of surface seiche characteristics in real lakes. Limnol. Oceanogr. **36**:187-192.

Lemmin, U., C. H. Mortimer, And E. Baüerle. 2005. Internal seiche dynamics in Lake Geneva. Limnol. Oceanogr. **50:** 207–216.

Leonard, B.P. 1991. The ULTIMATE conservative difference scheme applied to unsteady one dimensional advection Comp. Meth. in Applied Mech. and Eng. **88**: 17–74

Levy, D.A., R. L. Johnson, and J. M. Hume. 1991. Shifts in fish vertical distribution in response to an internal seiche in a stratified lake. Limnol. Oceanogr. **36**: 187-192.

Lofquist, K. 1960. Flow and stress near an interface between stratified liquids. Phys. Fluids. **3**(2): 158-169.

Lorke, A., F. Peeters and A. Wüest. 2005. Shear-induced convective mixing in bottom boundary layers on slopes. Limnol. Oceanogr., **50**(5): 1612-1619.

MacIntyre, S. 1998. Turbulent mixing and resource supply to phytoplankton, p. 539-567. *In* J. Imberger, [ed.] Physical Processes in Lakes and Oceans, *Coastal and Estuarine Studies*, AGU.

MacIntyre, S., J. R. Romero, and G.W. Kling. 2002. Spatial-Temporal Variability in Mixed Layer Deepening and Lateral Advection in an Embayment of Lake Victoria, East Africa. Limnol. Oceanogr. **47**(3): 656-671.

MacManus, J., and R.W. Duck 1988. Internal seiches and subaqueous landforms in lacustrine cohesive sediments. Nature **334**: 511-513.

Margalef, R. 1983. Limnologia, ed. Omega, Barcelona.

Martin, D. B. and R. D. Arneson. 1978. Comparative limnology of a deep discharge eservoir and a surface discharge lake on the Madison river (Montana). Freshwat. Biol. **8**: 33–42.

McManus, M.A., O.M. Cheriton, P.J. Drake, D.V. Holliday, C.D. Storlazzi, P.L. Donaghay, and C.F. Greenlaw. 2005. Effects of physical processes on structure and transport of thin zooplankton layers in the coastal ocean. Marine Ecology Progress Series. **301**: 199-215.

McCord, S. A., and S. G. Schladow. 1998. Numerical simulations of degassing scenarios for CO_2-rich Lake Nyos, Cameroon. J. Geophys. Res. **103**(B6): 12,355–12,364.

Michallet, H. and G.N. Ivey. 1999. Experiments on mixing due to internal solitary waves breaking on uniform slopes. Journal of Geophysical Research. **104**(C6)**:** 13,467-13,477.

Morillo, S., J. Imberger and J. Antenucci. 2006. Modifying the residence Time and Dilution Capacity of a Reservoir by Altering Internal Flow-Paths. Journal of River Basin Management. (*In press*).

Mortimer, C.H., 1952. Water movements in lakes during summer stratification; Evidence from the distribution of temperature in Windermere. Phil. Trans. B., **236**: 355-404.

Mortimer, C.H., 1953. The resonant response of stratified lakes to wind. Schweiz. Z. Hydrol. XV, 1.

Mortimer, C. H. 1974. Lake Hydrodynamics. Verh. Int. Ver. Limnol. **20:** 124–197.

Münnich, M.A., A. Wüest, and D.M. Imboden. 1992. Observations of the second vertical mode of the internal seiche in an alpine lake. Limnol. Oceanogr. **37**(8): 1705–1719.

Münnich, M. 1993. On the influence of bottom topography on the vertical structure of internal seiches. PhD Thesis, Swiss Federal Institute of Technology, Zürich.

Münnich, M. 1996. Influence of Bottom topography on internal seiches in stratified media. Dyn. Atmos. Oceans. **23**: 257-266.

Mysak, L. A., G. Salvadé, K. Hutter, and T. Scheiwiller. 1985. Topographic waves in a stratified elliptical basin, with application to the Lake of Lugano. Phil. Trans. R. Soc. Lond. A. **316:** 1–55.

Naithani, J., E. Deleersnijder, and P.D. Plisnier. 2003. Analysis of Wind-Induced Thermocline Oscillations of lake Tanganyika. Environmental Fluid Mechanics. **3**: 23-39.

Neumann, J. and G. Stanhill. 1978. The general meteorological background, p. 49–58. *In* S. Serruya [ed.], Lake Kinneret. Dr. W. Junk.

Ostrovsky, I., Y. Z. Yacobi, P. Walline, and I. Kalikhman. 1996. Seiche-induced mixing: Its impact on lake productivity. Limnol. Oceanogr. **41:** 323–332.

Patterson, J.C., P.F. Hamblin and J. Imberger. 1984. Classification and dynamic simulation of the vertical density structure of lakes. Limnol. Oceanogr. **29**(4): 845-861.

Perez-Losada, J., E. Roget, and X. Casamitjana. 2003. Evidence of High Vertical wave-number behaviour in a continuously stratified reservoir. Journal of Hydraulic Engineering. **129**(9): 734-737.

Pickrill, R.A. and J. Irwin. 1982. Predominant headwater inflow and its control of lake-river interaction in Lake Wakatipu. New Zealand Journal of Marine and Freshwater Research. **16**: 201-213.

Pierson, D. C. and G. A. Weyhenmeyer. 1994. High resolution measurements of sediment resuspension above an accumulation bottom in a stratified lake. Hydrobiologia. **284**: 43–57.

Reynolds, C.S. 1990. Temporal scales of variability in pelagic environments and the response of phytoplankton. Freshwater Biology. **23** (1):25-53.

Rigosi , A. A physical-ecological model of lake Beznar ecosystem. Propagation of uncertainty from physical to population dynamic predictions. Master Theses. University of Granada. 89 pp.

Riley, J.P., Skirrow, G., 1974. Chemical Oceanography. Academic Press, New York.

Robson B.J. and D.P. Hamilton. 2004. Three-dimensional modelling of a Microcystis bloom event in the Swan River estuary, Western Australia. Ecological Modelling. **174** (1-2): 203-222.

Roget, E., G. Salvadé, and F. Zamboni. 1997. Internal seiche climatology in a small lake where transversal and second vertical modes are usually observed. Limnol. Oceanogr. **42**: 663-673.

Rojo, C. and M. Alvarez-Cobelas. 2001. Phytoplankton structure and dynamics at a daily temporal scale: Response to the thermal overturn. Archiv für Hydrobiologie. **151** (4): 549-569.

Romero J.R. and J. Imberger. 2003. Effect of a flood underflow on reservoir water quality: Data and three-dimensional modelling. Archiv Fur Hydrobiologie. **157** (1): 1-25.

Romero J.R., J.P. Antenucci and J. Imberger. 2004. One- and three-dimensional biogeochemical simulations of two differing reservoirs. Ecological Modelling. **174** (1-2): 143-160.

Rueda, F. J., S. G. Schladow and S. O. Palmarsson. 2003. Basin-scale internal wave dynamics during a winter cooling period in a large lake. J. Geophys. Res. **108:** art. no. 3097.

Rueda, F.J., S.G. Schladow, S.G. Monismith SG, and M.T. Stacey. 2005. On the effects of topography on wind and the generation of currents in a large multi-basin lake. Hydrobiologica. **532**(1): 139-151.

Rueda, F.J., E. Moreno-Ostos and J. Armengol. 2006. The residence time of river water in reservoirs. Ecological Modelling. 191: 260-274.

Sabater, F, J. Armengol and S. Sabater. 1991. Physico-chemical disturbances associated with spatial and temporal variation in a Mediterranean river. Journal of the North American Benthological Society. **10**: 2-13.

Safaie, B. 1979. Mixing of Buoyant Surface Jet over Sloping Bottom. ASCE Journal of Waterway, Port, Coastal and Ocean Engineering Division. **105**(4): 357-373.

Saggio, A. and J.Imberger. 1998. Internal wave weather in a stratified lake. Limnol. Oceanogr. **43**(8): 1780-1795.

Salvadé, G., F. Zamboni, and A. Barbieri. 1988. Three-layer model for the North Basin of the Lake of Lugano. Annales Geophysicae. **6**: 463-474.

Schwab, D.J. and K.W. Bedford. 1995. Operational Three Dimensional Circulation Modeling in the Great Lakes, *in* Computer Modelling of Seas and Coastal Regions, Comp. Mech. Pubs., Boston, pp. 387-395.

Serra, T., T. C. Granata, J. Colomer, A. Stips, F. Møhlenberg, and X. Casamitjana. 2003. The role of advection and turbulent mixing in the vertical distribution of phytoplankton. Estuarine, Coastal and Shelf Science. **56**(1): 53-62.

Serra, T., J. Vidal, J. Colomer, X. Casamitjana, and M. Soler. 2007 The role of surface vertical mixing in phytoplankton distribution in a stratified reservoir. Limnol. Oceanogr. In press.

Serruya, S., E. Hollan and B. Bitsch. 1984. Steady winter circulation in Lakes Constance and Kinneret driven by wind and main tributaries. Arch. Hydrobiol.Suppl.**70**(1): 33-110.

Sherman, F. S., J. Imberger and G.M. Corcos. 1978. Turbulence and mixing in stably stratified waters. Ann. Rev. Fluid Mech. **10**: 267-288.

Singh, B., and C.R. Shah. 1971. Plunging Phenomenon of Density Currents in Reservoirs. La Houille Blanche. **26**(1): 341-352.

Spigel, R.H., J. Imberger and K.N. Rayner. 1986. Modeling the diurnal mixed layer. Limnol. Oceanogr. **31**: 533–556

Spiegel, R.H., and J. Imberger, 1980. The classification of mixed layer dynamics in lakes of small to medium size. J. Phys. Oceanogr. **10**: 1104-1121.

Stefan, H.G., T.R. Johnson, C.R. Ellis, G.J. Farrell and J. Akiyama. 1988. Physical limnology, laboratory studies on the initiation of density currents by inflows to lakes and reservoirs. Verhandlungen Internationale Vereinigung für Theoritische und Angewandte Limnologie, Stuttgard, Germany. **23**:58-61

Stevens, C. and J. Imberger. 1996. The initial response of a stratified lake to a surface shear stress. Journal of Fluid Mechanics. **312**: 39-66.

Stevens, C., G. Lawrence, P.Hamblin, E.Carmack. 1996. Wind forcing of internal waves in a long narrow stratified lake. Dyn. Atmos. Oceans, **24**: 41-50.

Stevens, C. L., and G. A. Lawrence. 1997. Estimation of wind-forced internal seiche amplitudes in lakes and reservoirs, with data from British Columbia, Canada. Aquatic Sciences. **58**(4): 1-19.

Straškraba, M, J.G. Tundisi and A. Duncan. 1993. State-of-the-art of reservoir limnology and water quality management. *In* Comparative Reservoir Limnology and water Quality Management. (ed. M. Straskraba, J. G. Tundisi and A. Duncan), pp. 213-288: Kluwer Academic Publishers.

Swart, D.H.. 1974. A Schematization of Onshore-Offshore Transport. *In*: Proceedings of the 19th International Conference on Coastal Engineering, ASCE.

Thorpe, S. A. 1974. Near-resonant forcing in a shallow two-layer fluid: A model for the internal surge in Loch Ness? J. Fluid Mech. **63:** 509–527.

Vidal, A. 1977. Eutrofización del embalse de sau en el transcurso de sus primeros años (1963-1972). *In* Trabajos de la II Asamblea Nacional de Geodesia y Geofísica., pp. 1955-1997. Barcelona.

Vidal, A. and J. Om. 1993. The eutrophication process in Sau reservoir (NE Spain): A long term study. Verhandlungen der Internationale Vereinigung für theoretische und angewandte Limnologie. **25**: 1247-1256.

Vidal, J., X. Casamitjana, J. Colomer, and T. Serra. 2005. The internal wave field in Sau reservoir: Observation and modeling of a third vertical mode. Limnol. Oceanogr. **50**(4): 1326–1333.

Wanninkhof, R., 1992. Relationship between wind speed and gas exchange over the ocean. J. Geophys. Res. **97**: 7373–7382.

Wiegand, R. C., and V. Chamberlain. 1987. Internal waves of the second vertical mode in a stratified lake. Limnol. Oceanogr. **32**(1): 29-42.

Wilson, B. W. 1972. Seiches. *In* Advances in Hydrosciences, edited by V. T. Chow. Academic, San Diego, Calif. pp. 1-94.

Winterwerp, J.C., 1998. A simple model for turbulence induced flocculation of cohesive sediment. J. Hydraulic Res. **36**: 309–326.

Wüest, A. G. Piepke and D.C. Van Senden. 2000. Turbulent kinetic energy balance as a tool for estimating vertical diffusivity in wind-forced stratified waters. Limnol. Oceanogr. **45**: 1388-1400.

Wüest, A and A. Lorke. 2003. Small-scale hydrodynamics in lakes. Annu. Rev. Fluid Mech. **35**: 373-412.

Wunderlich, W.O., and R.A. Elder 1973. Mechanics of Flow through Man-Made Lakes, Man-made Lakes: Their Problems and Environmental Effects. W.C. Ackermann, G.F. White, and E.B. Worthington, eds., American Geophysical Union, Washington, D.C., pp. 300-310.